MULTISCALE MODELING APPLICATIONS IN CARDIOVASCULAR DISEASE AND PUBLIC HEALTH

A DISSERTATION

Presented to the faculty of the
School of Engineering and Applied Science
in partial fulfillment of the requirements for the degree of

Doctor of Philosophy

---

by STEPHANIE MICHAELA RIKARD

August 2021

DEPARTMENT OF BIOMEDICAL ENGINEERING

UNIVERSITY *of* VIRGINIA

APPROVAL SHEET

This dissertation is submitted in partial fulfillment of the requirements for the degree of
Doctor of Philosophy in Biomedical Engineering

S. Michaela Rikard
Dissertation Author

This dissertation has been read and approved by the examining committee:

Shayn Peirce-Cottler, Ph.D.
Dissertation Advisor
Department of Biomedical Engineering

Jefferey Saucerman, Ph.D.
Committee Chair
Department of Biomedical Engineering

Silvia Blemker, Ph.D.
Committee Member
Department of Biomedical Engineering

Laura Barnes, Ph.D.
Committee Member
Department of Engineering Systems and Environment

Michael D. Williams, M.D.
Committee Member
Frank Batten School of Leadership and Public Policy
Department of General Surgery

Accepted for the School of Engineering and Applied Science:

Jennifer L. West, Ph.D.
Dean, School of Engineering and Applied Science

ii

DEDICATION

Well, I can't think of a better time to write this than on the way to celebrate the wedding of Dr. Molly Kelly-Goss – fellow Peirce Pirate, office mate, friend, supporter, and colleague who guided me through the first three years of graduate school. When I started this PhD program, I knew it would be one of the hardest things I had done yet, but I didn't anticipate how incredibly rewarding the journey would be and the amazing people I would meet and friends I would make along the way. There are so many people who have supported me on this journey and I wouldn't be here or the person that I am today without their guidance, mentorship, and friendship.

I owe the biggest thank you to my incredible advisor, Dr. Shayn Peirce-Cottler. From the very first day I stepped in lab, Shayn has been nothing but supportive of all of my crazy ideas, ambitions, extracurricular pursuits, and career goals. I'm pretty sure it was my very first meeting with Shayn where I was already floating ideas about also getting an MPH or taking classes in public policy. Instead of doing what any other advisor would have done which is to tell me to focus on my PhD and research, she sent me to a public policy conference in D.C. my very first semester in graduate school. It was the beginning of an important journey for me to discover and explore a passion for science policy, and Shayn has been there to support that journey every step of the way. Shayn, I am continually amazed and inspired by your ability to juggle so many responsibilities and roles with such poise and humility. Your passion for teaching and mentoring students through their unique journeys is your superpower. I have learned so many things under your mentorship, but I especially appreciate what you have taught me about being an effective communicator. Your skills as an eloquent writer and engaging presenter are unparalleled and I have learned so much from your example. I'm truly sorry that I am so terrible at sending regular updates and told you most things after I had already done them, but thank you for always having the trust and confidence in me to make my own mistakes and come to you when I really needed a lifeline. You were always there to back me up and be my number one advocate.

To the rest of the Peirce Pirates, both past and present, I couldn't have asked for a better group to spend these last five years with. I knew when I rotated in the lab my first semester that this group had just the right amount of humor and sarcasm to make even the tough times in graduate school bearable. Whether it was rollercoasters, happy hours, wing day, dog play dates, hiking, or trips to CVS for sour patch kids and M&Ms, thanks for all of the laughs and memories and making this a truly memorable experience. To the current members of the lab – this past year has been incredibly challenging for everyone. The lack of happy hours, and coffee runs,

and comradery of being together in the lab has made a difficult time even more challenging. But as someone told me this past year, it is tough for all of us and it will get better. Graduate school does getter better. Lean on each other, support each other, and bring back all of those traditions that make the Peirce-Cottler lab one of the best and start some new traditions of your own. The "lab mom" role must go on.

If all of this weren't enough, I have had the incredible fortune to found and lead the National Science Policy Network during my time in graduate school. I had no intention of doing any of this, or any idea that this was possible. I have been unbelievably lucky to meet the most amazing people and have the support of some incredible mentors through this work. I owe the biggest heartfelt thank you to Robbie Barbero and Kumar Garg, who believed in me and pushed me to do things I didn't know were possible. Your ability to be force-multipliers and inspire others is remarkable and I am constantly learning from your example and leadership. It's been a ride, but a rewarding one filled with so much growth, and I'll always take your call. Through this organization, I have also had the pleasure of meeting other graduate students all across the country who are true innovators and leaders. I am so honored to call you all my friends and witness the amazing contributions you have already made and I am sure will continue to make throughout your careers. I am so excited to continue on this journey with all of you and see where it takes us next.

To the countless other people who have made these past five years memorable – everyone in the BME department, graduate students in other departments, my volleyball crew – thank you for your friendship and support. And to my parents, yes school is going well and yes, I'm very busy. Thank you for supporting me no matter what and being proud of my accomplishments even if you have no idea what I do. And yes, this means I'm done with school now…I think. Thank you to everyone who made this possible and I am eagerly looking forward to what the next stop in this journey will bring. Onward!

<div align="right">

-Michaela
June 5, 2021

</div>

ABSTRACT

Multiscale computational models are powerful tools that integrate data and systems across spatial, temporal, and biological scales in order to make predictions about the behaviors of complex systems. Continued advancements in experimental methods and biomedical technology are generating vast amounts of data that require more sophisticated computational models and analytical methods in order to draw conclusions about complex processes and outcomes that span multiple scales of resolution. In the context of biomedical sciences and human health, these models are particularly relevant in the area of drug design and discovery where small molecules are designed with sub-cellular targets, but have effects across many biological and temporal scales. Experimental data from preclinical animal models can be expansive and have high variability, and multiscale computational models can be leveraged to predict how therapies will translate to humans. Additionally, the rapid growth of big data in health care in recent years including wearable sensors, telehealth, and electronic health records provides an opportunity for multiscale models to integrate disparate data sources to inform evidence-based interventions and transform the delivery of health care. Multiscale computational models provide a unique platform for high-throughput and systematic perturbation of parameters and conditions that may not be otherwise feasible due to time, cost, technological, or ethical considerations. An integrated approach that combines experiments with computational models can aid the design of preclinical and clinical studies, as well as public health interventions. The work presented in this thesis demonstrates novel applications of multiscale modeling approaches to design interventions in the case of diabetic wound healing, infarct healing following myocardial infarction, and the use of electronic health records to identify individual social risk factors and their impact on patient-level health outcomes.

CONTENTS

LIST OF FIGURES

LIST OF TABLES

CHAPTER 1

Introduction

Overview

Multiscale computational models are powerful tools to accelerate and enhance biomedical research discovery and health care innovation with wide-ranging applications across these sectors. Consequently, this thesis will not focus on one specific disease model or system, but instead demonstrates how the fundamental assumptions and core principles of multiscale modeling can be applied to important challenges in the treatment of cardiovascular disease and innovations in public health. This chapter aims to provide an overview of the core principles and topics that will be integrated throughout the multiscale modeling applications presented in this thesis. First, I will start with a comprehensive overview of the applications of multiscale computational models and a deeper discussion of agent-based modeling, a specific type of multiscale model. This will be followed by an overview of population health and opportunities for multiscale models to inform interventions and innovations in the delivery of health care and public health. Finally, I will describe the epidemiology and physiology of cardiovascular disease in particular, with a focus on the biological processes and cell types involved in wound healing in the context of diabetic wound healing and scar formation following myocardial infarction.

Multiscale computational modeling

Continued advancements in experimental methods and technology has enabled measurements with finer resolution and precision in addition to generating very large datasets using new technologies such as single cell RNA-seq, proteomics, diagnostic imaging, wearable sensors, and electronic health records.[1] These advancements necessitate similar advancements in computational methods and data analytics in order to make assumptions and draw conclusions for complex biomedical phenomenon spanning multiple scales of spatial and temporal resolution. This

is particularly relevant in the area of drug design and discovery where small molecules are designed with targets at the cellular or sub-cellular level, but often have effects across many length scales from the single cell to multi-organ systems, and time scales from milliseconds to years.[2] Computational models are powerful tools that can integrate data and processes across all of these scales to make predictions in a systematic and high-throughput manner about how perturbations to individual parameters influence the behavior of complex systems.

Multiscale computational models are a broadly defined class of models that explicitly represent processes which occur across multiple spatial, temporal, or biological scales.[3] An example application of multiscale models for drug development in cardiac disease is predicting the tissue-level effects of antiarrhythmic drugs, which have targets on potassium and sodium channels in the heart. Multiscale models attempt to link individual models that describe the mechanisms of drug interactions with ion channels at the molecular scale, with models at the multi-cellular and tissue level that describe the electrophysiology of cardiomyocytes and predict the potential for arrythmias, which are an emergent phenomenon at this spatial scale.[2, 4] Multiscale computational models are useful for extracting understanding from highly dynamic temporal and spatially heterogeneous systems by linking processes from the molecular scale, to cell-cell and cell-matrix interactions, up to tissue-level remodeling, and multi-organ system effects, and even population-level outcomes. By coupling experimental methods with theoretical and computational models, we can gain further understanding of complex biomedical systems by identifying emergent phenomenon that are not otherwise apparent at the individual scales of resolution. This approach can be used to couple and validate data across many scales of resolution and generate new questions and hypotheses that can be further explored experimentally.

Multiscale computational models have several unique advantages that make them a powerful tool in biomedical research and health care innovation including the ability to: i) measure parameters that are impossible to measure with experimental methods[5, 6], ii) perform high-throughput perturbation and analysis of parameters that would not be feasible experimentally[7], iii) develop patient-specific models (e.g. "digital twins") to inform diagnoses and intervention strategies[8-10], iv) aid the design of preclinical and clinical studies by translating results from animal models to human patients[11-13], and v) model population-level behaviors to identify new interventions and innovations in the delivery of health care.[14-16]

The following examples highlight a few of these key advantages and contributions of multiscale models to advancing biomedical research and health care innovation. A network model of cardiac fibroblast signaling by Zeigler et al. was developed to perform high-throughput *in silico* screening of 36 unique drug-target interactions of FDA-approved drugs to predict their effects on collagen deposition and fibrosis.[17] Klank et al. developed a model of tumor progression and metastasis to predict how alterations to single cell migration and proliferation rates impacted the rate of tumor growth.[5] An agent-based model of neovascularization in tissue-engineered scaffolds developed by Artel et al. identified the optimal pore size for tissue scaffolds in order to promote vascularization in engineered tissues.[7] Bruce et al. developed an agent-based computer simulation to predict the most effective strategies for vaccine allocation and distribution during an H1N1 influenza outbreak.[15] These examples also highlight that computational models can be used at all phases of the pipeline in biomedical research, biomedical device design and development, and innovation in the delivery of health care. Multiscale computational models can be leveraged to design experimental studies by identifying the most promising parameters or hypothesis to test, to

synthesize the results of many experimental studies and develop new understanding of the underlying mechanisms, and to inform new strategies and policies in the delivery health care.

While there have been many recent advancements in linking models across several spatial, temporal, and functional scales to generate multiscale models, the field is still far from generating complete "gene-to-organism" models. There is a need for improvement and standardization in the data sources, parameterization and validation methods, computational resources, and software platforms to generate more comprehensive and usable multiscale computational models.

Agent-based modeling

The application of agent-based models in the biomedical sciences is a relatively new approach, but agent-based models have been widely used in epidemiology, ecology, and the social sciences.[18-22] While continuum-based modeling methods generally assume a homogenous cell population or global environmental parameters, agent-based models represent cells as discrete entities that can modify their behavior based on the local environment and interactions with other agents. The overarching assumption of agent-based modeling is that local interactions between agents results in complex emergent phenomenon that cannot otherwise be explained by other methods. Local interactions between agents may include cell-cell or cell-matrix interactions defined by parameters that govern cell migration, proliferation, matrix properties, biochemical or biomechanical stimuli, and other finely tunable parameters.

The basic components of an agent-based model include the agents, value layers or environment, rules that govern agents' behavior, and initial conditions. Agent-based models can be 2D or 3D models and represent a wide range of spatial scales ranging from a single cell model where agents represent individual proteins or components of a cell, to tissue or organism level

models where agents represent individual or groups of cells. An example of the former is an agent-based model of the Notch signaling pathway in angiogenesis, where the agents are individual signaling receptors that are shuttled from the cell membrane to the nucleus within a single cell.[23] However, the most common scale of spatial resolution in agent-based models is the depiction of individual cells as agents, where there can be a single class of agents representing one cell type, or multiple classes of agents each representing a different cell type that behave by their own set of governing rules. A model of pulmonary fibrosis, which included agents representing both fibroblast and epithelial cell populations, was able to identify novel interventions that targeted the co-regulatory behaviors of these cell populations as pro-fibrotic mediators.[24]

The rule set that governs agents' behavior is typically defined based on literature and experimentally determined values in combination with a conceptual understanding of the biological processes involved. These rules can be either deterministic or stochastic in nature.[3] Systems of ordinary differential equations (ODEs) or partial differential equations (PDEs) are generally used to represent receptor signaling or reaction-diffusion kinetics and are typically deterministic[25], whereas rules governing cell migration, for example, may be defined by a probability distribution that can be modified by local chemokine concentrations or mechanical stimuli.[26] One of the unique advantages of agent-based modeling is the explicit representation of spatial scales of resolution. However, the choice of spatial resolution and continuous or discrete spatial scale can significantly impact model predictions and consideration of the appropriate spatial scale is essential in the conceptualization of an agent-based model.[27] This explicit representation of spatial parameters is particularly useful for predicting emergent spatial patterning in biological systems, such as vessel branching patterns during angiogenesis in vascular biology,[28, 29] or tumor angiogenesis.[30, 31] Similarly, the timescale of agent-based models can vary widely from milliseconds

to hours or days and is an important consideration based on the hypothesis or objective of the model.[32]

Agent-based models are particularly amenable to multiscale modeling since they can be easily coupled with other modeling approaches. ODE or PDE models, for example, can even act as sub-models or modules operating with different temporal or spatial scales within an agent-based model. A common example of this is the coupling of an ODE network model to inform the intracellular signaling state of individual cells represented spatially in an agent-based model.[33] The network model will likely have a time step several orders of magnitude smaller than that of the agent-based model. Agent-based models can also be coupled with models at higher tiers of spatial or temporal resolution. This has been achieved by coupling finite element models that predict local changes in tissue mechanics and strains using a mesh that corresponds to locations in the agent-based model value layers.[27, 34]

Defining rules and parameters for agent-based models is quite challenging. Modelers often discover that the exact parameters needed are not readily available in existing literature, or even feasible to measure in experimental studies. Furthermore, validating parameters or model outputs that are not easily measured experimentally makes model validation difficult. It is important to consider the experimental data available for model validation when designing an agent-based model and the relevant outputs that should be quantifiable. One strategy that has been suggested for the validation of multiscale models is "hierarchical validation" where individual sub-models are validated at a single scale of resolution before validating the systems-level multiscale predictions.[3, 35] Parameter estimation, model validation, and uncertainty analysis are ongoing and important topics of discussion in agent-based modeling.

Multiscale models in health care and public health

Agent-based models also have applications in policy analysis and public health. They are useful tools for simulating social networks by representing individuals as agents and modeling their behavior and decisions.[36, 37] In this manner, agent-based models have been used to simulate everything from how the spread of misinformation on the Internet impacted health behaviors during a norovirus outbreak,[38] to modeling COVID-19 vaccine distribution and its impact on the number of infections.[39] Furthermore, there has been an explosion of data in health care in the past two decades – from wearable sensors and remote monitoring, to telehealth, and the introduction of electronic medical records.[40] Advancements in multiscale modeling and predictive analytics have the potential to transform the delivery of health care by integrating all of these data sources to inform new strategies that can improve health outcomes and reduce health care costs.

Motivated partially by the evolution of the U.S. healthcare system from fee-for-service to value-based payment models, there have been more efforts to utilize data analytics and predictive models particularly for identifying high-risk and high-cost patients.[41] It has been estimated that up to one-third of hospital admissions are avoidable, which presents an obvious opportunity to improve the delivery of health care and reduce costs.[41, 42] In 2012, the Centers for Medicare and Medicaid Services (CMS) introduced the Hospital Readmissions Reduction Program (HRRP), which reduces payments for hospitals that have high 30-day hospital readmission rates, incentivizing healthcare systems to implement new processes and interventions to reduce preventable readmissions.[43, 44] This has prompted an increasing number of efforts to develop and improve predictive models for hospital readmission risk.[45, 46] These predictive models have typically utilized electronic medical records and insurance claims data to access measures such as laboratory

results, vital signs, comorbidities, or history of health care utilization, but these models have relatively poor predictive performance.[46] Efforts to improve the predictive performance of these models have focused on integrating other sources of data, with a particular emphasis on capturing the socioeconomic factors that contribute to an individual's health.[47] The future of multiscale modeling in healthcare will involve linking data from many different sources, to potentially include genomics and proteomics data, real-time remote monitoring, insurance claims, electronic medical records, smart phone data, and more.

Population health and determinants of health

Increased emphasis on the social and economic conditions that contribute to individual health and well-being are a result of the historic shifts in the determinants of health and evolution of medicine and health care. The innovations in medicine and public health over the last century have led to a change in the leading causes of death worldwide from infectious diseases to chronic diseases, with cardiovascular disease now the leading cause of death globally.[48] With this shift in the primary causes of death also brings a new and evolving set of determinants that affect the health of individuals and populations.

In the first half of the 20th century, the leading causes of death included pneumonia, diarrhea, and enteritis, which were largely associated with poor sanitation and unhealthy living conditions.[49] Public health interventions focused on motor-vehicle safety, occupational safety, food safety, and the fluoridation of drinking water.[50-52] The middle of the 20th century saw a dramatic increase in the rates of heart disease and cancer. The focus of the healthcare system shifted to improving health care services including childhood vaccination, maternal and prenatal care, and treatments for high blood pressure.[53] Some interventions such as screening for high blood pressure

began to emphasize preventative care, but largely the focus of health care was on the treatment of disease. Large seminal studies in the second half of the 20th century, such as the Framingham study, began to point to the contributions of individual health behaviors such as smoking, diet, physical inactivity, and alcohol use to the leading causes of death, which were heart disease, cancer, stroke, and lung disease.[54] The overwhelming sentiment at this time was that lifestyle choices were the primary determinants of health and well-being, which were deemed to be modifiable and entirely within the control and personal responsibility of individuals.[55]

The era of precision medicine at the turn of the century brought with it an understanding of the association between genetic risk factors and disease outcomes, in addition to the individual health behaviors identified previously. The idea that pharmacologic interventions could be tailored to individuals based on their genetic profile emerged, and the complete sequencing of the human genome accelerated genome-wide association studies[56] and the use of genomics for diagnosis and treatment.[57] The focus of precision medicine has been on tailoring drug prescribing based on an individual's biomarkers[58], or developing patient-specific models to guide interventions.[59, 60]

More recently, public health efforts are shifting to focus on the "upstream factors" or social and economic conditions that contribute to morbidity, mortality, and quality of life. Increasingly, research points to the social and economic determinants of health (i.e. socioeconomic status, race and ethnicity, housing conditions, income inequality, educational attainment, etc.) that account for up to 80% of modifiable determinants of health.[61-64] Access to medical care and quality of care comprise only 20% of these modifiable factors, as outlined by County Health Rankings.[65] These social determinants of health are the conditions in which people are born, grow, live, and work, and are largely outside the control of the individual. Instead, they are shaped by local and national policies and the amount of money, power, and resources that individuals and communities can

access.[66] The next era of health care and public health will involve the coordination of care between health systems and social services or community-based organizations to address the many facets of individual health and well-being. These efforts will require data-driven approaches linking many sources of data to identify high-risk patients and provide appropriately personalized care.

Epidemiology and health care burden of cardiovascular disease

Cardiovascular disease (CVD) is the leading cause of death worldwide, accounting for more than 900,000 deaths annually in the U.S., and 18.6 million globally.[67, 68] Nearly 50% of these deaths are attributed to ischemic heart disease.[68] Advances in treatment options and preventative care helped promote large declines in CVD mortality in the late 20th century, but this trend has slowed significantly in the past decade and the CVD mortality rate is no longer demonstrating the same improvements.[69] There also exists alarming geographic variation in the burden of CVD and mortality rates at the state and county levels, with some localities experiencing an increase in the burden of CVD and even a decrease in the life expectancy for some groups, while other regions have seen marked improvements in CVD burden and mortality.[67] There are also significant disparities in CVD burden across sex, race, ethnicity, and socioeconomic status,[70, 71] and the disparities are staggering; African Americans and non-Hispanic whites are 30% more likely to die from heart disease.[72]

The increasing burden of CVD has also contributed significantly to rising health care costs in the U.S., accounting for nearly 15% of all health expenditures.[73] Direct costs are over $200 billion annually, with another $130 billion attributed to lost productivity.[73] The rise of other chronic diseases including diabetes and obesity also contribute to increasing costs and utilization of health care, with nearly 50% of the U.S. population suffering from chronic disease and

comprising more than 85% of all health care costs.[74] CVD and diabetes are often closely linked, with CVD being the most common cause of morbidity and mortality in diabetic patients. Many of the risk factors for CVD including obesity, hypertension, and high cholesterol and blood glucose are prevalent in diabetic patients.[75] Chronically elevated blood glucose levels and insulin resistance have deleterious effects on the cardiovascular system, particularly the capillaries, which are the smallest blood vessels in the body. Diabetes is associated with chronic low-grade inflammation through the overexpression of many inflammatory cytokines in adipose tissue including tumor necrosis factor-α (TNFα), IL-1, IL-6, and others.[75] This inflammation and elevated blood glucose levels can have many consequences for the vasculature including endothelial dysfunction, atherosclerosis, impaired wound healing, retinopathy, and nephropathy.[76] Normal physiologic responses to injury allow for functional recovery of the cardiovascular system whether due to cutaneous wounds, or ischemic events, such as stroke and myocardial infarction. However, the chronic inflammation and impaired wound healing associated with CVD has widespread impacts on multiple disease progressions ranging from peripheral arterial disease, diabetic retinopathy, acute myocardial infarction, to cutaneous wound healing.

Physiologic wound healing and tissue repair

Wound healing is a complex and coordinated series of cellular and molecular events comprised of four distinct phases: coagulation and hemostasis, inflammation, proliferation, and tissue remodeling.[77, 78] Following injury to a tissue, hemostasis marks the first phase of wound healing as the damaged blood vessels initiate vasoconstriction and formation of a platelet plug through activation of circulating platelets.[79] Following hemostasis, the inflammatory phase is marked by the increase of inflammatory cytokines including IL-1β and TNFα leading to capillary

vasodilation.[80] Increased vascular permeability allows neutrophils and monocytes to emigrate from the vascular circulation to the wound site within 24 hours, and inflammatory cell populations peak within the first week of wound healing.[81] Neutrophils are the first inflammatory cell population recruited to the site of injury and remove bacteria from the wound.[82] Macrophages phagocytose and digest tissue debris and include both monocytes recruited from the bone marrow that differentiate to macrophages and tissue-resident macrophages.[79] However, monocyte-derived macrophages are the primary source of inflammatory macrophages; the role of tissue-resident macrophages during wound healing in not well documented. Some macrophage subpopulations secrete TGFβ which stimulates fibroblast recruitment and proliferation and may also contribute to the transformation of macrophages to a more anti-inflammatory phenotype.[83]

As the inflammatory phase subsides, the proliferative phase may last for days to weeks and is marked by the proliferation of fibroblasts and transition to a myofibroblast phenotype, along with synthesis of many extracellular matrix (ECM) components including collagen.[81] Myofibroblasts express αSMA and are a contractile cell type that deposits collagen to form the scar tissue and coordinates contraction to physically close the wound.[79] During this proliferation phase, endothelial cells also rapidly proliferate and angiogenesis supplies granulation tissue with the necessary oxygen and nutrients to aid healing. Remodeling of the tissue and ECM turnover may continue for weeks to months and is directed by myofibroblasts.[77] Myofibroblasts are eventually cleared from the injured tissue through a combination of apoptosis and possibly their differentiation back to a quiescent fibroblast phenotype.[79] The persistence of a myofibroblast population and collagen deposition can lead to interstitial and perivascular fibrosis.

Physiologic wound healing requires precise and complex temporal and spatial coordination of the cell types and chemokine signals that direct each of these distinct phases. Improvements in single-cell technology have increased the understanding of the amount of heterogeneity that exists in these cell types, particularly fibroblast and macrophage populations. Dysregulation of any one of these phases of wound healing can lead to chronic wounds that do not heal or aberrant scar formation leading to fibrosis. In diabetes, for example, chronic inflammation prolongs or delays normal wound healing and can prevent wound closure in the case of diabetic ulcers.[84] Wound healing in cardiac tissue is unique because cardiomyocytes cannot replicate and instead, myofibroblasts deposit large amounts of collagen to replace necrotic tissue with collagen-rich scar.

Macrophage recruitment and polarization during wound healing

Recruitment of inflammatory cells (i.e., macrophages and neutrophils) is essential for wound healing and are the primary source of the cytokines and chemokines that drive cell migration and proliferation, and resolve inflammation in physiologic wound healing. Macrophages are broadly classified into two phenotypes: classical, or pro-inflammatory (M1) macrophages and alternative, or anti-inflammatory (M2) macrophages.[83, 85] Circulating monocytes are recruited to the wound site, extravasate from the vasculature, and differentiate to M1 type macrophages. Bruce et al. have previously demonstrated that circulating monocytes are recruited exclusively from postcapillary venules during arteriogenesis following spinotrapezius ligation in a murine model.[86] In acute wound healing, pro-inflammatory macrophages phagocytose foreign debris, necrotic cells, and clear neutrophils. As wound healing progresses, macrophages assume a more anti-inflammatory M2 phenotype that promotes the migration and proliferation of fibroblasts, and produces matrix metalloproteinases (MMPs) which are important for ECM turnover during scar

formation.[87] Macrophages also important in promoting the proliferation of endothelial cells, directing angiogenesis, and vessel stabilization through the recruitment of pericytes.[85] In chronic wounds, inflammation often persists and the proliferative and remodeling phases of wound healing cannot proceed.[87]

It is now widely accepted that there are multiple origins of macrophage lineages and a dynamic range of macrophage phenotypes, surface markers, and secreted cytokine profiles. Currently, there exist at least five different classifications for macrophage phenotypes.[85, 87, 88] While macrophage polarization implies two static states of macrophage phenotypes, many prefer to describe the dynamic range of macrophage phenotypes as a spectrum that is transient.[85] The extent to which differentiated macrophages can switch between these phenotypes and the role of tissue-resident macrophages in wound healing is not well known.[87, 89]

There are a variety of stimuli that drive macrophage activation pathways and are present at varying times and levels following an injury or ischemic event, creating a heterogenous and dynamic macrophage population. Several computational models have investigated the recruitment and dynamics of M1 and M2 macrophages following injury.[90, 91] Martin et al. published an agent-based model of inflammation following skeletal muscle injury that predicts the time course of macrophage infiltration as well as phenotype switching between an inflammatory (M1) and reparative (M2) phenotype.[91] Wang et al. developed a mathematical model that describes the dynamics of macrophage activation following myocardial infarction based on levels of IL-1, IL-10, and TNFα.[90] Computational models that accurately capture macrophage dynamics and heterogeneity will require the integration of many varying spatial and temporal cues. Multiscale

modeling is an important tool for understanding and modeling perturbations to macrophage dynamics following injury.

Wound healing in the context of myocardial infarction

Approximately 605,000 Americans will experience their first myocardial infarction (MI) this year, and another 200,000 will experience a recurrent MI[73]. Early treatment options including reperfusion therapy and pharmacologic intervention have led to a steady decline over the past several decades in the 30-day mortality rate.[92, 93] While the short-term outcomes are improving, the long-term complications are becoming more apparent and difficult to mitigate. The 5-year mortality rate for patients over 65 is over 50%[94], largely due to the risks of life-threatening complications including recurrent MI, stroke, infarct rupture, and left ventricular remodeling leading to heart failure.

Scar remodeling following MI is a dynamic process involving both temporally and spatially varying cell types, extracellular matrix (ECM) composition, cytokines, and growth factors. Myocyte death due to prolonged ischemia initiates an inflammatory response led by cytokines such as IL-1β and TNFα.[80] Neutrophils and macrophages are recruited to the wound site within 24 hours and inflammatory cell populations peak within the first week of wound healing and then subside as the proliferative phase begins.[81] Inflammatory macrophages secrete TGFβ which stimulates fibroblast recruitment and proliferation and may also contribute to macrophage conversion to a more anti-inflammatory phenotype.[83] The proliferative phase may last for days to weeks and is marked by the proliferation of fibroblasts and transition to a myofibroblast phenotype, along with synthesis of many ECM components including collagen.[81] Infarct healing is a complex

process involving both temporally and spatially varying cell types, cytokines, and constant ECM turnover, all further complicated by the unique mechanical environment of the heart.

The development of anti-fibrotic therapies for cardiac fibrosis is complicated because complete elimination of fibrosis would increase the likelihood for infarct rupture since some amount of scar tissue is necessary to reinforce and replace the damaged myocardium. Preliminary studies indicate that surgical reinforcement of the infarct[95], or injection of stiff polymers[96, 97] can improve LV function, but require invasive procedures.[98] Current pharmacological approaches, while less invasive, generally act by mitigating the risk factors associated with development of heart failure, but do not directly target cardiac fibroblasts and fibrosis. This class of drugs (e.g., ACE inhibitors, beta-blockers, angiotensin receptor blockers, etc.) largely target the renin-angiotensin-aldosterone system (RAAS) to reduce blood pressure and cardiac hypertrophy that leads to heart failure. TGFβ inhibitors more directly target ECM synthesis and fibrosis, but TGFβ is important in many complex signaling pathways affecting multiple cells types and may play different roles throughout the time course of wound healing, making therapies targeted specifically at fibroblasts and ECM synthesis difficult. Pirfenidone is a novel anti-fibrotic drug approved for treatment of idiopathic pulmonary fibrosis that inhibits the synthesis and secretion of TGFβ1. In animal models it has shown the ability to increase survival and attenuate collagen deposition, and clinical trials are currently ongoing.[98, 99]

One concern with any therapy that alters collagen deposition in the heart is that it will modify interstitial fibrosis in both the surviving healthy myocardium and scar, altering pump function of the heart. The ideal pharmacologic intervention will enhance scar formation in the infarct, while reducing interstitial fibrosis in the remote myocardium. Our novel approach to this

problem is to exploit the distinctive and dynamic signaling contexts in the infarct and remote myocardium, with a particular focus on the dynamics of pro-inflammatory and pro-fibrotic signals, to achieve the desired outcome of increased collagen deposition in the scar and reduced fibrosis in the remote myocardium. This multiscale framework for cardiac fibrosis that spans drug targets in fibroblast signaling networks to tissue-scale changes in extracellular matrix composition (Figure 1-1) will allow for systematic screening of novel drugs and combination drug therapies.
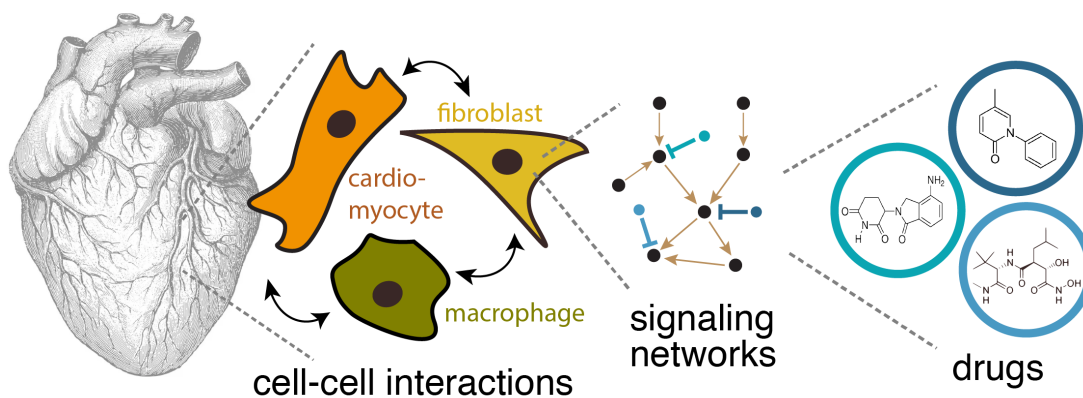
Figure 1-1. Multiscale model of cardiac fibrosis will span from drug-target interactions to tissue level infarct healing.

Wound healing in the context of diabetes

Diabetic foot ulcers are a type of chronic wound that can persist for months to years because the normal mechanisms of wound healing are profoundly impaired in diabetic patients. Over 30 million Americans are affected by diabetes, and nearly 15% of these patients experience diabetic foot ulcers in their lifetime.[100, 101] Diabetic foot ulcers are the leading cause of hospitalizations for patients with diabetes, and they are associated with significant pain, suffering, loss of quality of life, and increased risk for lower extremity amputation.[100] During acute wound healing in healthy individuals, cells respond dynamically to chemotactic cues (e.g., inflammatory cytokines and growth factors) to coordinate a linear progression of wound healing, which eventually leads to

complete wound closure. However, this coordinated progression is dysregulated in the case of chronic wounds. In particular, patients with diabetes experience microvascular dysfunction[77] combined with chronic inflammation[102], which delay or prohibit the normal wound healing process.

The key components for the treatment of chronic diabetic wounds include 1) pressure relief, 2) debridement, 3) infection control, and 4) revascularization.[103] Several novel therapies have been introduced to address each of these components including negative pressure wound therapy, hyperbaric oxygen therapy, tissue-engineered skin substitutes, antimicrobial biomaterials, stem cell therapies, and growth factors and cytokines to promote angiogenesis.[104] Numerous treatments designed to promote effective wound healing in diabetic patients have been evaluated in pre-clinical and clinical studies with limited efficacy and chronic diabetic wounds remain a costly and challenging clinical problem.[105-107] Stimulation of angiogenesis, or new microvessel formation[108, 109], has been pursued as one approach to jump-start the wound healing cascade in the angiogenesis-impaired setting of diabetes. Many growth factors have been investigated in the treatment of diabetic ulcers to promote angiogenesis, including platelet derived growth factor (PDGF), vascular endothelial growth factor (VEGF), fibroblast growth factor (FGF), and insulin like growth factor (IGF), but they each have complex effects at different phases in the wound healing process.[110] Combination therapies are a promising approach to target different cell types and phases of wound healing, but more studies are needed to identify the most effective approaches.[109]

Diabetic wound healing is another example of a complex biological process that requires precise spatial and temporal control of many cell types, cytokine and growth factors, and extracellular matrix components. Multiscale modeling is an important complement to

experimental methods in order to provide insight into the complex spatial and temporal interactions between cells and environmental factors and identify potential therapeutic targets.

Outline of thesis

Multiscale computational models can be leveraged to investigate processes spanning a wide range of spatial, temporal, and biological scales. Commonly used modeling approaches include: (1) ordinary differential equations (ODEs) which are often used to depict cell signaling and receptor kinetics or time dependent cell populations[90, 111, 112]; (2) partial differential equations (PDEs) which describe both temporal and spatial kinetics of phenomenon such as chemokine production and diffusion[113, 114]; (3) agent-based models (ABMs) which prescribe stochastic behaviors for individual agents that result in emergent behavior of the population[26, 115, 116]; and (4) statistical models which can be used to describe correlations between individual level predictors and population level outcomes. Multiscale models in particular, aim to integrate these modeling approaches across molecular, cellular, tissue, organ, organism, and population scales. Using multiscale modeling approaches, perturbations to parameters at the molecular or cellular level can predict quantitative changes at the tissue or organ level. This approach has been used in the design of preclinical and clinical studies where simulations of molecular perturbations, such as gene-editing or pharmacologic interventions, can predict quantitative changes in tissue-level structure and function.[91, 111, 115] In this thesis, many of these multiscale modeling approaches are utilized to design novel interventions in the case of infarct healing following myocardial infarction (Chapters 2 and 3), drug delivery for diabetic wound healing (Chapter 4), and utilizing electronic health records to identify individual social risk factors and their association with patient-level health outcomes (Chapter 5).

In Chapter 2, we developed a multiscale model of cardiac fibrosis by coupling a logic-based network model of fibroblast intracellular signaling with an agent-based model of multicellular tissue remodeling. The work presented in Chapters 2 and 3 was done in collaboration with the Saucerman and Holmes labs at the University of Virginia. Pathological remodeling of scar following an infarct can lead to complications including scar rupture and left ventricular dilation resulting in heart failure. The ability to effectively improve infarct healing will require spatial control of fibrosis. Previous computational models have extensively characterized cardiac fibroblast signaling pathways and expression profiles to provide information about fibroblast activation and kinetics[25, 117, 118], but fibroblast activation has generally been studied in response to single stimuli *in vitro*. Other researchers in the field have noted the need to understand fibroblast activation in response to mixed stimuli, and have called for the development of computational models that can integrate the effects of spatial and temporal shifts in fibroblast activation, with the cell-cell interactions and cell-matrix interactions that coordinate the short and long-term remodeling of scar tissue.[119] We developed a coupled logic-based network model of fibroblast intracellular signaling and agent-based model of tissue fibrosis, and then prescribed gradients of inflammatory and fibrotic cues to simulate the interactions between fibroblast intracellular signaling and spatially heterogeneous extracellular cues such as cytokines and collagen content. A subset of model predictions was validated by comparison to *in vitro* experiments using human cardiac fibroblasts treated with combinations of TGFβ1 and IL-1β. This multiscale model is the first example of coupling of a large-scale network model with an agent-based model to make predictions about individual cell network states and tissue-level changes in ECM composition. Further extension of this model and application in the context of post-MI wound healing will allow for predictions with

more precise spatial and temporal resolution with regards to cytokine concentrations, collagen content and heterogeneity, and cell behaviors and can ultimately be leveraged for high-throughput screening of drugs for the mitigation of cardiac fibrosis. This work has been published previously in *Frontiers in Physiology*.

In Chapter 3, we characterize the spatiotemporal dynamics of macrophage infiltration and polarization during the early phases of wound healing following myocardial infarction. The multiscale model developed in Chapter 2 demonstrated the importance of cytokine gradients and history-dependent behavior of fibroblast activation states. We sought to understand the upstream inflammatory cells that are responsible for the dynamic spatial and temporal gradients of inflammatory cues that direct fibroblast migration, proliferation, and activation to myofibroblasts. Using a rat model of myocardial infarction induced by permanent occlusion of the left descending artery, we harvested tissue biopsies from the left ventricular wall on days 1-6 post-infarction. A combination of histological techniques and immunohistochemistry were used to identify changes in the tissue architecture and collagen composition as well as the spatiotemporal dynamics of both M1 and M2-like macrophages at these time points. Image analysis methods were developed in order to quantify the trends in macrophage distribution and heterogeneity across spatially distinct regions of the infarct. We provide examples of unique spatial patterns of macrophage colocalization with cardiac fibroblasts in the infarct and evidence of a CD68+CD163+ macrophage population, which challenges traditional M1/M2 classifications to describe the diverse macrophage phenotypes observed *in vivo*. This work is one of the first examples of characterizing the spatiotemporal dynamics of macrophage populations in the heart following myocardial infarction and will inform future studies that aim to target macrophages for novel therapeutics to treat cardiac fibrosis and the development of heart failure.

In Chapter 4, we adapted a previously published mathematical model of cutaneous wound healing to simulate and modify spatial parameters of drug delivery with a modified VEGF-A mRNA to accelerate impaired diabetic wound healing. This work was done in collaboration with colleagues at AstraZeneca in Sweden. Diabetes causes chronic low grade-inflammation that impairs the normal wound healing process and can lead to chronic wounds or ulcers. We have previously demonstrated that injections with a modified RNA designed to upregulate VEGF-A protein expression in the skin and promote angiogenesis can accelerate healing in a murine model of diabetic wound healing. Previous studies have investigated the impacts of dose and timing of drug delivery on wound healing, but no studies have described the impact of spatial parameters such as location of injection or diffusivity of the drug on the rate of wound closure. We implemented a previously published model of cutaneous wound healing based on a system of coupled partial differential equations (PDE) that describe the density of sprouting capillary tips, chemoattractant concentration, and density of blood vessels in a circular wound and then modified this model to also include a PDE that describes the spatiotemporal dynamics of mRNA and VEGF-A production following injections with the modified mRNA drug. This new system of coupled PDEs was then used to predict how diffusivity of mRNA and location of the injection affect angiogenic sprouting, vascularization of the wound bed, and time to wound closure in a model of diabetic wound healing. The model predicted that wound healing could be accelerated by delivering injections a short distance inside the wound border. Perturbations to the diffusivity of mRNA predicted that limited diffusion could delay wound healing, while very high diffusivity would have no effect on wound healing. These findings highlight the importance of understanding the spatial parameters of drug delivery when designing preclinical and clinical models with

proangiogenic factors to promote wound healing. The work presented in Chapter 4 has been previously published in *Cellular and Molecular Bioengineering*.

In Chapter 5, we utilized electronic health records to identify individual social risk factors and developed mixed-effects statistical models to determine the association of those factors with increased risk for unplanned readmissions, emergency department utilization, and extended length of stay. This work was done in collaboration with Data Science at the UVA Health System and the Center for Health Policy in the Frank Batten School for Leadership and Public Policy. As the health care system in the U.S. begins to evolve from a fee-for-service to a value-based payment model, social and economic determinants of health have becoming an increasing area of focus for intervention since their impacts on a person's health and quality of life have been widely documented. Social determinants of health broadly describe factors including health behaviors (e.g., alcohol and drug use, physical activity, etc.), socioeconomic factors (e.g., employment, income, educational attainment, social support systems, etc.), and the physical environment (e.g., access to transportation, air and water quality, etc.). Up to 80% of modifiable determinants of population health outcomes (i.e., life expectancy and quality of life) can be attributed to social determinants of health, but these are not routinely considered in the development of patient care plans and impact on health outcomes. Even in the absence of standardized screening tools to assess a patient's social determinants of health, physicians are often aware of these conditions that impact their patient's health and document these findings in electronic health records. In this study, we used data in electronic health records to identify individual social and economic determinants of health for a set of inpatients treated at the UVA Health System over a one-year study period. These social determinants of health were used as a predictor variable in addition to clinical predictors such as severity of illness, sex, and age, in a set of statistical models that predict risk for

unplanned impatient readmission, emergency department admission, and extended length of stay. These models demonstrated that social determinants of health have significant impacts on all of these outcomes studied, but were the single most important predictor of emergency department revisits within 30 days of discharge from the hospital. This work in one of the first examples of using individual social determinants of health to predict health outcomes and provides an example for how health care systems can use existing data to determine the prevalence of social and economic needs in their patient population and prioritize further data collection or intervention programs to address these needs.

Finally in Chapter 6, I will conclude with a discussion of the key contributions and innovation of this work. I will expand on some of the most promising future directions for each of these studies and provide a commentary on the state of multiscale modeling, recommendations for advancement in the field, and potential new applications for multiscale modeling in preclinical and clinical studies. I will conclude with an overview of the broader societal implications of this work.

CHAPTER 2

Multiscale coupling of an agent-based model of tissue fibrosis and a logic-based model of intracellular signaling

[1]Department of Biomedical Engineering, Johns Hopkins University, Baltimore, MD, USA
[2]Department of Pharmacology, University of Virginia, Charlottesville, VA, USA
[3]Department of Biomedical Engineering, University of Virginia, Charlottesville, VA, USA
[4]Robert M. Berne Cardiovascular Research Center, University of Virginia, Charlottesville, VA, USA
[5]Department of Medicine, University of Virginia, Charlottesville, VA, USA

Abstract

Wound healing and fibrosis following myocardial infarction (MI) is a dynamic process involving many cell types, extracellular matrix (ECM), and inflammatory cues. As both incidence and survival rates for MI increase, management of post-MI recovery and associated complications are an increasingly important focus. Complexity of the wound healing process and the need for improved therapeutics necessitate a better understanding of the biochemical cues that drive fibrosis. To study the progression of cardiac fibrosis across spatial and temporal scales, we developed a novel hybrid multiscale model that couples a logic-based differential equation (LDE) model of the fibroblast intracellular signaling network with an agent-based model (ABM) of multi-cellular tissue remodeling. The ABM computes information about cytokine and growth factor levels in the environment including TGFβ, TNFα, IL-1β, and IL-6, which are passed as inputs to the LDE model. The LDE model then computes the network signaling state of individual cardiac fibroblasts within the ABM. Based on the current network state, fibroblasts make decisions regarding cytokine secretion and deposition and degradation of collagen. Simulated fibroblasts respond dynamically to rapidly changing extracellular environments and contribute to spatial heterogeneity in model predicted fibrosis, which is governed by many parameters including cell density, cell migration speeds, and cytokine levels. Verification tests confirmed that predictions of the coupled model and network model alone were consistent in response to constant cytokine inputs and furthermore, a subset of coupled model predictions were validated with *in vitro* experiments with human cardiac fibroblasts. This multiscale framework for cardiac fibrosis will allow for systematic screening of the effects of molecular perturbations in fibroblast signaling on tissue-scale extracellular matrix composition and organization.

Introduction

Approximately 605,000 Americans experience their first myocardial infarction (MI) each year, and another 200,000 experience a recurrent MI.[73] Approximately 82% of males and 77% of females survive at least one year following their MI[73], making management of post-MI recovery an increasingly important topic.

Wound healing and scar remodeling following myocardial infarction (MI) is a dynamic process involving many cell types, extracellular matrix, and inflammatory cues. Myocyte death due to prolonged ischemia initiates an inflammatory response led by cytokines such as IL-1β and TNFα[80]. Neutrophils and macrophages are recruited to the wound site within 24 hours and begin to phagocytose debris and propagate the inflammatory response. Inflammatory cells peak within the first week of wound healing and then begin to subside as the proliferative phase begins.[81] Inflammatory macrophages secrete TGFβ, which stimulates fibroblast recruitment and proliferation.[83] The release of TGFβ may also contribute to the conversion of macrophages to a more anti-inflammatory phenotype.[83] The proliferative phase may last for days to weeks and is marked by the proliferation of fibroblasts and transition to a myofibroblast phenotype, along with synthesis of many ECM components including collagen.[81] ECM deposition produces a scar in the infarct region that contributes to its structural stability during wound healing. This proliferative phase is followed by weeks to months of scar remodeling and significant ECM turnover.

Post-MI cardiac wound healing is a complex and dynamic process with many overlapping phases. The cardiac fibroblast is the key effector cell throughout the phases of wound healing that creates and remodels scar tissue.[120, 121] However, fibroblasts are a highly dynamic and plastic cell type that can transition from a pro-inflammatory phenotype in the early phases of wound healing

to an anti-inflammatory and pro-fibrotic phenotype later in the wound healing cascade.[121, 122] Fibroblast response to single cytokine inputs are well documented,[123-125] but fibroblast activation and cytokine secretion in response to multiple cytokines and other stimuli *in vivo* that shift over the time course of MI wound healing are not well described.[119] This lack of understanding of activation shifts over the time course of healing is at the core of the failure of many attempts to improve post-MI wound healing by modulating scar formation.[126] Inhibition of inflammation too early in the wound healing cascade can lead to thinning of the LV wall and scar rupture.[127-129] Aberrant fibrosis can lead to LV dilation and heart failure. This inherent complexity of the biological phenomenon necessitates the development of computational models to design and test therapeutic interventions that potentially have opposite effects at different phases throughout the wound healing cascade. Previous computational models have extensively characterized cardiac fibroblast signaling pathways and expression profiles to provide information about fibroblast activation and kinetics[25, 117, 118], but fibroblast activation has generally been studied in response to single stimuli *in vitro*. Other researchers in the field have noted the need to understand fibroblast activation in response to mixed stimuli, and have called for the development of computational models that can integrate the effects of spatial and temporal shifts in fibroblast activation, with the cell-cell interactions and cell-matrix interactions that coordinate the short and long-term remodeling of scar tissue.[119] A multiscale model that can translate cardiac fibroblast gene and protein expression to tissue level functional remodeling with spatial and temporal precision could provide an invaluable platform for identifying, testing, and validating new therapeutic interventions for inducing functional regeneration and mitigating fibrosis.

Our group has recently developed computational models to study distinct scales of cardiac wound healing, including a logic-based differential equation (LDE) model of intracellular

signaling in individual cardiac fibroblasts and an agent-based model (ABM) of collagen remodeling by multiple cells in the infarct.[25, 26] Each model represents a different spatial and temporal scale of the wound healing process. The LDE model provides detailed information about the network state of 91 different signaling nodes in an individual fibroblast, while the ABM predicts fibroblast number, collagen area fraction, and collagen alignment at the tissue level. In the work presented here, we couple these LDE and ABM models in order to capture the dynamic interplay between fibroblast intracellular signaling and spatially heterogeneous extracellular cues such as cytokines and ECM composition, which themselves are modulated by individual fibroblast behaviors. Verification tests confirmed that the coupled model and network model alone exhibit consistent behavior in response to constant cytokine and growth factor inputs, allowing for the establishment of a framework that can readily incorporate updates from either the network model or ABM without affecting the integrity of the individual model predictions. Furthermore, a subset of coupled model predictions was validated by comparison to measurements of pro-collagen 1, αSMA, and F-actin expression in human cardiac fibroblasts treated with combinations of cytokines and growth factors *in vitro*. We believe this work demonstrates the first coupling of a large-scale network model to predict tissue-level changes in ECM composition in the setting of fibrosis with feedback from environmental cues (e.g., diffusible cytokines) to regulate the signaling of individual cells. Predictions about cytokine and growth factor production from fibroblasts are computed in physical units, which were not previously possible with a logic-based network model alone. This coupled model provides a platform for systematically testing molecular interventions with the ability to measure their effects on single cell signaling and ECM composition with detailed spatial resolution.

Materials and Methods

Description of Individual Models

Agent–based Model

An agent-based model (ABM) is comprised of value layers and agents.[130] The value layers in this two-dimensional ABM represent features of the extracellular space, including collagen, latent TGFβ, active TGFβ, IL-1β, IL-6, and TNFα. All cytokines are stored as concentrations in pg/mL, and collagen is quantified as an area fraction. The value layers are divided into a 10x10 grid, where each individual grid space measures 10μm x 10μm. A volume for each grid space is approximated based on cell culture conditions in a 96 well plate, which is the primary source of experimental data used to inform this model. For soluble cytokines (active TGFβ, IL-1β, IL-6, and TNFα), it is assumed that these cytokines are uniformly distributed in the media above each cell, resulting in a compartment of 10μm x 10μm x 3125μm (3.125e-7 mL). Latent TGFβ binds to the extracellular matrix[131], and is thus assumed to occupy the space immediately surrounding the cell, or 10μm x 10μm x 10μm (1e-9 mL). The individual grid space approximates the footprint of a single fibroblast, allowing the model to simulate a maximum of 100 fibroblasts simultaneously. The total number of fibroblasts is kept relatively low to allow for calculation of the entire network state of each fibroblast while minimizing computational time for the purposes of method development. Value layers store a unique quantity in each grid space that can be modulated by parameters including degradation rates, activation rates, and the agents that move over them. The agents in this model represent cardiac fibroblasts that migrate and modulate their extracellular space by depositing and degrading collagen, and secreting cytokines.

Logic–Based Network Model

The logic-based differential equation (LDE) network model is a previously published[25] model of cardiac fibroblast signaling that integrates 10 signaling pathways with 11 biochemical or mechanical stimuli that are important for myofibroblast activation and ECM remodeling. These stimuli include IL-1 (interleukin 1), IL-6 (interleukin 6), TNFα (tissue necrosis factor α), NE (norepinephrine), NP (natriuretic peptide), β-integrins, TGFβ (tissue growth factor β), angiotensin II, PDGF (platelet derived growth factor), ET1 (endothelin 1), mechanical stimulation, and forskolin. The network includes 91 nodes connected by 142 reactions, which are supported by *in vitro* data collected from cardiac fibroblasts. The network was constructed using a logic-based ordinary differential equation modeling approach, where the activity of each node is modeled using a normalized Hill ODE with default parameters and logic gating. Default reaction parameters include weight (0.9), Hill coefficient (1.4), and EC_{50} (0.6), and species parameters include $y_{init}(0)$, $y_{max}(1)$, and τ. The τ parameter (time constant) was scaled according to the type of reaction: 6 min for signaling reactions, 1 h for transcription reactions, and 10 h for translation reactions. The baseline level of input is defined as 25% activity for all input nodes. The system of ODEs is generated using the Netflux software available at: https://github.com/saucermanlab/Netflux, and implemented in MATLAB.

Coupled Model

Interactions that drive the coupled model

Figure 2-1 provides an overview of the components and interactions between the network model and ABM. The ABM contains the value layers that represent the extracellular space and the cardiac fibroblasts that migrate over and interact with these value layers. The time step for this

coupled model is 1 hour, representing the approximate timescale for a change in input to the cell signaling network to affect production of cytokines and ECM proteins that will be deposited in the ABM.[132, 133] Agents execute a series of methods at each time step: receive input from value layers, update network state, secrete latent TGFβ and IL-6, deposit collagen, migrate. Migration occurs randomly for all simulations, and cell proliferation and death are not simulated. One agent is allowed to occupy an individual grid space, and agent migration is confined to the borders of the simulation space. This series of methods is repeated for 1,008 time steps (6 weeks).
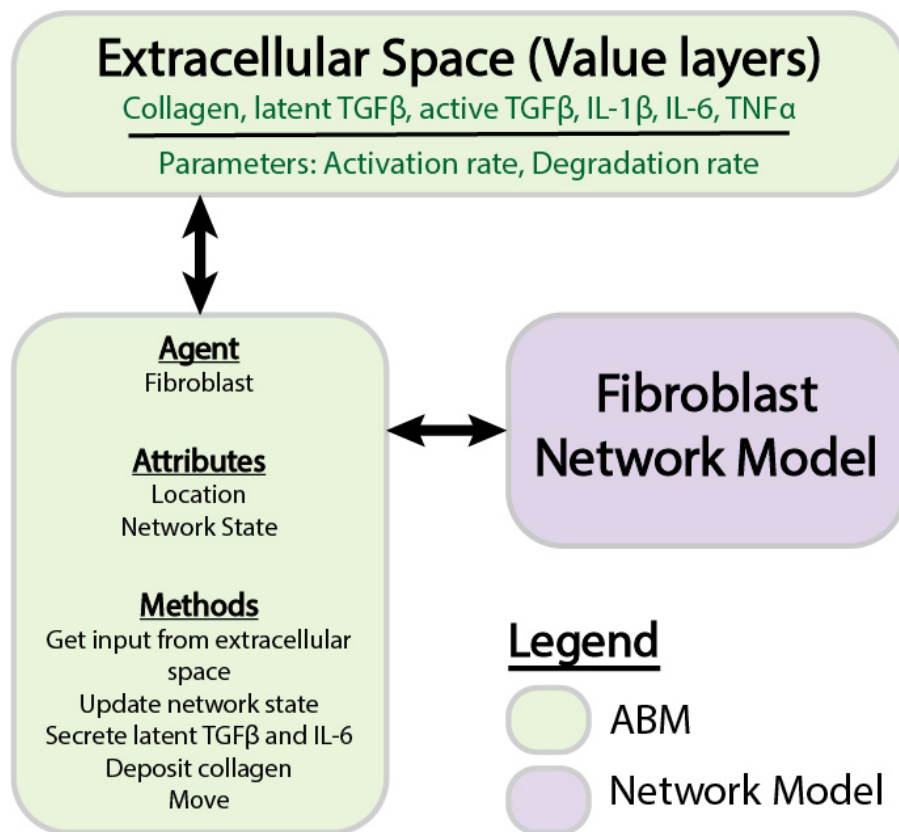
Figure 2-1. Components of individual ABM and network models.
The ABM is comprised of agents that store information about attributes and perform methods. Value layers can be modified independently by defined parameters or by the activity of agents. Individual agents store a network state, which is updated by the fibroblast network model.

Interactions between the network model and ABM are described by equations 1-10. These equations are used to define the behavior at the interface of the two models and are distinct from the equations that define the network model alone. The network model operates using normalized values between 0 and 1, whereas the ABM stores values in terms of physical concentrations. This set of equations act as a translator between these two systems. Figure 2-2 describes how these equations interact with components of each model and the order in which these methods are executed.

Network Model Inputs

Equations 1-4 are used to translate the cytokine levels stored as concentrations in the value layers of the ABM into inputs for the network model. Input weights for the network model range from 0 to 1, representing receptor activation between 0-100%. These weights are determined using the quantitative dissociation constants (Table 2-1) for the inputs of interest (IL-6, IL-1β, TNFα, TGFβ). The dissociation constant is the concentration of ligand at which approximately half of the free ligand is bound to receptor at equilibrium. Receptor activity is described by a Hill equation, where a concentration of ligand equal to the K_d is considered 50% activation of the input node. Values for each of these dissociation constants are listed in Table 2-1.

$$w_{IL-6} = \frac{[IL\text{-}6_{ABM}]}{[IL\text{-}6_{ABM}] + K_{d,IL\text{-}6}} \quad (1) \qquad w_{TNF\alpha} = \frac{[TNF\alpha_{ABM}]}{[TNF\alpha_{ABM}] + K_{d,TNF\alpha}} \quad (3)$$

$$w_{IL-1\beta} = \frac{[IL\text{-}1\beta_{ABM}]}{[IL\text{-}1\beta_{ABM}] + K_{d,IL\text{-}1\beta}} \quad (2) \qquad w_{TGF\beta} = \frac{[TGF\beta_{ABM}]}{[TGF\beta_{ABM}] + K_{d,TGF\beta}} \quad (4)$$
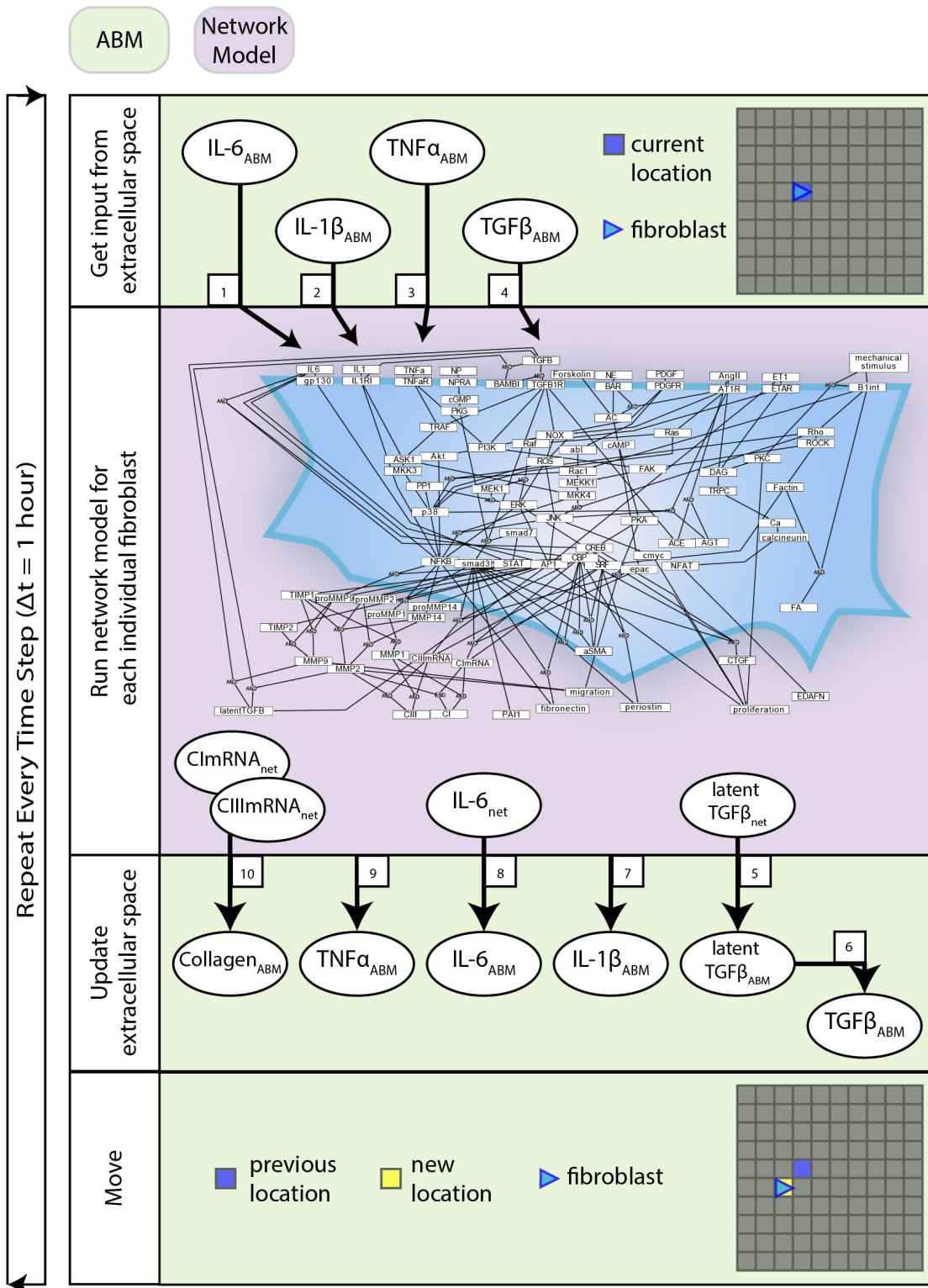
Figure 2-2. Coupled model process diagram.
A detailed process diagram illustrates the methods and order in which they occur at each time step (1 hour), and components of the ABM and network model that interact. Boxed numbers refer to the equation number which describes that process.

Table 2-1. Dissociation constants

Parameter	Description	Equation #	Value	Unit	Value	Unit	Citation
$K_{d,IL\text{-}6}$	Dissociation constant for IL-6	1	22	nM	462,000	pg/mL	[134]
$K_{d,IL\text{-}1\beta}$	Dissociation constant for IL-1β	2	500	pM	8,750	pg/mL	[135, 136]
$K_{d,TNF\alpha}$	Dissociation constant for TNFα	3	19	pM	323	pg/mL	[137, 138]
$K_{d,TGF\beta}$	Dissociation constant for TGFβ	4	28	pM	700	pg/mL	[139]

Active TGFβ and Latent TGFβ

Equation 5 describes the production of latent TGFβ from sources other than fibroblasts (k_{gen}), secretion of latent TGFβ from fibroblasts (k_{sec}) based on the network activity of latent TGFβ (latentTGFβ$_{net}$), degradation of latent TGFβ (k_{deg}), and activation of latent TGFβ (k_{act}) based on the concentration of latent TGFβ in the ABM (latentTGFβ$_{ABM}$). The generation rate (k_{gen}) describes the production of latent TGFβ from sources that are not currently represented in this model (e.g., macrophages, neutrophils, etc.) and is used to maintain the gradient setup as described below under Initial Conditions. The secretion rate (k_{sec}) describes the maximum physiological secretion of latent TGFβ from fibroblasts under stimulated conditions and this rate is scaled based on the network activity level (0-1) of latent TGFβ for each fibroblast. The degradation rate is a first-order rate based on the stability of latent TGFβ *in vitro*, and the activation rate describes the proportion of latent TGFβ that is converted to active TGFβ. Based on literature review, we chose a value for $k_{act,latentTGFb}$ that maintains active TGFβ at 4-5% of total TGFβ, which is consistent with values measured in both *in vitro* and *in vivo* studies.[140, 141] In equation 6, we use a rapid equilibrium assumption for active TGFβ concentration because the degradation rate of active TGFβ is on the order of minutes, much faster than our model time step of one hour. Thus, we assume that the

kinetics of active TGFβ are rate limited by the kinetics of latent TGFβ and come to a rapid quasi-equilibrium based on current latent TGFβ concentrations. Parameter values for equations 5 and 6 can be found in Table 2-2.

$$\frac{\partial latentTGF\beta_{ABM}}{\partial t} = k_{gen,latentTGF\beta} + k_{sec,latentTGF\beta} * latentTGF\beta_{net} - k_{deg,latentTGF\beta} *$$

$$latentTGF\beta_{ABM} - k_{act,latentTGF\beta} * latentTGF\beta_{ABM} \qquad (5)$$

$$TGF\beta_{ABM}(t) = k_{act,latentTGF\beta} * latentTGF\beta_{ABM}(t) \qquad (6)$$

Table 2-2. Parameters for active and latent TGFβ kinetics

Parameter	Description	Equation #	Value	Unit	Citation
$k_{gen,latentTGF\beta}$	Generation rate of latent TGFβ required to create gradient	5	530,000	$\dfrac{pg}{mL*hr}$	Mass balance constraint
$k_{sec,latentTGF\beta}$	Latent TGFβ secreted by fibroblasts	5	23,700	$\dfrac{pg}{mL*hr}$	139, 142-145
$k_{deg,latentTGF\beta}$	First-order degradation rate for latent TGFβ	5	0.0096	/hr	146
$k_{act,latentTGF\beta}$	Activation rate of latent TGFβ to active TGFβ	5 & 6	0.045		140, 141

Inflammatory Cytokines

Equations 7-9 describe the production and degradation of IL-1β, IL-6, and TNFα. IL-1β and TNFα are not secreted by the current fibroblast network model, so these equations simply consist of a generation rate and first-order degradation rate. The generation rates are selected to maintain prescribed cytokine gradients as described below under Initial Conditions. The equation for IL-6 kinetics simply has the addition of a secretion rate that represents the maximum physiological secretion of IL-6 from fibroblasts under stimulated conditions and is scaled based on

the network activity level (0-1) of IL-6 for each fibroblast. Parameter values for equations 7-9 can

be found in Table 2-3.

$$\frac{\partial IL-1\beta_{ABM}}{\partial t} = k_{gen,IL-1\beta} - k_{deg,IL-1\beta} * IL-1\beta_{ABM} \qquad (7)$$

$$\frac{\partial IL-6_{ABM}}{\partial t} = k_{gen,IL-6} + k_{sec,IL6} * IL-6_{net} - k_{deg,IL6} * IL-6_{ABM} \qquad (8)$$

$$\frac{\partial TNF\alpha_{ABM}}{\partial t} = k_{gen,TNF\alpha} - k_{deg,TNF\alpha} * TNF\alpha_{ABM} \qquad (9)$$

Table 2-3. Parameters for inflammatory cytokine kinetics

Parameter	Description	Equation #	Value	Unit	Citation
$k_{gen,IL-1\beta}$	Generation rate of IL-1β required to create gradient	7	4,847	$\frac{pg}{mL * hr}$	Mass balance constraint
$k_{deg,IL-1\beta}$	First-order degradation rate for latent IL-1β	7	0.277	/hr	[147, 148]
$k_{gen,IL-6}$	Generation rate of IL-6 required to create gradient	8	256,000	$\frac{pg}{mL * hr}$	Mass balance constraint
$k_{sec,IL-6}$	IL-6 secreted by fibroblasts	8	79,360	$\frac{pg}{mL * hr}$	[125, 149-151]
$k_{deg,IL-6}$	First-order degradation rate for IL-6	8	0.277	/hr	[152]
$k_{gen,TNF\alpha}$	Generation rate of TNFα required to create gradient	9	895.4	$\frac{pg}{mL * hr}$	Mass balance constraint
$k_{deg, TNF\alpha}$	First-order degradation rate for TNFα	9	1.386	/hr	[153]

Collagen

Equation 10 describes the deposition and degradation of collagen in the ABM based the

collagen I and III mRNA nodes in the network model. Deposition of collagen occurs only where

a fibroblast is present and is based on the value of the collagen I and III mRNA nodes in the

network model for each fibroblast. Degradation is modeled as a first-order process based on the

current collagen concentration in the ABM and thus occurs at every grid location, regardless of the presence of a fibroblast. This assumes evenly distributed MMP activity since we are not explicitly representing MMP production in this model.

These two parameters (Table 2-4) were fit based on previously published data in a rat model of myocardial infarction.[154] Baseline collagen area fraction was considered to be 4%, based on typical measurements from a healthy rat prior to an infarction.[155] Collagen I and III mRNA activity levels from the network model run at a baseline condition for 6 weeks (0.25 for all input nodes) were used to fit the baseline experimental data. This was done by analytically solving equation 10 for the ratio of k_{dep}/k_{deg} that produces a steady state collagen area fraction of 4%. Then, the network model was run for 6 weeks to simulate a stimulated condition (0.5 input for TGFβ, IL-1β, IL-6, and TNFα network nodes) and used to fit the infarct experimental data. This was accomplished by doing a parameter sweep of values for k_{dep} while constraining k_{deg} to satisfy the ratio determined previously and minimizing the sum of squared error (SSE) between the model fit and infarct experimental data.

$$\frac{\partial Collagen_{ABM}}{\partial t} = k_{dep,Collagen}(ColIRNA_{net} + ColIIIRNA_{net}) - k_{deg,Collagen} * Collagen_{ABM} \quad (10)$$

Table 2-4. Parameters for collagen deposition and degradation

Parameter	Description	Equation #	Value	Unit	Citation
$k_{conv,Collagen}$	Coefficient of collagen deposition	10	0.0056	Area fraction	Fit to exp. data
$k_{deg,Collagen}$	Coefficient of collagen degradation	10	0.0035	Area fraction	Fit to exp. data

Initial Conditions

To evaluate the effects of spatial gradients in fibrotic and inflammatory cues, the value layers are initialized with a gradient of TGFβ increasing from bottom to top, and a gradient of inflammatory cytokines (IL-1β, IL-6, and TNFα) increasing from left to right. Thus, each individual grid space contains a unique combination of fibrotic and inflammatory cues. Cytokine gradients were specified by scaling the generation rate (k_{gen}) along the x or y axis to result in concentrations ranging up to twice the dissociation constant for that particular cytokine or growth factor, corresponding to receptor activation rates between approximately 16-67% (Figure 2-3A - C). The purpose is two-fold: to explore a dynamic range of inputs to the network model and to create an environment where fibroblasts migrate through spatially varying environmental cues.
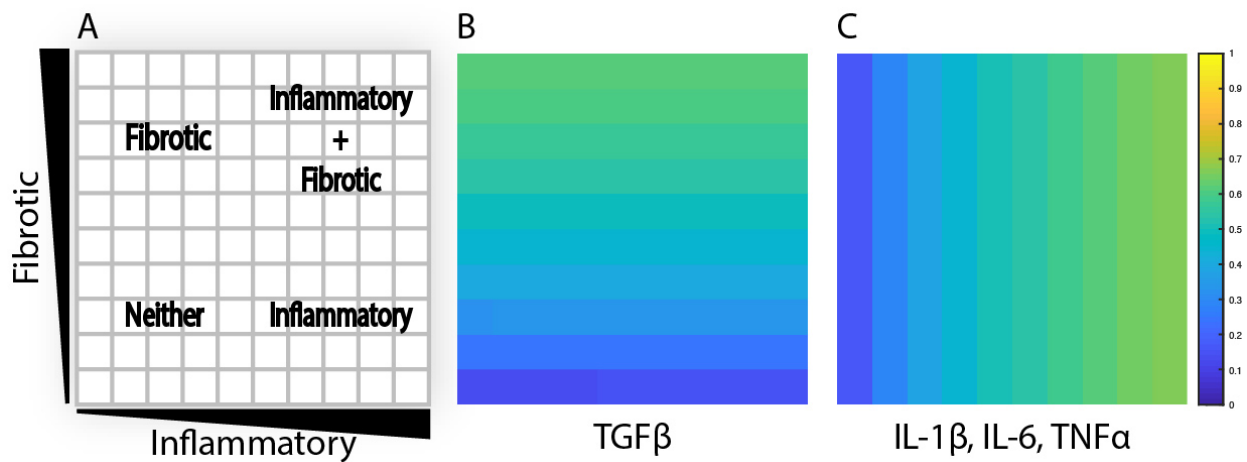
Figure 2-3. Agent-based model is initialized with cytokine gradients.
(A) Four phenotypic regions are created by a combination of fibrotic and inflammatory cues. **(B)** TGFβ is initialized with an increasing gradient from bottom to top. **(C)** IL-1β, IL-6, and TNFα are initialized with an increasing gradient from left to right.

Parameter Estimation and Fitting

A total of 17 parameters are defined in this set of 10 equations. Of these parameters, 11 are based on literature and 6 are estimated, or fit to experimental data, as noted in Tables 2-1 – 2-

4. The dissociation constants, degradation rates, and production rates from fibroblasts are based on literature. The generation rates are estimated based on a mass balance constraint in order to create the specified initial gradient, which are ultimately based on the dissociation constants found in literature. Coefficients for collagen deposition and degradation are fit based on experimental data.

Sensitivity Analysis

A sensitivity analysis of all 17 model parameters was conducted. Each parameter was decreased individually by an order of magnitude (0.1x) and compared to the results of a model run with all parameters at baseline values. A sensitivity coefficient was calculated using equation 11, where y_o and y_i are the measured state variable when parameters are at baseline or perturbed, respectively, and p_o and p_i are the values of the baseline parameter and perturbed parameter.

$$S = \frac{y_i - y_o}{p_i - p_o} * \frac{p_o}{y_o} \qquad (11)$$

The state variables measured in the sensitivity analysis are the total collagen content, global semivariance (r_{xy}), and semivariance in either the x (r_x) or y (r_y) dimension. Collagen content is measured by summing collagen area fraction across all individual grid spaces. Global semivariance is (r_{xy}) defined as:

$$r_{xy} = \frac{1}{2s_0} \sum_i \sum_j W_{ij} (x_i - x_j)^2 \qquad (12)$$

$$s_0 = \sum_i \sum_j W_{ij}$$

where x_i is an observed data point, x_j is an adjacent observation, W_{ij} is a matrix of spatial weights, and s_0 is the sum of all W_{ij}. If two data points are immediate neighbors, W_{ij} is assigned as 1,

otherwise W_{ij} is set to 0.[27] Semivariance in the x dimension is calculated by assigning 1 to W_{ij} for adjacent observations in the x direction and 0 otherwise, and vice versa for the y dimension.

Model Implementation

This model was implemented using Repast Simphony 2.6 with a java engine to connect to MATLAB R2018b, which was used to run the network model and perform all data analysis. All simulations here were performed on a single CPU (Intel® Xeon® E5-2640 v4 @2.4GHz). The approximate runtime to simulate 100 fibroblasts for a period of 6 weeks is 1 hour and 17 minutes.

Cardiac fibroblast *in vitro* experiments

Primary human ventricular cardiac fibroblasts were purchased from PromoCell (PromoCell C-12375; PromoCell GmbH, Germany). Cells were cultured in DMEM containing 10% FBS and 1% Pen/Strep, and were kept in an incubator maintained at 5% CO_2. Cells were plated in a 96-well plate at 5,000 cells/well and then grown in 10% FBS for 24 hours, serum starved for 24 hours, and then treated with the following conditions for 96 hours: 0%FBS control media, 0%FBS media with 20ng/mL TGFβ1 (Cell Signaling Technology, 8915LC), and 0% FBS media with 10 ng/mL human IL1β (Cell Signaling Technology, 8900SC). Cells were then fixed in 4% PFA in PBS for 30 minutes, permeabilized and blocked for 1 hour in a solution containing 3% BSA and 0.2% Triton, and then stained overnight at 4°C with a 1:500 primary Anti-Collagen I antibody (Abcam, ab34710). After an overnight incubation, cells were washed 3x in PBS and stained with 1:5000 Dapi, 1:1000 Phalloidin CruzFluor 647 stain (Santa Cruz Biotechnology, sc-363797), 1:250 α-Smooth Muscle Actin preconjugated antibody (Sigma-Aldrich, C6198), and 1:1000 Goat-anti-Rabbit (secondary for Anti-Collagen I) (ThermoFisher Scientific, A-11034).

Microscopy and image analysis

96-well plates we imaged using the Operetta CLS High-Content Analysis System with confocal view, and Dapi, Alexa 488, TRITC, and Alexa 647 imaging channels (Perkin Elmer). Three wells for each condition were imaged and quantified. To identify individual cells, an automated image analysis pipeline was employed in CellProfiler.[156] Fibroblast nuclei were identified by DAPI signal, and fibroblast boundaries corresponding to each nuclei were segmented based on collagen and phalloidin (actin) signals using the "propagate" algorithm. αSMA, pro-collagen I, and phalloidin signals were integrated within each cell's boundary to determine fluorescence per cell. To reduce error from edge effects, only cells in the center tile of each well were measured. The median fluorescence for all cells in a given well was reported (n=3 replicate wells per treatment group, 250-450 cells per well imaged). Significance between groups was determined by one-way ANOVA with Tukey HSD post-hoc test, p-value ≤ 0.05 considered significant.

Results

Coupled model can reproduce predictions made by network model alone

Verification tests were performed to evaluate whether coupling of LDE and ABM models affected results obtained from each model individually. This was accomplished by seeding one fibroblast in each grid space with no migration and simulating either an unstimulated condition (0.25 input for all nodes) or stimulated condition (0.5 input for TGFβ, IL-1β, IL-6, and TNFα). We compared the activity level of all 91 nodes of the fibroblast network state at steady state for each condition and calculated the sum of squared error (SSE) between the network-only and coupled models. The SSE for the unstimulated condition is 3.865e-7 (Figure 2-4A) and 1.168e-

6 for the stimulated condition (Figure 2-4B). We next examined the SSE between the network

states of the coupled model and network model alone for all 100 combinations of cytokine inputs

from Figure 2-3, resulting in SSEs in the range of [2.07e-8 - 8.88e-5]. Thus, the network-only

and coupled models produce equivalent network states for non-migrating fibroblasts when

cytokine inputs are maintained at a constant level for individual cells.
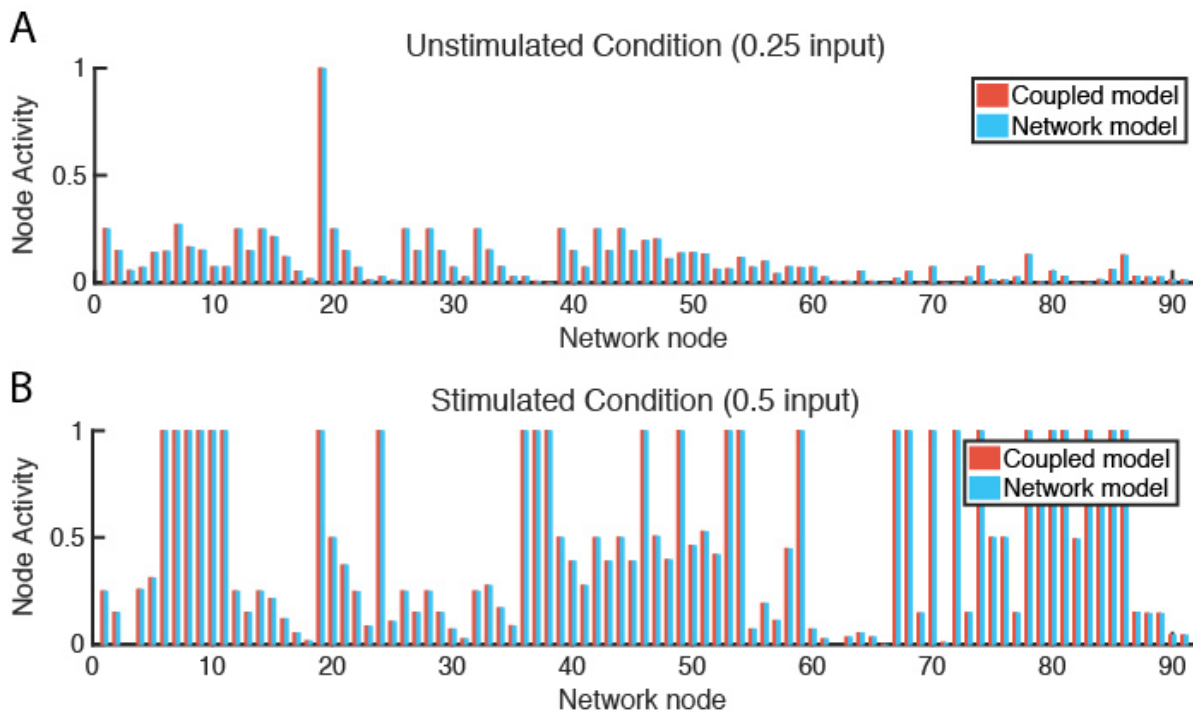
Figure 2-4. Verification tests confirm that coupled model and network model produce equivalent fibroblast network states.
(A) In an unstimulated condition (0.25 input for all nodes), and a **(B)** stimulated condition (0.5 input for TGFβ, TNFα, IL-1β, and IL-6 nodes), the network state of a fibroblast using the coupled model or network model alone are comparable with an SSE of 3.865e-7 **(A)** and 1.168e-6 **(B)**.

Coupled model predicts that inflammatory cytokines antagonize TGFβ-induced collagen accumulation

Model parameters for collagen deposition and degradation were fit to match experimental

data obtained previously from a rat model of myocardial infarction.[154] For these simulations, a

single fibroblast was placed in every grid space and not allowed to migrate. Model simulations were initialized to match the measured rise in collagen area fraction in healing infarcts when fibrotic and inflammatory inputs to the coupled model (TGFβ, IL-1β, IL-6, and TNFα) were maintained at an elevated level of 0.5, and to match the normal myocardial collagen area fraction when the same inputs were maintained at their baseline values of 0.25 (Figure 2-5A). Expanding to a broader range of cytokine combinations (100 combinations of fibrotic vs. inflammatory cytokines), the coupled model predicted biologically plausible variations in steady-state collagen content. As shown in Figure 2-5B, collagen content is highest in areas with high TGFβ input and low inflammatory input, and is reduced as inflammatory input increases for the same magnitude of TGFβ input.
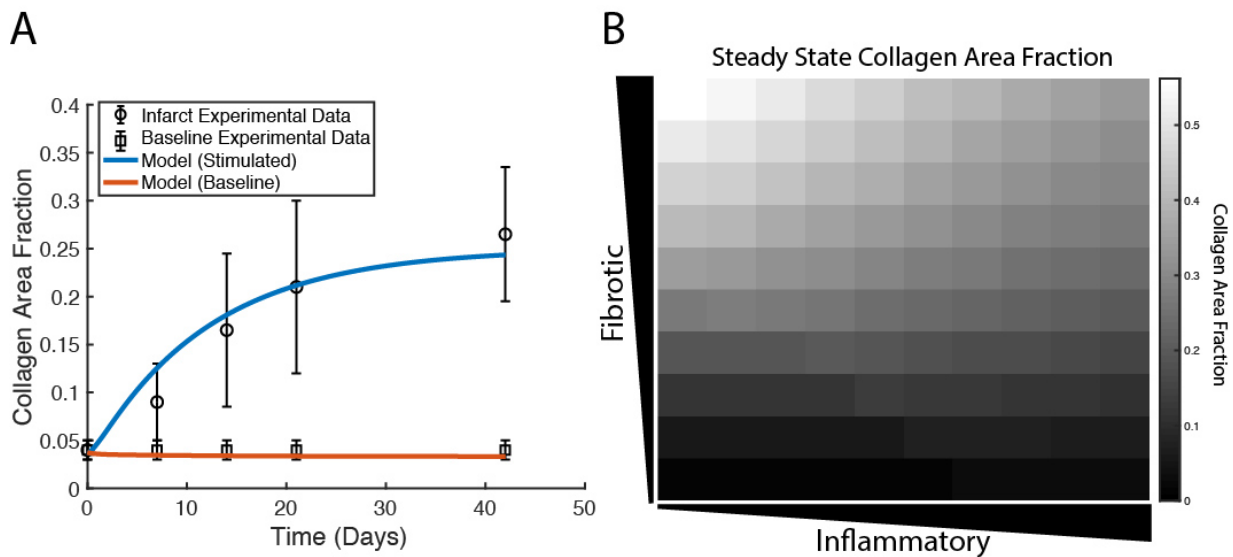
Figure 2-5. Coupled model predicts collagen profile over a range of physiological conditions.
(A) Collagen area fraction for an unstimulated condition (0.25 input for all nodes) is compared to baseline collagen area fraction (4%) in a healthy rat. Model predictions for a stimulated condition (0.5 input for TGFβ, TNFα, IL-1β, and IL-6 nodes) are compared to results from a rat model of myocardial infarction up to 6 weeks post-MI. Error bars = SEM. **(B)** Collagen area fraction predictions at 6 weeks from a model simulation with gradient initial conditions and a fibroblast in each grid space (n = 100).

Crosstalk between TGFβ and inflammatory extracellular cues produces complex signaling behaviors

The fibroblast network model exhibits complex behaviors due to its integration of 10 interdependent signaling pathways. Figure 2-6 illustrates representative nodes in the fibroblast network and their activity level under conditions of constant cytokine inputs for many combinations of inflammatory and fibrotic inputs, as described previously. Network receptors display a range of activation patterns based on their extracellular cues (Figure 2-6A – C). IL-1β receptor activation closely follows the gradient created by the initial conditions. In contrast, TGFβR1 and endothelin-1 (ET-1) are influenced by autocrine feedback loops. Inflammatory cytokines cause inhibition of TGFβR1 that increases along the x-axis as the concentration of inflammatory cytokines increase. TGFβR1 activation is also influenced by the rate of latent TGFβ activation, which occurs in the agent-based model value layers. Fibroblasts secrete latent TGFβ, which is then activated to active TGFβ. But as noted in Figure 2-6G there is minimal latent TGFβ produced in environments of low TGFβ and inflammatory input. As a result, there is decreased TGFβR1 activation in this quadrant. In contrast to the gradual applied input gradients, ET-1 receptor displays switch-like activation, due to autocrine feedback of activator protein 1 (AP1) downstream of both TGFβ and IL-1β.

Some nodes downstream of each of these inputs display similar activation patterns (Figure 2-6D - F), while others integrate multiple unique upstream inputs. Smad7, which is immediately downstream of STAT and IL-1β receptor, displays an activity pattern similar to the IL-1β receptor. Smad3 is downstream of TGFβR1, and it regulates many network outputs including collagen mRNA, fibronectin, periostin, and αSMA. NF-κB activity is regulated by many inputs,

including IL-1βR, ERK, p38, and AKT. But ERK and p38 (which are immediately downstream of the ET-1 receptor) dominate the response of NF-κB, so it displays an activation pattern most similar to ET-1 receptor. NF-κB contributes to the expression of MMPs, fibronectin, and provides feedback to IL-6 input.

Network outputs represent the integration of many upstream inputs (Figure 2-6G - I). Latent TGFβ expression is primarily influenced by AP1 transcriptional activity, which itself is regulated by ERK and JNK. The model predicts that IL-1β antagonizes TGFβ-induced collagen I mRNA and αSMA mRNA, which is validated by experimental studies in lung and dermal fibroblasts.[157] Expression of collagen I mRNA is predicted to be a product of input from Smad3, SRF (serum response factor), and CBP (CREB binding protein). proMMP 1 expression is a prime example of integration of multiple upstream inputs that each exhibit distinct activation patterns including AP1, Smad3, and NF-κB. Visualization of how this combination of transcription factors regulates proMMP 1 expression is shown in Supplemental Figure 1. In summary, the coupled model provides a platform to investigate how combinations of dynamic inputs affect downstream intermediate network nodes and network outputs.
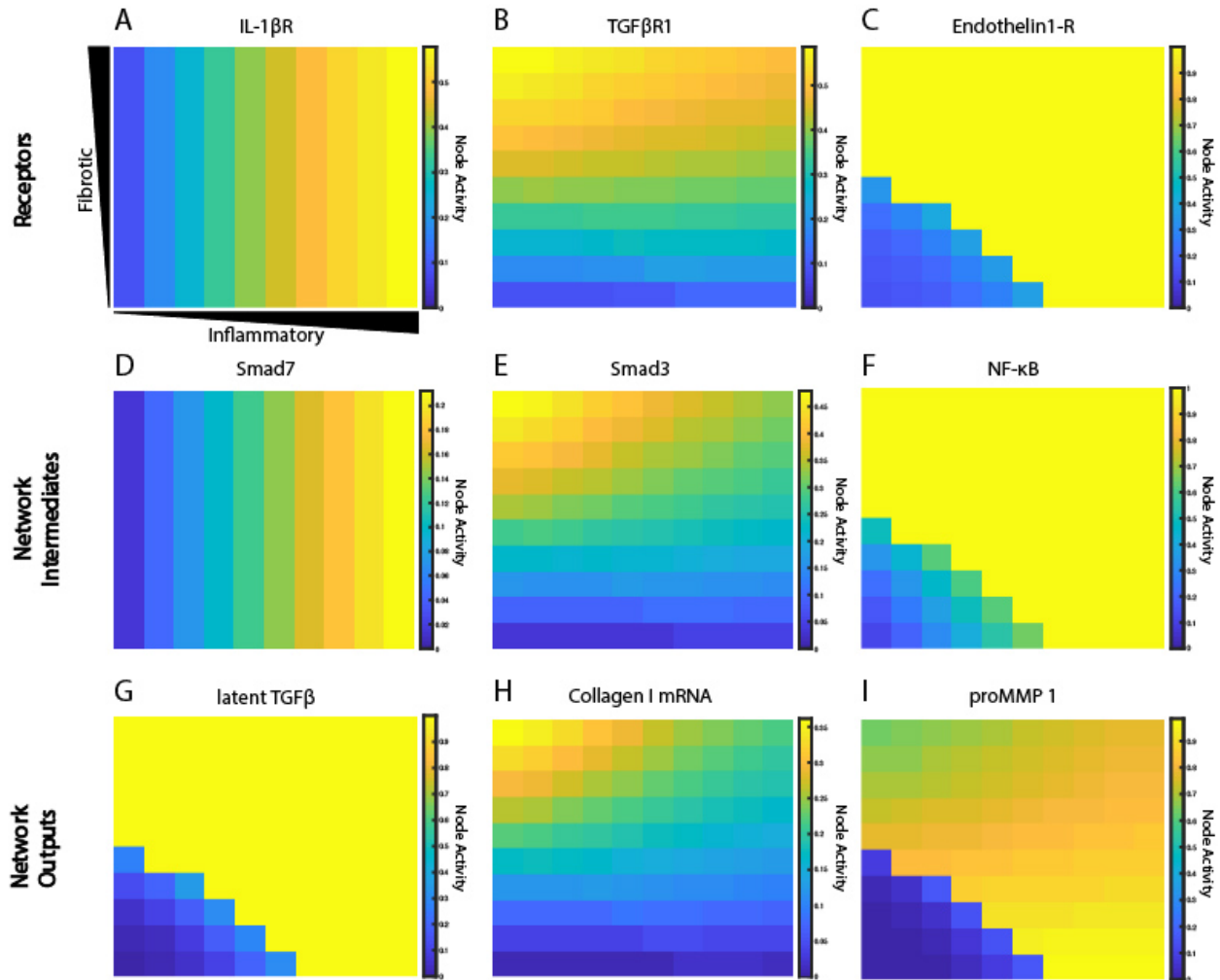
Figure 2-6. Signaling network exhibits a range of activation patterns in response to extracellular cues.
Node activity level of individual network nodes for each fibroblast at steady state (6 weeks). Model simulation with gradient initial conditions and a fibroblast in each grid space (n = 100). Heat maps show network states for input receptors (A, B and C), intermediate network nodes (D, E, and F), and network outputs (G, H, and I).

Key parameters affect spatial gradient of collagen deposition

A sensitivity analysis was conducted to determine the relative influence of decreasing the values of parameters associated with ABM-network coupling on overall collagen content (area fraction) and collagen heterogeneity (semivariance, either globally, or in the x or y dimension). Parameters were individually decreased by an order of magnitude (0.1x), and normalized sensitivity

coefficients were computed, in which positive coefficients indicate positive correlation of the parameter with the output measured (see Eq. 11). Parameters were ranked by their positive influence on collagen area fraction (Figure 2-7A). Parameters related to TGFβ production, activation, and degradation are the most influential in determining collagen content, because TGFβ input is important in altering downstream collagen I and III mRNA activity in the fibroblast signaling network. As expected, the coupled model is also highly sensitive to the two parameters in equation (10) that govern deposition and degradation in the collagen layer. In terms of inflammatory inputs, this analysis reveals that IL-1β and IL-6 are more influential in determining the collagen profile than TNFα input. This is likely because IL-6 has a downstream effect on Smad3, which promotes collagen mRNA activity, and IL-1β upregulates NF-κB, which has a positive feedback on IL-6. TNFα has a smaller effect on NF-κB signaling and no direct connection to Smad3 signaling. It is also noted that the two parameters related to secretion of latent TGFβ and IL-6 ($k_{sec,latentTGF\beta}$ and $k_{sec,IL-6}$) from the fibroblast have little effect on the overall collagen profile, yet TGFβ and IL-6 inputs themselves seem to be very influential. This is likely because the production rates from fibroblasts are not high enough to significantly impact the gradients that are created in the initial conditions.
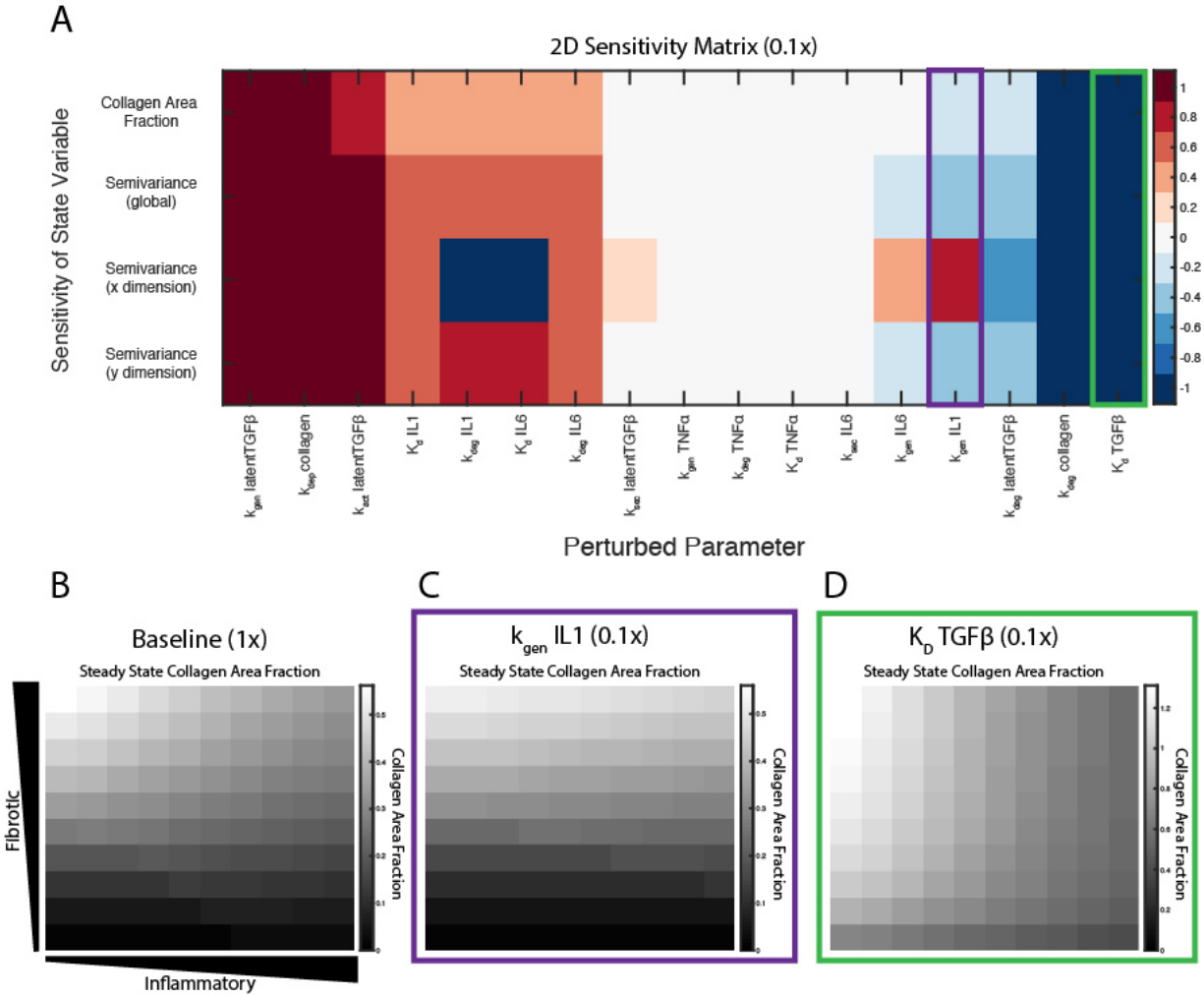
Figure 2-7. Key parameters affect spatial gradient of collagen deposition.
(A) Sensitivity coefficients calculated based on equation 11 with individual parameter perturbations of 0.1x. State variable outputs include total collagen area fraction, global semivariance, semivariance in the x direction, and semivariance in the y direction. Collagen area fraction heat maps at 6 weeks with **(B)** all parameters at baseline, **(C)** $k_{gen,IL\text{-}1\beta}$ parameter multiplied by 0.1, and **(D)** $K_{d,TGF\beta}$ parameter multiplied by 0.1.

Interestingly, some parameters may have different effects on overall collagen content and collagen spatial heterogeneity. Decreasing parameters such as the K_d of TGFβ for its receptor, increase both collagen content and collagen heterogeneity (Figure 2-7A and 2-7D), compared to a collagen profile at 6 weeks when all parameters are at baseline values (Figure 2-7B). Decreasing

parameters associated with synthesis of latent TGFβ or collagen, or degradation of IL-6, cause a decrease in both collagen content and heterogeneity in both dimensions. In contrast, decreasing the IL-1 generation term ($k_{gen,IL-1}$) has little effect on the total collagen content, but has opposite effects on collagen heterogeneity in the x and y dimension, as measured by semivariance in either direction (Figure 2-7C).

Single cell dynamics in response to a changing extracellular environment

To test the role of fibroblast migration on collagen remodeling, fibroblasts were seeded sparsely in the coupled model and allowed to migrate stochastically at a rate of one grid space per hour. Fibroblasts were seeded at moderate density (20 fibroblasts) within the fibrotic vs. inflammatory cytokine grid and responses simulated for 6 weeks. Fibroblasts experience changes in their extracellular environment as they migrate, which causes their intracellular signaling network state and rate of collagen deposition to change accordingly. Figure 2-8 illustrates single cell migration trajectories (panels A and C), local cytokine inputs, and gene expression (panels B and D) for two representative fibroblasts migrating within the cytokine gradient environment. The fibroblast shown in panels A and B remains in areas with high to moderate TGFβ levels and with increasing levels of inflammatory cytokines. Correspondingly, this fibroblast exhibited relatively high levels of collagen mRNA expression that mirrored the level of TGFβ input. As this fibroblast migrated to regions of increasing IL-6, there was a delayed but then rapid increase in MMP mRNA expression, consistent with switch-like responses seen in Figure 2-6I.

Figure 2-8C and 2-8D track a separate fibroblast that remains in areas of low to moderate TGFβ levels, but migrates from a region of high to low inflammatory inputs. This simulation shows similarly that collagen mRNA expression closely follows TGFβ inputs. Interestingly, it also

demonstrates that exposure to high IL-6 levels triggers a rapid and sustained increase in MMP

mRNA expression, which persists well after the cell migrates to a region with lower levels of

inflammatory cytokines. Thus, some network nodes respond with close coordination to particular

cytokine inputs, whereas other nodes may be activated in a switch-like manner consistent with the

activation patterns seen in Figure 2-6. Videos provided in the supplemental material offer a visual

of how the entire network state changes over time for the individual fibroblasts presented in Figure

2-8.
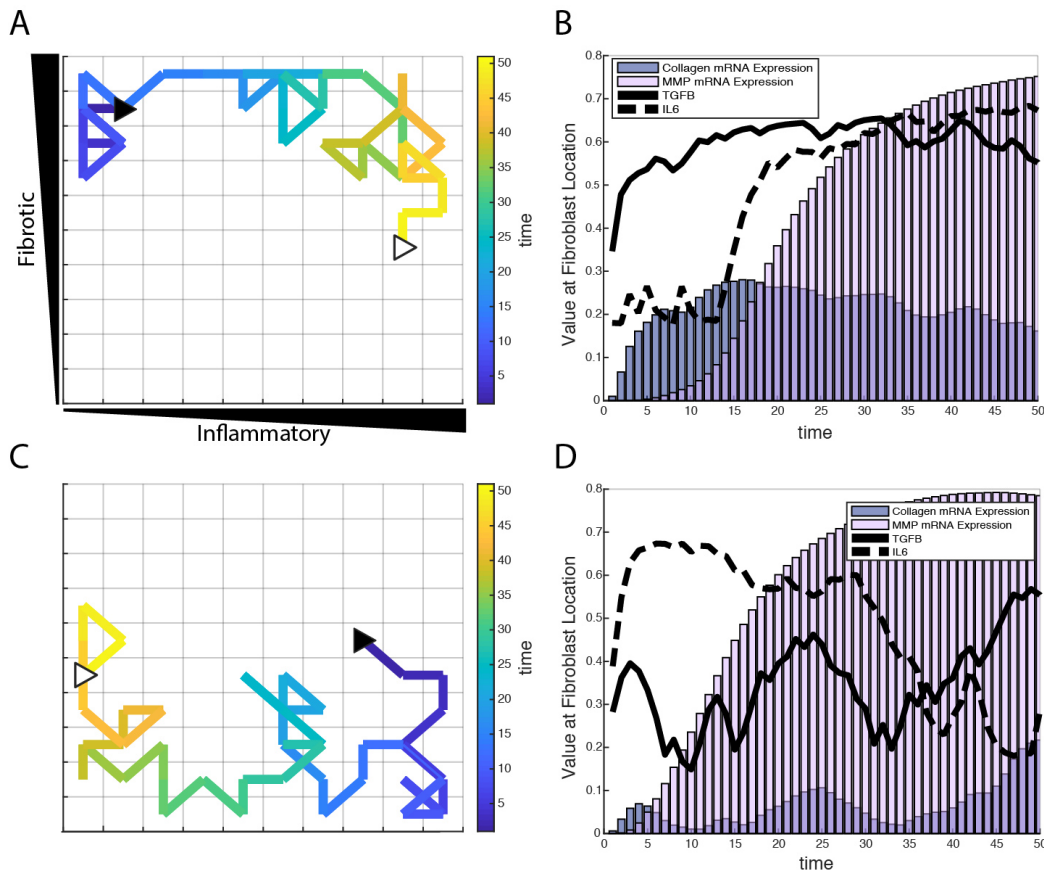
Figure 2-8. Individual fibroblasts respond dynamically to extracellular environment.
(A and C) Fibroblast migration path for a single fibroblast over a period of 50 hours. Fibroblast starting location indicated by filled black triangle and end location indicated by open white triangle. (**B and D**) Corresponding TGFβ and IL-6 inputs for the fibroblasts tracked in **(A)** and **(C)**, and their respective collagen and MMP mRNA activity over the time course of 50 hours.

Fibroblast migration speed and density affect collagen spatial heterogeneity

Under normal conditions, fibroblasts migrate at a speed of approximately 10μm/hr, but this can vary significantly in the presence of growth factors and cytokines.[158, 159] As noted above, individual grid spaces are 10μm x 10μm, so the baseline migration speed was set at 1 grid space per hour. To test the impact of altered migration speed, migration speeds were set to default values (1 grid/hr), decreased (1 grid space/10 hr) or increased (10 grid spaces/hr). Slower migration speed resulted in greater heterogeneity in the collagen profile, while faster migration speed resulted in a more homogenous collagen profile (Figure 2-9A-C). In contrast, overall collagen content was linearly dependent on fibroblast density, but not migration speed or initial cell location (n=10 simulations per condition) (Figure 2-9D). As with the sensitivity analyses, heterogeneity in collagen was quantified by global, x-direction, or y-direction semivariance (see Eq. 12). Consistent with qualitative observations from Figure 2-9A - C, decreasing the migration speed enhanced both the average magnitude and run-to-run variance in collagen heterogeneity. Faster migration decreased collagen heterogeneity globally and in the y dimension, but not in the x dimension. The coupled model predicts that fibroblast migration can have a substantial impact on the spatial heterogeneity and stochasticity of collagen deposition.
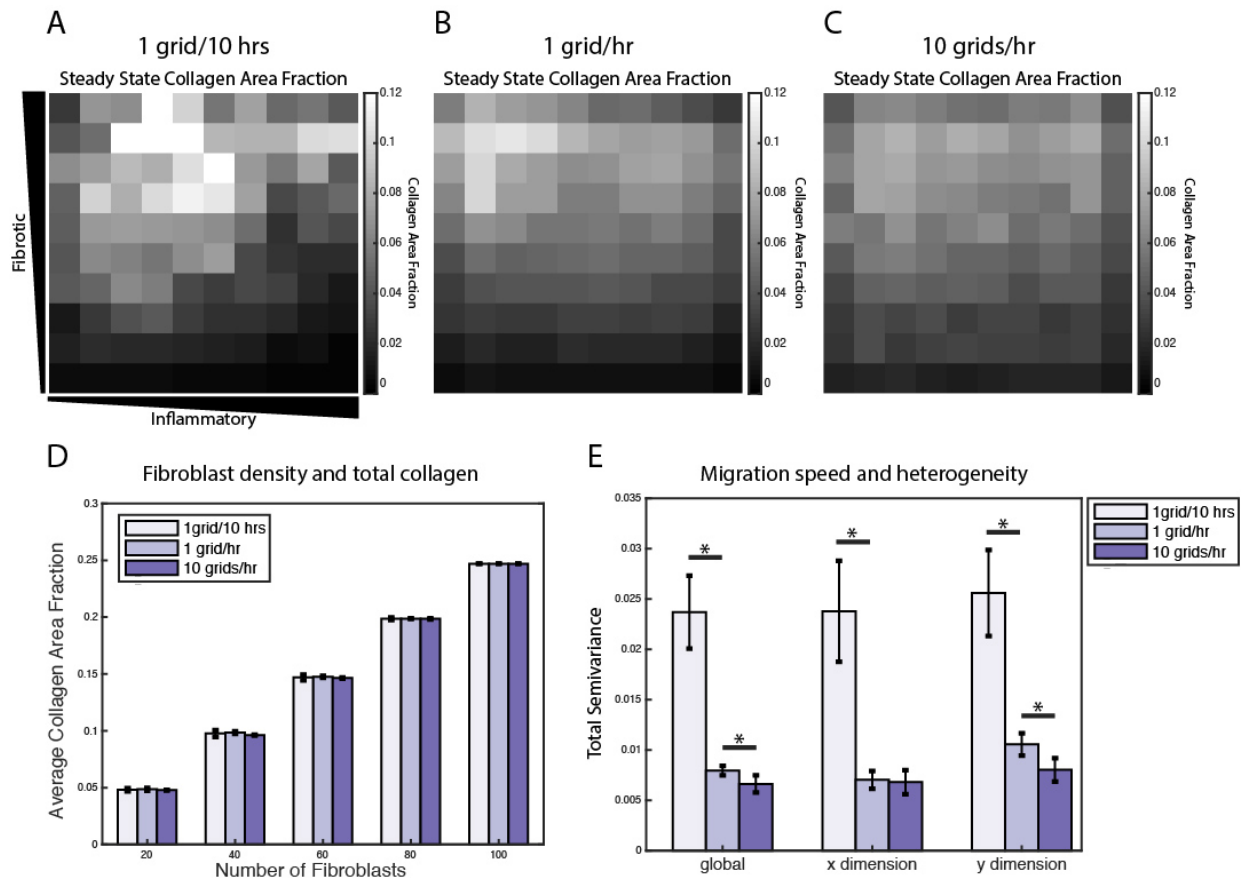
Figure 2-9. Fibroblast migration speed and density affect spatial heterogeneity of collagen.
Collagen area fraction heat map at 6 weeks for simulations with 20 randomly migrating fibroblasts with a migration speed of **(A)** 1grid/10hrs, **(B)** 1grid/hr, and **(C)** 10grids/hr. **(D)** Average collagen area fraction at 6 weeks for each migration speed and simulations with 20, 40, 60, 80, or 100 fibroblasts. Mean reported for 5 runs. Error bars = standard deviation. **(E)** Semivariance calculated globally, in the x direction, and y direction for each migration speed. Mean reported for 10 runs. Error bars = standard deviation. *p<0.05.

A subset of coupled model predictions was validated by comparison to in vitro experiments

In order to perform experimental validation of our coupled model predictions, we ran a series of simulations wherein input cytokine (IL-1β) and growth factor (TGFβ1) levels were varied from baseline to simulate those tested with *in vitro* experiments using primary human cardiac fibroblasts (HCFs). HCFs were treated with either TGFβ1 (20 ng/mL), IL-1β (10 ng/mL), or TGFβ1 (20 ng/mL) + IL-1β (10 ng/mL), and compared to a control condition in media without FBS (since

this is also a source of TGFβ1). Pro-collagen I, αSMA, and F-actin expression were quantified using immunocytochemistry and image processing to quantify the median fluorescence in each of these experimental conditions (Figure 2-10A). Treatment with TGFβ1 significantly increased expression of pro-collagen I, αSMA, and F-actin compared to the control condition, while IL-1β treatment alone had no significant effect on pro-collagen I, αSMA, or F-actin expression when compared to the control condition. The combination of TGFβ1 and IL-1β treatment decreased expression of pro-collagen I, αSMA, and F-actin when compared to TGFβ1-only treatment, and was statistically significant in the cases of pro-collagen I and F-actin. Representative images of pro-collagen 1 (green), αSMA (orange), and F-actin (blue) expression in HCFs for each of these treatment conditions indicate the trends described above (Figure 2-10C). These experimental measurements were compared to *in silico* predictions that simulated the addition of these factors at the same concentrations tested experimentally: TGFβ1 (20 ng/mL), IL-1β (10 ng/mL), or TGFβ1 (20 ng/mL) + IL-1β (10 ng/mL). As with the experimental results, predictions were compared to a control simulation in which all parameters were set to baseline levels (Figure 2-10B). Most model predictions qualitatively agreed with the trends observed with *in vitro* experiments. For example, network expression of collagen I mRNA, αSMA, and F-actin were increased relative to the control simulation in response to TGFβ1 stimulation. Similar to observed experimental results, IL-1β treatment alone had no effect on collagen I mRNA, αSMA, or F-actin network expression compared to the control simulation, but the combination of TGFβ1 and IL-1β treatment was predicted to decrease the expression of collagen I mRNA and αSMA when compared to TGFβ1 only treatment. Unlike experimental results, however, simulating this combined treatment predicted no change in F-actin network expression when compared to

simulating TGFβ1 only treatment. These model predictions were further validated by published experimental studies wherein IL-1β attenuated TGFβ1-induced collagen I synthesis and αSMA expression of lung and dermal fibroblasts.[157]
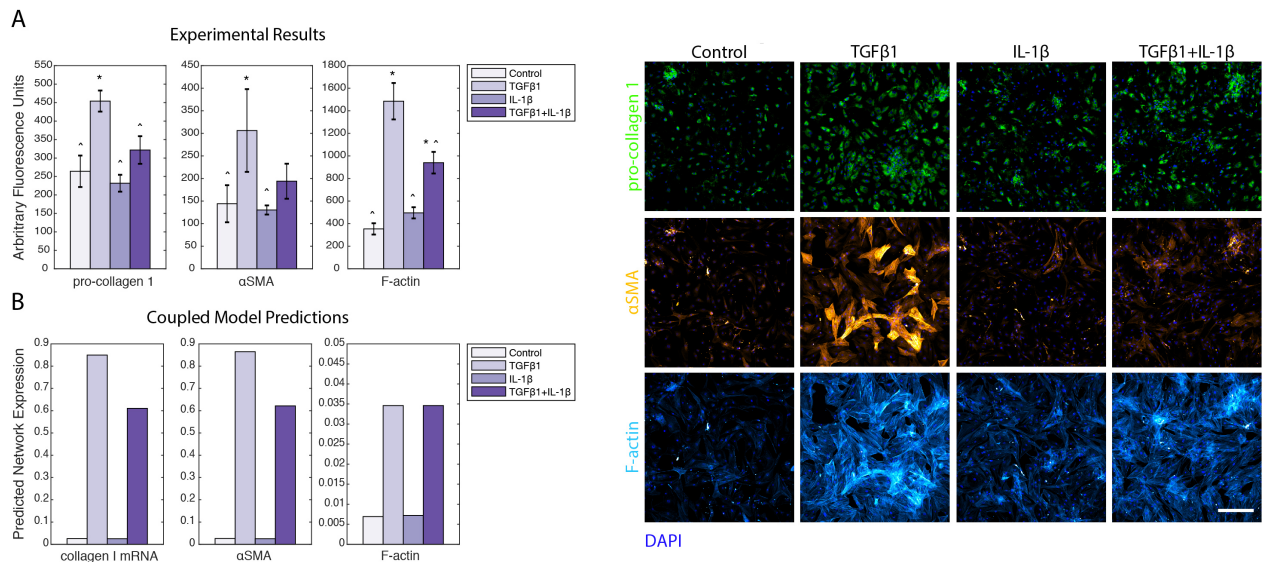
Figure 2-10. Coupled model predictions were compared to independent *in vitro* experiments using human cardiac fibroblasts treated with TGFβ1 and/or IL-1β.
(A) Pro-collagen 1, αSMA, and F-actin expression from in vitro experiments with human cardiac fibroblasts were quantified by image analysis to measure the median fluorescence for all individual cells in each well (n=3). Treatment conditions included control, TGFβ1 (20 ng/mL), IL-1β (10 ng/mL), and TGFβ1 (20 ng/mL) + IL-1β (10 ng/mL). Error bars = standard deviation. *p<0.05 with reference to control condition. ^p<0.05 with reference to TGFβ1 condition. **(B)** Coupled model predicts network expression of collagen I mRNA, αSMA, and F-actin when simulating the addition of TGFβ1 (20 ng/mL), IL-1β (10ng/mL), and TGFβ1 (20 ng/mL) + IL-1β (10 ng/mL), compared to a simulation with all parameters at baseline. **(C)** Representative images of human cardiac fibroblast expression of pro-collagen 1 (green), αSMA (orange), and F-actin (purple) when treated with TGFβ1 (20 ng/mL), IL-1β (10 ng/mL), and TGFβ1 (20 ng/mL) +IL-1β (10 ng/mL), compared to control. Nuclei are stained with DAPI (blue). Scale bar = 500 microns.

Discussion

A novel hybrid multiscale model of tissue fibrosis

Here we present a novel hybrid multiscale model of tissue fibrosis that couples a logic-based differential equation model of cardiac fibroblast intracellular signaling with an agent-based model of multi-cellular tissue remodeling. Prescribed gradients of inflammatory cues (IL-1β, IL-6, and TNFα) and fibrotic cues (TGFβ) stimulate migrating fibroblasts to respond dynamically to their locally varying extracellular environment. Under conditions with no fibroblast migration and constant cytokine input levels, the coupled model was verified to exhibit consistent network states predicted by the network model alone (Figure 2-4). In contrast, the addition of fibroblast migration across a gradient of cytokine inputs demonstrated that fibroblasts respond dynamically to both their local cytokine environment and their previous history of cytokine exposure. Spatial heterogeneity of collagen was dependent on the speed of fibroblast migration and key parameters (e.g., Il-1β synthesis rate) identified in a sensitivity analysis as having distinct effects on semivariance in the x or y dimension. Additionally, several parameters were identified to be influential in contributing to the overall amount of collagen deposition, including cell density and model parameters related to TGFβ production and activation.

The effects of pro-fibrotic stimuli (TGFβ) on increasing collagen expression and other myofibroblast markers is well established.[160-162] However, the crosstalk of IL-1β with other fibrotic signaling pathways is not as well described. This coupled model provides a framework for investigating the effects of combined inflammatory and pro-fibrotic cues on spatial fibroblast activity and ECM composition. A subset of coupled model predictions was validated by comparison to experiments with human cardiac fibroblasts treated with combinations of TGFβ1

and IL-1β *in vitro*. The model accurately predicted TGFβ1-enhanced expression pro-collagen I, αSMA, and F-actin, as well as negative crosstalk on pro-collagen I and αSMA by IL-1β. However, the model did not predict the experimentally-observed attenuation of TGFβ1-enhanced F-actin expression by IL-1β, suggesting that additional cross-talk mechanisms may need to be explored in future experiments and model revisions.

Previous mathematical models of fibrosis have used deterministic, continuum methods to holistically represent the complex processes of fibrosis.[113, 163] For example, Hao et al., describe a model of liver fibrosis using a system of 24 partial differential equations (PDEs) that represent many different cell types, cytokines and growth factors, and interactions between cells, and then use this model to interrogate different treatment options.[163] Other continuum-based models have focused more on specific mechanisms that contribute to the progression of fibrosis, such as macrophage activation and polarization.[90, 111] A model developed by Wang et al, for example, explores how the timing of monocyte recruitment and macrophage differentiation affects left ventricular remodeling following MI.[90] However, an interesting study by Figueredo et al. suggested that stochastic differential equation approaches that assume continuous space and time could not capture the individual variability and spatial heterogeneity predicted by an agent-based modeling approach applied to the same biological case study, and that emergent behavior of the ABM contributed additional insight about the system.[164]

An increasing number of hybrid models couple continuum with discrete approaches. These hybrid models typically couple agent-based models, which use a discrete representation of 2D space or 3D volumes, with continuum based approaches that represent cytokine gradients and/or receptor-ligand kinetics.[24, 115, 165] For example, Warsinske et al. simulated granuloma-associated

fibrosis by incorporating a system of ODEs and PDEs that describe molecular level diffusion of chemokines (TGFβ and prostaglandin) and receptor ligand signaling, coupled with discrete cellular agents whose behaviors were defined by a set of rules that related receptor activation levels to cell proliferation, differentiation, chemotaxis, and secretion of ECM proteins. In these hybrid continuum-ABM models, outcomes at the tissue scale are the emergent product of actions of the individual agents governed by rules that are informed by molecular scale interactions simulated using continuum assumptions.[165]

The hybrid multiscale model presented here represents the coupling of a large-scale intracellular network model, comprising 10 cytokine/neurohormonal inputs and 134 reactions, with an agent-based model that maps physiologically relevant *in vitro* concentrations of cytokines and ECM components to normalized network activity levels and vice versa. We believe that this represents the first coupling of a large-scale network model to make predictions about tissue-level changes in extracellular matrix composition in the setting of fibrosis. This coupled model and its use of concentration scaling between the logic-based model and physical units enables the quantitative prediction of fibroblast production of cytokines and growth factors and spatial gradients of cytokine concentrations, which was not previously possible with the network model alone. This coupled model framework will ultimately enable quantitative comparisons of model predictions to *in vivo* experimental data such as measurements of multiple cytokine concentrations over time, spatial profiles and gradients of ECM components, cell densities, and single cell mRNA expression.

Impact of spatially varying environmental cues on fibroblast signaling

The response of a complex signaling network to multiple simultaneous cues is rarely intuitive, and we have demonstrated that individual nodes of the signaling network respond with distinct patterns of activation (Figure 2-6). Some receptors respond in sync with their input, such as IL-1βR, whose activity level mimics the gradient initial conditions of IL-1β input. Meanwhile other receptors, such as TGFβR1, display a more complex pattern of activation reflecting not only the gradient initial conditions but also feedback from latent TGFβ activation and inhibition by IL-1 activity. Intermediate nodes often display a similar pattern of activation to their immediate upstream receptors (e.g., Smad7 and IL-1βR, Smad3 and TGFβR1, NF-κB and Endothelin1-R), while network outputs integrate the effects of many upstream network nodes that represent a combination of stimulatory and inhibitory inputs. MMP1, for example, is upregulated by NF-κB and AP1 (activator protein 1) activity, and inhibited by Smad3 activity. Tracking the response of individual fibroblasts moving through varying levels of inflammatory and fibrotic inputs revealed a complex kinetic relationship between the locally sensed extracellular environment and network state of a migrating fibroblast (Figure 2-7). For example, a fibroblast that experiences a high inflammatory context will upregulate its MMP activity, which remains elevated even if the fibroblast moves to an environment with low inflammatory and fibrotic inputs. The fibroblast's network state is highly dependent on the current extracellular environment in some cases (e.g., collagen mRNA expression in response to TGFβ input) but displays history-dependence of previous environments in other cases.

Processes that contribute to spatial heterogeneity of collagen deposition

The artificially prescribed cytokine gradient environment employed in these simulations (Figure 2-3) was not intended to represent a particular *in vivo* situation, but was used to evaluate the ability of the coupled signaling and multicellular model to predict the progression of fibrosis across a wide range of signaling contexts. Thus, changes in heterogeneity discussed here reflect the range of responses a population of fibroblasts would be expected to generate across those varied signaling contexts (Figure 2-5B). For example, we found fibroblast migration speed to be an important determinant of collagen heterogeneity in our simulations (Figure 2-9). Slower migration speed leads to pockets of high collagen deposition and overall higher heterogeneity. Faster migration produces a more uniform collagen distribution. In healing wounds where cytokine concentrations vary in both space and time, we expect that high migration speeds could similarly blur the effects of variable cytokine levels while slow migration speeds could accentuate them. In contrast, migration speed did not substantially affect average collagen accumulation across the entire simulated range of cytokine combinations. Rather, overall collagen accumulation was strongly dependent on fibroblast density. In addition to fibroblast density, model parameters related to TGFβ production, activation, and degradation are among the most important model parameters in determining total collagen content as well as the gradient of collagen deposition in either dimension (Figure 2-7), which agrees with the findings from similar models of fibrosis.[24] Other parameters such as the degradation or synthesis of IL-1β had opposite effects on collagen heterogeneity in two dimensions. One advantage of coupling an agent-based model is that it produces stochastic predictions as a result of individual-based rule sets and a spatial context

(Supplemental Figure 2). Repeated runs of the coupled model may help to capture individual variability of spatial fibrosis seen in animal models.

Computational requirements for scaling up

Simulations were performed on a single CPU (Intel® Xeon® E5-2640 v4 @2.4GHz). The runtime for 100 fibroblasts for a period of 6 weeks with access to 10 cores is 1 hour and 17 minutes. This model is structured such that parallel computing can be implemented across multiple CPUs to reduce simulation runtime. The limit of computational efficiency is reached when the number of cores is equal to the number of fibroblasts in a simulation, allowing the network state of each fibroblast to be updated simultaneously at each time step. We anticipate that with access to 100 cores, this model with 100 fibroblasts for 6 weeks of simulated time would be computed in approximately 8 minutes. Simulation on a high-performance computing system with thousands of cores is expected to enable simulation of up to 100,000 fibroblasts (comparable to a myocardial infarct).

Limitations and sources of error

The prescribed input cytokine gradients employed here were used to explore the dynamic range of the network model and create an environment where fibroblasts migrate through a rapidly changing extracellular environment. However, this environment is not representative of a specific physiological environment. Cytokine diffusion was not enabled in the current simulations, in order to maintain the prescribed cytokine input gradients over small spatial area (100x100μm). Furthermore, the current model did not include proliferation and apoptosis, which have been simulated in previous work.[24, 165] Future applications will incorporate cell migration and proliferation rates that are driven by the dynamic network state of individual fibroblasts.[166, 167] Additionally, this model focused specifically on the contributions of fibroblasts in the progression

of fibrosis, through the coupling of a fibroblast signaling network, but future work will incorporate inflammatory cells that serve as local sources of many of the inflammatory cytokines that affect fibroblast signaling.[115]

State of the multiscale modeling field and contributions of this multiscale model

A primary focus of the computational modeling community is to develop methods for integrating biological data across spatial, temporal, and functional scales.[3] Continued advancements in the capabilities and availability of high-performance computing has allowed models to tackle more complex problems with greater resolution. Perturbations to fine-grained parameters, such as protein or gene expression data, can predict observable changes to coarse-grained parameters (e.g. cell distributions, tissue patterning).[28, 165, 168] Furthermore, the use of multiscale models allows for *in silico* predictions for a wide range of parameter values in a high-throughput manner that would otherwise not be feasible with experimental assays, either due to time or cost constraints, or lack of the appropriate technology. For example, the multiscale model presented here allows for real time tracking of individual fibroblasts and continuous measurements of their network states, which would not be feasible *in vivo*. While models cannot fully replace experimental studies, they can offer insight into unexpected predictions that can then be experimentally tested or lead to new hypotheses entirely, as demonstrated by Martin *et al.*, who predicted a new therapeutic approach as a result of their *in silico* experiments of muscle regeneration following injury.[91]

In summary, we have contributed a hybrid multiscale model of tissue fibrosis by coupling models across spatial and temporal scales. This represents the coupling of a large-scale network model with an agent-based model to make predictions about fibroblast production of cytokines and growth factors and tissue-level changes in ECM composition. This coupled model makes

predictions about fibroblast production of cytokines and growth factors in physical units, which was not possible previously with the logic-based model alone. Verification tests confirmed that the model coupling did not disrupt the behavior of the individual models, allowing for future model revisions or software implementations of individual modules. Application of this coupled model in the context of post-MI wound healing will allow for further investigation and validation of cytokine concentrations, collagen content and heterogeneity, and cell behaviors with both fine spatial and temporal resolution. Experimental studies suggest that collagen density alone may have effects on fibroblast behavior, including adhesion, migration, and gene expression[169], and that furthermore, collagen density and fibroblast density play an important role in the mechanical properties of the myocardium.[170, 171] This multiscale model framework allows for further investigation and understanding of emergent phenomena that result from the dynamic interplay between molecular signaling, cell behavior, ECM composition, and tissue mechanics. For example, previous computational models have demonstrated that simultaneous targeting of multiple cells types rather than fibroblasts alone can enhance the efficacy of therapies for pulmonary fibrosis.[24] Inflammatory cells, including macrophages and neutrophils, will be incorporated into a model of post-MI wound healing as the primary source and modulators of inflammatory cytokines and TGFβ input, as has been demonstrated previously in simulations of skeletal muscle and lung fibrosis.[24, 115, 172] This will add another layer of complexity to the spatial heterogeneity of the coupled model by representing cytokine production from individual cells, diffusion of soluble cytokines and growth factors, and migration that is driven by chemokine gradients. Our goal is to develop a hybrid multiscale model that can systematically screen the effect of therapeutic interventions on

the progression of cardiac fibrosis, from the level cell signaling to a tissue level of ECM remodeling, with both spatial and temporal resolution.

Acknowledgements

Author Contributions

SR and TA developed the code for the coupled model; SR, AN, JL, SP, JH, and JS contributed to the development of model parameters and rule sets; SC and AN performed *in vitro* experiments and image analysis; SR wrote the initial draft of the manuscript; JH, SP, and JS contributed to manuscript revision. All authors read and approved the submitted version of the manuscript.

Funding

Conflicts of Interest

The authors declare that the research was conducted in the absence of any commercial or financial relationships that could be construed as a potential conflict of interest.

CHAPTER 3

Spatiotemporal dynamics of macrophage infiltration and polarization during early-stage inflammation following myocardial infarction

[1]Department of Biomedical Engineering, University of Virginia
[2]Robert M. Berne Cardiovascular Research Center, University of Virginia
[3]Department of Medicine, University of Virginia

Abstract

Macrophages are a target for novel therapeutics to prevent adverse ventricular remodeling leading to heart failure following myocardial infarction (MI). Improvements in single cell sequencing and transcriptomics have improved our knowledge of the heterogeneities that exists in cardiac macrophage populations and the distinct temporal dynamics and roles that they play in wound healing following MI. However, few studies have characterized the spatial heterogeneity of macrophage populations and activation states during the early inflammatory stage of post-MI wound healing. Understanding macrophage spatial and temporal dynamics will likely be necessary to identify novel therapeutics that target inflammatory processes that contribute to the development of heart failure. In this study, we describe the spatiotemporal dynamics of M1 and M2 macrophage infiltration in the heart in a rat model of myocardial infarction induced by permanent occlusion of the coronary artery. To our knowledge, this represents the first data set to characterize the spatial distributions of macrophages in the heart post-MI and their colocalization with cardiac fibroblasts and other unique regions of interest in the infarct, including regions of necrosis and intramyocardial hemorrhage. We also present evidence of a CD68+CD163+ macrophage population that defies M1/M2 classifications and further supports the need to fully characterize the diverse macrophage phenotypes that exist *in vivo* and their unique functions. This work contributes important findings about the spatiotemporal dynamics of macrophages in the heart during post-MI wound healing that will inform future studies that aim to identify novel therapeutics targeting the inflammatory response that leads to adverse remodeling of the heart and cardiac fibrosis.

Introduction

Timely reperfusion therapy following MI has dramatically improved short-term survival, but ventricular remodeling resulting in heart failure remains a significant clinical challenge associated with high morbidity and mortality in the long-term impacts of MI.[173-176] Current therapeutics including ACE inhibitors and beta blockers have failed to prevent deaths related to the development of heart failure.[177] There is a need to better understand the processes that regulate maladaptive remodeling of the heart following MI in order to develop novel therapeutic targets.[178]

Wound healing following MI includes three unique, but integrated phases: inflammation, proliferation, and remodeling. Macrophages play important roles throughout all of these phases including phagocytosis of cell debris, recruitment of fibroblasts, and promotion of scar formation and angiogenesis.[179, 180] Inflammation and scar formation are necessary for wound healing and repair, but excess inflammation or fibrosis causes maladaptive ventricular remodeling leading to heart failure.[178] Macrophages are important regulators of this remodeling, with pro-inflammatory M1 macrophages directing early phases of wound healing, which then switch to an anti-inflammatory M2 phenotype that promotes angiogenesis and scar formation.[180, 181] This M1/M2 classification of macrophages is based on *in vitro* polarization of bone marrow-derived macrophages in response to LPS and IFN-γ (M1 macrophages), or IL-4 and IL-13 (M2 macrophages)[182-184], and has been recognized as an oversimplification of the macrophage phenotypes that exist *in vivo*.[178, 179]

New experimental techniques including single-cell RNA sequencing (scRNA-seq) and mass spectrometry have enabled more complete descriptions of macrophage polarization states using unbiased clustering of cell populations based on their expression profiles.[181, 185, 186] Mouton et

al. performed whole transcriptome analysis of cardiac macrophages isolated from the infarct region at days 1, 3, and 7 following permanent coronary artery ligation. Using principal component analysis, macrophages from each day formed their own cluster, indicating that they exhibit unique expression profiles at these time points. Day 1 macrophages expressed pro-inflammatory genes related to cytokine signaling and extracellular matrix degradation; day 3 macrophages differentially expressed genes related to metabolic reprogramming processes and demonstrated increased phagocytosis and proliferation; day 7 macrophages displayed a more reparative phenotype, upregulating genes related to ECM assembly and scar formation. They also demonstrated that day 7 macrophages expressed collagen I and periostin mRNA, indicating that they may be important direct contributors to ECM remodeling.[185] Furthermore, Walter et al. showed that while day 3 macrophages generally express pro-inflammatory markers and day 7 macrophages express ant-inflammatory markers, these phases are overlapping and macrophages simultaneously expressed classical M1 and M2 markers, indicating that this classification system does not accurately capture the nuances of macrophage phenotypes.[186]

While these studies have contributed important knowledge about the temporal dynamics of macrophage transcriptional profiles and polarization following MI, there is a need to also describe the spatial dynamics and heterogeneity of macrophage infiltration and colocalization with cardiac fibroblasts. Macrophages play an important role in fibroblast recruitment and differentiation to myofibroblasts, which are the primary cells that deposit collagen to form scar in the infarct. Scar heterogeneity that develops as a result of differences in fibroblast alignment and local collagen deposition is an important determinant of the mechanical function of the heart and will be an important consideration in the design of therapeutics for cardiac fibrosis.[187-189] We hypothesize that the spatial heterogeneity of macrophage recruitment and polarization following

MI is a significant contributor to subsequent fibroblast and scar heterogeneity. Our objective in this study was to describe the spatiotemporal dynamics of macrophage populations in the heart following MI and their spatial localization with unique regions of interest and cell types within the infarct, including cardiac fibroblasts. Using an animal model of myocardial infarction by permanent occlusion of the coronary artery, we utilize histological techniques and image analysis to quantify CD68, CD163, and αSMA density within the infarct region of the myocardium during the early inflammatory and proliferative phases (days 1-6) of post-MI wound healing.

Materials and Methods

Animal model of myocardial infarction

Adult male Sprague-Dawley rats weighing 275-300 g (age 8-9 wk) were used in this study. Animals were allowed to acclimate for at least 1 week prior to surgery and were provided ad libitum access to food and water for the duration of the study. Animals were anesthetized with intraperitoneal injection of ketamine (60-80 mg/kg) and xylazine (5-10 mg/kg), intubated, and ventilated with oxygen and supplemental isoflurane (0.5-1%). Bupivacaine was administered locally at the site of incision. Following left thoracotomy, large transmural infarcts were created by permanent occlusion of the left anterior descending (LAD) coronary artery with a 6-0 suture. The chest wall was closed in layers and subcutaneous buprenorphine (0.05-0.2 mg/kg) was administered immediately with additional doses every 8-12 hours as needed for postoperative pain. All procedures were approved and conducted in accordance with the requirements of the Institutional Animal Care and Use Committee at the University of Virginia.

Histological Analysis

At days 1, 2, 3, 4, 5, and 6, animals were anesthetized with 3% isoflurane in 100% oxygen, intubated, and ventilated with oxygen and supplemental isoflurane (2.5-3%). The chest was opened via a midline sternotomy the heart was arrested by retrograde perfusion with cold 2,3-butanedione monoxime (BDM) in phosphate-buffered saline (PBS) and removed. A rectangular sample of the infarct scar (8-10 mm on each side) was dissected from the heart for histological analysis. Scar samples were embedded in OCT compound and snap frozen using isopentane immersed in liquid nitrogen. Frozen tissue was stored at -80C and then sectioned parallel to the epicardial surface at 7 um thickness through the entire depth of the heart wall. Tissue sections taken from the myocardium (50% wall depth) were subsequently stained and analyzed with the following assays.

Immunohistochemistry

Tissue sections were thawed at room temperature, rehydrated with PBS, and permeabilized in a solution of TBS containing 0.1% TWEEN and 2% BSA for 30 minutes. Samples were then blocked for 30 minutes in a solution of TBST with 10% mouse serum, and then incubated for 1.5 hours at room temperature with 1:300 anti-actin, α-smooth muscle antibody pre-conjugated to Cy3 (Millipore Sigma, C6198), 1:100 CD68 pre-conjugated to Alexa Fluor 488 (Bio Rad MCA341A488), and 1:100 CD163 pre-conjugated to Alexa Fluor 647 (MCA342A647). Following antibody incubation, samples were washed 3x with PBS for 10 minutes and then ProLong Diamond (Thermo Fisher, P36962) with DAPI mountant and coverslip was applied. Samples were allowed to dry completely overnight in the dark at room temperature before imaging with a Leica THUNDER high resolution imaging system. Complete tissue sections were imaged

with tile scanning at 20x and automating stitching of the tiles performed with LAS X Navigator (Leica Microsystems).

Hematoxylin and Eosin

Frozen sections were thawed and then fixed in cold acetone at -20°C for 10 minutes. Sections were then cleared and dehydrated in a series of serial washes with xylenes and ethanol. Nuclei were stained with Harris modified hematoxylin solution (Sigma-Aldrich, HHS16) and blued with running tap water for 10 minutes. Samples were then counterstained with eosin containing phloxine (Sigma-Aldrich, HT110316), and then dehydrated and cleared with serial washes of ethanol and xylenes. Slides were coverslipped with Cytoseal mounting media and imaged with a Leica THUNDER high resolution imaging system at 10x with automatic tile scanning using LAS X Navigator (Leica Microsystems) under brightfield light.

Picrosirius Red

Frozen sections were thawed and then fixed in cold acetone at -20°C for 10 minutes. Sections were then cleared and dehydrated in a series of serial washes with xylenes and ethanol. Sections were rinsed for 1 minute in DI water and then stained with picrosirius red F3BA stain (Polysciences, Inc. #24901) for 90 minutes. Sections were rinsed for 2 minutes with 0.1 N hydrochloride acid and then dehydrated in serial washes of ethanol. Slides were coverslipped with Cytoseal mounting media and imaged with a Leica THUNDER high resolution imaging system at 10x with automatic tile scanning using LAS X Navigator (Leica Microsystems) under polarized light to visualize type I and III collagen fibers.

Image Analysis

All image analysis was performed using ImageJ (version 2.1.0). Hematoxylin and eosin (H&E) stained tissue sections were manually annotated to identify regions of interest in the

infarct. Regions of interested identified for annotation included the entire tissue section, necrotic region, areas of hemorrhage, and any regions of healthy cardiomyocytes (Figure 3-1). Necrotic regions were identified by a lack of nuclei staining and non-injured regions were identified by highly aligned and elongated nuclei. Additionally, a cross-section of the left ventricular cavity was visible in some tissue sections and was excluded from any area measurements and subsequent analysis.
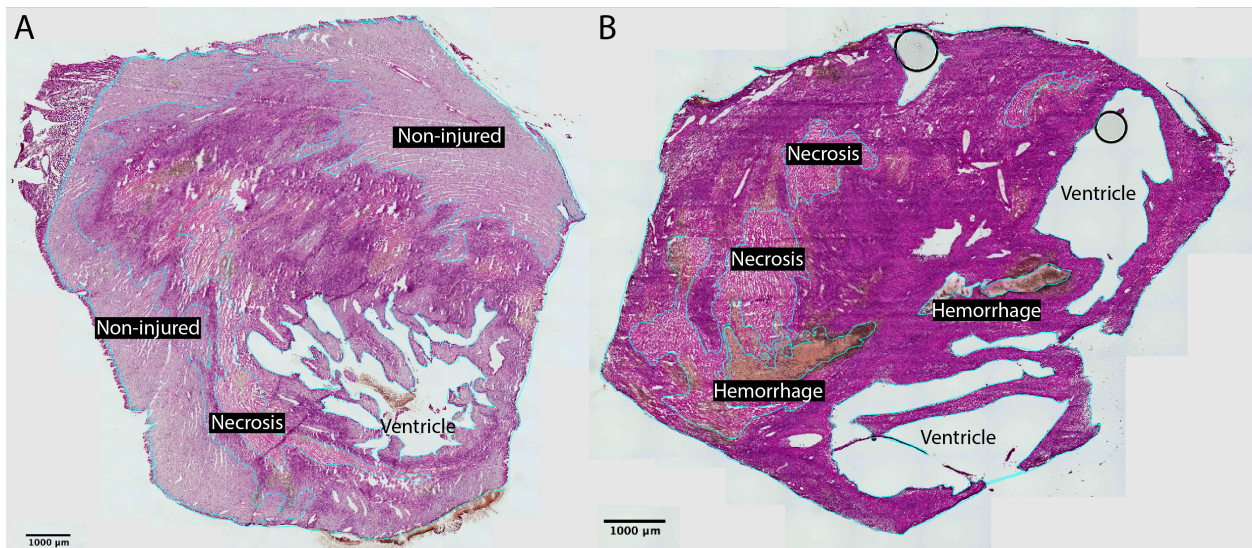
Figure 3-1. H&E image annotation
Example hematoxylin and eosin staining and image annotation for a cardiac section on **(A)** day 3 and **(B)** day 5 following myocardial infarction.

Immunohistochemistry images were analyzed by annotating these same regions of interest by visual comparison to a serial section stained with hematoxylin and eosin (H&E) from the same animal (Figure 3-2). DAPI staining was used to identify the border of the tissue section and the necrotic region, which was identified by a complete lack of DAPI staining within the tissue section. Additionally, a border region adjacent to the necrotic area was defined by enlarging the necrotic region of interest (ROI) by 500 μm and including only this 500 μm band of tissue adjacent to necrosis as a separate ROI. Any areas of non-injured tissue or sectioning artifact (including regions

corresponding to cross-sections of the left ventricle) were excluded from the infarct region. All image channels (DAPI, ED1, ED2, αSMA) were thresholded using the default auto threshold method in ImageJ and the pixel area within each ROI was measured for all channels.
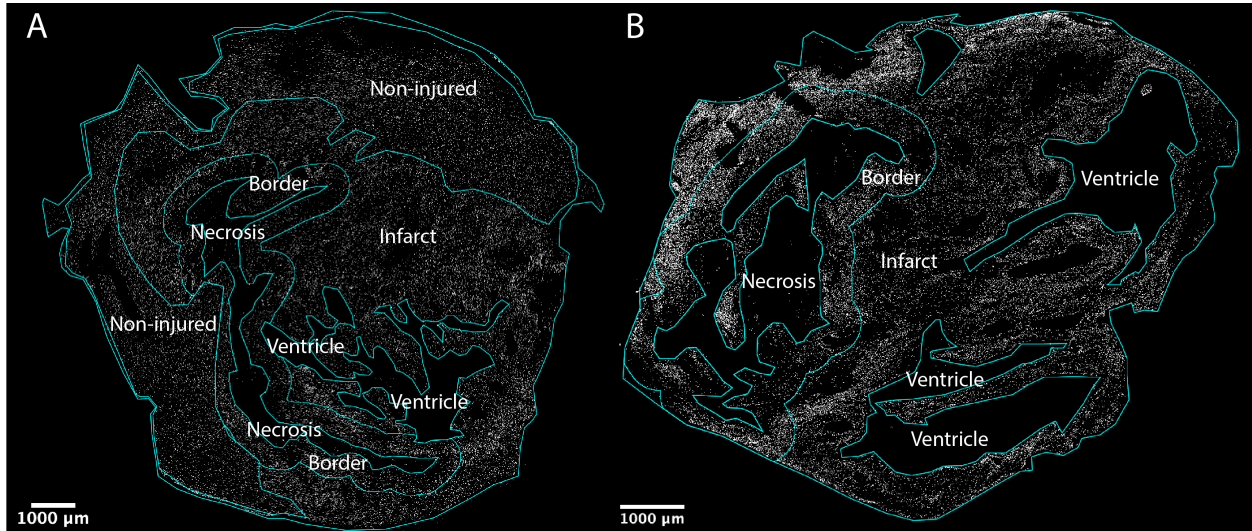
Figure 3-2. IHC image annotation with DAPI
Example DAPI staining and image annotation for a cardiac section on (A) day 3 and (B) day 5 following myocardial infarction.

Results

Macroscopic regions of interest within the infarct area

Tissue sections stained with H&E were analyzed to quantify the area fraction of several unique macroscopic regions of interest within the infarct that appeared on days 1-6 (Figure 3-3). Areas of non-injured tissue that contained elongated nuclei and highly aligned cardiomyocytes were present up to day 3. Necrotic regions lacking any nuclei staining appeared in these tissue sections as early as day 2, and were most prominent on day 4. Areas of intramyocardial hemorrhage were identifiable in one infarct on day 4, and two of three infarcts on days 5 and 6. Previous models of myocardial infarction with ischemia reperfusion (I/R) have similarly noted significant edema leading to intramyocardial hemorrhage in the most severe infarcts.[190]
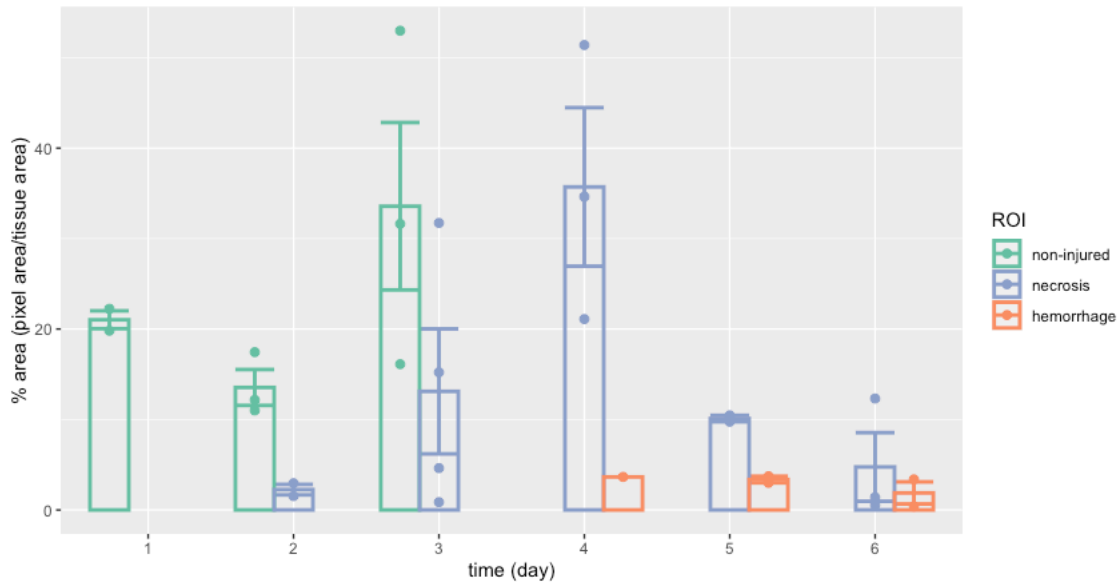
Figure 3-3. Area fraction of annotated ROIs in H&E Images
Percent area as a fraction of the total tissue section area for annotated regions of interest in H&E stained sections. Error bars = SEM.

Tissue-resident macrophages are lost in necrotic regions of the infarct

CD163+ cells, which represent a M2-like tissue-resident macrophage population, were present in a regularly-spaced pattern in areas of non-injured tissue that were identifiable at early time points (Figure 3-4A). These non-injured regions were also characterized by a lack of M1-type (CD68+) macrophages and minimal αSMA+ cells that were not otherwise easily identifiable as vascular smooth muscle cells. Interestingly, necrotic regions which lacked any DAPI staining, which would indicate intact nuclei, maintained this regularly-spaced pattern of CD163 staining that was observed in non-injured tissue at earlier time points (Figure 3-4B). This suggests that M2-like macrophages were previously present in this ischemic area, and that potentially these cells have recently undergone apoptosis and the CD163 membrane protein is more stable than the DNA contained in the nucleus identified by DAPI staining. CD163+ pixel area was quantified as

a fraction of the total tissue section area for several regions of interest identified previously (i.e., non-injured tissue, infarct, border region). CD163+ macrophages were present on day 1 in regions of non-injured tissue and the infarct region at densities comparable to that of healthy control animals, but these tissue-resident macrophage populations were reduced in all regions on days 2 and 3 (Figure 3-4C). CD163+ cell area slowly recovered on days 4 and 5, reaching an area fraction similar to initial densities by day 6. We hypothesized that macrophages would be present in higher numbers at the border of necrosis as the site of the most severe injury. However, there was no significant difference in CD163+ cells in the border region of necrosis compared to the entire infarct region.
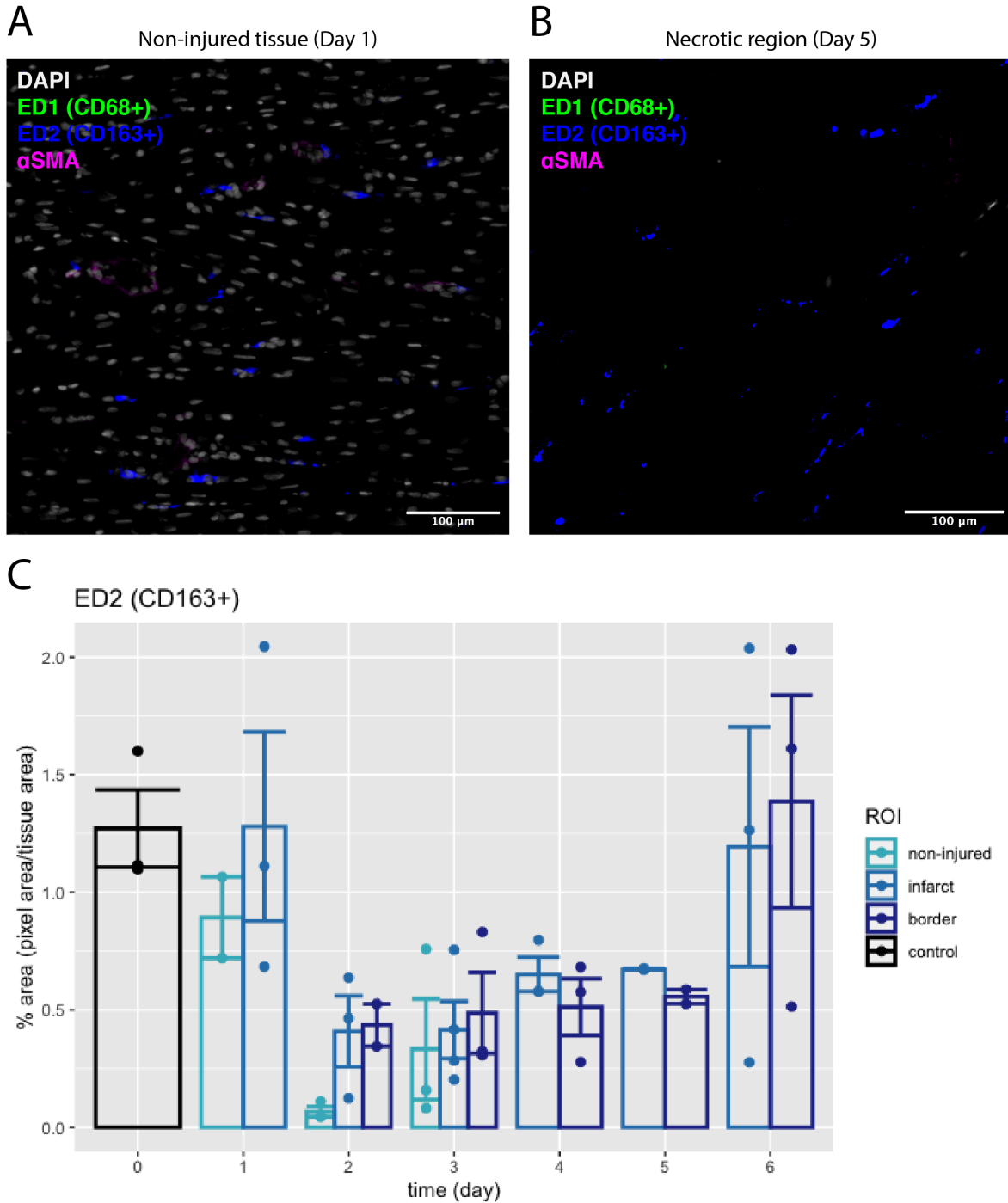
Figure 3-4. Tissue-resident macrophages (CD163+) are lost from necrotic regions in the infarct.
M1 (CD163+) and M2 (CD68+) macrophages are identified in **(A)** a region of non-injured tissue at day 1 and **(B)** a necrotic region at day 5. **(C)** CD163+ pixel area was quantified for regions of non-injured tissue, infarct area, and a 500 μm border region of necrosis at days 1-6 following myocardial infarction and compared to a control tissue sample obtained from a healthy animal. Error bars = SEM. Scale bar = 100 μm.

Inflammatory and tissue-resident macrophages have distinct time courses of infiltration

CD68+, or M1-like inflammatory macrophage densities were quantified as a fraction of the total area for several regions of interest on days 1-6 following myocardial infarction in additional to control samples obtained from a healthy rat heart (Figure 3-5). M1 macrophages were present in very low numbers in non-injured areas at early time points that was comparable to the densities observed in control samples, but appeared at higher densities in the infarct and border regions on day 2 and increased significantly on day 4. There was not a significant difference in M1 macrophage density between the border region and entire infarct, except for on day 6 where there was a higher density of M1 macrophages at the border of the necrosis. There was also evidence of a CD68+CD163+ subpopulation of macrophages (Figure 3-6A). This could indicate phenotype switching of tissue-resident macrophages to a more inflammatory phenotype, or a unique subpopulation of M2 macrophages.[85, 191, 192] When comparing M1 (CD68+) and M2 (CD163+) densities they demonstrate unique time courses of infiltration following myocardial infarction (Figure 3-6B). M2 tissue-resident macrophages are present on day 1 at a density seen in healthy control samples, but their density quickly drops on day 2 and is followed by a slow return to initial densities by day 6. M2 inflammatory macrophages are present at very low densities initially and experience a rapid increase on day 4 that is sustained through day 6.
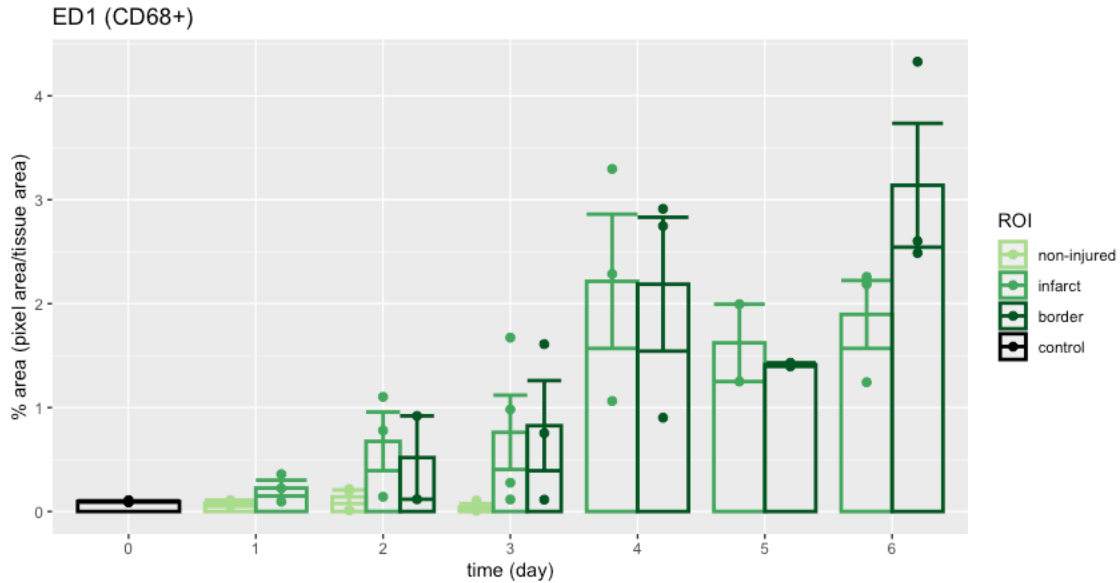
Figure 3-5. Inflammatory macrophages increase in number during week 1 following myocardial infarction.
CD68+ pixel area was quantified for regions of non-injured tissue, infarct area, and a 500 μm border region of necrosis on days 1-6 following myocardial infarction and compared to a control tissue sample obtained from a healthy animal (day 0). Error bars = SEM.
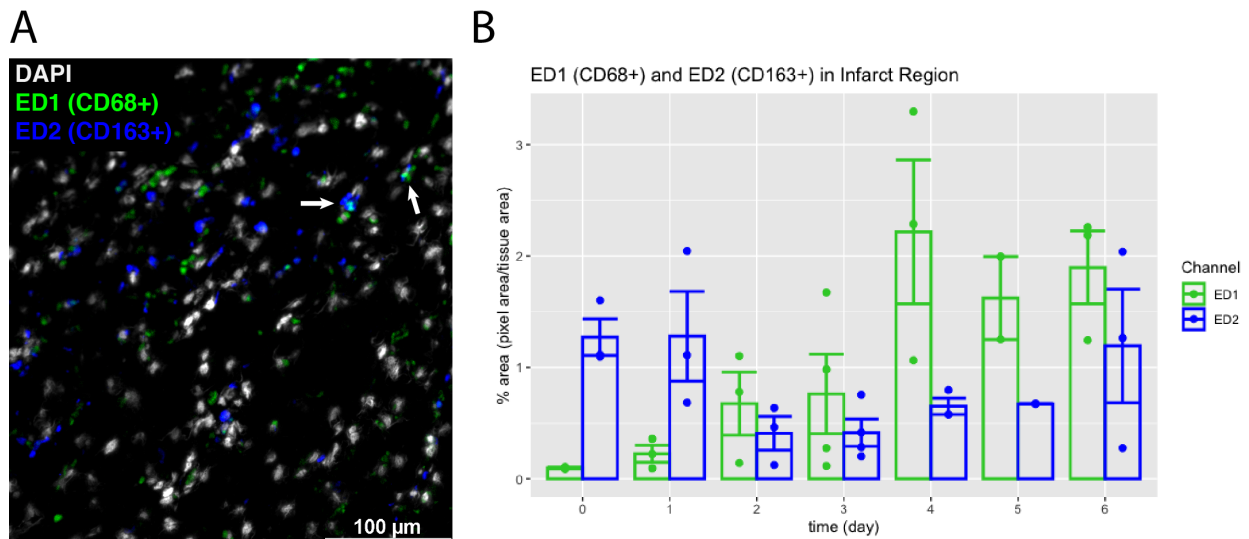
Figure 3-6. Comparing M1 and M2-like macrophage density following myocardial infarction and the presence of a CD68+CD163+ macrophage population.
(A) Example of CD68+ (green), CD163+ (blue), and DAPI (grey) staining in the infarct region on day 5 following myocardial infarction. White arrows indicate CD68+CD163+ cells. Scale bar = 100 μm.
(B) CD68+ and CD163+ pixel area was quantified as a fraction of total infarct area on days 1-6 following myocardial infarction and compared to a control tissue sample obtained from a healthy animal (day 0). Error bars = SEM.

αSMA+ myofibroblasts are present with unique spatial patterns of localization with macrophages

Interstitial myofibroblasts were visually identified by αSMA+ cells which were not immediately adjacent to a blood vessel. While quantification of αSMA+ pixel area cannot rule out the inclusion of vascular smooth muscle cells or mural cells[193, 194], interstitial myofibroblasts could be identified visually by their elongated morphology (Figure 3-7A and B). Presented here are two striking examples of myofibroblast spatial distribution in the infarct region from the same animal on day 4 following myocardial infarction. In the first example (Figure 3-7A), myofibroblasts appear to be evenly distributed and intermixed with other CD68+ and CD163+ cells. This is contrary to the example image in Figure 3-7B, where myofibroblasts appear to be highly concentrated in one area and distinct from other CD68+ or CD163+ cell populations. When quantifying αSMA+ pixel area as a fraction of total tissue area for several regions of interest (Figure 3-7C) there was a low density of αSMA on days 1-3 in all regions, likely accounting for vascular smooth muscle cells of the surviving vasculature since a similar density was observed in healthy control samples. There was an increase in αSMA+ density on day 4 that was sustained through day 6. There was little difference in αSMA+ density between any of these regions of interest, except for on day 5 where αSMA+ density was slightly higher in the infarct region compared to the border region surrounding the necrosis.
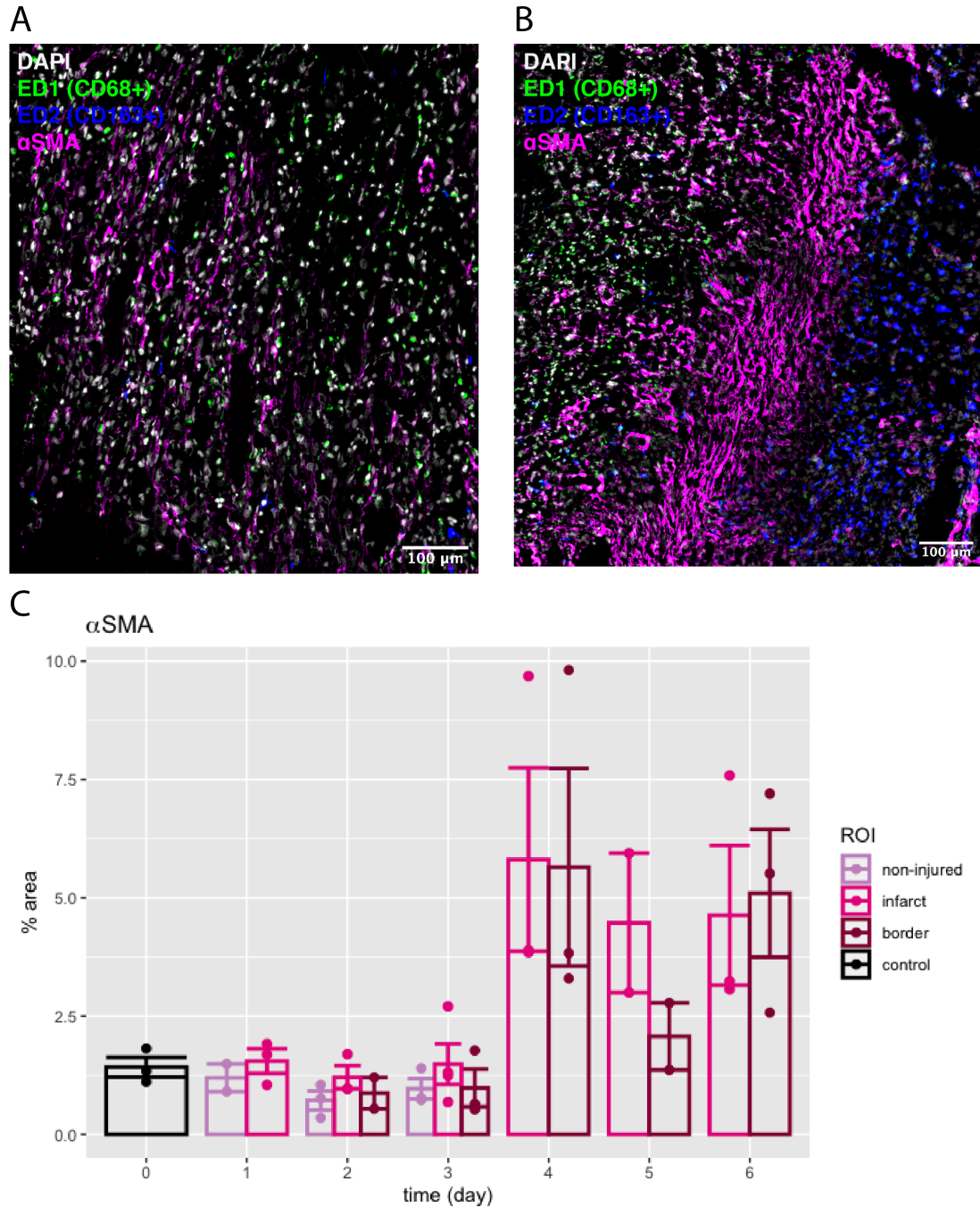
Figure 3-7. αSMA+ unique spatial distribution and time course following myocardial infarction
(A and B) Example images from the same tissue section taken on day 4 following myocardial infarction where myofibroblasts are identified by αSMA (magenta), as well as CD68+ (green) and CD163+ (blue) macrophages. Nuclei are stained with DAPI (grey). Scale bar = 100 μm. **(C)** αSMA pixel area fraction was quantified for several regions of interest on days 1-6 following myocardial infarction and compared to a control tissue sample obtained from a healthy animal (day 0). Error bars = SEM.

High density of macrophages, including CD68+CD163+ macrophages, present in the epicardium

All previous staining and quantifications were done with tissue sections taken from the myocardium (50% wall depth) of the left ventricle. Previous studies suggest that the epicardium is a source of cardiac progenitor cells that may differentiate to macrophages or vascular smooth muscle cells during wound healing.[195-199] Immunohistochemistry of the epicardium on day 5 following myocardial infarction revealed a high density of both CD68+ and CD163+ macrophages (Figure 3-8), 3.3x and 6.5x higher, respectively, than in a tissue section from the myocardium of the same animal. There also appears to be a much higher density of double-positive CD68+CD163+ macrophages, indicated with white arrows in Figure 3-8B. The density of αSMA+ cells was also 1.6x higher than in the myocardium from the same animal, but this appears to most likely reflect the high density of coronary arteries in the epicardium as opposed to interstitial fibroblasts (Figure 3-8C). There was no region of apparent necrosis in the epicardium of this animal at day 5, suggesting that the region of necrosis is primarily restricted to the myocardium.

Capillary dropout adjacent to region of necrosis

A tissue section taken from the myocardium on day 5 following myocardial infarction was stained with CD31 to identify the endothelium of the surviving capillary network (Figure 3-9). A dense vascular network is observed at the border of the infarct with vascular smooth muscle cells and interstitial fibroblasts identified as αSMA+ cells. The region of necrosis is identified as the area lacking DAPI staining and is outlined with a dashed white line. Extensive capillary dropout is observed near the border of necrosis and within the necrotic region, indicating that this area is experiencing severe ischemia. Additionally, within this same tissue section CD31+ staining

identified the endothelial lining of the left ventricular cavity, which was also lined with a ring of highly aligned αSMA+ cells (Figure 3-10). This endocardial layer was surrounded by an approximately 250 μm wide band of αSMA+ cells, which may also be a source of progenitor cells that contribute to arteriogenesis following myocardial infarction.[200, 201]
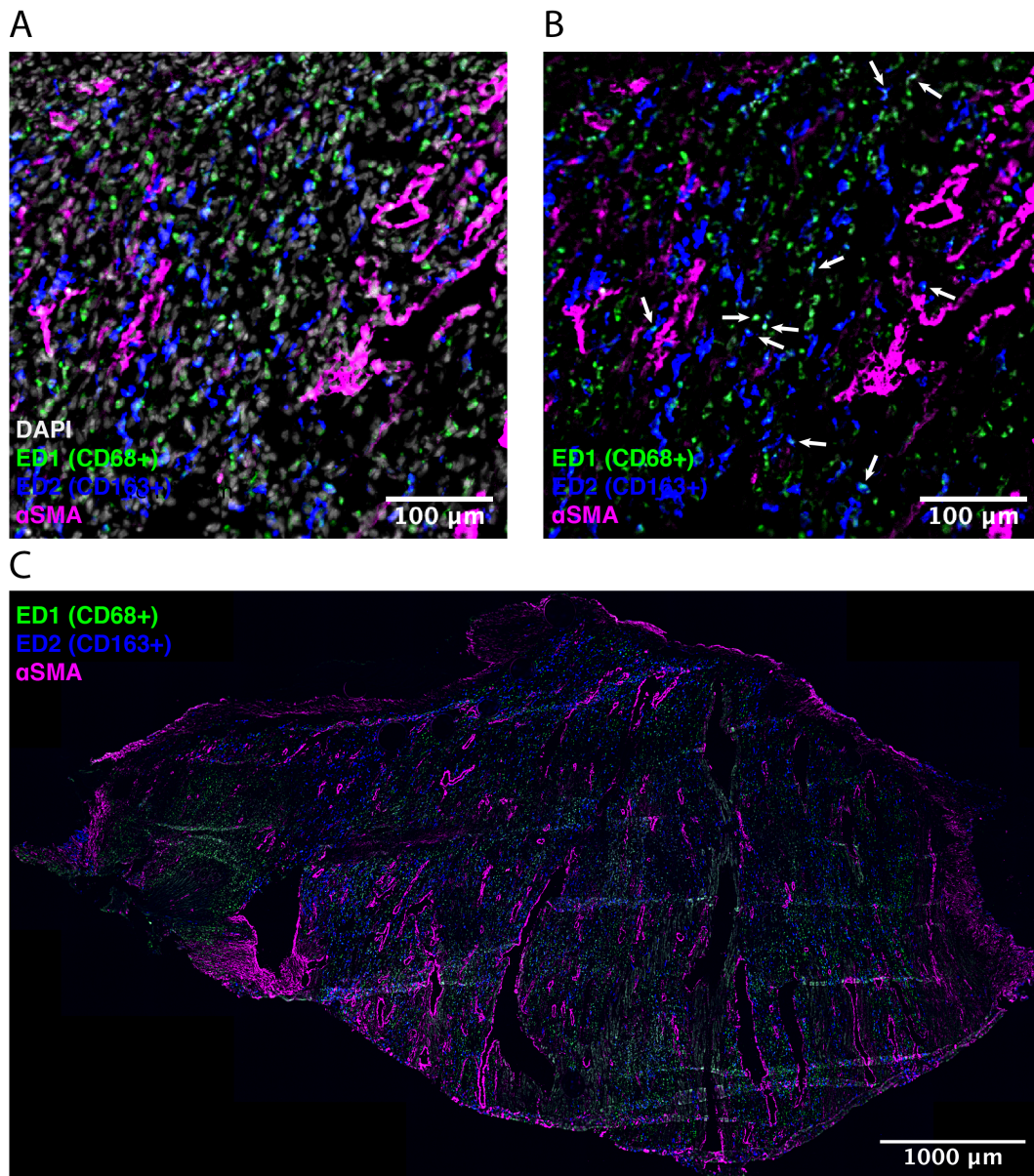
Figure 3-8. High density of macrophages in the epicardium.
(A and B) Example of CD68+ (green), CD163+ (blue), αSMA+ (magenta) and DAPI (grey) staining in the epicardium at day 5 following myocardial infarction. White arrows indicate CD68+CD163+ cells. Scale bar = 100 μm. (C) Tile scan at 20x of epicardium tissue section. Scale bar = 1000 μm.
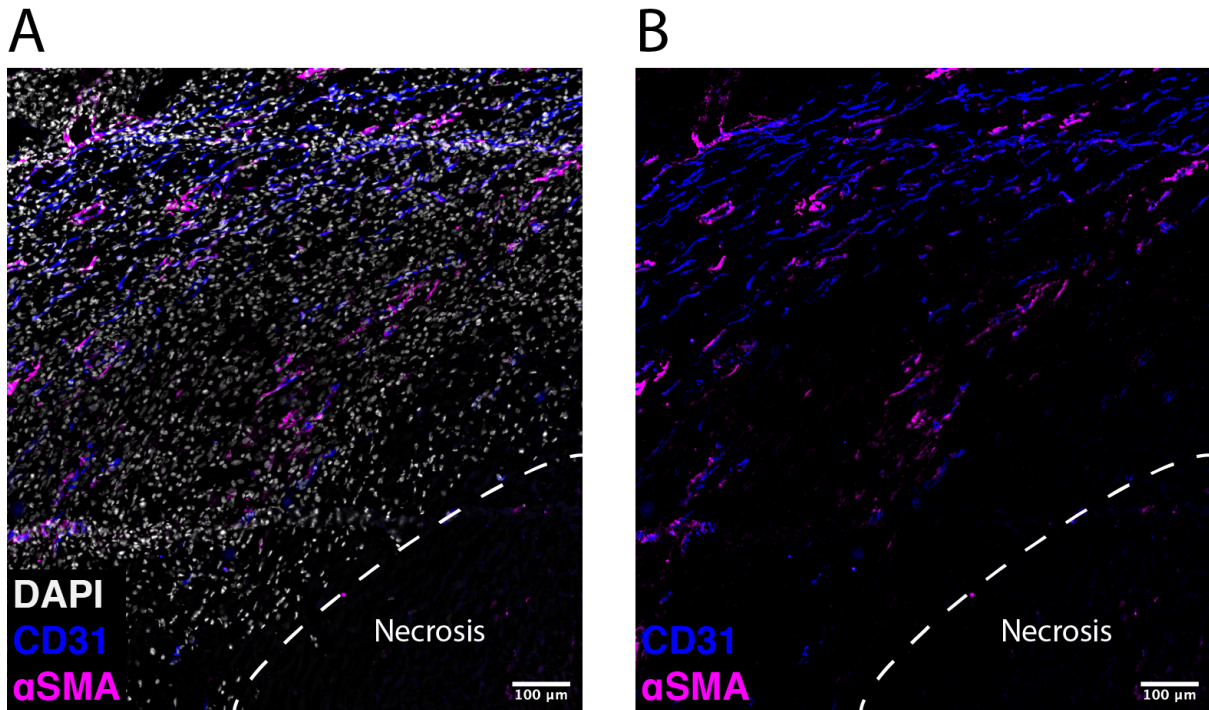
Figure 3-9. Capillary dropout adjacent to region of necrosis.
(A and B) CD31 (blue), αSMA+ (magenta), and DAPI (grey) staining in the myocardium on day 5 following myocardial infarction. Region of necrosis is indicated by dashed white line. Scale bar = 100 μm.
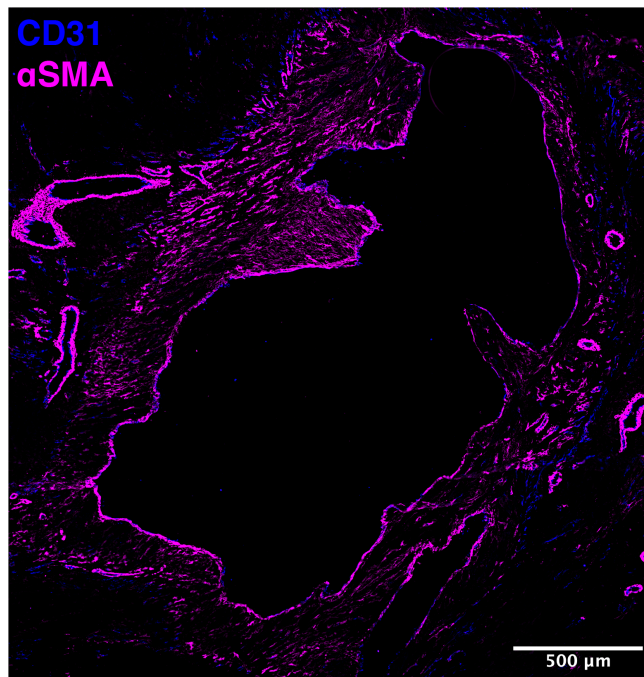
Figure 3-10. Endocardial lining of the left ventricle is surrounded by αSMA+ cells.
Cross-section of left ventricular cavity on day 5 following myocardial infarction stained with CD31 (blue) and αSMA+ (magenta). Scale bar = 500 μm.

Minimal collagen deposition during week one following myocardial infarction

Picrosirius red stain is used to identify collagen fibers in the infarct, where yellow-red staining indicates type I collagen fibers and green staining indicates type III collagen fibers. Type III collagen fibers are immature, thin collagen fibers that are deposited by fibroblasts during healing and are later replaced by stronger type I collagen fibers.[202, 203] An example of picrosirius red staining of collagen fibers for a tissue section on day 5 following myocardial infarction is provided in Figure 3-11A. Collagen area fraction was quantified by calculating the ratio of picrosirius red pixel area as a fraction of total tissue area (Figure 3-11B). Collagen area fraction was approximately 6% throughout week 1 following myocardial infarction, but dropped to nearly 3% on day 3, which may indicate when the heart is most susceptible to myocardial rupture.[204, 205]
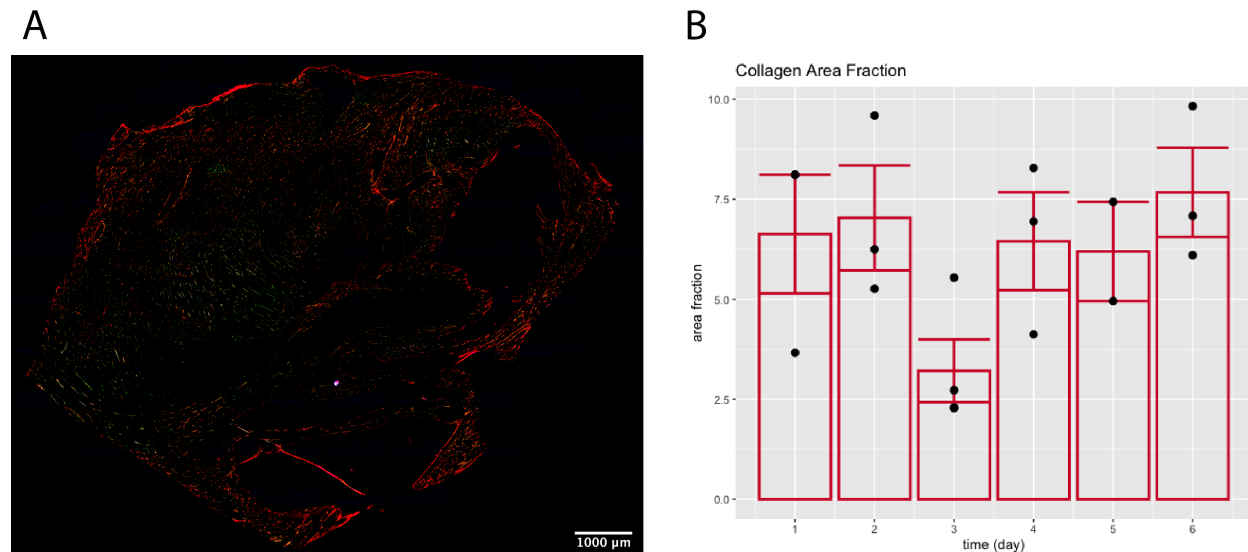
Figure 3-11. Collagen area fraction following myocardial infarction.
(**A**) Example of picrosirius red staining in a tissue section on day 5 following myocardial infarction. Scale bar = 1000 μm. (**B**) Collagen area as a fraction of total tissue area is quantified on days 1-6 following myocardial infarction. Error bars = SEM.

Discussion

In this work, we characterize the spatiotemporal dynamics of CD68+ and CD163+ macrophage infiltration in the heart on days 1-6 following permanent occlusion of the coronary artery in a rat model of MI. We identify distinct macroscopic regions of interest in the infarct, including a region of necrosis that appears between days 2 and 3, and intramyocardial hemorrhage that appears between days 4 and 5. Resident cardiac macrophages (CD163+) are present in a regularly spaced pattern in non-injured regions of tissue that borders the infarct at early time points, and are lost from ischemic regions of necrosis that lack capillary perfusion. CD163+ macrophage populations are reduced significantly in the infarct region on days 2 and 3, and subsequently recover to initial densities by day 6. Inflammatory (CD68+) macrophages are not present in non-injured tissue, or in the infarct at early time points, but increase substantially in density on day 4 which is sustained through day 6. This is consistent with previous studies that have reported that M1 macrophages peak between days 3 and 5, and M2 macrophages peak around day 7, with total macrophage infiltration reaching maximum levels on day 7 in models of permanent coronary artery occlusion.[178, 181, 206, 207] Furthermore, we showed in this work that macrophages demonstrated multiple distinct patterns of spatial colocalization with αSMA+ cardiac fibroblasts. In some cases, macrophages were evenly dispersed within populations of αSMA+ cardiac fibroblasts, yet there were examples within the same tissue section where fibroblasts occupied a unique spatial niche distinct from macrophage populations. We demonstrated evidence of a CD68+CD163+ positive macrophage population which does not fit the canonical M1/M2 classifications, and appears to be enriched within the epicardium.

Previous studies have documented the temporal dynamics and heterogeneity that exists in macrophage phenotypes and transcriptional profiles following myocardial infarction,[181, 185, 208] but there are few examples of the spatial localization of these macrophage phenotypes in the infarct. Recently, Chakarov et al. demonstrated that there are unique populations of resident tissue macrophages in lung, fat, heart, and dermal tissues that occupy different spatial niches. Lyve1^{lo}MHCII[hi] macrophages were enriched near nerve bundles and Lyve1^{hi}MHCII[lo] macrophages were localized near endothelial cells and upregulated genes related to angiogenesis.[209] This study provides evidence that there is a link between macrophage phenotypes and the spatial niches that they occupy, but no study to date has mapped the spatial distribution of macrophages in the heart following MI to their dynamic phenotypes and functions. To our knowledge, this work is the first example of the spatial distributions of macrophage populations in the heart following MI and their colocalization with cardiac fibroblasts and other unique regions of interest within the infarct, including regions of necrosis and the epicardium. This work will inform future studies that aim to target macrophages for novel therapeutics to treat cardiac fibrosis and the development of heart failure.

Developing therapies that target the roles of macrophages in post-MI wound healing is complex. There exist many different sources of macrophages that play opposing roles throughout the time course of wound healing. Studies in both mice and humans have documented a correlation between increased monocyte infiltration following MI and reduced ventricular function.[210, 211] Alternatively, resident cardiac macrophages have been shown to improve outcomes and limit maladaptive remodeling of the ventricle following MI.[212, 213] However, the complete depletion of circulating monocytes during the early inflammatory phase of wound healing increased necrotic tissue and apoptotic cells, and depletion of monocytes during the later reparative phase decreased

collagen deposition and angiogenesis.[206] Therapies that successfully improve wound healing and long-term improvement in cardiac function will require a robust understanding of the complex spatiotemporal dynamics, and varied sources and activation states of macrophages that contribute unique and important functions throughout the course of wound healing. Current therapies have focused on either limiting monocyte recruitment to the infarct, or altering the phenotypes of macrophage populations with varying levels of success.[178] One approach that has demonstrated promising results is the use of a monoclonal antibody to IL-1β, canakinumab, which has been shown to reduce additional cardiovascular events following MI, but the complete mechanisms by which this contributes to improved outcomes is not fully understood.[214, 215]

The model systems used to study MI also present challenges to translating these findings to the clinical setting. Permanent occlusion of the coronary artery is a widely used animal model because it induces severe ischemia and a reproducible inflammatory response, but with increasing widespread access and success of reperfusion therapy the findings of these studies may be limited in their translation to clinical therapeutics and outcomes. Ischemia-reperfusion (I/R) models more accurately mimic the clinical scenario of primary angioplasty, but these models have important documented differences. A study by Yan et al. described the difference in the temporal dynamics of macrophage recruitment between models of permanent total occlusion of the coronary artery and timely reperfusion of the occluded coronary artery. They demonstrated that macrophage infiltration peaked nearly 4 days earlier in the I/R model, shifting from day 7 to day 3 compared to the permanent occlusion model, and exhibiting smaller infarct size and less adverse remodeling.[181] Furthermore, the mortality rate is high for animal models of permanent occlusion due to cardiac rupture. Since these animals are excluded from the results of these studies, an

important question that is difficult to answer is how the inflammatory response and macrophage populations differ in animals that experience cardiac rupture.[185]

One approach to identifying novel therapeutic targets is leveraging computational models to reduce complexity of systems with heterogenous spatial and temporal dynamics.[216] Computational models are useful for integrating large data sets to explain experimental observations, to identify the biological mechanisms involved, and to generate new hypothesis for further exploration. Wang et al. developed a mathematical model that describes how IL-1, IL-10, and TNFα contribute to monocyte differentiation and macrophage activation states following myocardial infarction.[90] A large-scale network model of macrophage signaling developed by Liu et al. demonstrated how combinations of conflicting pro-inflammatory and anti-inflammatory stimuli contributed to a wide range of gene expression patterns, which more accurately represented the macrophage activation phenotypes observed *in vivo*.[217] Similarly, computational models of cardiac fibroblast signaling were able to predict how dynamic pro-inflammatory and pro-fibrotic stimuli regulate the differentiation of cardiac fibroblasts to myofibroblasts, and the temporal dynamics of post-MI stimuli that drive the progression of fibroblast phenotypes during wound healing and scar formation.[25, 218] Network models of this scale are also useful tools for performing high-throughput screening of drugs to identify the most promising drug candidates for novel therapeutics, as Zeigler et al. demonstrated in their *in silico* screen of FDA-approved drugs to target cardiac fibroblast signaling mechanisms that contribute to the progression of fibrosis.[17] The experimental insight gained from the work presented here will help to inform future computational models that aim to integrate the spatiotemporal dynamics of macrophage and fibroblast populations during post-MI wound healing and their contributions to scar formation and fibrosis.

These models could further be coupled with mechanical models (e.g., finite element models) to predict how the mechanical environment of the heart is modified during wound healing and the impacts on cardiac output and function.[27]

There are several limitations to the work presented here, notably the simplified classification of macrophages as M1 and M2 phenotypes based on a limited set of available markers. As has been discussed here, this classification is an over-simplification of the varied phenotypes that macrophages adopt *in vivo,* and this is supported in our work by the identification of a subpopulation of macrophages that simultaneously express M1 (CD68+) and M2 (CD163+) markers. Future studies should aim to more comprehensively describe the heterogenous macrophage expression profiles that exist, and investigate whether these macrophage phenotypes are present in spatially heterogenous patterns in addition to the temporal dynamics of macrophage activation that have been documented previously.[181, 185] A combination of single-cell and spatial transcriptomics will likely be required to answer these questions and exhaustively characterize the spatial heterogeneity of macrophage populations within the infarct.[219]

An additional limitation of this study is that αSMA by itself is not sufficient to uniquely identify cardiac fibroblasts since this also labels vascular smooth muscle cells and other mural cells. Cardiac fibroblasts can typically be identified visually by their spindle-like morphology, but the quantification of fibroblast density by image analysis methods is complicated by the lack of a unique marker for fibroblasts. There exists no single unique marker for identifying cardiac fibroblasts, but recent studies have identified novel markers that are more specific.[220, 221] Lineage reporter animal models could be utilized to investigate macrophage or fibroblast populations with specific lineages.[222] Despite these limitations, we believe this work provides valuable contributions

to the understanding of the spatial dynamics of macrophage infiltration in the infarct during the inflammatory and proliferative phases following myocardial infarction. A comprehensive description of the spatiotemporal dynamics of macrophage infiltration and activation will be required to identify novel therapeutics that can reduce maladaptive remodeling of the ventricle that leads to heart failure following myocardial infarction.

CHAPTER 4

Mathematical model predicts that acceleration of diabetic wound healing is dependent on spatial distribution of VEGF-A mRNA (AZD8601)

Acknowledgments: Paul J. Myers[1], Joachim Almquist[2,3,4], Peter Gennemark[2,5], Anthony C. Bruce[6], Maria Wågberg[8], Regina Fritsche-Danielson[8], Kenny M. Hansson[8], Matthew J. Lazzara[1,6], Shayn M. Peirce[6,7]

[1]Department of Chemical Engineering, University of Virginia, Charlottesville, VA, USA
[2]Drug Metabolism and Pharmacokinetics, Research and Early Development, Cardiovascular, Renal and Metabolism, BioPharmaceuticals R&D, AstraZeneca, Gothenburg, Sweden
[3]Fraunhofer-Chalmers Centre, Chalmers Science Park, Gothenburg, Sweden
[4]Clinical Pharmacology and Quantitative Pharmacology, Clinical Pharmacology and Safety Sciences, R&D, AstraZeneca, Gothenburg, Sweden
[5]Department of Biomedical Engineering, Linköping University, Linköping, Sweden
[6]Department of Biomedical Engineering, University of Virginia, Charlottesville, VA, USA
[7]Robert M. Berne Cardiovascular Research Center, University of Virginia, Charlottesville, VA, USA
[8]Bioscience Cardiovascular, Research and Early Development, Cardiovascular, Renal and Metabolism, BioPharmaceuticals R&D, AstraZeneca, Gothenburg, Sweden

Abstract

Introduction: Pharmacologic approaches for promoting angiogenesis have been utilized to accelerate healing of chronic wounds in diabetic patients with varying degrees of success. We hypothesize that the distribution of proangiogenic drugs in the wound area critically impacts the rate of closure of diabetic wounds. To evaluate this hypothesis, we developed a mathematical model that predicts how spatial distribution of VEGF-A produced by delivery of a modified mRNA (AZD8601) accelerates diabetic wound healing.

Methods: We modified a previously published model of cutaneous wound healing based on coupled partial differential equations that describe the density of sprouting capillary tips, chemoattractant concentration, and density of blood vessels in a circular wound. Key model parameters identified by a sensitivity analysis were fit to data obtained from an *in vivo* wound healing study performed in the dorsum of diabetic mice, and a pharmacokinetic model was used to simulate mRNA and VEGF-A distribution following injections with AZD8601. Due to the limited availability of data regarding the spatial distribution of AZD8601 in the wound bed, we performed simulations with perturbations to the location of injections and diffusion coefficient of mRNA to understand the impact of these spatial parameters on wound healing.

Results: When simulating injections delivered at the wound border, the model predicted that injections delivered on day 0 were more effective in accelerating wound healing than injections delivered at later time points. When the location of the injection was varied throughout the wound space, the model predicted that healing could be accelerated by delivering injections a distance of 1-2 mm inside the wound bed when compared to injections delivered on the same day at the wound border. Perturbations to the diffusivity of mRNA predicted that restricting diffusion of

mRNA delayed wound healing by creating an accumulation of VEGF-A at the wound border. Alternatively, a high mRNA diffusivity had no effect on wound healing compared to a simulation with vehicle injection due to the rapid loss of mRNA at the wound border to surrounding tissue.

Conclusions: These findings highlight the critical need to consider the location of drug delivery and diffusivity of the drug, parameters not typically explored in pre-clinical experiments, when designing and testing drugs for treating diabetic wounds.

Introduction

Diabetic foot ulcers are a type of chronic wound that can persist for months to years because the normal mechanisms of wound healing are profoundly impaired in diabetic patients. Over 30 million Americans are affected by diabetes, and nearly 15% of these patients experience diabetic foot ulcers in their lifetime.[100, 101] Diabetic foot ulcers are the leading cause of hospitalizations for patients with diabetes, and are associated with significant pain, suffering, loss of quality of life, and increased risk for lower extremity amputation.[100] Current therapies for treating chronic diabetic wounds have limited efficacy, and diabetic wounds remain a costly and challenging clinical problem. The development of new therapies for healing chronic diabetic wounds would have a substantial impact on individual patients and on society, but is challenged by a lack of model systems for designing drug delivery strategies that predict the influences of dosages, delivery routes and locations, and mechanisms of action. A novel approach that has been shown to accelerate angiogenesis and the healing of cutaneous wounds in a murine model of diabetic wound healing is the delivery of a modified mRNA (AZD8601) designed to enhance VEGF-A expression in the skin.[223] There is limited spatially resolved data available about the diffusion and degradation of this modified mRNA and a limited number of drug delivery parameters that have been tested in

preclinical models. To address this challenge, we developed a mathematical model that predicts how location of delivery and spatial distribution of AZD8601 impacts the rate of wound closure in an established murine model of diabetic wound healing.

Wound healing is a complex and coordinated series of cellular and molecular events comprised of coagulation, inflammation, granulation tissue formation, angiogenesis, reepithelization and extracellular matrix remodeling.[77] During acute wound healing in healthy individuals, cells respond dynamically to chemotactic cues (e.g., inflammatory cytokines and growth factors) to coordinate this cascade of events, which eventually leads to complete wound closure. However, this coordinated progression is dysregulated in the case of chronic wounds. In particular, patients with diabetes experience microvascular dysfunction[77] combined with low grade chronic inflammation[102], which delays or prohibits the normal wound healing process via a peak in inflammation that triggers the proliferative phase.

For decades, numerous pharmacological treatments designed to promote effective wound healing in diabetic patients have been evaluated in pre-clinical and clinical studies.[105-107] Stimulation of angiogenesis, or new microvessel formation[108, 109], has been pursued as one approach to jump-start the wound healing cascade in the angiogenesis-impaired setting of diabetes. For example, delivery of both recombinant VEGF-A protein and naked or adenoviral vector-mediated gene transfer to upregulate VEGF-A have been shown to accelerate wound healing in pre-clinical[224, 225] and clinical studies.[226] Our team has recently shown that intradermal injection of AZD8601, an mRNA designed to upregulate VEGF-A expression, accelerates angiogenesis and the healing of cutaneous wounds without causing edema or micro-hemangioma formation in an established murine model of diabetic wound healing.[223] While these results were encouraging, the reproducibility and extensibility of our experiments, like most pre-clinical studies in the diabetic

wound healing field, are challenged and constrained by the fact that only a limited number of drug dosages, drug injection timings, and spatial locations of intradermal injections were tested *in vivo*, allowing for the possibility that a more effective injection protocol was not evaluated.

Mathematical and computational models have demonstrated utility in leveraging experimental data to predict the outcomes of hypothetical experiments that have not yet been tested at the bench.[227] Running *in silico* experiments using computational and mathematical modeling can also save time, money, and reduce the number of animals needed for experimentation. Previous computational models have been developed to study mechanisms of cutaneous wound healing[228-233] and to identify drug targets for stimulating angiogenesis in wound healing.[234] Almquist et al. recently reported an empirical pharmacokinetic and pharmacodynamic model of AZD8601 in diabetic wound healing, which captures statistical variation in wound healing dynamics at both the individual and the population level using a nonlinear mixed effect (NLME) modelling approach.[235] While this model describes the time-dependent aspects of wound healing, it does not account for spatial heterogeneity of drug delivery and wound healing. Therefore, we modified a previously published partial differential equation (PDE) model of cutaneous wound healing originally reported by Pettet et al.[114] that describes the spatiotemporal regulation of chemoattractant production, capillary tip sprouting, and neovascularization to also include a PDE that describes the spatiotemporal dynamics of mRNA and VEGF-A production following injections of AZD8601. We then used this new system of coupled PDEs to predict how diffusivity of mRNA and location of AZD8601 injection in the wound affect angiogenic sprouting, vascularization of the wound bed, and time to wound closure in a model of diabetic wound healing.

Materials and Methods

Murine model of diabetic wound healing

All procedures were conducted in accordance with the guidelines of the University of Virginia Animal Care and Use Committee or the Local Ethics Committee on Animal Experiments in Gothenburg, Sweden. Three different experimental studies were carried out in two different research laboratories: 1) in the Biomedical Engineering Department at the University of Virginia, Charlottesville, VA, USA, and 2) in the Bioscience Cardiovascular Department, Research and Early Development, Cardiovascular, Renal and Metabolism, BioPharmaceuticals R&D, AstraZeneca, Gothenburg, Sweden. The data acquired in these experiments have been published, along with detailed experimental methods by Sun et al.[223] and Almquist et al.[235] Briefly, circular, full-thickness, cutaneous wounds approximately 1 cm in diameter were surgically made on the dorsum of anesthetized eight-week old diabetic B6.BKS(D)-Lepr[db]/J mice (Jackson Laboratory). Mice received injections of either vehicle or AZD8601 in 10 μL of 10 mM citrate/130 mM saline intradermally at four equidistant points around the wound edge. Some groups of mice received injections at a single timepoint (on day 0 or day 3), and some groups received injections on multiple days (days 0 and 3). For the study groups that were injected twice, the four injection sites were shifted 45° on day 3 in order to avoid injecting the same location twice (Figure 4-1A). Wounds in anesthetized mice were serially imaged using an iPhone6 (Apple) or a Canon 600D with a Tamron SP 900 mm F/2.8 objective under bright-field illumination. The open wound area, identified as the region in the center of the wound lacking an epithelial layer, was measured by tracing the border of the wound in ImageJ. The study groups and time points at which images were acquired and quantified for each study are provided in Table 4-1. In total, 584

open wound area measurements were made. Percent open wound area was calculated by dividing the wound area measurement at each time point by the initial wound area (at t = 0 days) for individual animals. It should be noted that some wounds increased in size by day 3 due to initial wound recoil, leading to wound area measurements at day 3 that were greater than the initial area for some individual animals.
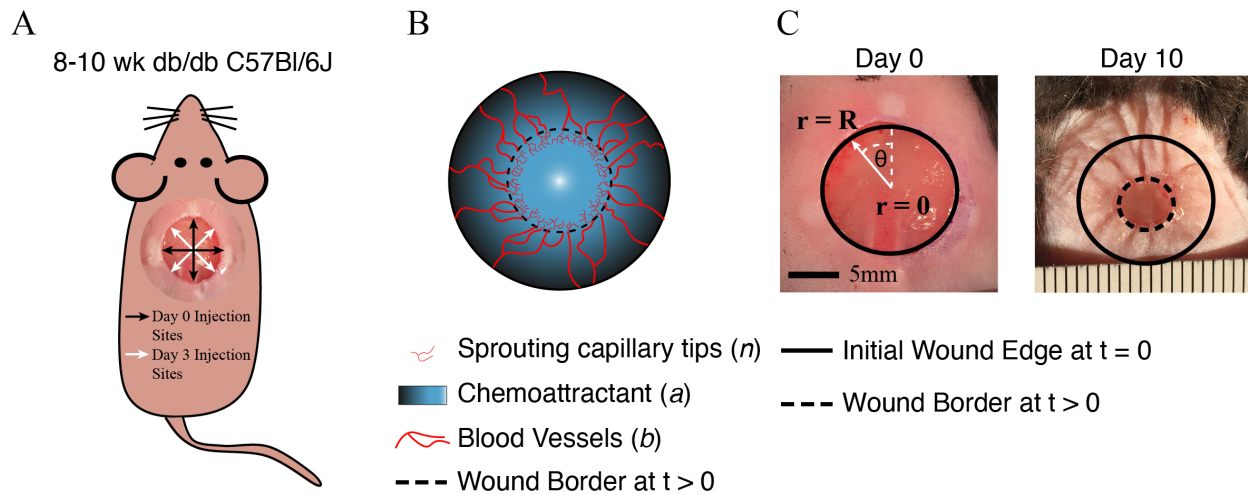
Figure 4-1. Experimental model and PDE model geometry.
(A) Full thickness cutaneous wounds of approximately 1 cm in diameter were made on the dorsum of db/db mice and injected with AZD8601 at four injection sites at the initial wound edge separated by 90 degrees. **(B)** The PDE model describes the density of sprouting capillary tips (n), chemoattractant concentration (a), and blood vessel density (b) in a healing wound. **(C)** Model geometry in cylindrical coordinates depicting uniform circular healing. At t = 0, the initial wound edge is at r = R (5 mm), and healing occurs towards r = 0. Healing occurs uniformly with respect to θ. Examples of a wound on the dorsum of a mouse are shown on day 0 and day 10.

Table 4-1. Summary of experimental design across all studies.

	Location	Study Groups	Treatment	Time Points Measured
Study 1	University of Virginia	Group 1	Vehicle Day 0	Days 0, 3, 6, 10, 13, and 18
		Group 2	100 µg AZD8601 Day 0	
		Group 3	Vehicle Days 0 and 3	
		Group 4	100 µg AZD8601 Days 0 and 3	

Study 2	University of Virginia	Group 1	Vehicle Days 0 and 3	Days 0, 3, 6, 10, and 13
		Group 2	30 µg AZD8601 Days 0 and 3	
		Group 3	100 µg AZD8601 Days 0 and 3	
		Group 4	200 µg AZD8601 Days 0 and 3	
Study 3	AstraZeneca, Sweden	Group 1	Vehicle Day 3	Days 0, 3, 7, 10, 14, and 17
		Group 2	100 µg AZD8601 Day 3	
		Group 3	Vehicle Days 0 and 3	
		Group 4	100 µg AZD8601 Days 0 and 3	

Pharmacokinetic model

In a separate study, the pharmacokinetics (PK) of VEGF-A protein was measured after injection of a single dose of 100 µg AZD8601 intradermally in mice without wounds. Briefly, intradermal injections were given in up to three different locations (n=13 mice). Mice were sacrificed at 6, 24, 48, 72, and 144 hours after injection, and the amount of VEGF-A protein in the skin was quantified according to methods that have been published previously.[223] The lower limit of quantification (LLOQ) for VEGF-A was 0.156 pg/mg tissue. At 144 h, 10 out of 12 observations were below LLOQ. This study, including the bioanalytical methods for quantifying the amount of VEGF-A protein in skin, is described in detail by Sun et al (2018).[223]

The PK of AZD8601 (VEGF-A mRNA) and VEGF-A protein was represented by the following model:

$$\frac{dmRNA(t)}{dt} = -k_1 \times mRNA(t) \tag{1}$$

$$\frac{dVEGF(t)}{dt} = k_2 \times mRNA(t) - k_3 \times VEGF(t) \tag{2}$$

$$mRNA(0) = VEGF(0) = 0 \tag{3}$$

where $mRNA(t)$ is the amount of AZD8601 and $VEGF(t)$ is the concentration of VEGF-A protein. The parameters k_1, k_2, and k_3 are kinetic parameters describing degradation of mRNA, synthesis of VEGF-A, and degradation of VEGF-A, respectively (Table 4-2). Note that these parameters are only valid for full-thickness wounds of 1cm in diameter. A complete description of this model and its underlying data is reported by Almquist et al.[235]

Table 4-2. Pharmacokinetic model parameters.

Description	Symbol	Unit	Value
mRNA degradation	k_1	hr^{-1}	0.055
VEGF synthesis	k_2	pg (VEGF-A) mg^{-1} (tissue) µg^{-1} (mRNA) hr^{-1}	0.16
VEGF degradation	k_3	hr^{-1}	0.23

Partial differential equation model

A PDE model was implemented in MATLAB (R2020a, The MathWorks, Natick, MA) based on the wound healing model previously described by Pettet et al.[114] This model treats the wound as a one-dimensional geometry with healing occurring in one direction, from the edge to the center of the wound. The system of coupled PDEs (Eqs. 4-6) published by Pettet et al. describes three dependent variables: sprouting capillary-tip density (n), chemoattractant concentration (a), and blood vessel density (b). A schematic of these variables in a healing wound is illustrated in Figure 4-1B. The dimensionless conservation equations from Pettet et al. in Cartesian coordinates are given by:

$$\frac{\partial n}{\partial t} = \mu_n \frac{\partial^2 n}{\partial x^2} - \chi \frac{\partial}{\partial x}\left(n \frac{\partial a}{\partial x}\right) + \lambda_1 ab - \lambda_2 n - \lambda_0 n^2 \tag{4}$$

$$\frac{\partial a}{\partial t} = \frac{\partial^2 a}{\partial x^2} + \frac{\lambda_4}{2}\left(1 + \tanh\left(\frac{1-b}{\delta}\right)\right) - (\lambda_4 + \lambda_5 b)a \tag{5}$$

$$\frac{\partial b}{\partial t} = \mu_b \frac{\partial}{\partial x}\left(n \frac{\partial b}{\partial x}\right) - \mu_n \frac{\partial n}{\partial x} + \chi n \frac{\partial a}{\partial x} \tag{6}$$

Descriptions and values for the constant parameters in these equations are given in Table 4-3. In this model, chemoattractant is defined broadly to represent proangiogenic factors secreted by macrophages that promote migration of sprouting endothelial cells and wound healing. Macrophages are assumed to be evenly distributed throughout the wound space. The chemoattractant profile drives the wave-like ingrowth of capillary-tip sprouts and new blood vessel formation, representing angiogenesis that occurs during wound healing. The formation and chemotaxis of sprouting endothelial cells from the existing vasculature occurs via both random motility of sprouts and migration up the chemotactic gradient. The kinetic terms associated with sprouting capillary-tip density include production via budding and loss of capillary-tips due to decay and tip-to-tip anastomosis (Eq. 4). The equation for chemoattractant concentration (Eq. 5) describes the diffusion of chemoattractant, the production by macrophages in the wound space, removal via the vasculature, and decay of chemoattractant. The blood vessel density (Eq. 6) is described primarily by the maturation of migrating capillaries connected with the existing vasculature and random motility of the capillary tips. Full details for the original system of equations are described by Pettet et al.

Table 4-3. PDE model parameters in Cartesian and cylindrical coordinate systems.

Parameter	Parameter Description	Parameter Value in Cartesian Coordinates described by Pettet et al. (Dimensionless)	Parameter Value in Cylindrical Coordinates (Dimensionless) [fitted value]
λ_0	Rate of tip anastomosis	100	200 [856]
λ_1	Tip production	100	800 [3860]
λ_2	Decay of sprouting tips	10	40
μ_n	Capillary tip coefficient of random motility	10^{-3}	10^{-3}
χ	Capillary tip coefficient of chemotaxis	0.1	0.1 [0.146]
$\hat{n}$	Tip density at wound edge	1	2
α	Rate of decay of tip density	2.5	10
λ_4	Decay of chemoattractant concentration	100	400
λ_5	Removal of chemoattractant via vasculature	10	40
λ_7	Constant rate of blood-borne removal	10	20
δ	Rate of decreasing chemoattractant production	0.01	0.01
μ_b	Blood vessel coefficient of random motility	10^{-3}	0.5×10^{-3}
$\hat{b}$	Blood vessel density at wound edge	1.5	1.5
$\tilde{r}$	Margin around wound edge that delineates inflammation zone in initial response	0.05	0.95

Conversion to cylindrical coordinates

We converted the equations described by Pettet et al. from Cartesian to cylindrical coordinates to represent the geometry of the wound more accurately. In the converted model, the wound is circular with an initial radius $r = R$, placing the center of the wound at $r = 0$, with healing occurring in the negative r direction (Figure 4-1C). The governing equations in Cartesian form (Eqs. 4-6) were rewritten in general differential form and then recast in cylindrical coordinates. The characteristic length in the model described by Pettet et al. is L = 2.5 mm, whereas our model is defined with a radius R = 5 mm to reflect the conditions of our experimental wound healing model. Thus, in our model, the radial coordinate (r) is non-dimensionalized by R = 5 mm and the time coordinate (t) is non-dimensionalized by R^2/D = 2.89 days, considering a representative chemoattractant diffusivity of D = 10^{-6} cm^2/s based on the diffusivity of acidic fibroblast growth factor in agarose.[235] Additionally, all dimensionless parameters that appear in Eqs. 4-6 retain their original definitions (found between Equations 9 and 10 in Pettet et al.) in the new set of cylindrical model equations, except that the wound half-width (L) from the original definitions has been replaced by the wound radius (R) in our system. A detailed explanation of the model transformation from Cartesian to cylindrical coordinates is described in the supplemental material (Supplemental Notes 1 and 2).

Because the wounds in the murine models are full-thickness, we assume that no healing occurs in the z-direction. Additionally, because the wound diameter (~1 cm) is much greater than the wound thickness, we assume that the field variables can be lumped in the z-direction and therefore modeled solely in the r-direction. This results in a new set of dimensionless conservation equations for n, a, and b:

$$\frac{\partial n}{\partial t} = \mu_n \frac{1}{r}\frac{\partial}{\partial r}\left(r\frac{\partial n}{\partial r}\right) - \chi n \frac{1}{r}\frac{\partial}{\partial r}\left(r\frac{\partial a}{\partial r}\right) - \chi \frac{\partial a}{\partial r}\frac{\partial n}{\partial r} + \lambda_1 ab - \lambda_2 n - \lambda_0 n^2 \qquad (7)$$

$$\frac{\partial a}{\partial t} = \frac{1}{r}\frac{\partial}{\partial r}\left(r\frac{\partial a}{\partial r}\right) + \frac{\lambda_4}{2}\left[1 + \tanh\left(\frac{1-b}{\delta}\right)\right] - (\lambda_4 + \lambda_5 b)a \qquad (8)$$

$$\frac{\partial b}{\partial t} = \mu_n\left[n\frac{1}{r}\frac{\partial}{\partial r}\left(r\frac{\partial b}{\partial r}\right) + \frac{\partial b}{\partial r}\frac{\partial n}{\partial r}\right] - \mu_n\frac{\partial n}{\partial r} + \chi n\frac{\partial a}{\partial r} \qquad (9)$$

The dimensionless initial conditions in cylindrical coordinates are given by:

$$n(r,0) = \begin{cases} \frac{\hat{n}}{\tilde{r}^3}(r-\tilde{r})(2r^2 - \tilde{r}r - \tilde{r}^2), & \tilde{r} < r \le 1 \\ 0, & 0 \le r \le \tilde{r} \end{cases} \qquad (10)$$

$$a(r,0) = 0, \qquad 0 \le r \le 1 \qquad (11)$$

$$b(r,0) = \begin{cases} \left(\frac{\hat{b}-\tilde{b}}{\tilde{r}^3}\right)(r-\tilde{r})(2r^2 - \tilde{r}r - \tilde{r}^2) + b, & \tilde{r} < r \le 1 \\ \tilde{b}, & 0 \le r \le \tilde{r} \end{cases} \qquad (12)$$

where it is assumed that the wound margin has penetrated an initial distance $1 - \tilde{r}$ such that the radius of the open wound in dimensionless terms is $\tilde{r}$. We note that the initial conditions for n and b (Eqs. 10 and 12) are those reported by Pettet et al. and were justified by their monotonic behavior in the inflammation zone. The dimensionless boundary conditions in cylindrical coordinates are given by:

$$\frac{\partial n}{\partial r}(0,t) = 0 \qquad (13) \qquad\qquad n(1,t) = \hat{n}e^{-\alpha t} \qquad (14)$$

$$\frac{\partial a}{\partial r}(0,t) = 0 \qquad (15) \qquad\qquad \frac{\partial a}{\partial r}(1,t) = -\lambda_7 a(1,t)\hat{b} \qquad (16)$$

$$\frac{\partial b}{\partial r}(0,t) = 0 \qquad (17) \qquad\qquad b(1,t) = \hat{b} \qquad (18)$$

where $\hat{n}$ is the capillary tip density at the wound edge; α is rate of decay of tip density; λ_7 is the rate of removal of chemoattractant via vasculature; and $\hat{b}$ is the blood vessel density at the wound edge.

The model equations were solved using an explicit finite difference method, as described in the supplemental material (Supplemental Note 3).

Since wound area is not a direct output of the PDE model, in order to compare model predictions to experimental measurements of wound area, the percent open wound area in the PDE model was determined by the area where the blood vessel density (*b*) was less than 0.1 (dimensionless units) divided by the initial wound area (πR^2). This is intended to represent the border of granulation tissue, composed of neovessels, which fills in the wound during healing and was quantified in experimental studies (Figure 4-1B and 4-1C).

Sensitivity analysis and parameter fitting

A sensitivity analysis was performed to determine the influence of each of the 13 model parameters (Table 4-3) on the rate of wound healing, as described by the percent open wound area. Each parameter was increased and decreased by 10%, varying only one parameter at a time, and a simulation using the perturbed parameters was compared to a simulation using the unperturbed parameters. Specifically, a sensitivity coefficient, *S*, was calculated using

$$S = \frac{y_i - y_o}{|p_i - p_o|} * \frac{p_o}{y_o} \tag{19}$$

where y_o and y_i are the measured percent open wound area at t = 18 days when parameters are set to baseline or perturbed levels, respectively, and p_o and p_i are the values of the baseline parameter and perturbed parameter, respectively. By measuring the absolute difference between the baseline and perturbed parameter, the sign of the sensitivity coefficient, S, can be interpreted as the direction of change in the measured output. Therefore, a positive sensitivity coefficient would indicate an increase in percent open wound area at t = 18 days, and a negative sensitivity coefficient would indicate a decrease in percent open wound area. Additionally, the sensitivity coefficient is

normalized by the baseline parameter value and wound area to account for order of magnitude variations in parameter values.

Subsequent parameter fitting was performed using an optimization function (the *particleswarm* function with default settings in MATLAB, R2020a, The MathWorks, Natick, MA) to search the parameter space for a combination of parameter values that minimize the objective function. The objective function used was the sum of squared errors (SSE) between experimental measurements of wound area and model simulated wound area at the specified experimental time points. The parameter space was constrained by lower and upper bounds of 0.1-fold and 10-fold changes from the baseline value to maintain parameter values within physiologically plausible ranges.

Simulating injections of AZD8601 with the PDE model

Injections of AZD8601 were modeled by a PDE to describe the spatiotemporal distribution of mRNA in the wound space, which was then coupled to the equation for chemoattractant (Eq. 8) to describe VEGF-A synthesis as a function of the local mRNA concentration. In dimensionless form, the conservation equation for mRNA is given by

$$\frac{\partial m}{\partial t} = \frac{D_m}{D_a} \frac{1}{r} \frac{\partial}{\partial r}\left(r \frac{\partial m}{\partial r}\right) - \left(\frac{R^2}{D_a}\right) k_1 m \qquad (20)$$

where m is the dimensionless concentration of mRNA, D_m is the diffusivity of mRNA, D_a is the diffusivity of chemoattractant, and k_1 is the first-order rate constant of mRNA degradation as defined above by the PK model. We set D_a to be the the typical diffusivity of chemoattractant (10^{-6} cm^2/s) as previously reported by Pettet et al. [114, 236] Reported values in literature for the diffusivity of mRNA are in the range of $2\times10^{-9} - 4\times10^{-9}$ cm^2/s[237-239], so we set mRNA diffusivity (D_m) to be 3×10^{-9} cm^2/s. In equation 20, m has been scaled and non-dimensionalized using the concentration

of 100 ug mRNA in a total injection volume of 40 µL (2,500 µg/cm³), as described in the murine

experimental model. Note that the quantity $\left(\frac{R^2}{D_a}\right)$ is required to non-dimensionalize k_1. A no-flux

boundary condition is imposed at the wound center:

$$\frac{\partial m}{\partial r}(0, t) = 0 \qquad\qquad (21)$$

and clearance of mRNA at the wound edge is described by the Robin boundary condition

$$\frac{\partial m}{\partial r}(1, t) = -\lambda_8 \hat{b} m(1, t) \qquad\qquad (22)$$

where λ_8 is the dimensionless rate constant of mRNA removal via vasculature at the wound edge.

We assume that this rate of clearance by the vasculature is comparable for chemoattractant and

mRNA, so we set $\lambda_8 = \lambda_7$ (the rate of blood-borne removal for chemoattractant).

The governing equation for chemoattractant is modified to include an mRNA-

dependent chemoattractant generation term to yield, in dimensionless form,

$$\frac{\partial a}{\partial t} = \frac{1}{r}\frac{\partial}{\partial r}\left(r\frac{\partial a}{\partial r}\right) + \frac{\lambda_4}{2}\left[1 + \tanh\left(\frac{1-b}{\delta}\right)\right] - (\lambda_4 + \lambda_5 b)a + k_{gen}m \qquad (23)$$

where k_{gen} is the dimensionless first-order rate constant for VEGF generation. All other

variables and parameters are as previously defined. The dimensionless VEGF generation rate

constant (k_{gen}) was fit by minimizing the SSE between the net amount of chemoattractant

generated by the PDE model and experimental measurements of VEGF-A following an injection

with 100 µg of AZD8601 previously reported by Almquist et al.[235] Since the PK experiments were

performed in non-injured tissue, the PDE model was run to steady state to simulate a healed

wound and then 100 µg of mRNA was uniformly distributed throughout the wound space.

VEGF-A generated by injections with AZD8601 is considered part of the chemoattractant pool

in this model implementation. The net amount of generated chemoattractant from the PDE

model was calculated by subtracting the total amount of chemoattractant from the unperturbed PDE model (without injections) from the total amount of chemoattractant in a simulation with a single 100 μg injection. The dimensionless fitted value for k_{gen} was 1.53×10^5.

Results

Sensitivity analysis identifies parameters for model fitting

The original system of equations described by Pettet et al. was based on a rabbit model of wound healing in the ear skin. Our experimental model of wound healing is in the dorsum of mice, which contains a layer of thin muscle, termed the "panniculosus carnosus", and causes rapid contraction of the wound in the late stages of acute wound healing leading to faster rates of wound closure.[240] This phenomenon is apparent in the image of a healing wound in a mouse at day 10 (Figure 4-1C), as evidenced by the lines of tented skin extending radially outward from the wound. Because of this difference in experimental models, we conducted a sensitivity analysis to identify a set of parameters appropriate for fitting the computational model to the rate of wound healing observed in our experimental murine model of diabetic wound healing (see Methods Section 3.5). Figure 4-2 depicts the unitless sensitivity coefficient (S) when 13 model parameters were increased or decreased by 10% one at a time. Due to the high complexity of the parameter fitting problem and data sparsity, the number of free parameters was limited to three. The parameters with greatest sensitivity coefficients were selected as candidates for parameter fitting, namely λ_0, λ_1 and χ.
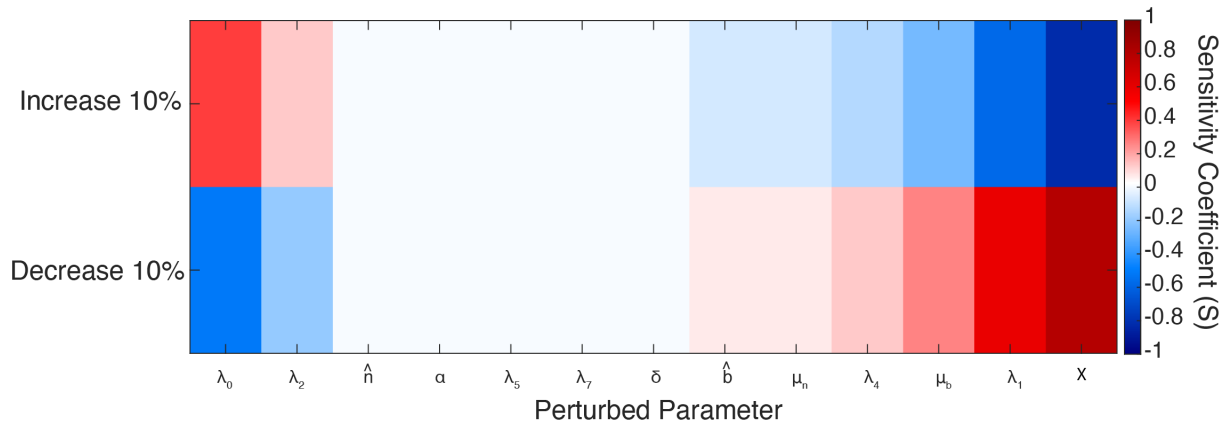
Figure 4-2. Sensitivity analysis of open wound area with respect to individual model parameters. Sensitivity coefficients (S) were calculated when individual parameters were increased or decreased by 10% one at a time while holding all other parameters at baseline values. S values around zero correspond to low sensitivity, while positive S values indicate an increase in open wound area, and negative S values indicate a decrease in open wound area at t = 28 days.

In order to calibrate the computational model to the basal rate of wound healing in our murine experimental model, we used these selected parameters to fit the PDE model to experimental data from all of the vehicle-injected groups in Studies 1, 2, and 3. The predicted wound areas were compared to experimental measurements of wound area following vehicle injections in all three studies. Parameters were fit by simultaneously varying λ_0, λ_1, and χ over a range of values constrained by 0.1-fold and 10-fold changes from baseline parameter values, and minimizing the sum of squared error (SSE) between the model predicted wound area and experimental measurements of wound area at all time points for vehicle-injected groups. The fitted values for these dimensionless parameters that minimized the SSE were $\lambda_0 = 856$, $\lambda_1 = 3860$, and $\chi = 0.146$, or fold changes from baseline values of 4.3, 4.8, and 1.5, respectively. After parameter fitting, the model generated a time course of healing that was similar to the time course of healing across all vehicle-injected experimental groups (Figure 4-3). The experimental data presented here from vehicle-injected groups demonstrates variability in the rate of wound healing

between studies. Evaluating the causes and implications of this variability was not the main objective of this study, but is discussed comprehensively in Almquist et al.[235] Notably, Study 2 demonstrated a slower rate of wound closure than Studies 1 and 3 and did not include late time points beyond day 13. Furthermore, considering that Study 2 comprised less than 20% of the data points used for fitting, it is reasonable that parameter fitting resulted in a model output that is in better agreement with Studies 1 and 3.
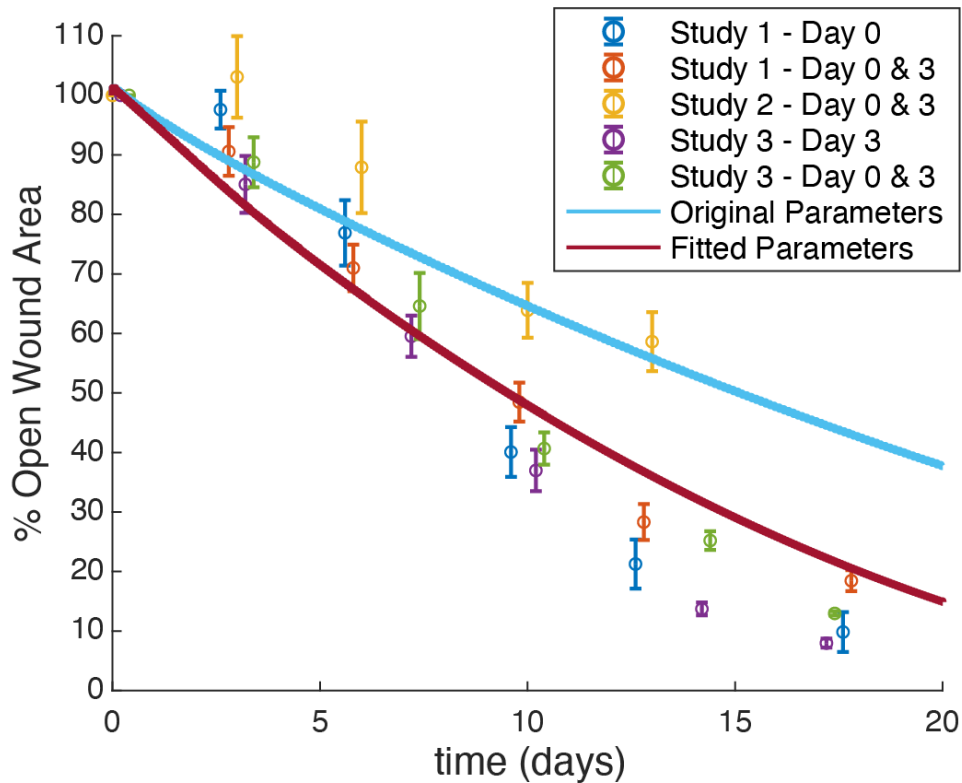
Figure 4-3. Model parameters were fitted using vehicle data from all experimental studies.
The mean of percent open wound area for all animals is plotted as open circles for Study 1 vehicle groups (injected on day 0 <u>or</u> days 0 and 3), Study 2 vehicle groups (injected on days 0 and 3), and Study 3 vehicle groups (injected on day 3 <u>or</u> days 0 and 3), error bars = SEM. Horizontal dodging of up to 0.6 days has been applied to the data so that overlapping data and error bars are more easily visible, but the precise time point of wound area measurement is reported in Table 4-1. Wound area predicted by the PDE model is shown for a simulation with original parameter values (solid light blue line) and after parameter fitting (solid dark red line).

PDE model describes spatiotemporal regulation of chemoattractant concentration and angiogenesis during cutaneous wound healing

The PDE model provides spatial and temporal information about the dynamics of wound healing with respect to three dependent variables: chemoattractant concentration, sprouting capillary-tip density, and blood vessel density (Figure 4-4A-C). The radial coordinate in these plots represents the radial coordinate of the wounds (spanning 0-5 mm), the azimuthal (θ) coordinate corresponds to time (0-36 days) that increases in a clockwise direction, and the color bar indicates the magnitude of the dependent variables. The chemoattractant profile (Figure 4-4D), which is assumed to be produced by macrophages located throughout the wound space, is initially high throughout the wound space and diminishes towards the center of the wound as the wound heals. Figure 4-4E demonstrates the wave-like ingrowth of capillary-tip sprouts, as was originally described by Pettet et al. Intact blood vessels at the edge of the wound extend sprouts that move towards the center of the wound. As the sprouting capillary-tips migrate, they leave in their path a new capillary that matures to become part of the established blood vessel network. The mature blood vessels are able to provide blood and oxygen supply to the healing wound while removing chemoattractant (Figure 4-4F). The effects of geometry on the solutions of capillary tip and blood vessel density can be observed at late time points (t = 35 days) in the center of the wound (r = 0 mm) by comparing our model, which uses a cylindrical coordinate system, to the original solutions reported by Pettet et al. The densities of capillary tips and blood vessels increase as they crowd into a smaller wound area and the rate of wound closure slows.
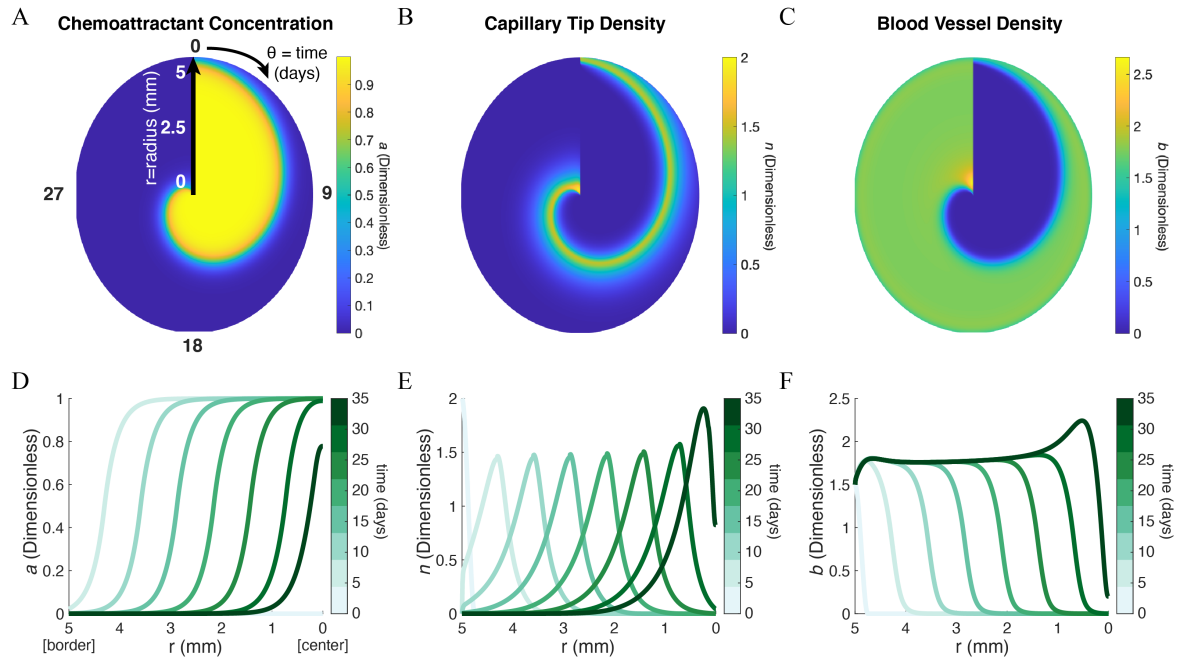
Figure 4-4. PDE model provides spatial and temporal resolution of wound healing.
Heat maps in polar coordinates of the solutions for the governing equations: **(A)** chemoattractant concentration (a), **(B)** sprouting capillary-tip density (n), and **(C)** blood vessel density (b). Radial coordinate corresponds to radius of the wound where r = 0 mm is at the center of the wound and r = 5 mm at the border of the wound, θ coordinate corresponds to time (0-36 days), and color bar indicates value of the corresponding solution. **(D-F)** 2-D snapshots of the heatmaps in A-C at t = 0, 5, 10, 15, 20, 25, 30, and 35 days.

Pharmacokinetic model of AZD8601 injections

The PK model published by Almquist et al.[235] was used to describe the degradation of mRNA, as well as synthesis and degradation of VEGF-A protein in the skin following administration of AZD8601. The kinetic parameters (k_1 and k_3) correspond to half-lives of 13 hours and 3 hours for degradation of mRNA and protein, respectively. VEGF-A protein levels peaked around 8 hours after injection of 100 μg AZD8601, and by day 6, ten of twelve measurements were below the lower limit of quantification. Due to the lack of available data about the spatial parameters of AZD8601 diffusion and clearance rates, we fit a VEGF generation rate (k_{gen}) based on the PK model-predicted time course of VEGF-A synthesis following a single

injection with 100 µg AZD8601. After parameter fitting, the PDE model predicted mRNA and chemoattractant time courses that were consistent with the PK model predictions and experimental measurements of VEGF-A (Figure 4-5). However, the PDE model predicted a nearly instantaneous increase in VEGF-A following the addition of mRNA unlike the PK model output which peaks around 8 hours (Figure 4-5B). This is likely because the PDE model does not account for the time required for cells to uptake the mRNA and begin protein production. It has been shown previously that VEGF-A can be detected in the eluates from interstitial microdialysis sampling approximately 4 hours following intradermal injection of AZD8601 in rabbits.[241]
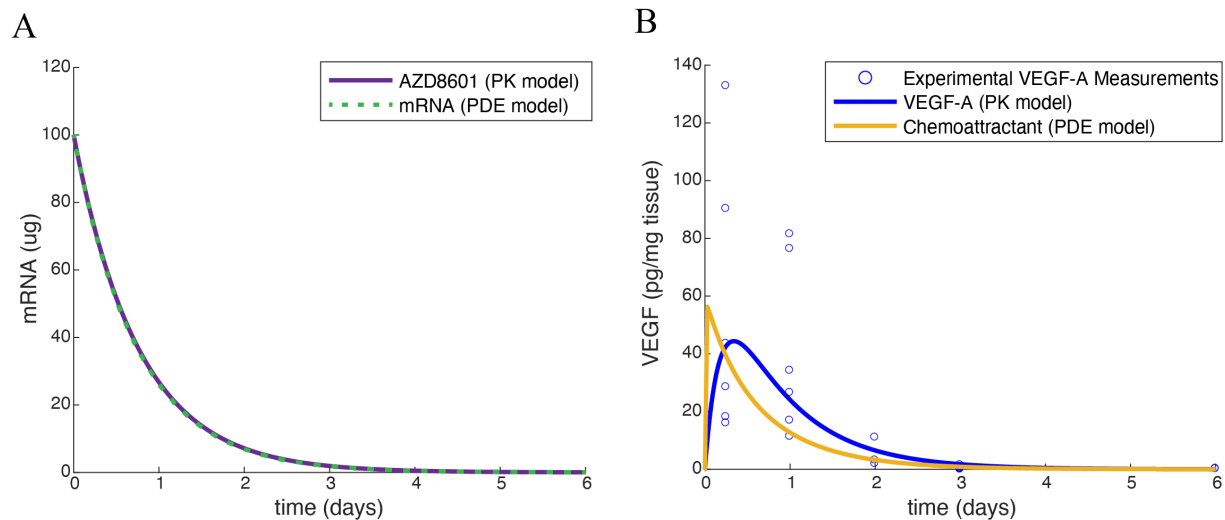
Figure 4-5. VEGF generation rate is fit using pharmacokinetic model of AZD8601 injections.
(A) PK model (solid purple line) and PDE model (dashed green line) predict mRNA amount (µg) following injection of 100 µg AZD8601. **(B)** Experimental measurements of VEGF-A concentration were taken at 6, 24, 48, 72, and 144 h after injection with 100 µg AZD8601 (blue circles). PK model (solid blue line) and PDE model (solid yellow line) predict temporal dynamics of VEGF-A concentration (pg/mg tissue) following injection of 100 µg AZD8601.

Modeling the spatiotemporal distribution of mRNA following injections with AZD8601 predicts varied effects on wound healing that are dependent on the timing of injections

An additional PDE was coupled to the system of equations originally described by Pettet et al. to simulate injections of AZD8601. The spatial parameters of AZD8601 including effective diffusion length scales and clearance rates are not well understood at this time. However, the PK model reported by Almquist et al.[235] describes the temporal dynamics of mRNA and VEGF-A following an injection. We used the PK model to fit a VEGF generation rate that produced a spatially averaged concentration of VEGF-A in the PDE model consistent with the temporal dynamics of mRNA and VEGF-A predicted by the PK model. This model approach allowed us to investigate the impact of parameters related to the spatial distribution of AZD8601 on the rate of wound healing, and simulate experimental conditions that were not tested *in vivo*.

The mRNA delivered by injections of AZD8601 at the wound border diffuses into the wound based on the reaction-diffusion parameters of the governing equation (Eq. 20) and is translated to VEGF-A at a rate dependent on the local concentration of mRNA (Eq. 23). This model predicted varied effects on the rate of wound healing that were dependent on the time of delivery of the injection (Figure 4-6). Simulation of a single injection of 100 μg AZD8601 on day 0 was predicted to accelerate time to 50% wound closure by 3.1 days. Both a single injection of 100 μg AZD8601 on day 3, or repeated injections on days 0 and 3, were predicted to have no significant impact on time to 50% wound closure and instead caused a temporary reversal of blood vessel growth towards the initial wound border. A single injection of 100 μg AZD8601 on day 6 was predicted to delay time to 50% wound closure by 2.9 days.
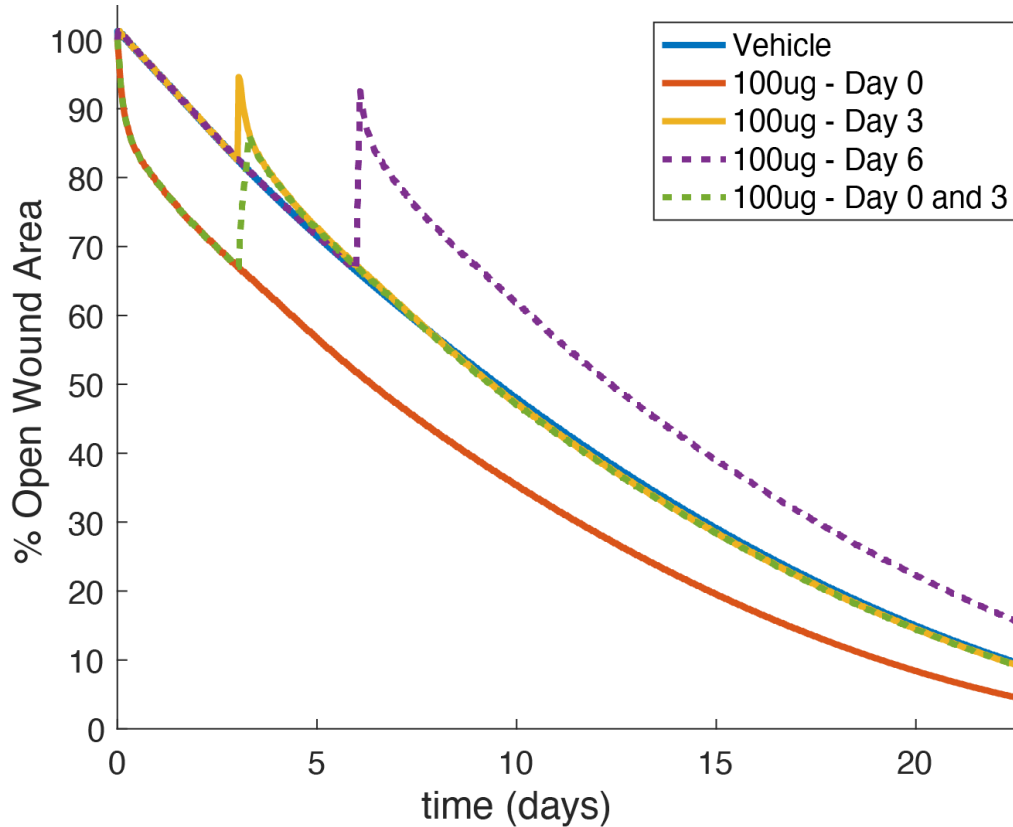
Figure 4-6. Wound closure is dependent on time of delivery of AZD8601 when injected at the wound border.
Percent open wound area over time is presented for PDE model simulations with a vehicle injection (solid blue line), or injections of 100 µg AZD8601 on day 0 (solid red line), day 3 (solid yellow line), day 6 (dashed purple line), and days 0 and 3 (dashed green line).

Heat maps of the solution to the governing equations of the PDE model depict the profiles

for a (Figure 4-7A), n (Figure 4-7B), and b (Figure 4-7C) for a simulation with repeated injections

of 100 µg AZD8601 on days 0 and 3. The chemoattractant profile (Figure 4-7A and 4-7D) shows

that the chemoattractant concentration peaks at a distance of approximately 0.4 mm inside the

wound border and returns to baseline values approaching the wound center. This results in a peak

in capillary tip density at a similar distance inside the wound border following injections with

AZD8601 (Figure 4-7B and 7-E). Injections of AZD8601 at the wound border on day 0 cause

an increase in the rate of capillary tip migration towards the center of the wound; however, a second

injection on day 3 causes an accumulation of capillary tips and blood vessels at the wound border, preventing the migration of capillary tips towards the center of the wound (Figure 4-7C and 4-7F). The injection on day 3 results in an increase in the density of blood vessels near the wound border that persists throughout the time course of wound healing.
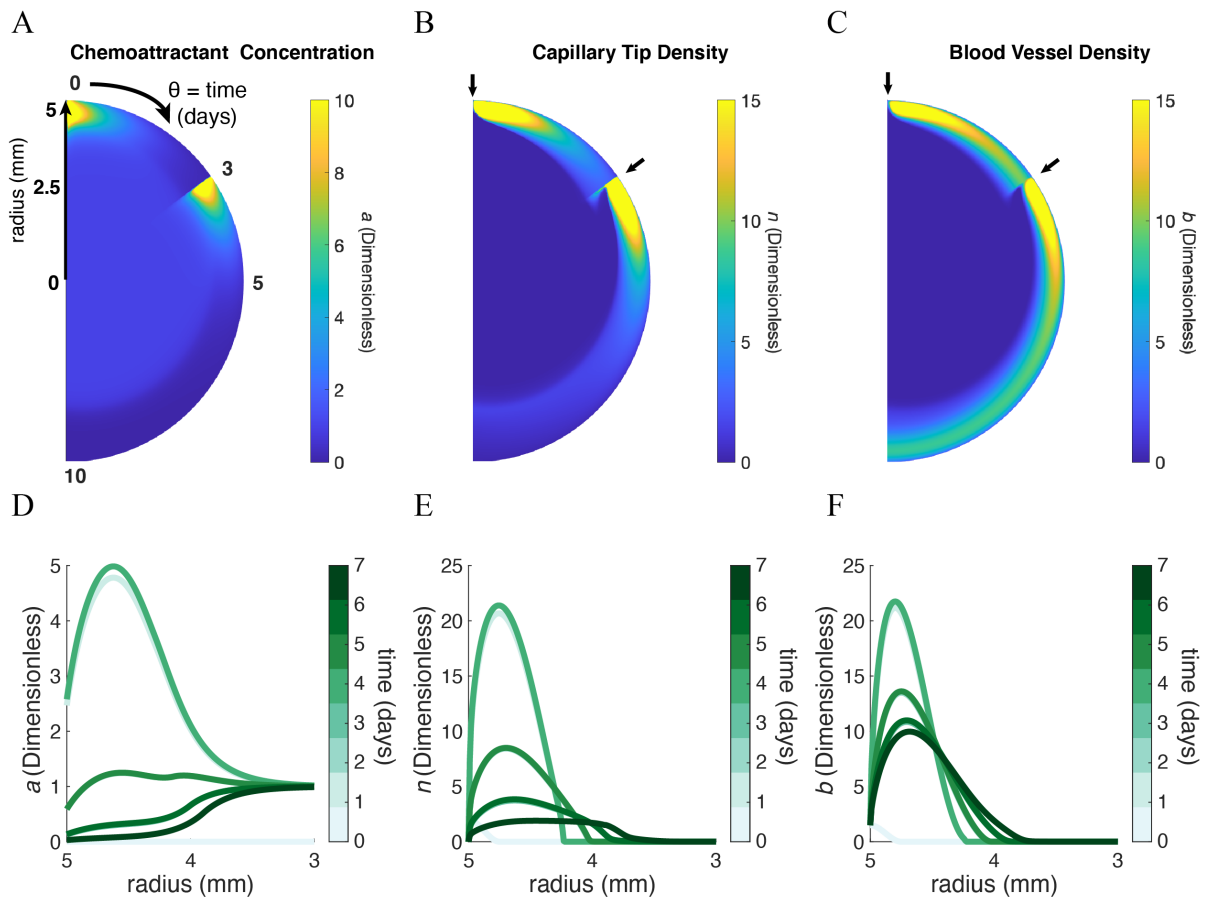
Figure 4-7. Repeated injections of AZD8601 on days 0 and 3 cause an increase in density of capillary tips and blood vessels at the wound border.
Heat maps in polar coordinates of the solutions for the governing equations: **(A)** chemoattractant concentration (*a*), **(B)** sprouting capillary-tip density (*n*), and **(C)** blood vessel density (*b*) for a simulation with repeated injections of 100 μg AZD8601 on days 0 and 3 (indicated by arrows). Radial coordinate corresponds to radius of the wound (0 - 5 mm), *θ* coordinate corresponds to time (0 - 10 days), and color bar indicates value of the corresponding solution. **(D-F)** 2-D snapshots of the heatmaps in C-E at t = 0, 1, 2, 3, 4, 5, 6 and 7 days at the wound border (r = 3 - 5 mm).

The diffusion and degradation kinetics of mRNA delivered at the wound border cause the VEGF-A concentration to peak a short distance inside the wound border and then return to baseline towards the center of the wound. The resulting gradient of VEGF-A can accelerate the rate of wound closure when delivered on day 0. However, this causes a regression of the blood vessel network towards the wound border and even delays wound closure when an injection is delivered on day 6 compared to a simulation with no injection. At these later time points the border of the blood vessel network has migrated a distance into the wound space that is closer to the center of the wound than the peak VEGF-A concentration created by an injection at the wound border. Thus, this model predicts an effect on wound healing that is dependent on the timing of the injection and spatial distribution of the chemoattractant gradient with respect to the border of the healed blood vessel network at the time of injection.

Location of AZD8601 injections impacts rate of wound healing

We used this model to predict the effects of varying the location of injections within the wound space, something that was not tested experimentally. Simulating injections of AZD8601 delivered on day 0 at various locations ranging from the border of the wound (r = 5 mm) to the center of the wound (r = 1 mm) substantially impacted the rate of wound closure (Figure 4-8A). When injections on day 0 were delivered at the wound border (r = 5 mm), time to 50% wound closure was predicted to be accelerated by 3 days compared to no injections. The rate of wound closure was predicted to be dramatically accelerated by delivering injections of AZD8601 a short distance inside the wound border on day 0. The maximum impact on time to 50% wound closure was observed at r = 4 mm, but this effect was diminished at locations closer to the center of the wound (r = 3 mm, 2 mm, and 1 mm). However, the simulation with an injection at r = 4 mm predicted a longer time to 100% wound closure than the simulations with an injection delivered

further into the wound space. An injection delivered at r = 4 mm is predicted to dramatically increase the rate of wound closure at early time points, but this effect is not sustained throughout the time course of wound healing, whereas injections delivered further in the wound space demonstrate a more consistent rate of wound closure. Model predictions were compared with experimental measurements of wound area for animals that received 100 μg injections of AZD8601 on day 0 at the wound border (r = 5 mm) (Figure 4-8A) and showed close agreement with experimental data at late time points (days 10, 13, and 18), but discrepancies at early time points (days 3 and 6) when compared to a simulated injection at the wound border (r = 5 mm).

Simulations were repeated for injections of 100 μg AZD8602 on day 3 at various distances from the wound center (Figure 4-8B). An injection at the wound border (r = 5 mm) on day 3 was predicted to cause a temporary regression in blood vessel density and wound area, but had no measurable impact on the time to 50% wound closure. However, injections delivered further from the wound border (r = 4 mm, 3 mm, and 2 mm) were all predicted to accelerate the time to 50% wound closure by approximately 6 days. This effect was slightly diminished by delivering injections near the center of the wound (r = 1 mm), where time to 50% wound closure was predicted to be accelerated by 4 days compared to a simulation with no injections. Model predictions were compared with experimental measurements of wound area for animals that received 100 μg injections of AZD8601 on day 3 at the wound border (Figure 4-8B) and demonstrated the most agreement with a simulated injection near the center of the wound (r = 1 mm).

We also simulated the impacts of varying the location of injections with repeated injections on days 0 and 3 (Figure 4-8C). When injections were delivered at the wound border (r = 5 mm) wound healing was accelerated at early time points, but the second injection on day 3 caused a

regression of the blood vessels and wound area that resulted in no significant difference in time to 50% wound closure compared to a simulation with a vehicle injection. Similar to simulations with injections on day 0 or 3, an injection delivered at r = 4 mm was predicted to significantly increase wound closure at early time points, but that rate of wound healing was not sustained through later time points. Thus, an injection at r = 4 mm was predicted to result in the fastest time to 50% wound closure, but injections further in the wound space (r = 3 mm, r = 2 mm, and r = 1mm) were predicted to have faster times to 100% wound closure. Model predictions were compared to experimental measurements of wound area for animals from experimental groups in three separate studies that received 100 μg injections of AZD8601 on days 0 and 3 at the wound border (Figure 4-8C). Experimental data reveal study to study variation in the rate of wound healing, but demonstrated the closest agreement with a simulated injection closer to the center of the wound (r = 1 mm) at late time points.
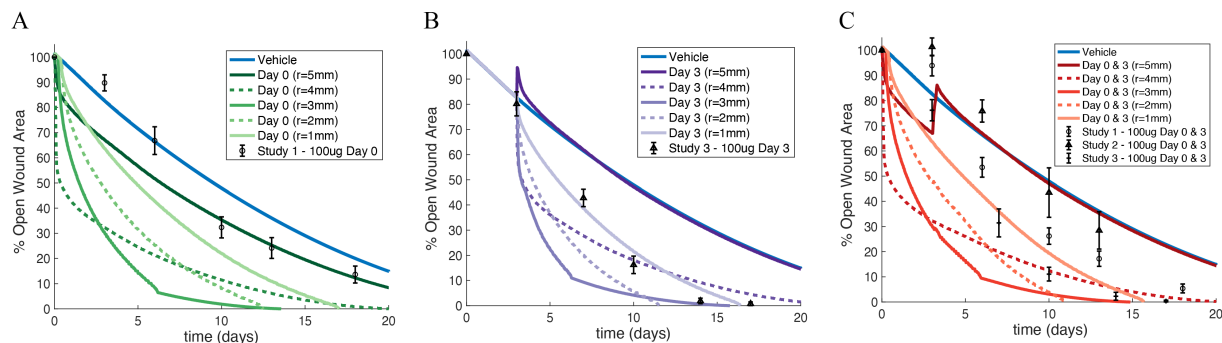
Figure 4-8. Delivery of AZD8601 at various depths in the wound space impacts rate of wound healing.

Percent open wound area is predicted for simulations with injections of 100 μg AZD8601 at locations ranging from the border of the wound (r = 5 mm) to near the center of the wound (r = 1 mm) for injections delivered on (**A**) day 0, (**B**) day 3, or (**C**) days 0 and 3. These simulations are compared to a simulation with a vehicle injection (solid blue line) and experimental measurements of wound area from a murine wound healing model where injections of 100 μg AZD8601 were delivered at the wound border (r = 5 mm) on (**A**) day 0, (**B**) day 3, and (**C**) days 0 and 3. Error bars = SEM.

Experimental data showed close agreement with simulated injections delivered at the wound border (r = 5 mm) on day 0, but experimental data that included injections delivered on day 3 showed closer agreement to simulated injections delivered at r = 1 mm for later time points. Model simulations of an injection at the wound border (r = 5 mm) on day 3 show no difference compared to a vehicle simulation, suggesting that the model may underestimate the ability of the mRNA to penetrate the wound space and promote an increase in capillary tips at the healing wound border. We explore the impacts of altering the diffusivity of mRNA on wound healing in the next section. Furthermore, many of these simulations predict a very dramatic or nearly instantaneous acceleration of wound closure which may not be physiologically probable and can likely be attributed to the limited spatially resolved data available to fit parameters related to mRNA diffusion and VEGF-A generation rate. Since wound area is not a direct output of the PDE model, this instantaneous healing could also be an indication that blood vessel density may not correspond directly to wound area as quantified visually in an experimental model. However, the predicted relative differences in the rate of wound closure for injections delivered at various locations in the wound space remains an important finding.

The diffusivity of mRNA affects its ability to promote wound healing

Due to the limited availability of data regarding the spatial distribution of AZD8601 in the wound bed, we performed simulations with perturbations to the diffusion coefficient of mRNA to understand the impact of this spatial parameter on wound healing. This provides some insight about the effective diffusion length scale of AZD8601, but also provides an opportunity to apply this model to other drugs or methods of drug delivery with varied diffusion profiles.

We first performed model simulations with an mRNA diffusion coefficient (D_m) of 0 cm²/s, which assumes that mRNA delivered at the wound border does not diffuse and is translated to

VEGF-A only at the border. VEGF-A that is generated at the border due to the injection can diffuse some distance into the wound space as determined by the parameters of the chemoattractant equation (Eq. 23). For all simulated injection times (day 0, day 3, day 6, or day 0 and 3) this model predicted a delay in wound healing compared to a simulation with vehicle injection (Figure 4-9A). A high concentration of VEGF-A is produced at the wound border, which causes an accumulation of capillary tips and blood vessels at the wound border (Supplemental Figure 3). This model implementation suggests that a drug intervention with restricted diffusion results in an accumulation of VEGF-A at the initial wound border, inhibiting normal capillary tip migration towards the center of the wound and thereby slowing the rate of wound healing.

Next, we performed model simulations with $D_m = 10^{-7}$ cm²/s, two orders of magnitude higher than the literature reported values of intracellular mRNA diffusion used for simulations in Figures 4-6 – 4-8. In this model implementation, an injection at day 0 is predicted to accelerate time to 50% wound closure by 5.5 days compared to a vehicle injection. When injections are delivered on both days 0 and 3, the second injection on day 3 causes some delay in wound closure, but accelerates time to 50% wound closure by 3.6 days compared to a vehicle injection. A single injection delivered on day 3, or day 6 causes an initial regression of wound area, but the day 3 injection is able to promote an acceleration in time to 50% wound closure of 2.6 days, while the injection at day 6 results in a time to 50% wound closure that is similar to that of a vehicle injection (Figure 4-9B). Injections of AZD8601 create a gradient of VEGF-A inside the wound border, increasing the density of capillary tips and blood vessels at this location. The second injection at day 3 causes a temporary regression of capillary tips and blood vessels towards the wound border (Supplemental Figure 4). This model implementation demonstrates a better qualitative fit to the trends seen in

the murine model of wound healing, where injections at day 0, day 3, or days 0 and 3 all promote

an acceleration in wound healing compared to vehicle control groups.

Lastly, simulations with $D_m = 10^{-5}$ cm^2/s assumes that mRNA delivered by injections of

AZD8601 at the wound border diffuses rapidly throughout the wound space. In this model

implementation all simulated injection times (day 0, day 3, day 6, or days 0 and 3) showed no

notable difference in rate of wound healing compared with a vehicle injection (Figure 4-9C). In

this scenario mRNA diffuses rapidly throughout the wound space, but is also lost more rapidly at

the wound border to the surrounding tissue. The short-lived mRNA in the wound space increases

VEGF-A concentration modestly throughout the wound space, but does not accelerate the

migration of capillary tips or blood vessels towards the center of the wound (Supplemental Figure

5). All of these model implementations, however, assume that diffusivity of mRNA in the tissue

surrounding the wound border is equivalent to the diffusivity in the wound bed. It is unlikely that

the mRNA diffuses as rapidly in the surrounding tissue due to increased cellularity and density of

extracellular matrix, which is discussed in more detail later.
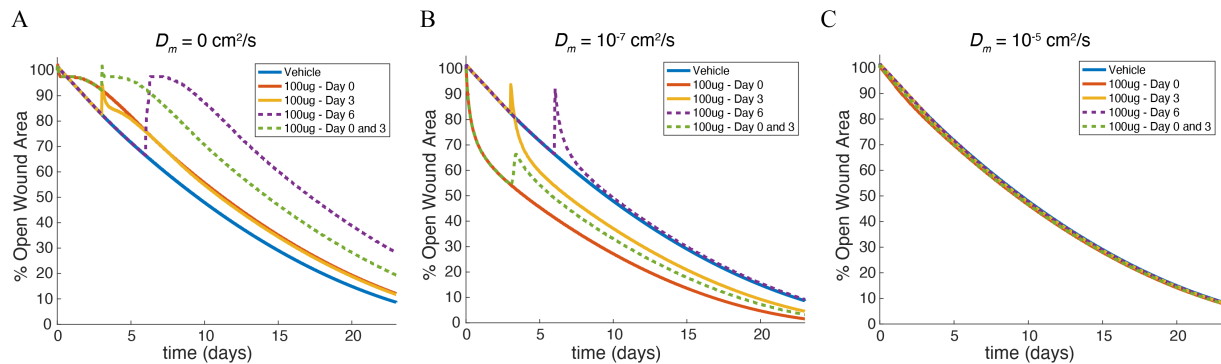
Figure 4-9. Diffusivity of mRNA impacts the rate of wound healing.
Model predictions are displayed for a simulated injection of 100 μg AZD8601 at the wound border (r = 5 mm) on day 0, day 3, day 6, or days 0 and 3 for a mRNA diffusion coefficient (Dm) of (A) 0 cm2/s, (B) 10-7 cm2/s, and (C) 10-5 cm2/s.

Discussion

We hypothesized that the location of proangiogenic drug delivery and the ensuing spatial gradients of growth factors would be a critical factor in the acceleration of diabetic wound healing. To investigate this hypothesis, we adapted a mechanistic mathematical model by Pettet et al.[114] and coupled it with pharmacokinetic and pharmacodynamic models of a modified mRNA (AZD8601) designed to enhance VEGF-A protein expression in the skin, to predict how spatial delivery of this drug affects diabetic wound healing. We converted this published model to a cylindrical coordinate system to more accurately reflect the geometry of the circular wounds in our experimental model. We then deployed a sensitivity analysis to identify parameters appropriate for model fitting in order to calibrate the basal rate of wound healing in our computational model to a murine model of diabetic wound healing. We coupled a PDE that describes the spatiotemporal distribution of mRNA in the wound to the equation for chemoattractant, such that mRNA delivered through injections of AZD8601 at specified times and locations produced VEGF-A concentrations consistent with previous experimental measurements. We then used the model to simulate injections of AZD8601 at various times and locations throughout the wound area. Our model made predictions about how the location of drug delivery, combined with timing of delivery, affected wound healing rates and suggests that wound healing acceleration can be best achieved by repeatedly administering drug injections at a location 1-2 mm inside the healed wound border.

There are numerous challenges associated with evaluating the bioactivity of developmental pharmaceuticals in pre-clinical studies. In addition to the experimental variability inherent to animal model systems, studies are frequently carried out in laboratories in different locations and at different times, and experimental designs often vary from one study to the next, given the initial

uncertainties in the dosage and dose scheduling. Experimental models are limited in the number of parameters that can feasibly be investigated (i.e., size of wound, dose of drug, route of drug delivery, timing of delivery, etc.), which often leads to arbitrary decisions about establishing parameters for experimental design. Computational models can be leveraged to conduct high-throughput variations in model parameters in order to identify those parameters that may be most consequential, and thus computational models can aid the design of pre-clinical and clinical studies. Previous computational models of wound healing have used differential equation-based methods to simulate the interactions between growth factors, cell populations, and ECM components. They have evaluated how different treatment protocols (timing and frequency of application) using commercially available engineered skin substitutes (Apligraf™ and Dermagraft™) impact healing[242], as well as other experimental treatments for diabetic ulcers, such as hyperbaric oxygen therapy[243]. In other fields of study, such as cancer therapeutics, mathematical and computational models have been used more extensively to design complicated drug dosing schedules for pre-clinical[244, 245] and clinical trials.[246]

We generally note that models of different spatial and temporal scales and complexity are useful as complementary views of the same system and can be used to investigate phenomenon across biological, spatial, and temporal scales. We have recently reported an empirical pharmacokinetic and pharmacodynamic model of AZD8601 in wound healing (Almquist et al. 2020). This previously published model captures wound healing dynamics at both the individual and the population level using a NLME modeling approach. Since the Almquist model is largely empirical, it may be difficult to interpret the biological consequences of model parameters. In comparison to the empirical NLME model, the advantage of the mechanistic model presented here is that it represents known biological processes, making model interpretation easy and

facilitating future model revisions and extensions. For example, the mechanistic model is likely suitable for expansion to more than one growth factor at the same time, i.e., combination therapies. One limitation of the presented mechanistic model is that averaging of experimental measurements of wound area from a system with nonlinear dynamics may be inappropriate, whereas this problem is inherently addressed in the NLME approach of the empirical model which represents the wound healing dynamics on both the individual and the population levels. Another limitation of the model presented here is that we assume radial symmetry in the distribution of mRNA due to the computational complexity of a 2-D finite volume approach, despite the fact that injections in the animal model were delivered at four discrete locations separated by 90 degrees around the wound edge (see Figure 4-1A).

Existing data for the experimental wound healing model is sparse, both with respect to the number of dependent variables that are currently accessible for measurement and the number of data-points in individual time and spatial series. Due to the lack of available spatially resolved data related to AZD8601 diffusion and clearance, we assumed a diffusion coefficient reported in literature for other mRNAs and a clearance rate by the vasculature comparable to that of protein. However, the diffusion coefficients reported in literature are representative of intracellular diffusion of mRNA and it is unclear what the effective length scale for extracellular diffusion would be especially in the setting of a cutaneous wound where there is likely less hindrance of diffusion due to increased matrix pore size and lack of, or remodeling extracellular matrix components.[247, 248] The wound healing cascade creates an extracellular environment that is constantly changing due to edema, neovascularization, altered cell density, and collagen content that would likely impact solute absorption through a wound site based on the timing of drug delivery and the phase of wound healing.[249]

This model provides unique and valuable insights about the spatial parameters of drug delivery that can be applied not only to future pre-clinical and clinical studies with AZD8601, but can also be generalized to the design of other wound healing studies with proangiogenic drugs. For example, previous studies with murine models of diabetic wound healing have also tested the efficacy of a recombinant VEGF-A applied topically to the wound.[223] The model presented here could be adapted to simulate VEGF-A production that occurs uniformly throughout the wound space, or is applied in a bolus at specified time points, to further explore this mode of drug delivery. Our model predicts that wound healing could be accelerated by delivering injections of AZD8601 at a location inside the border of the healed wound, which would imply delivering injections in the underlying skeletal muscle of the wound bed. AZD8601 is intended to be delivered intradermally, so it remains to be determined whether injections with AZD8601 would be able to produce similar levels of VEGF-A if delivered intramuscularly, but this conclusion can be generalized to any drug application that is able to promote VEGF-A concentration in the wound area. Furthermore, the model could be extended to include a region of healthy tissue beyond the wound border and to simulate drugs with other time courses of action – drugs encapsulated in nanoparticles with mechanisms for controlled release, for example.[250, 251]

Our model makes a number of assumptions about diabetic wound healing as it occurs in the murine model. Wound healing involves a complex cascade of molecular signals and cell behaviors that are not explicitly accounted for in our model, including hemostasis, inflammation, and extracellular matrix remodeling. In the diabetic wound, many aspects of the wound healing process are altered, and our model does not include the direct effects of disease on capillary sprouting, such as alterations in microRNAs that regulate these phases of inflammation and wound healing[252]. Previous computational models of chronic wound healing and ulcers have also described the

mechanical cues that regulate cell-cell adhesion and migration[233, 253], and key inflammatory mediators that contribute to ulcer formation.[254, 255] Furthermore, in order to make direct comparisons between the predictions of the PDE model and experimental measurements of wound area (which measured wound closure by the extent of re-epithelization), it was necessary to assume that the PDE model prediction of blood vessel density was appropriate for estimating the extent of re-epithelization. We argue this is a reasonable assumption given the fact that re-epithelization requires deposition of granulation tissue, which is predominantly comprised of neovessels. We note, however, the discrepancies between the model predicted wound areas and experimental measurements of wound area at early time points (Figures 4-3 and 4-8). In our murine model of wound healing, many wounds increase in size up to day 3 due to the effect of initial wound recoil[256], which is not currently captured in the mechanisms of this wound healing model. Furthermore, our model does not explicitly account for the time delay required for cells to uptake the mRNA and begin producing VEGF-A, which has been documented experimentally.[235, 241]

Although this model should be regarded as highly simplistic given the complex nature of diabetic wound healing, we believe that it provides a useful representation of the pre-clinical model and the effect of spatial delivery of AZD8601 on wound healing. Given the reported disconnects between small animal models of diabetic wounds and the clinical scenario in patients[257], it would be beneficial to identify methods and approaches that accurately scale findings in murine wound experiments to patient wounds, enabling data from pre-clinical studies to inform clinical trials more effectively. It is enticing to ponder whether and to what extent mathematical and computational models like ours and others[255] could assist in this endeavor; however, a number of challenges would first need to be overcome. First, diabetic wounds in patients, the most common of which are diabetic foot ulcers, are typically 1.5 – 5 times larger in diameter and 2-5 times deeper

than the standard small animal wound models (e.g., murine, rat, and rabbit), which range from 5 mm to 10 mm in diameter and 1 to 2 mm in depth, depending on the age and species of the animal. The assumptions that our model makes regarding the geometry may not hold in deeper wounds that have larger radii. Furthermore, the time scale of delayed healing in patient wounds can be orders of magnitude larger than what is typically observed in pre-clinical models, which is on the order of days-to-weeks, depending on the initial wound size, location, and species.[258] The validity of extrapolating our model predictions from the relatively rapidly healing murine wounds to the more slowly healing human wounds remains to be confirmed.

These caveats notwithstanding, our model makes the interesting and not necessarily intuitive predictions that: 1) modifying the location of delivery of AZD8601 at varying distances from the center of the wound can accelerate the rate of wound closure, 2) limited diffusion of mRNA resulting in a gradient of VEGF-A that is highest at the wound border can inhibit capillary tip migration towards the center of the wound and even cause regression of blood vessels and delay wound healing, and 3) significant increases in the diffusivity of mRNA results in more loss of the mRNA at the wound border which reduces its ability to accelerate wound healing. In patients, it is not uncommon for diabetic foot ulcers to persist indefinitely until the decision to amputate, so complete wound closure is often unachievable. Therefore, although the FDA currently views complete closure as the only acceptable endpoint for clinical trials, predicting time to partial closure (e.g., 25% or 50% wound closure) may be more clinically helpful, given that a small amount of healing can substantially reduce the risk of infection and mitigate bioburden (e.g., bacteria) in the wound. Upon further validation, these model predictions may be generalizable to patients and could impact clinical trial design and ultimately the use of this drug in the clinical care of wounds.

Author Contributions

MR and PM developed the code for the model and parameter fitting methods; PM converted the governing equations to cylindrical coordinates; SP, KH, AB, and MW designed the animal studies; AB and MW performed all animal experiments and quantification; JA developed the PK model; MR wrote the initial draft of the manuscript; SP, PM, JA, PG, ML, and KH contributed to revision of the manuscript. All authors read and approved the final version of the manuscript.

Conflict of Interest

The authors declare that the research was conducted in the absence of any commercial or financial relationships that could be construed as a potential conflict of interest. Maria Wågberg, Joachim Almquist, Peter Gennemark, Regina Fritsche-Danielson and Kenny Hansson are employees at AstraZeneca and may own stock or stock options.

Funding

Human and Animal Studies

No human studies were carried out by the authors for this article. All procedures were conducted in accordance with the guidelines of the University of Virginia Animal Care and Use Committee (Approved Protocol #3459) or the Local Ethics Committee on Animal Experiments in Gothenburg, Sweden.

CHAPTER 5

Identifying individual social risk factors from unstructured data in electronic health records and their association with patient-level outcomes

[1]Department of Quality and Performance Improvement, University of Virginia Health System
[2]Department of Biomedical Engineering, University of Virginia
[3]School of Medicine, University of Virginia
[4]Department of Engineering Systems and Environment, University of Virginia
[5]Frank Batten School of Leadership and Public Policy, University of Virginia

Abstract

Objective

Social determinants of health (SDoH) encompass a wide range of modifiable health factors that are significant predictors of health outcomes and are a focus of interventions to reduce health care costs and improve patient outcomes. Attempts to identify high-risk patients using electronic health records (EHRs) have relied on merging neighborhood-level SDoH data from external sources, or unreliable administrative and claims data. Newer approaches suggest that unstructured clinical notes in EHRs provide a richer and more complete understanding of individual-level social risk factors. The objective of this study was to evaluate the prevalence of individual-level social risk factors documented in unstructured data from electronic health records and the association of those risk factors with patient-level outcomes.

Methods

We queried electronic health record (EHR) data for 21,402 inpatient encounters over a one-year time span at the University of Virginia (UVA) Medical Center. We identified a set of 41 measures related to individual social risk factors in EHRs being documented by health care providers through existing documentation workflows and clinical notes. Multivariate logistic regression was performed to determine the association of individual social risk factors with increased risk for unplanned inpatient readmissions, post-discharge emergency department (ED) visits, and extended hospital length of stay (LOS).

Results

Independent predictors associated with higher risk for 30-day unplanned readmissions included severity of illness (OR = 3.96), location of residence in proximity to UVA Medical Center (OR =

1.31), and risk factors for social and community context (OR = 1.26) and economic stability (OR = 1.37). All SDoH domains, including economic stability (OR = 1.39), education (OR = 1.38), social and community context (OR = 1.39), and neighborhood and built environment (OR = 1.61) were associated with increased risk for 30-day post-discharge ED visits, in addition to age (OR = 0.60) and location of residence (OR = 2.56). All variables, with the exception of social and community context were significant independent predictors of extended LOS, with discharge to facilities (OR = 2.42) and severity of illness (OR = 2.14) having the most influence on this outcome. When social risk factors were aggregated into one score reflecting total SDoH burden, this was the single most influential predictor of 30-day post-discharge ED visits (OR = 3.64).

Conclusions

Individual-level social risk factors are widely documented as unstructured data in EHRs and are associated with higher risk for readmissions, post-discharge ED visits, and extended LOS. In particular, economic stability was associated with increased risk for all outcomes studied. While individual-level social risk factors are currently documented as unstructured data in EHRs on an ad-hoc basis, standardized screening tools for SDoH with validated measures could help eliminate bias in the data collection and ensure that all patients are screened regularly for changes to these risk factors.

Introduction

The U.S. spends far more on health care per capita than any other country – 17.7% of the nation's gross domestic product (GDP) in 2019.[259, 260] Despite high health care expenditures, the U.S. has some of the worst health outcomes among developed countries and is ranked last in access, equity, and health outcomes in a study of 11 countries.[261] Clinical care, including access and quality of care, is estimated to account for only 20% of modifiable determinants of health outcomes; up to 80% of population health outcomes are attributed to social determinants of health (SDoH).[65] These SDoH are the "conditions in which people are born, grow, live, work and age" as defined by the World Health Organization.[66] SDoH broadly encompasses health behaviors (e.g., tobacco and alcohol use, diet, physical activity, etc.), socioeconomic factors (e.g., educational attainment, financial strain, social support systems, stress, interpersonal safety, etc.), and the physical environment (e.g., air and water quality, housing conditions, access to transportation, etc.).[65] The links between individual SDoH and population-level health outcomes (i.e. life expectancy and quality of life) have been widely documented.[262-267] There is an often-repeated paradigm in public health that one's zip code is a better predictor of health than one's genetic code because of the profound impact an individual's neighborhood has on their environment and opportunities – from access, or lack thereof, to healthy foods, public transportation, good schools, affordable housing, air quality, and more.[268] It is the hope of many in healthcare and public health that by addressing these SDoH we can simultaneously promote better health outcomes, reduce inequities, and lower health care costs.[269]

The term "social determinants of health" has become widely used in many different contexts and with a variety of implications. Alderwick and Gottlieb recently outlined a SDoH

lexicon for healthcare systems that provides much more clarity around the terms used in this space and the tools to describe our work more precisely.[270] Social determinants are the conditions that shape health, but are neither positive or negative predictors of heath by default. Education is a social determinant of health, for example, where high educational attainment is associated with better health and low educational attainment is associated with poorer health. Social risk factors, however, are the specific adverse conditions associated with poor health outcomes, such as homelessness or food insecurity. A systematic review by Chen et al. on the integration of SDoH domains in electronic health records (EHRs) found that only 16% of studies identified social risk factors as opposed to social or behavioral determinants of health.[47] Furthermore, 57% of these studies report only neighborhood-level SDoH (e.g., median household income or neighborhood crime rates) and not individual-level SDoH (e.g., employment status or housing stability). In the studies that utilized SDoH data to improve prediction of high-risk or high-utilization patients, they found that models that incorporated only neighborhood-level SDoH demonstrated no improvement in predictive performance. Alternatively, models that incorporated individual-level SDoH reported significant improvements in model performance for predicting outcomes ranging from medication adherence[271] to risk for hospitalization.[47, 272]

The evolution of the U.S. healthcare system from fee-for-service based care to newer value-based payment models with the introduction of programs like the Hospital Readmissions Reduction Program (HRRP)[43], which reduces payments for hospitals that have excess 30-day readmission rates, has placed more focus on modifiable SDoH to improve health outcomes and thereby reduce health care costs. More health systems are exploring ways to integrate SDoH data collection into EHRs in order to implement SDoH-related referrals for non-clinical care into their

routine practices and improve quality performance.[47] There have been several proposed frameworks for integrating collection of SDoH data in electronic health records (EHRs) and calls for standardized SDoH screening tools. Multiple screening tools have been developed including the Accountable Health Communities Screening Tool[273], PREPARE assessment tool, Health Leads Social Needs Assessment[274], and others. Organizations such as the Institute of Medicine have developed recommendations for the relevant domains of social and behavioral health that should be captured in EHRs.[275] However, these types of standardized screening tools for structured data collection of social risk factors are not widely used in clinical practice because they require the implementation of new data systems and widespread adoption from health care providers. Some researchers have used insurance claims data to identify some social risk factors, but have found that these are often unreliably coded and that alternatively, text from physician notes can be used to identify individual social risk factors with a much higher prevalence than administrative data.[276]

While most studies to date have focused on unplanned readmissions, this is not the only outcome of interest to health care systems. Inappropriate ED visits contribute to high healthcare costs, ED overcrowding, and EDs are not equipped to provide the primary and preventative care that these patients need.[277, 278] Some studies have estimated that up to 40% of all ED visits are clinically inappropriate.[279] Furthermore, extended hospital length of stay contributes to high health care costs and increases the likelihood of hospital-acquired infections.[280] In this study, our objective was to determine the prevalence with which individual social risk factors are currently documented as unstructured data in EHRs, and to evaluate the association of those social risk factors with increased risk for patient-level outcomes including readmissions, ED revisits, and hospital LOS.

Methods

Patient sample

Data from EHRs was queried for all inpatient admissions to the UVA Medical Center that were discharged during a one-year timespan between July 1, 2018 and June 30, 2019. This query identified 30,924 inpatient admissions, representing 22,314 unique patients. We limited the study to adults (age ≥ 18 years old), and excluded labor and delivery patients, and admissions where the patient expired in hospital, was discharged to hospice, or was discharged against medical advice. The final study population included 21,402 inpatient admissions, representing 15,116 unique patients who had at least one inpatient admission during the study period.

Outcome measures and data sources

The primary data source for this study was EHR data at the UVA Medical Center through EpicCare. Additionally, 3M's All Patients Refined Diagnosis Related Groups (APR-DRG) model was used to obtain expected length of stay and severity of illness, which is categorized as minor, moderate, major, and extreme.[281] We investigated three outcomes in this study – 1) unplanned hospital readmissions, 2) ED revisit following discharge, and 3) extended hospital LOS. The primary endpoint for readmissions and ED revisits was 30 days following discharge from an index admission, with a secondary endpoint of 90 days. Unplanned readmissions were defined as a return to the hospital within 30 days of discharge from the index admission and excludes admissions for planned care or follow-up treatment, such as scheduled chemotherapy or planned surgeries. ED revisits following discharge from the index admission only include patients who visited the ED, but were not subsequently admitted to the hospital. If admitted through the ED, the outcome was considered an unplanned readmission. LOS was translated into a binary

outcome by determining whether the actual length of admission was greater than the expected

length of admission based on the APR-DRG model.

Social determinants of health

Despite efforts to develop standardized screening tools, a recent systematic review by Chen

et al. including over 70 studies that integrate SDoH data collection in EHRs notes that there is

currently no broad consensus on the specific questions, measures, or domains that should be

captured.[47] Chen et al. introduced a conceptual framework of SDoH domains and dimensions

based on the recommendations from the World Health Organization and Healthy People 2020,

and we utilize this conceptual framework for this study.[47] This framework broadly categorizes

SDoH into five domains – economic stability, education, health care access and quality,

neighborhood and built environment, and social and community context.

We queried EHR databases for intake forms, discharge instructions, questionnaires,

screening tools, social work and case management notes, and other existing note templates for any

recorded responses and measures that contained information relevant to these SDoH domains and

dimensions. This query identified a set of 41 different fields currently being captured in EHRs

(Supplemental Table 2) that were recorded by various disciplines of health care providers during

an encounter. These data sources identified within the EHR covered 11 different dimensions, and

four of the five domains of SDoH (Table 5-1). Next, we developed response criteria for each of

these EHR fields to determine whether the recorded response indicated the presence of a social

risk factor for that patient. Some fields had a pre-determined set of structured responses to choose

from, while most were documented by providers with free text comments, and keywords were used

to identify response criteria for those fields. For each index admission included in the study, we

queried all encounters for that patient with the UVA Medical Center (inpatient, outpatient, telehealth, etc.) for the 12 months preceding the index admission to determine the patient's exposure to social risk factors.

Table 5-1. Framework for identifying SDoH domains and dimensions

Domains	Dimensions	Identified in EHR data
Economic Stability	Employment	•
	Financial resource strain	•
	Housing instability	
	Food insecurity	
Education	High school graduation	•
	Early childhood development and education	•
	Language and literacy	•
Health Care Access and Quality	Access to health services	
	Access to primary care	
	Health literacy	
Neighborhood and Built Environment	Access to healthy foods	
	Neighborhood crime	
	Environmental conditions	
	Quality of housing	•
	Transportation	•
Social and Community Context	Family and community support	•
	Interpersonal violence or abuse	•
	Stress and depression	•
	Marital status	•
	Civic participation	
	Discrimination	
	Incarceration	

Statistical analysis

In addition to the individual social risk factors identified in EHRs, other variables included from EHRs in this analysis were age, sex, race, ethnicity, location of residence, discharge destination, and severity of illness. We first described the demographics (i.e., age, sex, race, ethnicity, primary language, number of admissions) for all patients in the study and for the subgroups of patients with identified risk factors in each of the SDoH domains. Next, we evaluated the impact of the presence of these social risk factors with increased risk for the following three patient-level outcomes: 1) unplanned readmissions, 2) post-discharge ED visits, and 3) extended LOS. We developed a set of three generalized linear mixed-effects logistic regression models corresponding to these outcomes and included the same six predictor variables in all models: age, sex, severity of illness, location of residence, discharge destination, and social risk factors. Quantitative variables (i.e., age, severity of illness, and number of social risk factors) were rescaled on a range from 0 to 1, and categorical variables (i.e., sex, location of residence, and discharge destination) were grouped into two levels. Location of residence was grouped by those who lived in the vicinity the of hospital (Albemarle County and Charlottesville City) and all others. Discharge destination was grouped by those who were discharged to home (or home health) and those discharged to facilities (i.e., skilled nursing facilities, long term care, rehab). These six predictor variables were considered the fixed-effects, and since a patient may have multiple encounters within the study period these mixed models included random intercepts for each unique patient. All analysis was performed using R Studio and the statistical package lme4 (version 1.1.26) was used for model implementation.

Results

Patient and encounter characteristics

A total of 30,924 inpatient encounters occurred during the study period, and 21,402 of those encounters met the inclusion criteria, representing 15,116 unique patients treated at the UVA Medical Center over the 1-year study period (Figure 5-1). The median age of all patients was 62 with slightly more male (51.3%) than female (48.7%) patients. The majority of patients were white (80.1%), non-Hispanic (96.6%), and English-speaking (97.4%). The mean number of inpatient admissions per patient was 1.42 admissions during the study period, with 25.0% of patients having two or more admissions. Characteristics for all patients and subgroups of patients with identified risk factors for each SDoH domain are summarized in Table 5-2. The median age was lower for patients with identified risk factors for economic stability (58) and neighborhood and built environment (50), while the median age was similar for patients with risk factors for education (61) and social and community context (62). While females had a higher prevalence of risk factors for social and community context (53.3%), males had a much higher prevalence of risk factors for neighborhood and built environment (63.2%). Black patients had a higher prevalence of risk factors across all SDoH domains, but most notably economic stability (22.5%) and education (20.8%). Patients with identified risk factors for economic stability had the highest mean number of inpatient admissions during the study period (1.55).

For all inpatient encounters included in the study (21,402), 12.8% had a readmission within 30 days, 6.3% had a 30-day post-discharge ED visit, and 42.9% had a greater LOS than expected based on admission diagnosis and severity of illness. The median length of stay for all encounters was 4.1 days with a mean severity of illness of 2.24. The majority of patients resided outside of

Albemarle County (75.9%) and were discharged to home (80.1%), while 19.9% were discharged to skilled nursing facilities, long-term care, or rehab facilities. A summary of characteristics for all inpatient encounters based on outcome is described in Table 5-3. Encounters with a 30-day unplanned readmission and extended LOS had a higher mean severity of illness at admission, 2.59 and 2.36, respectively. Encounters with a 30-day unplanned readmission or ED visit were more likely to reside in Albemarle County, 29.8% and 43.6%, respectively. Discharge to care facilities from the hospital was more prevalent for encounters with a 30-day unplanned readmission (25.4%), and extended LOS (26.6%). Encounters with 30-day unplanned readmissions and ED visits had a higher prevalence of risk factors for economic stability, 44.2% and 44.5%, respectively. Risk factors for education were more prevalent among encounters with a 30-day unplanned readmission (8.4%) and 30-day ED visit (8.7%). Risk factors for neighborhood and built environment were most prevalent among encounters with a 30-day ED visit (6.4%). Encounters with a 30-day unplanned readmission and 30-day ED visits had a higher prevalence of risk factors for social and community context, 44.2% and 44.4%, respectively.
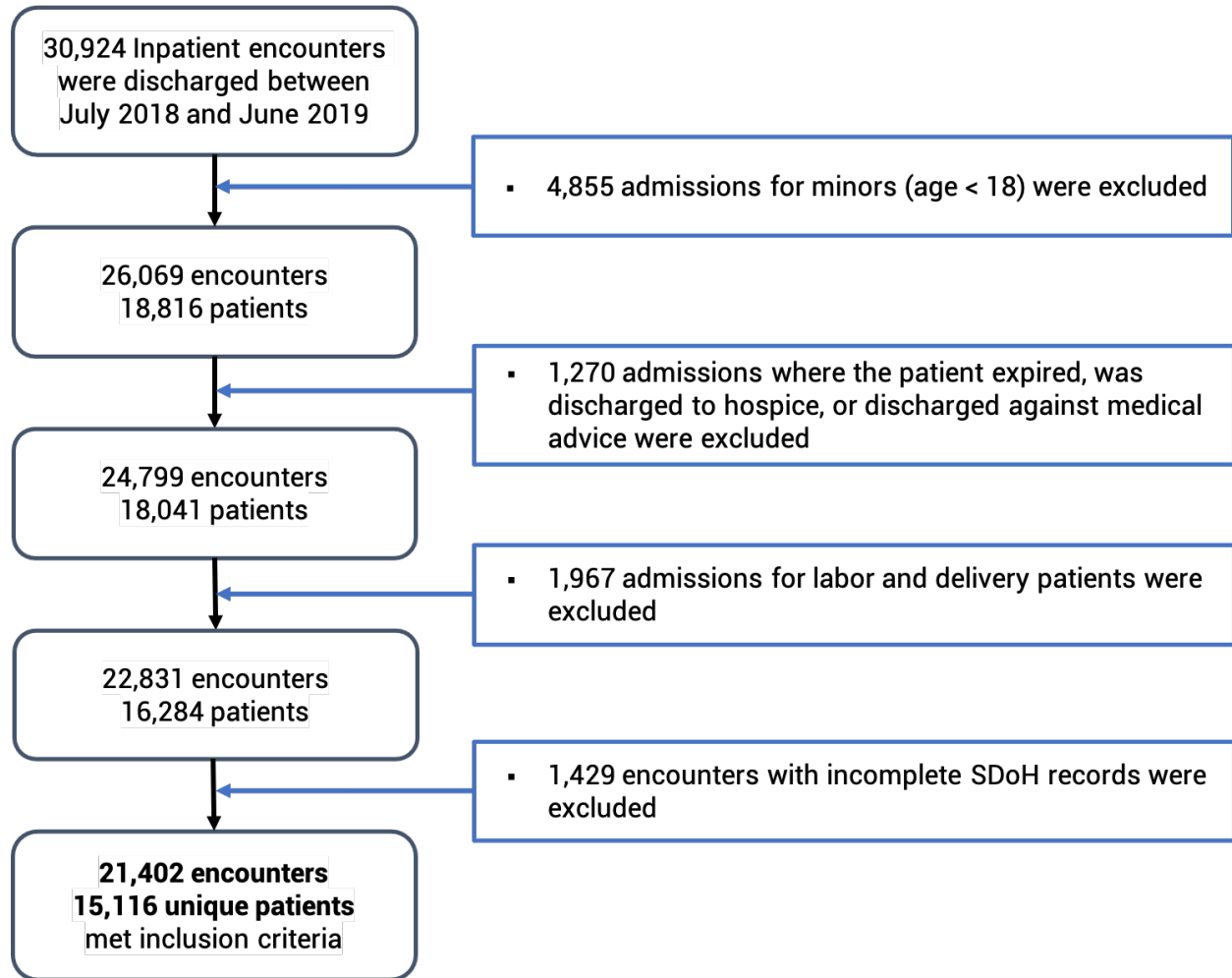
Figure 5-1. Study inclusion criteria

Table 5-2. Patient characteristics for all patients and patient subgroups with identified risk factors in each of the SDoH domains

Patient Characteristics	All patients (n = 15,116)	Economic Stability (n = 4,613)	Education (n = 850)	Neighborhood and Built Environment (n = 454)	Social and Community Context (n = 4,591)
Age (median)	62	58	61	50	62
Age (%)					
18 - 34	11.0%	13.5%	12.7%	22.2%	13.4%
35 - 54	22.4%	28.4%	23.8%	38.1%	22.2%
55 - 64	22.7%	22.4%	22.9%	24.4%	19.7%
65 - 74	24.3%	17.5%	19.9%	9.3%	20.7%
75 - 84	14.6%	12.5%	13.9%	4.6%	15.2%
>= 85	5.0%	5.7%	6.8%	1.3%	8.8%
Sex (%)					
Male	51.3%	50.2%	53.8%	63.2%	46.7%
Female	48.7%	49.8%	46.2%	36.8%	53.3%
Race (%)					
White	80.1%	73.1%	63.4%	76.2%	78.0%
Black	15.8%	22.5%	20.8%	18.5%	17.9%
Asian	0.7%	0.5%	1.8%	0.2%	0.7%
Other	3.2%	3.8%	13.5%	5.1%	3.2%
Unknown/declined	0.3%	0.1%	0.5%	0.0%	0.3%
Ethnicity (%)					
Non-Hispanic	96.6%	95.6%	82.5%	94.9%	96.8%
Hispanic	2.8%	3.9%	16.8%	4.8%	2.5%
Unknown/declined	0.5%	0.4%	0.7%	0.2%	0.7%
Primary Language (%)					
English	97.4%	96.0%	78.6%	96.0%	98.0%
Non-English	2.6%	4.0%	21.4%	4.0%	2.0%
Inpatient admissions during study period (mean)	1.42	1.55	1.50	1.50	1.53
Inpatient admissions during study period (%)					
1	75.0%	69.9%	72.5%	71.6%	70.6%
2	16.0%	17.6%	15.2%	16.7%	17.4%
3	5.1%	6.6%	7.4%	7.3%	6.4%
4	1.9%	2.7%	2.7%	1.8%	2.7%
5+	1.9%	3.2%	2.2%	2.6%	2.9%

Table 5-3. Admission characteristics by outcome

Admission Characteristics	All Admissions (n = 21,402)	With 30-day readmission (n = 2,739)	With 30-day emergency department visit (n = 1,350)	With extended LOS (n = 9,178)
Length of stay (median)	4.1	5.1	4.2	6.7
Severity of Illness (mean)	2.24	2.59	2.27	2.36
Severity of Illness (%)				
1 - Minor	22.6%	10.2%	20.4%	18.7%
2 - Moderate	38.8%	33.5%	39.5%	37.2%
3 - Major	30.4%	43.0%	32.7%	33.7%
4 - Extreme	8.2%	13.3%	7.4%	10.4%
Location of Residence				
Albemarle County (including City of Charlottesville)	24.1%	29.8%	43.6%	23.1%
Other	75.9%	70.2%	56.4%	76.9%
Discharge Destination				
Home (including home health)	80.1%	74.6%	79.3%	73.4%
Facilities (skilled nursing facility, long-term care, rehab)	19.9%	25.4%	20.7%	26.6%
SDoH Need (%)				
Economic Stability	33.4%	44.2%	44.5%	36.1%
Education	6.0%	8.4%	8.7%	5.8%
Neighborhood and Built Environment	3.2%	4.4%	6.4%	3.6%
Social and Community Context	32.9%	44.2%	44.4%	36.0%

Prevalence of individual social risk factors in EHRs

All 41 identified fields in the EHR related to SDoH domains were not documented for each encounter, or for every patient during the study period. Since these variables were not systematically collected, it is possible that the absence of data was not random and subject to the bias of the health care providers documenting findings in the EHR. In order to reduce the impact of bias and missing data, we identified all encounters that a patient had with the health system over the 12 months preceding the index admission to determine if they had any exposure to social

risk factors during this time frame. We found that at least one measure within each of SDoH domains was documented within the 12-month time frame preceding an encounter for more than 94% of all inpatient admissions. Of the 21,402 encounters with complete SDoH records, 33.2% of encounters had a risk factor identified in one SDoH domain, 16.3% had risk factors in two SDoH domains, 2.9% had risk factors in three domains, and less than 0.5% had a risk factor identified in all four SDoH domains.

Individual social risk factors are associated with increased risk for adverse patient-level outcomes

In these models, we included individual SDoH domains (i.e., economic stability, education, built neighborhood and environment, and social and community context) as independent predictors to determine whether certain SDoH domains were associated with higher risk for adverse outcomes than others (Table 5-4). We found that 30-day unplanned readmissions were associated with higher severity of illness (OR = 3.96), location of residence in proximity to the UVA Medical Center (OR = 1.31), and social risk factors for social and community context (OR = 1.26) and economic stability (OR = 1.37). Risk factors for neighborhood and built environment and education were not significant predictors of 30-day readmissions. Significant independent predictors of 30-day ED visits included age (OR = 0.60), location of residence in proximity to the UVA Medical Center (OR = 2.56) and risk factors in all of the SDoH domains – social and community context (OR = 1.39), economic stability (OR = 1.39), neighborhood and built environment (OR = 1.61), and education (OR = 1.38). All variables with the exception of social and community context were significant independent predictors of extended LOS - age (OR = 0.51), sex (OR = 1.18), severity of illness (OR = 2.14), discharge to facilities (OR = 2.42), location of residence (OR = 0.82), economic stability (OR = 1.14), neighborhood and built environment (OR = 1.31), and education (OR = 0.79).

Table 5-4. Individual SDoH domains and association with risk for adverse patient-level outcomes

Predictors	30-day unplanned readmission			30-day ED visit without admission			Extended length of admission		
	Odds Ratio	95% CI	p	Odds Ratio	95% CI	p	Odds Ratio	95% CI	p
Intercept	0.04	0.03-0.04	**<0.001**	0.03	0.02-0.04	**<0.001**	0.58	0.50-0.67	**<0.001**
Age	1.09	0.81-1.47	0.570	0.60	0.41-0.88	**0.009**	0.51	0.41-0.64	**<0.001**
Sex (Female)	0.95	0.86-1.05	0.331	1.04	0.92-1.18	0.538	1.18	1.09-1.27	**<0.001**
Severity of Illness	3.96	3.36-4.67	**<0.001**	1.04	0.83-1.29	0.743	2.14	1.88-2.42	**<0.001**
Discharge Destination (Facilities)	1.12	1.00-1.26	0.050	0.95	0.80-1.11	0.506	2.42	2.20-2.67	**<0.001**
Location of Residence (Albemarle County)	1.31	1.17-1.46	**<0.001**	2.56	2.24-2.93	**<0.001**	0.82	0.75-0.90	**<0.001**
Social and community context	1.26	1.14-1.40	**<0.001**	1.39	1.21-1.59	**<0.001**	1.08	0.99-1.17	0.075
Economic stability	1.37	1.23-1.51	**<0.001**	1.39	1.22-1.59	**<0.001**	1.14	1.06-1.24	**0.001**
Neighborhood and built environment	1.13	0.87-1.46	0.359	1.61	1.21-2.16	**0.001**	1.31	1.06-1.62	**0.013**
Education	1.16	0.97-1.40	0.112	1.38	1.09-1.74	**0.007**	0.79	0.68-0.93	**0.004**
Total Observations	21,402			21,402			21,402		
Random Effects									
ICC	0.21			0.25			0.28		
N	15,116			15,116			15,116		

Aggregated SDoH risk score is associated with highest risk for 30-day post-discharge ED visits

In these model implementations, risk factors for each SDoH domain were aggregated to reflect a total burden of SDoH on a range from 0 (no risk factors) to 4 (risk factors in all four domains). This aggregated SDoH risk score was rescaled on a range from 0 to 1 and included as a single predictor to compare the influence of other clinical and demographic variables with the presence of any SDoH risk factor on adverse patient outcomes (Table 5-5). Severity of illness remained the most influential predictor of 30-day readmissions (OR = 3.98) with aggregated

SDoH risk being the second most influential predictor (OR = 2.67). Location of residence remained a significant predictor of readmissions (OR = 1.32), and discharge to facilities was also a significant predictor in this model (OR = 1.13). Aggregated SDoH risk was associated with the highest risk (OR = 3.64) for 30-day ED visits among all independent predictors in this model. Other significant independent predictors of 30-day ED visits remained age (OR = 0.58) and location of residence (OR = 2.65). All variables were significant independent predictors of extended LOS, with discharge to facilities having the highest associated risk (OR = 2.43), followed by severity of illness (OR = 2.21), SDoH risk (OR = 1.38), sex (OR = 1.17), location of residence (OR = 0.82), and age (OR = 0.60).

Furthermore, we compared 30-day (a commonly used industry standard) vs. 90-day endpoints for unplanned readmissions and ED revisits to see if there was a difference in the significance of predictors at a later end point for these outcomes (Supplemental Table 3). We found that discharge to facilities was a significant predictor of 30-day unplanned readmissions, but not a significant predictor for the 90-day endpoint. Significance of all other predictors across the two outcomes remained the same, but predictors had slightly higher odds ratios for 90-day outcomes since these outcomes would be more likely to occur within this endpoint.

Table 5-5. Aggregated SDoH risk factors and association with risk for adverse patient-level outcomes

Predictors	30-day unplanned readmission			30-day ED visit without admission			Extended length of admission		
	Odds Ratio	95% CI	p	Odds Ratio	95% CI	p	Odds Ratio	95% CI	p
Intercept	0.04	0.03-0.05	**<0.001**	0.03	0.02-0.04	**<0.001**	0.60	0.51-0.69	**<0.001**
Age	1.06	0.79-1.43	0.699	0.58	0.40-0.85	**0.005**	0.49	0.39-0.62	**<0.001**
Sex (Female)	0.95	0.87-1.05	0.351	1.02	0.90-1.16	0.786	1.17	1.09-1.27	**<0.001**
Severity of Illness	3.98	3.38-4.69	**<0.001**	1.03	0.83-1.28	0.810	2.12	1.87-2.40	**<0.001**
Discharge Destination (Facilities)	1.13	1.01-1.27	**0.039**	0.95	0.80-1.12	0.574	2.43	2.20-2.68	**<0.001**
Location of Residence (Albemarle County)	1.32	1.18-1.47	**<0.001**	2.65	2.32-3.04	**<0.001**	0.82	0.75-0.90	**<0.001**
SDoH	2.67	2.13-3.34	**<0.001**	3.64	2.72-4.86	**<0.001**	1.38	1.15-1.65	**0.001**
Total Observations	21,402			21,402			21,402		
Random Effects									
ICC	0.21			0.25			0.28		
N	15,116			15,116			15,116		

Discussion

In this study, we demonstrated that measures of individual-level social risk factors are already widely captured in EHRs without the addition of a specific SDoH screening tool for an inpatient population treated at the UVA Medical Center. More than 94% of all inpatient encounters had a least one measure documented for each of the SDoH domains included in this study. The presence of individual-level social risk factors had significant effects on all outcomes, but was the single most important predictor of 30-day ED revisits. Individual risk factors for economic stability were significant independent predictors for all outcomes studied here. One-third of all patients had a risk factor identified in at least one SDoH domain and risk factors for

economic stability and social and community context were the most prevalent among this patient population. While risk factors for neighborhood and built environment were rare in this patient population (3%), they were a significant independent predictor of 30-day ED visits and extended LOS, and associated with higher risk for these outcomes than all other SDoH domains.

Social and behavioral determinants of health and associated risk factors have been a focus of research to improve predictive models for high-cost and high-risk patients.[41] In a systematic review by Chen et al. that identified thirteen studies that examined the impact of including SDoH data for risk prediction, all but one study reported that neighborhood-level SDoH had minimal contribution to improving predictive performance.[47] In contrast, inclusion of individual-level SDoH resulted in significant improvements in model performance for predicting outcomes ranging from medication adherence[271], to HIV risk[282], and hospital readmissions.[272] A study recently published by Zhang et al. compared the addition of individual-level and neighborhood-level SDoH to improving existing predictive models of 30-day unplanned readmissions. They found that SDoH did not improve prediction for a general patient population, but that the combination of individual-level and neighborhood-level SDoH significantly improved predictive performance for patient subgroups including Medicaid patients, patients over age 65, and obese patients.[283] The collection of individual-level social and behavioral risk factors will likely be necessary to improve upon current methods to accurately identify high-risk and high-cost patients.

While many clinicians acknowledge that SDoH affect the health and well-being of their patients, there are several concerns and considerations for involvement of clinicians and health care systems in SDoH screening. Clinicians are sensitive to the perception that this is not necessarily their area of expertise and are worried that health care systems do not have the resources and experience to coordinate effective interventions, which would necessitate non-clinical

interventions or referrals.[284] Nevertheless, widespread usage of SDoH screening is likely necessary for health systems to be able to identify and therefore mitigate their effects. Important considerations for implementing SDoH screening tools include the format of a screening tool, who administers it, and the frequency of assessing needs. Electronic formats for self-disclosure, compared to in-person interviews, have been shown to have higher rates of disclosure for sensitive issues such as household violence and substance abuse.[285] It is as yet unclear as to the appropriate frequency of assessment; should SDoH screening be administered at every patient encounter, annually, or on some other frequency? The varied domains of social and behavioral health may change frequently and need to be assessed regularly, while others may be more stable especially in adulthood.[275]

There is still much research and work to be done to develop intervention strategies that do not medicalize the treatment of SDoH, which could inadvertently lead to even higher health care costs.[269] Effective interventions have hinged on close partnerships and coordination between health systems and non-clinical community organizations. For example, housing assistance programs for chronically homeless individuals have demonstrated the ability to decrease medical costs 6-12 months after intervention.[286] Accountable care organizations (ACOs), such as that operated by Hennepin Health, have invested in community-level partnerships to address multiple SDoH for Medicaid patients and have seen a reduction in ED visits and increase in outpatient and primary care utilization.[287] The Johns Hopkins Children's Center provides an example of tailoring SDoH screening to the specific community-based agencies and programs that are available. Families are referred to Health Leads, a non-profit organization that uses trained advocates to connect families with the appropriate local services, and social domains for screening are tailored to those available

services.[288] Interventions and partnerships will be unique to each community's specific needs and priorities.

Not all health care systems will be poised to implement widespread standardized screening for individual social risk factors immediately, but this study demonstrates an opportunity for health systems to set priorities for interventions or further screening by identifying the risk factors that are most prevalent in their patient population. Others have discussed an "opportunity index" for SDoH that could help health care systems identify priorities for quality improvement that would provide the greatest cost savings and benefit to patients and the community.[269, 289] While there may be hesitancy from clinicians to implement SDoH screening for the reasons described above, we have demonstrated in this study that individual-level social risk factors are already widely documented in EHRs and associated with increased risk for multiple patient-level outcomes. This type of data, while imperfect, may provide health systems with a useful starting point to understand the prevalence of certain SDoH among their patient populations and design appropriate targeted interventions in partnership with community organizations.

There are several limitations to this study – most notably the lack of standardized and validated SDoH screening questions or measures. Without a standardized screening tool and work flow there is likely implicit bias involved in the collection of this data when clinicians make decisions about which questions are relevant to ask of individual patients.[290] The measures that currently exist in the EHR typically do not cover all of the dimensions of social risk outlined in Table 5-1. For example, existing measures related to quality of housing stability primarily capture those individuals experiencing chronic homelessness, and not those individuals experiencing housing insecurity, which might include not being able to pay rent, potential for eviction, or inability to pay utilities. Similarly, transportation measures only assess the individual's need for

transportation at discharge from the hospital, but do not ask about access to transportation for follow-up appointments, or to obtain prescriptions. For these reasons, we anticipate that the prevalence of risk factors for many of these SDoH domains is potentially much higher than these EHR measures currently capture. Furthermore, EHR data was obtained from a single academic medical center and cannot capture readmissions to other medical centers or emergency departments. Since the UVA Medical Center serves a wide geographic distribution and many patients reside in rural areas, this may artificially decrease readmissions and ED revisits for these populations. Despite the limitations of this data, we believe that this study provides a useful example of how health systems can use their existing EHR data to estimate the prevalence of individual social risk factors in their patient population and develop priorities for screening, interventions, and community partnerships.

Conclusions

Individual-level social risk factors are widely documented in existing EHR unstructured data and are associated with increased risk for 30-day readmissions, 30-day ED revisits, and extended length of stay. Of these outcomes, individual social risk factors were the most significant predictor of 30-day ED revisits. Even in the absence of standardized SDoH screening tools, health systems can use existing EHR data to understand the prevalence of individual social risk factors in their patient population to prioritize further screening or interventions.

Author Contributions

SMR, BK, and JDM contributed to the design of the study. SMR performed data collection and analysis. BK and LEB advised on data analysis and methodology. SMR drafted the initial manuscript. All authors contributed to manuscript revision and approved the final version submitted for publication.

Acknowledgements

Ethics Approval

This study was approved by the University of Virginia Institutional Review Board for Health Science Research with an exemption (IRB-HSR # 22081).

Competing Interests

The authors declare that this research was conducted in the absence of any commercial or financial relationships that could be construed as a potential conflict of interest.

CHAPTER 6

Discussion and Future Directions

Overview

In the work presented in this thesis, multiscale modeling approaches were developed and deployed to aid in the design of novel intervention strategies. The exponential rate of growth in data produced in the biomedical sciences and health care, combined with the complex relationships that exist across spatial, temporal, and functional dimensions of this data creates an opportunity for multiscale models to synthesize and make novel predictions about the behaviors of these complex systems. Multiscale models provide a framework that can uniquely predict how perturbations to individual parameters will impact outputs or outcomes at multiple levels of resolution in a systematic and high-throughput manner that would otherwise not be feasible with experimental methods. In the work presented here, we combined multiscale computational models with experimental models and methods to predict the effect of varying individual parameters on systems-level outcomes, provide insight into the mechanisms that contribute to these outcomes, identify novel hypotheses for further investigation, and demonstrate the value in unstructured and heterogenous sources of data.

The multiscale models presented in this work focused on applications in the treatment of cardiovascular disease, diabetes, and public health interventions. In Chapters 2 and 3, we investigated the spatial and temporal heterogeneity that exists in the cellular responses to injury following myocardial infarction, and developed a multiscale model that integrates a complex network model of intracellular signaling with a multicellular agent-based model to make predictions about tissue-level remodeling and scar formation following cardiac injury. This multiscale model can be leveraged to test novel therapeutic options for cardiac fibrosis and inform the design of future preclinical and clinical studies. In Chapter 4, we integrated data produced by

three separate preclinical studies into a mechanistic model of diabetic wound healing to predict the impact of varying spatial parameters of drug delivery that were not tested experimentally. This enabled us to make novel predictions about the impact of modifying the location of drug delivery and diffusivity of proangiogenic drugs on the rate of wound healing that will inform future studies and drug development for cutaneous wound healing. Finally, in Chapter 5 we utilized electronic health records as a novel source of unstructured data for identifying individual social risk factors and demonstrated that these risk factors are associated with adverse patient-level outcomes including unplanned readmissions, ED visits, and extended hospital length of stay. This work provides the framework for utilizing unstructured data in electronic health records to identify individual social risk factors, which will likely be a necessary component to improve predictive models for identifying high-risk patients.

This final chapter will highlight the innovations and contributions of this work, in addition to the exciting avenues for future areas of study. I will also provide some recommendations for advancing the applications of multiscale models based on my experience developing and designing models for cardiovascular disease and public health. I will conclude this chapter with a broad overview of the societal impacts of this research.

Innovation

The applications of multiscale modeling presented in this thesis cover a wide scope of challenges in biomedical sciences and public health and make several novel and innovative contributions to these fields. In Chapter 2, we describe the development of the first multiscale model of cardiac fibrosis that integrates a large-scale cell signaling network model with a model of multicellular tissue-level remodeling. Previous models have included large-scale network models

of single cells[25], and the temporal dynamics of inflammation and fibrosis following myocardial infarction[90, 111], but this demonstrates the first model that combines large-scale signaling networks for many cells in an infarct with spatially-dependent signaling and extracellular matrix remodeling. The novel approach of this modeling framework allows us to perturb the dynamic pro-inflammatory and pro-fibrotic contexts that change over the course of infarct healing and test molecular perturbations that may having opposing effects throughout the course of healing. Previous experimental and computational models have investigated the effects of pharmacologic interventions on myofibroblast activity and collagen deposition[118, 291, 292], but this multiscale computational model will additionally be able to predict the spatial heterogeneity of collagen deposition in an infarct and co-localization of inflammatory and fibroblast cell populations. Scar heterogeneity that develops as a result of differences in fibroblast alignment and local collagen deposition is an important determinant of the mechanical function of the heart and will be an important consideration in the design of therapeutics for cardiac fibrosis.[187, 188] This model can be deployed to identify candidate pharmacologic therapies or combination therapies that would improve functional recovery following myocardial infarction and leveraged to design future preclinical studies.

In Chapter 3, we present one of the first examples of high-resolution images that characterize the spatiotemporal dynamics of macrophage infiltration in the heart during post-MI wound healing. Previous studies have characterized the temporal dynamics of macrophage phenotypes and transcription profiles at early time points following myocardial infarction,[121, 181, 208] but our work contributes the first example of the spatial distributions and heterogeneity of macrophage populations across the entire infarct during post-MI wound healing. We quantify changes in macroscopic regions of interest within the infarct including regions of necrosis and

intramyocardial hemorrhage, and M1 and M2 macrophage densities within each of these distinct regions. We show that M2 (CD163+) resident macrophages are lost by day 2 following infarction, which corresponds to the first appearance of regions of necrosis. Necrosis becomes most pronounced at day 4, and then subsides in parallel with a marked increase in M1 (CD68+) inflammatory macrophage infiltration, which is sustained through day 6. We also present evidence of a CD68+CD163+ macrophage population that appears to be enriched in the epicardium following MI, and that defies the canonical M1/M2 classifications that have been developed based on the polarization of macrophages *in vitro*.[182-184] This provides further support to calls from other researchers in the field to fully characterize the diverse macrophage phenotypes that exist *in vivo* and their unique sources, signaling pathways that lead to differential activation states, and functions during post-MI wound healing and scar development.[178, 179, 219] This work contributes important findings about the spatiotemporal dynamics of macrophages in the heart during post-MI wound healing that will inform future studies that aim to identify novel therapeutics targeting the inflammatory response that leads to adverse remodeling of the heart and cardiac fibrosis.

In Chapter 4, we describe a novel mechanism-based PDE model to predict how spatial parameters of drug delivery with a modified VEGF-A mRNA impact the rate of healing in a murine model of diabetic wound healing. Previous computational models have been developed to study mechanisms of cutaneous wound healing[228-232] and to identify drug targets for stimulating angiogenesis in wound healing.[234] Almquist et al. have reported an empirical pharmacokinetic and pharmacodynamic model of AZD8601 in diabetic wound healing, which captures statistical variation in wound healing dynamics at both the individual and the population level using a nonlinear mixed effect modelling approach.[235] While this model describes the time-dependent aspects of wound healing, it does not account for spatial parameters of drug delivery and wound

healing. Previous models of drug delivery systems have studied the effects of dosage and temporal release[235, 251, 293], but this is the first model to our knowledge that presents the effects of varying the location and diffusivity of a locally injected drug in a model of cutaneous wound healing. This multiscale model can be used to specify drug delivery locations for the design of preclinical and clinical studies that will optimize healing of diabetic wounds. It could also further be extended to investigate the efficacy of combination therapies that use multiple growth factors (e.g., VEGF, PDGF, FGF, etc.) to promote angiogenesis and accelerate wound healing.[109, 294, 295] Furthermore, this model could be applied to other methods of drug delivery, particularly controlled-release drug delivery systems, to predict how changes to the diffusivity of a proangiogenic drug or delivery system impacts the spatial distribution of the drug and rate of wound healing.[251, 296]

In Chapter 5, we demonstrate one of the first examples of using unstructured data in electronic health records to identify individual social risk factors. We showed that these individual social risk factors, even when controlling for other clinically relevant risk factors, are associated with increased risk for unplanned readmissions, emergency department visits, and extended hospital length of stay. Previous efforts to capture individual-level SDoH have identified domains such as age, sex, ethnicity, insurance coverage, and marital status, but the only studies that have captured individual social risk factors (i.e., homelessness, financial resource strain, food insecurity, etc.) have relied on the administration of new survey-based screening tools.[273, 274] Our work demonstrates that health systems can utilize data that is already widely captured in EHRs to determine the prevalence of social risk factors in their patient population. Modeling efforts such as this can help health systems develop an "opportunity index" for SDoH in order to identify the social risk factors present in their patient populations that contribute the most significantly to adverse patient outcomes and are modifiable targets for interventions. This approach can inform

intervention strategies and partnerships with community-based organizations to address the social and economic needs of individual patients that contribute to their health and well-being.

Extended applications and future directions

Multiscale models of cell dynamics and ventricular remodeling following myocardial infarction

We provide one of the first examples that characterizes the spatial distribution of macrophages in the heart following MI, and there are many opportunities to further expand our understanding of the spatial heterogeneity that exists in macrophage recruitment and polarization. In Chapter 3, we presented evidence of a CD68+CD163+ macrophage population that may be enriched in the epicardium. Previous studies have suggested that epicardial cells undergo epithelial-to-mesenchymal transition (EMT) following MI and are a source of progenitor cells that have the ability to adopt multiple cell fates and contribute to healing and neovascularization.[198, 297-299] Similarly, macrophages have been implicated in the promotion of endothelial-to-mesenchymal transition (EndoMT) which may contribute myofibroblasts during cardiac repair.[300, 301] We also showed examples of a dense band of αSMA+ cells surrounding the endocardium of the left ventricular cavity that may be a source of myofibroblasts that contribute to scar formation. While our quantification of macrophage infiltration focused on samples taken from the myocardium, future work should aim to quantify the spatiotemporal dynamics of macrophage and myofibroblast populations throughout the entire depth of the heart wall, from the epicardium to endocardium.

The temporal heterogeneity that exists in macrophage phenotypes and transcriptional profiles following myocardial infarction has been well documented,[181, 185, 208] but the spatial heterogeneity of macrophage populations that are present at each of these time points has not been

investigated. A recent study by Chakarov et al. demonstrated evidence of two transcriptionally unique populations of resident tissue macrophages that occupied different spatial niches across multiple tissues, including the heart. Lyve1^{lo}MHCII^{hi} macrophages were enriched near nerve bundles and Lyve1^{hi}MHCII^{lo} macrophages were localized near endothelial cells and upregulated genes related to angiogenesis.[209] This suggests that macrophages, both tissue resident macrophages and monocyte-derived macrophages, may play functional roles that are unique to the spatial niches that they occupy. It is unclear whether macrophages are activated to these different states as a result of the unique microenvironment that they experience, or whether they are programmed to differentiate to these states and then migrate to these spatial niches based on their function. A combination of single-cell and spatial transcriptomics will be required to answer these questions and exhaustively characterize the spatial heterogeneity of macrophage populations within the infarct.[219] Spatially resolved transcriptomics was named the method of the year in 2020 by Nature Methods, which allows researchers to analyze the transcriptomics of single cells and map that information to the positional context of that cell within the tissue.[302] The development and advancement of this method will be an important tool to determine the unique spatial niches that macrophages occupy during post-MI wound healing and how that contributes to their heterogenous phenotypes and transcriptional profiles.

Network models are useful tools for understanding how dynamic inputs and environmental cues are integrated in cell signaling networks and lead to differential activation states for individual cells. Liu et al. recently developed a large-scale computational model of the macrophage signaling network that predicts macrophage activation states based on combinations of nine different cytokine inputs.[217] Similarly to the multiscale model presented in Chapter 2, a network model of macrophage intracellular signaling could be integrated with an agent-based model of post-MI

wound healing to predict how local chemokine and cytokine inputs contribute to spatially heterogenous macrophage activation states. This model could also be used to predict the relative contributions of different sources of macrophages (e.g., progenitor cells from the epicardium, proliferation of tissue-resident macrophages in remote regions, monocyte recruitment from the vasculature) that most closely recapitulate the patterns observed *in vivo*.

The multiscale model presented in Chapter 2 could be expanded in several ways to develop a model of post-MI wound healing that would be a useful tool for *in silico* screening of therapeutics to improve cardiac fibrosis. The addition of inflammatory cells, including monocytes, macrophages, and neutrophils, would allow the simulation of cytokine production from individual cells, diffusion of soluble cytokines and growth factors, and migration rates that are driven by chemokine gradients. Macrophages and fibroblasts, informed by large scale network models, would modify their phenotypes including migration and proliferation rates, cytokine secretion, and ECM degradation and deposition, based on the integration of local biochemical and biomechanical stimuli. Furthermore, the spatial resolution of the model could be expanded to include both infarct, peri-infarct, and remote zones in the heart after myocardial infarction which have been shown to have different patterns of cell recruitment and activation.[219] This model could even be further coupled with a finite element model that predicts how changes in the ECM composition and scar heterogeneity alter the mechanics of the heart to predict pump function and cardiac output. In this manner, we could develop a validated multiscale model of cardiac fibrosis that depicts many scales of resolution from the level of cytokine and chemokine gradients, to individual cell signaling, to tissue level ECM remodeling, and even organ level mechanics and pump function.

A validated multiscale model of this nature would provide a platform for systematically screening the effects of therapeutic interventions on multiple cell types and ECM composition that contributes to the progression of cardiac fibrosis with a high degree of both spatial and temporal resolution. The ability to effectively improve infarct healing will require spatial control of fibrosis. Ideally, a post-infarction therapy would enhance collagen deposition in the infarct, while preventing fibrosis in the remote myocardium. We believe that this multiscale computational model will be a necessary tool to integrate the dynamic spatiotemporal and complex signaling environments and cell distributions in the heart in order to identify a pharmacologic approach that can achieve differential control of fibrosis across regions of the heart and mitigate the development of heart failure.

Improving drug delivery strategies for cutaneous wound healing

The multiscale model of diabetic wound healing presented in Chapter 4 is one of the first examples of utilizing a mechanistic model of wound healing to perturb spatial parameters of drug delivery. Pharmacokinetic and pharmacodynamic models of drug delivery often focus on the dose and timing of drug delivery, but few models have rigorously assessed the impact of spatial distribution on the delivery of a locally injected drug. There are several opportunities to further expand this model so that it can be used to inform evidence-based decisions about the location of drug delivery in the design of future preclinical and clinical studies. The current implementation of this model assumes that healing occurs uniformly with respect to θ, but injections were delivered at four discrete points separated by 90° around the wound border. Based on the predictions of our model that the spatial gradient of VEGF-A generated by injections is an important determinant of the rate of wound closure, we would hypothesize that these four discrete injections would create

a gradient of VEGF-A that would result in a non-uniform rate of healing with respect to θ. We could expand the model to account for the rate of wound closure in both the radial and azimuthal dimensions, which will be a more relevant factor in larger clinical wounds. Additionally, the radial dimension of the model could be expanded to include a border region of healthy tissue surrounding the wound space. Simulations that perturbed the diffusivity of mRNA demonstrated that the drug was consumed at the wound boundary at a rate dependent on this diffusivity. Extending the model to account for a region of healthy tissue surrounding the wound would also allow us to explicitly model the differences in the tissue properties and diffusivity of drugs in these mediums.

Due to the limited availability of data about the spatial parameters of AZD8601, we made several assumptions when modeling the spatial distribution of mRNA that warrants further experimental studies to validate these predictions prior to future clinical studies. We estimated the diffusivity of AZD8601 based on literature-reported values for the diffusivity of mRNA, but further experimental studies are needed to determine the precise length scale of diffusion for AZD8601 in both normal tissue and a healing wound. Furthermore, our model predicted that wound healing could be accelerated by delivery injections of AZD8601 at a distance inside the border of the healed wound, but it has yet to be determined if injections delivered within the wound space would result in similar levels of VEGF-A production. The pharmacokinetic model used to describe parameters of VEGF-A production and degradation was based on injections of AZD8601 delivered in healthy tissue. These experiments need to be repeated to determine the rates of VEGF-A production and degradation in a wound space.

These experiments are necessary to validate model predictions with injections of AZD8601 in order to translate model predictions to the healing of human wounds in the clinical setting,

which is the ultimate goal of models to inform drug delivery strategies in the clinic. Diabetic ulcers in humans can be 2-5x larger in diameter and depth than the wounds used in murine models of diabetic wound healing, and can take many weeks to months to heal. Translating the results of preclinical animal models to humans in the clinical setting is the ultimate challenge of biomedical research and the juncture where computational models can be valuable tools to predict how these therapies will translate. This model has the potential to be scaled in these ways to predict how injections with AZD8601 will impact the rate of wound closure in the clinical setting over larger spatial scales and longer temporal scales. Nevertheless, this model is also a valuable tool to design future preclinical animal models of wound healing whether with AZD8601 or other growth factors designed to stimulate angiogenesis. The focus of the murine model of diabetic wound healing used in these studies was to determine the impact of dose and timing of injections on the rate of wound closure, but spatial location of injections was not rigorously considered as a parameter for investigation. Models such as the one described here are valuable tools to prioritize and predict the impacts of experimental parameters of interest when designing preclinical animal studies in order to reduce the number of parameters required to test experientially and reduce time, cost, and animals required.

Similar to the multiscale model of cardiac fibrosis presented in this thesis, this model could be coupled with a network model of endothelial cell signaling to extend the biological scales of resolution explicitly accounted for in the mechanisms of drug action. An agent-based model previously developed by Walpole et al. incorporated Notch1-DLL4 signaling in endothelial cell-endothelial cell interactions to predict the microvascular network morphology during development.[28] A large scale endothelial cell network model could directly model the effects of VEGF and other growth factors such as PDGF, FGF, and EGF on parameters including

proliferation and migration rates, cell sprouting, tip and stalk cell phenotypes, and endothelial tube formation.[303] While VEGF, FGF, EGF, and other growth factors have been tested in preclinical and clinical trials, the only FDA-approved growth factor treatment currently available is Regranex®, a hydrogel containing PDGF.[304-306] Multiscale computational models that couple the mechanisms of drug interaction on individual cells with multicellular responses and tissue level predictions about wound closure could help accelerate the identification and development of novel therapeutics for the treatment of diabetic wound healing, including the possibility of combination therapies. These models could be adapted to simulate other systems of drug delivery as well, such as hydrogels, nanoparticles, and scaffolds.[304]

Utilizing health care data to improve predictive models of high-risk patients and target interventions to modify social risk factors

The Hospital Readmissions Reduction Program (HRRP), introduced in 2012, reduces payments for hospitals that have excess 30-day readmission rates.[43] This evolution from fee-for-service health care to new value-based payment models has placed more focus on modifiable SDoH to improve health outcomes and reduce readmissions. Health systems have a need to identify high-risk and high-cost patients, and the rapid growth in quantity and quality of data available through electronic health records presents an opportunity for the development and improvement of predictive computational models.

The ability to predict 30-day unplanned hospital readmissions, in particular, is an important area of research since this is a costly financial burden to patients and healthcare systems, and it has been estimated that 20% of patients discharged from the hospital are readmitted in a short time span.[307] This has prompted several groups to try and improve predictive models for 30-day readmission risk by including SDoH.[45, 283, 308, 309] These models have generally found that the

inclusion of SDoH data did not improve model predictive performance for a general patient population, but may improve risk prediction for subgroups of patients such as Medicaid patients, or those ages 65 and older.[283, 308, 310] However, these models have primarily incorporated neighborhood or census tract-level SDoH and not individual-level reported SDoH.[277, 307] In fact, a recent systematic review by Chen et al. found that studies that included only neighborhood-level SDoH reported no improvements in model predictive performance, but studies that incorporated individual-level SDoH reported improvements in model predictive performance for outcomes ranging from medication adherence, HIV risk, and hospital readmissions.[47] Only one study recently published in 2020 by Zhang et al. has attempted to combine individual-level and neighborhood-level social determinants of health, where the individual-level factors reported were age, sex, ethnicity, and marital status.[283] No predictive model has included individual-level data about social risk factors including housing stability, food security, transportation, personal safety, and other factors now commonly included in standardized SDoH screening tools such as the Accountable Health Communities Screening Tool,[273] and the Protocol for Responding to and Assessing Patients' Assets, Risks, and Experiences (PREPARE) survey.

We hypothesize that the inclusion of individual-level social risk factors will improve the performance of existing predictive models for 30-day unplanned hospital readmissions. These models have previously demonstrated poor predictive performance because hospital readmissions are a highly complex problem influenced by the contributions of many factors including the burden of confounding chronic diseases, provider and hospital level care indicators, coordination of care following discharge, and many other contributors. Currently, one of the most widely used predictive models of 30-day unplanned hospital readmissions is the HOSPITAL risk score. This is a prediction score that includes seven independent factors: hemoglobin at discharge, discharge

from an oncology service, sodium levels at discharge, procedure during admission, type of admission, number of admissions during the last 12 months, and length of stay.[311] We propose building on the work presented in this thesis by utilizing the individual social risk factors identified in EHRs to determine whether their inclusion can improve predictive performance of the HOSPITAL score for unplanned readmissions. Performance of predictive models is commonly evaluated by the C-statistic, or ROC (area under the receiver operating characteristic), and the HOSPITAL score has a reported C-statistic of 0.71 for a general patient population.[311] We will first determine the C-statistic for a model utilizing the HOSPITAL score for our patient population of interest treated at the UVA Medical Center. Then, we will compare versions of this model implementation that includes only individual-level or neighborhood-level SDoH, or a combination of both levels of SDoH factors. We hypothesize that the model that includes individual-level social risk factors will perform significantly better than the HOSPITAL score alone, and that the model that includes only neighborhood-level factors will demonstrate no significant improvement. A model that includes both individual and neighborhood-level factors may perform better than a model with only individual-level factors. There is also extensive literature that documents the impact of behavioral risk factors (e.g., alcohol use, drug abuse, physical inactivity, etc.) on health outcomes.[312, 313] We could additionally explore the impact of the inclusion of behavioral risk factors on the predictive performance of this model.

Even if a model that includes individual social risk factors is not able to achieve a higher predictive performance than existing models, it would still provide valuable insight to aid clinical decision making and interventions to target modifiable risk factors. These models could be used to prioritize interventions and community-aid programs that target the social risk factors identified to have the most impact on adverse outcomes. This could guide strategy and planning for health

systems as they try to determine the need for implementing SDoH screening tools and cultivating partnerships with community-based organizations for referral programs to address social and behavioral risk factors. Additionally, it is possible that the model would demonstrate higher predictive performance for a specific patient population such as those over age 65, Medicare or Medicaid beneficiaries, or specific medical subgroups such as surgical admissions. This model could be applied to specific patient subgroups to determine whether there are differences in model predictive performance, but would likely require a longer time span of data collection depending on the sample size of these patient subgroups.

Electronic medical records represent one source of health care data that is rapidly growing, but data analytics and computational models to improve the quality and value of health care delivery will integrate many sources of health data. This may include insurance claims data, Census data, wearable sensors such as smart watches, smart phone data, genomics and proteomics, real-time clinical remote monitoring, and many other heterogeneous and varied sources of data. Even data about individual social media usage and search history have been shown to be predictors of behavioral risk factors and mental health conditions.[314, 315] Researchers that hope to identify innovations in the delivery of health care by utilizing these varied data sources will also have to grapple with and address concerns related to privacy, data security, legal and ethical responsibilities, and data infrastructure and usage.

Recommendations for designing multiscale models

Based on the work presented in this thesis which encompasses a wide range of multiscale modeling approaches and applications, here I will summarize a few key recommendations and best practices for developing multiscale models. There exist many modeling techniques that can be

classified as continuous or discrete, stochastic or deterministic, and some hybrid methods that are each uniquely suited to different scales of spatial and temporal resolution.[3] For example, Boolean networks and flux balance analysis are well suited to genomic and proteomic scales of resolution. Continuous systems of ODEs and PDEs are useful for modeling intracellular and extracellular binding kinetics and diffusion of small molecules depending on whether both temporal and spatial resolution are needed in modeling the system of interest. Agent-based models are useful for modeling interactions between multiple cells and cell types, and finite element or finite volume methods can be utilized for tissue or organ-level modeling. The key question that should be considered when designing a new multiscale model is to determine which modeling approach is best suited for the question or objective based on the spatial and temporal scales that need to be explicitly modeled. In this manner, the choice of modeling approach should be chosen intentionally based on the task rather than forcing a specific type of model or previously published model to achieve an objective for which it is not well suited. Additionally, bigger is not always better when it pertains to the scope of a multiscale model. It is counterproductive to assume that model complexity is linearly correlated with the ability to produce novel or consequential predictions. There exists a trade-off in model development where increased complexity is often at the expense of model interpretability. Include only the model parameters, pathways, or components that are critical determinants of the question or objective of interest.

When designing a multiscale model, it is also crucial to think of the end at the beginning. Define clearly what outputs need to be measured quantitatively or qualitatively to sufficiently answer the question of interest or achieve the desired objective. This model design criteria is also crucial to performing rigorous model validation. Modelers may often find themselves with a complex model that produces predictions about parameters or outputs for which they have no

experimental data to validate those predictions. Model validation is a critical component of model development to ensure the accuracy and reliability of model predictions, and to also define the scope and specific conditions under which model predictions can be considered valid. There should be independent data sets used for model development and validation, which should be explicitly defined before beginning model construction and should guide the design of a model. One method for model validation that has been particularly useful in the validation of multiscale models is "hierarchical validation" where individual models are validated separately at a single scale of resolution before coupling models and validating predictions at the multiscale level.[3, 35]

Defining parameters for computational models is one of the key challenges in model development and relies on existing literature and complimentary experimental studies. Often, however, parameters must be defined for which there is no existing literature to support parameter selection and the parameter may be impossible or impractical to measure experimentally. One approach to developing models for biochemical interactions that require a large number of unknown parameters is logic-based models, where the qualitative behavior of activation or inhibition reactions are approximated using logical AND and OR gates.[316, 317] A review written by Peng et al. that explores the intersection of machine learning and multiscale modeling also provides several strategies for integrating machine learning techniques to estimate parameters from sparse or noisy data sets.[318]

There are few models that exist beyond the tissue or organ level spatial scale of resolution, and no single "gene-to-organism" level model has yet to be developed, likely because there still exist technical limits and a lack of computational power to discretely model all components or biological processes across an entire organism. Computational power is increasing at an exponential rate, but models must still be developed with computational limits and efficiency in

mind. Parallel computing and cloud computing have increasingly been used to increase the number of discrete agents or methods that can be incorporated in multiscale models. One method to structuring multiscale models is to design many sub-modules that can be executed independently and outputs are passed between these modules. There are also many lessons and best practices from computer science and software engineering that can be utilized to simply improve the computational efficiency of code design and execution. Kirschner et al. have also proposed a tunable resolution approach for multiscale models, where models can be easily adapted with finer or coarser grained resolution that would improve options to validate predictions at all of these levels of resolution and increase model efficiency where needed to increase computational speed.[319] Taken together, these recommendations can improve the quality and rigor of computational models and accelerate the advancement of their design and development.

Developing robust software platforms for multiscale modeling

Experimental papers should be published with sufficiently detailed methods for other researchers to reproduce the results. Similarly, computational models should be published with the necessary software and documentation to reproduce model simulations presented in a publication. For any computational biologist who has tried to implement another researcher's model, you know that this is no easy task. In PLOS Computational Biology's "Ten Simple Rules" collection, Taschuk and Wilson published "Ten simple rules for making research software more robust".[320] In this article they describe the scenario of a graduate student or postdoc trying to use another person's code to reproduce results or analyze their own data as a "rite of passage". What particularly stands out to me is that they state: "The potential new user is then faced with two unpalatable options: hack the existing code to make it work or start over." These are indeed unpalatable options, but

acutely relatable to the challenges I encountered throughout the course of this work, and unfortunately the choice more often than not was to start over. This hinders the progress of computational research if we cannot build upon the work of others and are consistently forced to start over on model development. Best practices exist in software engineering to increase robustness and usability that should be adopted in computational biology. Taschuk and Wilson define robust software by the requirements that "i) it can be installed on more than one computer with relative ease, ii) it works consistently as advertised, and iii) it can be integrated with other tools." They make recommendations about using version control, detailed code comments, avoiding hard-coded file paths in your program, providing the user a test set to ensure the software is working as desired, and providing clear documentation or tutorials. These are simple guidelines to follow, but if implemented consistently and rigorously would greatly improve the shareability and usability of software developed for computational biology and multiscale modeling.

Part of the challenge in agent-based modeling, in particular, is that it is used to study a wide range of biological mechanisms with limited consistency in the methods used and a wide range of existing software platforms and programming languages. Conversely, in finite element modeling, for example, there exists more standardized methods, guidelines, and software programs for the computational biology community. The application of agent-based modeling to study biological systems is a newer field and still grappling with standards for methods and model sharing. Agent-based modelers often find that even published computational models that explore similar disease states or cell types do not possess the functionality or extendibility to answer their question of interest and they must develop a new model from scratch for their purposes. New software platforms developed specifically for cell-based simulations have emerged in recent years, including CompuCell3D[321] and PhysiCell[322], that provide built-in methods and sub-modules for

common cell and biological processes including proliferation, apoptosis, migration, cell growth, and others that allow users to build upon and customize these modules rather than starting from scratch. More robust and standardized methods and software platforms will be required to advance multiscale modeling.

Broader societal impacts of this research

Ischemic heart disease and diabetes combined account for more than 20% of deaths in the U.S. annually and despite advancements in biomedical sciences and medicine there is still a lack of effective treatments. Only 4% of drugs for cardiovascular disease that enter Phase I clinical trials will ultimately be approved for use.[323] Cardiovascular disease and diabetes are complex biological phenomenon that cause systemic effects on many different cell types and tissues, across many scales of spatial and temporal resolution. We have a fairly limited understanding of how these diseases progress and the complex mechanisms by which they effect multiple systems, which makes current drug therapies ineffective at stopping or reversing the course of disease. As the scientific questions become more complex and large amounts of data become readily accessible, multiscale computational models will be a necessary tool in the advancement of biomedical sciences to integrate large data sets and make predictions about the behavior of complex systems.

The development and use of multiscale models enable us to test interventions in a high throughput manner that increases the efficiency of experimental studies by identifying the most relevant or consequential parameters to test experimentally. Models enable researchers to screen a large number of interventions or parameters that would not be feasible otherwise due to time, cost, technology, or ethical considerations. Ultimately, this allows us to accelerate the identification and development of novel therapeutics in a manner that reduces the number of animals required for

preclinical experiments and increases the chances that translation to humans in clinical trials will be safe and effective.

Moreover, there exist unsettling disparities in the burden of cardiovascular disease and health outcomes for underserved and underrepresented communities. The life expectancy after myocardial infarction is significantly lower for women than men, and even lower for African Americans and Hispanics. The social and economic conditions that determine individuals' access to education, nutritious food, safe neighborhoods, parks, transportation, and so many other determinants of health have greater impacts on the health outcomes of individuals and communities than the availability and quality of medical care. These social and economic determinants of health are influenced by money, power, and access to resources, which are largely shaped by policy and societal structures outside of the control of individuals. If our ultimate goal is to improve the health and well-being of all individuals, we must address these disparities in the development of more effective and individualized health care. In fact, it is my belief that the next era of "personalized medicine" will involve a rigorous assessment of individual social risk factors and targeted interventions in collaboration with social services and community-based organizations in a more coordinated and holistic approach to the delivery of value-based health care.

Luckily, multiscale models have the potential to integrate vast amounts of data and inform interventions to reduce health disparities as well. The explosion of data in health care and medicine in recent years from the introduction of electronic medical records, to wearable sensors, and real-time remote clinical monitoring creates an environment where increasing availability of data can be leveraged with the appropriate tools and questions to identify innovations in the delivery of health care. The most impactful analyses and models will require the integration of data from many

heterogeneous sources, both clinical and non-clinical in nature, and will necessitate policies to guide questions related to data privacy and security, legal and ethical responsibilities, and data infrastructure.

Concluding Remarks

This thesis has covered a diverse range of applications for multiscale models, which further underscores their power and flexibility to contribute understanding and innovation to a wide range of challenging problems. The applications presented have also utilized many different modeling approaches and scales of resolution, primarily because the modeling approach should be chosen based on the objective or question of interest and not vice versa. Multiscale computational models have the ability to integrate data and systems across many scales of resolution to make predictions about the behaviors of complex systems that would not be possible with other approaches. The field of multiscale modeling can learn from the expertise of computer scientists and best practices of software engineering to further advance the capabilities and adoption of multiscale modeling as an integral component of research and innovation in biomedical sciences and public health.

APPENDIX

Supplemental Material
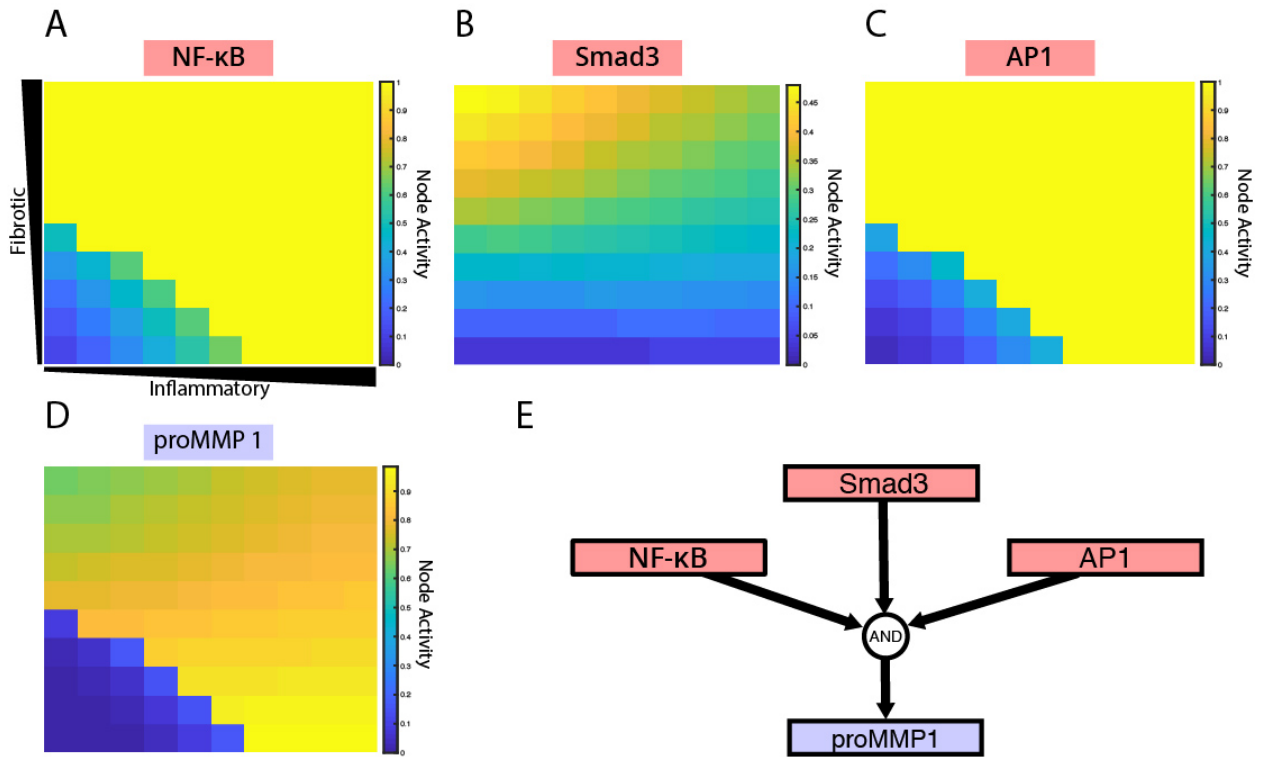
Supplemental Figure 1. proMMP 1 expression is a combination of multiple upstream inputs. Activation patterns of network intermediates **(A)** NF-κB, **(B)** Smad3, and **(C)** AP1. **(D)** proMMP 1 network node activity level **(E)** A simplified network model representation of the immediate upstream reactions that regulate proMMP 1 expression.
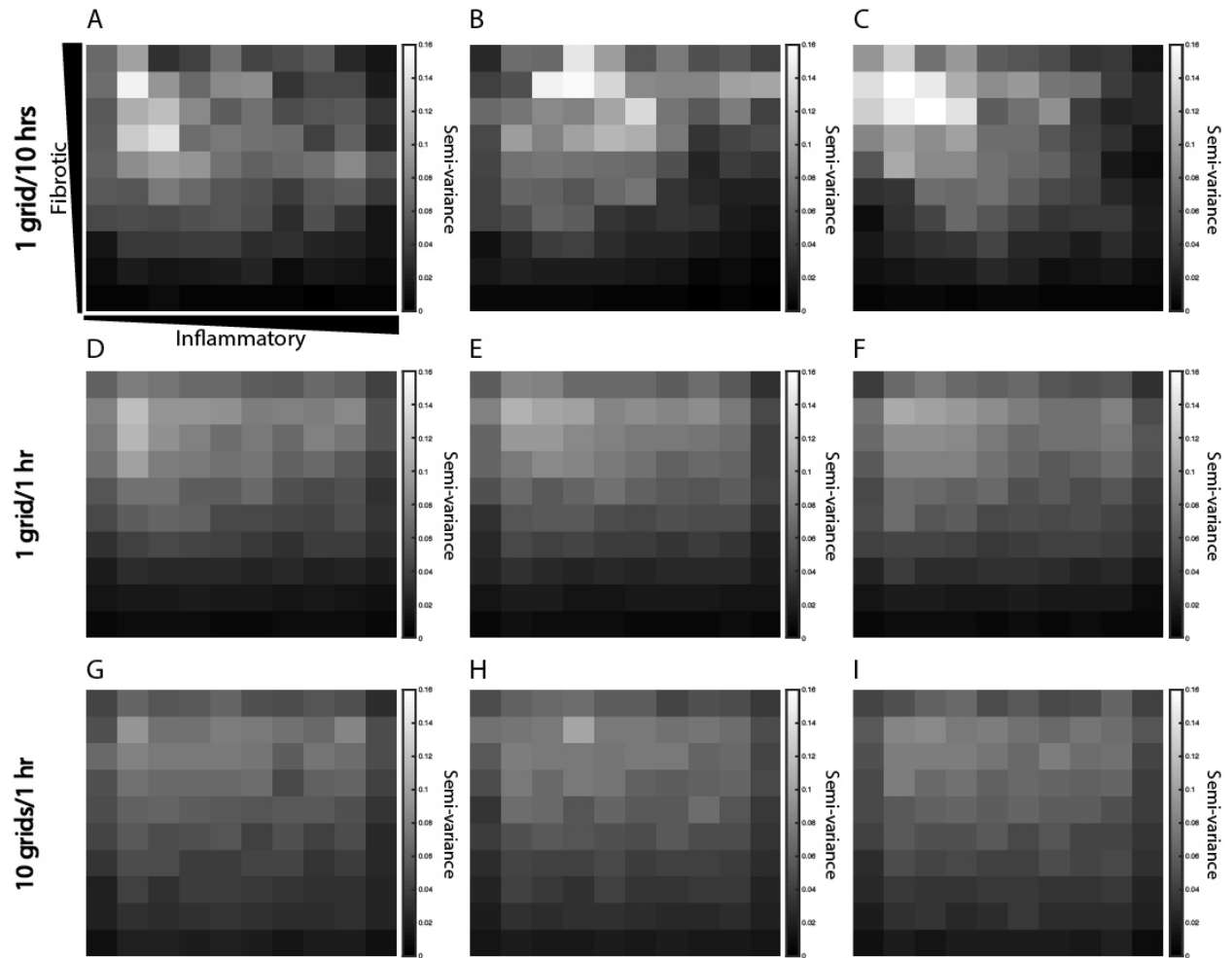
Supplemental Figure 2. Coupled model produces stochastic results.
Three representative images of the collagen profile at 6 weeks for simulations with migration speeds of 1 grid/10 hrs **(A-C)**, 1 grid/hr **(D-E)**, and 10 grids/hr **(G-I).**
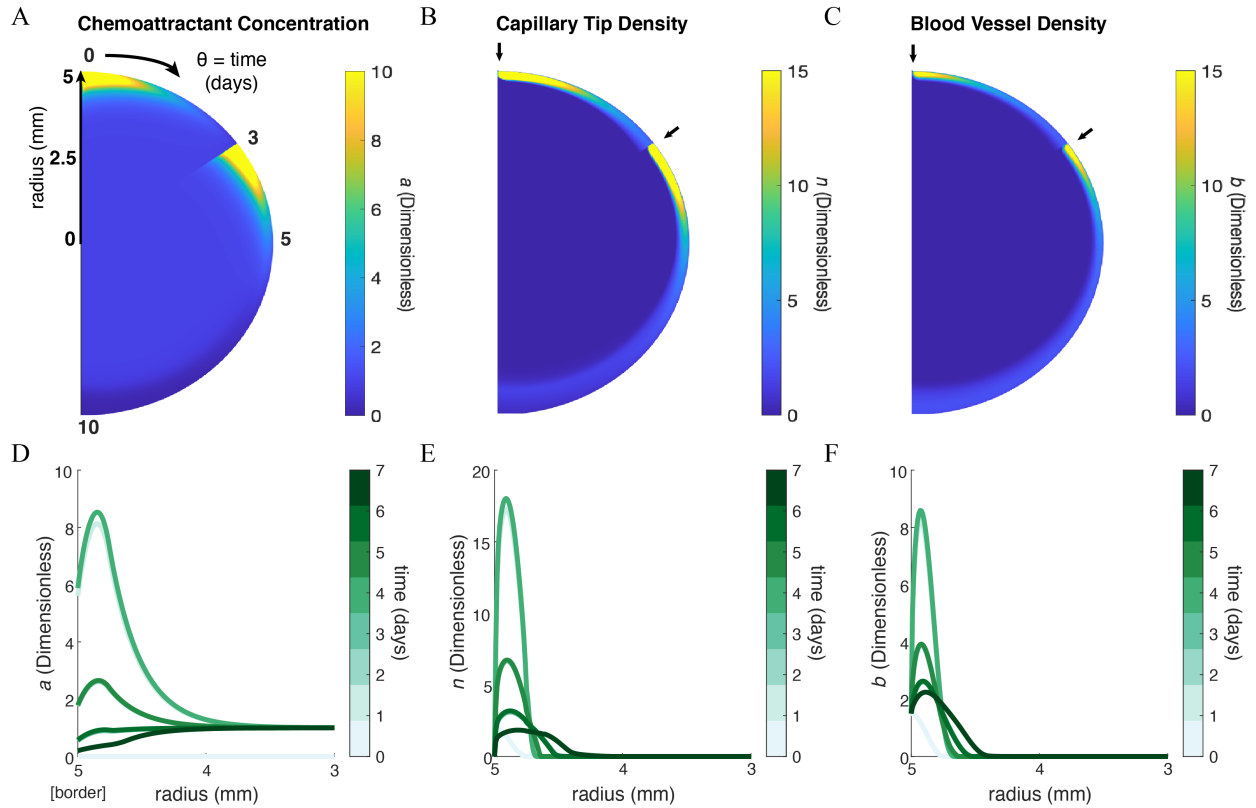
Supplemental Figure 3. Restricted diffusion of mRNA increases concentration of VEGF-A and density of capillary tips and blood vessels at the wound border following injections of 100 µg AZD8601 on days 0 and 3.

Heat maps in polar coordinates of the solutions for the governing equations: **(A)** chemoattractant concentration (*a*), **(B)** sprouting capillary-tip density (*n*), and **(C)** blood vessel density (*b*) for a simulation with restricted diffusion of mRNA (D_m = 0 cm2/s) and repeated injections of 100 µg AZD8601 on days 0 and 3 (indicated by arrows). Radial coordinate corresponds to radius of the wound (0 - 5 mm), θ coordinate corresponds to time (0 - 10 days), and color bar indicates value of the corresponding solution. (D-F) 2-D snapshots of the heatmaps in C-E at t = 0, 1, 2, 3, 4, 5, 6 and 7 days at the wound border (r = 3 - 5 mm).
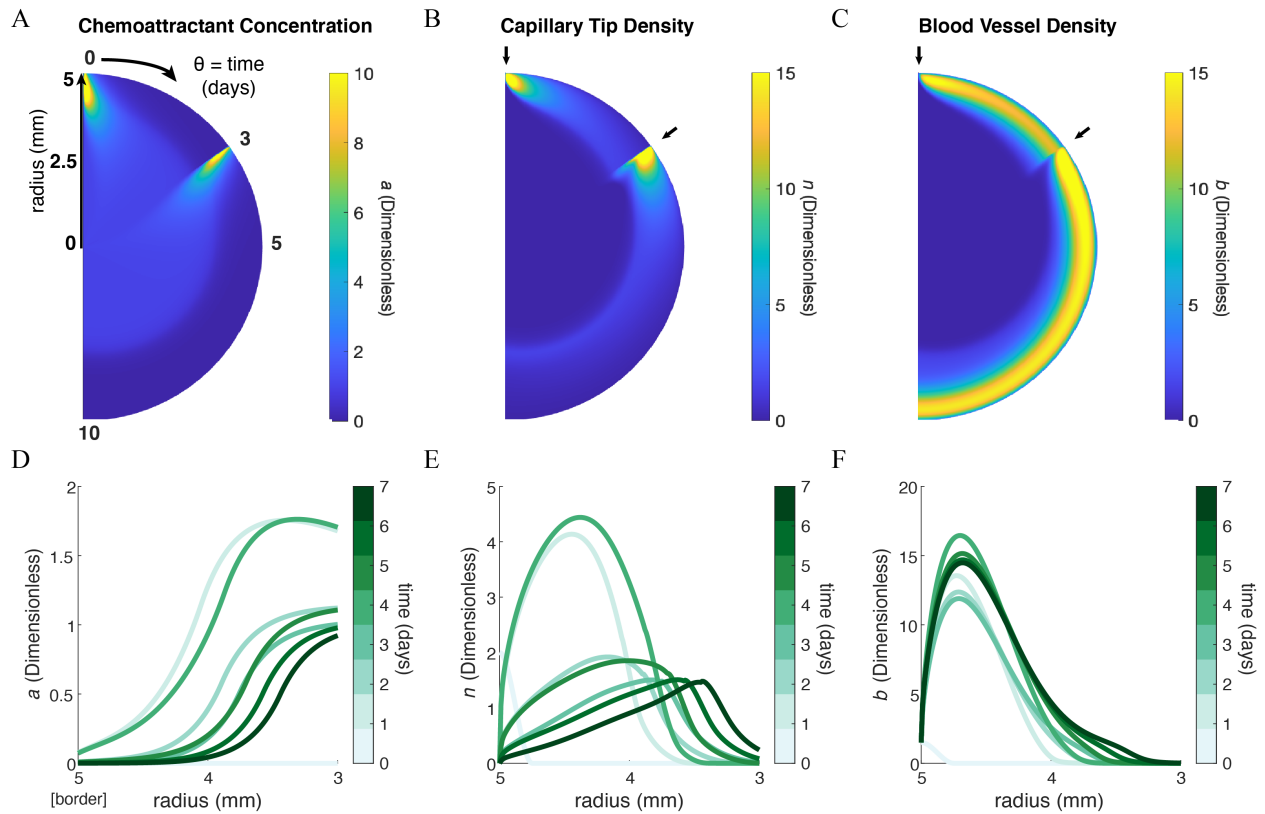
Supplemental Figure 4. Moderate diffusion of mRNA creates gradient of VEGF-A inside the wound border following injections of 100 µg AZD8601 on days 0 and 3.

Heat maps in polar coordinates of the solutions for the governing equations: **(A)** chemoattractant concentration (a), **(B)** sprouting capillary-tip density (n), and **(C)** blood vessel density (b) for a simulation with moderate diffusion of mRNA ($D_m = 10^{-7}$ cm^2/s) and repeated injections of 100 µg AZD8601 on days 0 and 3 (indicated by arrows). Radial coordinate corresponds to radius of the wound (0 - 5 mm), θ coordinate corresponds to time (0 - 10 days), and color bar indicates value of the corresponding solution. **(D-F)** 2-D snapshots of the heatmaps in C-E at t = 0, 1, 2, 3, 4, 5, 6 and 7 days at the wound border (r = 3 - 5 mm).
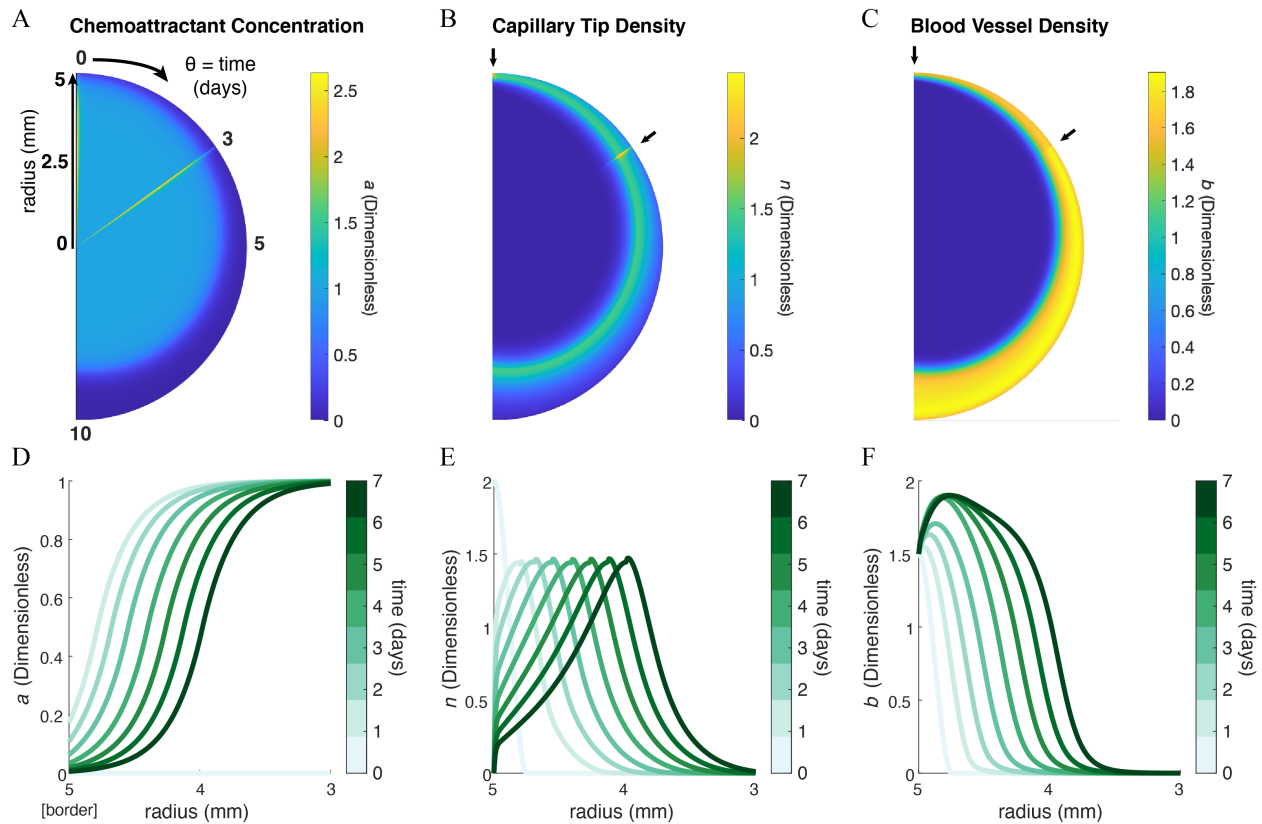
Supplemental Figure 5. Rapid diffusion of mRNA produces modest, but short-lived increase in concentration of VEGF-A throughout the wound area following injections of 100 μg AZD8601 on days 0 and 3.

Heat maps in polar coordinates of the solutions for the governing equations: **(A)** chemoattractant concentration (*a*), **(B)** sprouting capillary-tip density (*n*), and **(C)** blood vessel density (*b*) for a simulation with rapid diffusion of mRNA (Dm = 10-5 cm2/s) and repeated injections of 100 μg AZD8601 on days 0 and 3 (indicated by arrows). Radial coordinate corresponds to radius of the wound (0 - 5 mm), θ coordinate corresponds to time (0 - 10 days), and color bar indicates value of the corresponding solution. (D-F) 2-D snapshots of the heatmaps in C-E at t = 0, 1, 2, 3, 4, 5, 6 and 7 days at the wound border (r = 3 - 5 mm).

Supplemental Table 1. Experimental measurements of actin, collagen, and αSMA expression following cytokine stimulation of cardiac fibroblasts *in vitro*

Treatment Group	Integrated Intensity (Actin)	Integrated Intensity (Collagen)	Integrated Intensity (αSMA)
IL-1β	489.56	212.69	125.91
IL-1β	548.06	257.09	141.98
IL-1β	449.47	225.29	123.18
TGFβ	1557.17	440.14	261.35
TGFβ	1598.38	487.01	411.80
TGFβ	1300.40	435.36	245.84
TGFβ+IL-1β	1050.49	364.54	238.78
TGFβ+IL-1β	885.86	303.93	168.39
TGFβ+IL-1β	883.50	296.64	175.00
control	381.46	299.54	172.73
control	383.21	276.15	162.39
control	295.70	216.78	97.03

APPENDIX

Supplemental Table 2. SDoH domains and dimensions and corresponding EHR fields and response criteria

SDoH Domain	Dimension	EHR Field or Measure	Response Criteria
Education	Early childhood development and education	Special Teaching Barriers	"Cognitive" OR "Education" OR "Language"
Education	Early childhood development and education	Intellectual/Learning Disability	"Yes"
Education	High school graduation	Highest Level of Education	"Primary School" AND Age > 18
Education	High school graduation	Score 1 if patient has 12 years of education or less	"1" AND Age > 18
Education	Language and literacy	Do you have to call interpreter?	"Yes"
Education	Language and literacy	Interpreter Arranged/Needed	"Yes"
Education	Language and literacy	Literacy	"Deficits" OR "Illiterate"
Education	Language and literacy	What is the patient's literacy level?	"Deficits" OR "Illiterate"
Education	Language and literacy	What is the parent/guardian/caregiver's literacy level?	"Deficits" OR "Illiterate"
Economic Stability	Financial resource strain	Pay Range	"1" (100% INDIGENT) OR "2" (95% INDIGENT) OR "3" (80% INDIGENT) OR "4" (55% INDIGENT) OR "5" (30% INDIGENT)
Economic Stability	Financial resource strain	Does the patient have insurance coverage for potential prescription, DME, and other post-acute needs?	"Indigent program" OR "Self-pay"
Economic Stability	Employment	Income (wages, Social Security, welfare, etc.)	"Referral needed" OR "Assistance in place"
Neighborhood and Built Environment	Quality of housing	Home environment transitional concerns	"No electricity" OR "No running water"
Neighborhood and Built Environment	Quality of housing	Pt Resides in Unsafe Physical Environment	"homeless" OR "unstable living" OR "lives in car" OR "shelter" OR "Haven"
Neighborhood and Built Environment	Quality of housing	Discharge Destination	"Shelter" OR "Foster home"
Neighborhood and Built Environment	Quality of housing	Type of Residence	"homeless" OR "unstable living" OR "lives in car" OR "shelter" OR "Haven"

SDoH Domain	Dimension	EHR Field or Measure	Response Criteria
Neighborhood and Built Environment	Quality of housing	Living Arrangements	"homeless"
Neighborhood and Built Environment	Quality of housing	VIII. Appropriateness of Physical Living Space & Environment (SIPAT)	"3" (**Limited:** Unable to confirm reported arrangement or perceived to be inappropriate.) OR "4" (**Poor:** Non-existent; patient has no stable living arrangements -or- lives in environment that doesn't promote transplant health.)
Neighborhood and Built Environment	Transportation	Does the patient have transportation for PCP follow up and to obtain prescriptions?	"No"
Neighborhood and Built Environment	Transportation	Does the patient need discharge transport arranged?	"Yes"
Social and Community Context	Family and community support	Are there any custody orders?	"Yes"
Social and Community Context	Family and community support	Patient's support system includes	"None"
Social and Community Context	Family and community support	Family Behaviors	"Non-supportive" OR "Uncooperative"
Social and Community Context	Family and community support	Care Partner/Family Involvement	"Not Involved" OR "Sporadic"
Social and Community Context	Family and community support	Patient/Family Demonstrates Understanding of Procedure Related Education	"No"
Social and Community Context	Family and community support	VI. Availability of Social Support System (SIPAT)	"6" (**Limited:** The patient's identified support system appears tentative, inconsistent, unreliable, conflicted, uncertain or uncommitted. Identified backup system's reliability is questionable.) OR "8" (**Poor:** Patient unable to identify reliable support system, or identified caregiver has failed to present to clinic. No reasonable back-up support system is in place.)

SDoH Domain	Dimension	EHR Field or Measure	Response Criteria
Social and Community Context	Family and community support	VII. Functionality of Social Support System (SIPAT)	"6" (**Limited:** Member of the identified support system themselves has problems (e.g., medical or psychosocial) which may impair or limit their ability to reliably assist the patient -or- The identified person(s) have expressed doubts/hesitation/conflict/) OR "8" (**Poor:** Patient has suffered due to unreliable support system -or- the transplant team has not been able to effectively work with the support team.)
Social and Community Context	Interpersonal violence or abuse	Caregiver Substance Abuse History	"Yes"
Social and Community Context	Interpersonal violence or abuse	Caregiver History of Abuse/Neglect, Domestic Violence	"Yes"
Social and Community Context	Interpersonal violence or abuse	Is Patient at Risk for Suicidal/Homicidal Behavior?	"Yes (Psychosocial assessment required)"
Social and Community Context	Interpersonal violence or abuse	Evidence of Abuse/Neglect/Exploitation	"Yes"
Social and Community Context	Interpersonal violence or abuse	Physical Abuse	"Yes" OR "provider concern"
Social and Community Context	Interpersonal violence or abuse	Verbal Abuse	"Yes" OR "provider concern"
Social and Community Context	Interpersonal violence or abuse	Sexual Abuse	"Yes" OR "provider concern"
Social and Community Context	Interpersonal violence or abuse	Current Risk of Threats/Harm	"Yes"
Social and Community Context	Interpersonal violence or abuse	History of Threats/Harm	"Yes"
Social and Community Context	Stress and depression	Psychosocial Needs Anticipated	"Yes"
Social and Community Context	Stress and depression	Pt Reports Problems with Family Situational Stress	"Yes"

SDoH Domain	Dimension	EHR Field or Measure	Response Criteria
Social and Community Context	Stress and depression	IX. Presence of Psychopathology (SIPAT)	"6" (**Severe psychopathology**: Present or history of severe psychopathology (e.g., severe mood, anxiety or psychotic disorder with significant impairment of psychosocial functioning). Patient has needed psychiatric hospitalization(s) in the past or "+" history of SI/SA.) OR "8" (**Extreme psychopathology**: Present or severe psychopathology (e.g., as above) usually associated with repeated episodes of psychosis or suicidality; and associated with a history of multiple psychiatric hospitalizations and/or treatment with ECT; or history of multiple SI/SA). Patient may be in need of acute psychiatric intervention before proceeding.)
Social and Community Context	Stress and depression	PHQ-9 Depression Severity	"Severe" OR "Moderately Severe"
Social and Community Context	Marital status	Marital Status	"Widowed" AND Age > 65

Supplemental Table 3. Comparing 30-day vs. 90-day outcomes for readmissions and ED visits

Predictors	30-day unplanned readmission			90-day unplanned readmission			30-day ED visit without admission			90-day ED visit without admission		
	Odds Ratio	*95% CI*	*p value*	*Odds Ratio*	*95% CI*	*p value*	*Odds Ratio*	*95% CI*	*p value*	*Odds Ratio*	*95% CI*	*p value*
Intercept	0.04	0.03-0.05	**<0.001**	0.05	0.04-0.06	**<0.001**	0.03	0.02-0.04	**<0.001**	0.06	0.05-0.08	**<0.001**
Age	1.06	0.79-1.43	0.699	1.11	0.84-1.45	0.473	0.58	0.40-0.85	**0.005**	0.49	0.36-0.67	**<0.001**
Sex (Female)	0.95	0.87-1.05	0.351	0.97	0.89-1.06	0.488	1.02	0.90-1.16	0.786	1.03	0.93-1.15	0.537
Severity of Illness	3.98	3.38-4.69	**<0.001**	4.73	4.07-5.48	**<0.001**	1.03	0.83-1.28	0.810	1.03	0.86-1.23	0.781
Discharge Destination (Facilities)	1.13	1.01-1.27	**0.039**	1.04	0.94-1.16	0.438	0.95	0.80-1.12	0.574	0.92	0.80-1.05	0.221
Location of Residence (Albemarle County)	1.32	1.18-1.47	**<0.001**	1.45	1.30-1.60	**<0.001**	2.65	2.32-3.04	**<0.001**	2.82	2.52-3.16	**<0.001**
SDoH	2.67	2.13-3.34	**<0.001**	3.25	2.64-4.00	**<0.001**	3.64	2.72-4.86	**<0.001**	4.19	3.28-5.36	**<0.001**
Total Observations	21,402			21,402			21,402			21,402		
Random Effects												
ICC	0.21			0.27			0.25			0.23		
N	15,116			15,116			15,116			15,116		

Supplemental Note 1: Derivation of Governing Equations in Cylindrical Coordinates

The dimensionless model equations (Eqs. 1-3) described in Pettet *et al.*, *Mathematical Biosciences* 1996, were converted from Cartesian coordinates to cylindrical coordinates by first defining the wound as a circle of radius R and rewriting the Cartesian form of the generalized, dimensionless governing equations (described in Pettet et al.) in general form (Eqs. 4-6), followed by evaluating the general forms in cylindrical coordinates. The conversion of the initial and boundary conditions to cylindrical coordinates is described in Section S2.

The dimensionless governing equations in 1-D Cartesian coordinates, as defined in Pettet et al., are

$$\frac{\partial n}{\partial t} = \mu_n \frac{\partial^2 n}{\partial x^2} - \chi \frac{\partial}{\partial x}\left(n \frac{\partial a}{\partial x} \right) + \lambda_1 ab - \lambda_2 n - \lambda_0 n^2 \qquad (1)$$

$$\frac{\partial a}{\partial t} = \frac{\partial^2 a}{\partial x^2} + \frac{\lambda_4}{2}\left[1 + \tanh\left(\frac{1-b}{\delta} \right) \right] - (\lambda_4 + \lambda_5 b)a \qquad (2)$$

$$\frac{\partial b}{\partial t} = \mu_b \frac{\partial}{\partial x}\left(n \frac{\partial b}{\partial x} \right) - \mu_x \frac{\partial n}{\partial x} + \chi n \frac{\partial a}{\partial x} \qquad (3)$$

These equations can be written more generally as

$$\frac{\partial n}{\partial t} = -\nabla \bullet \mathbf{J_n} + f_n(n,a,b,\nabla n,\nabla a,\nabla b) \qquad (4)$$

$$\frac{\partial a}{\partial t} = -\nabla \bullet \mathbf{J_a} + f_a(n,a,b,\nabla n,\nabla a,\nabla b) \qquad (5)$$

$$\frac{\partial b}{\partial t} = -\nabla \bullet \mathbf{J_b} + f_b(n,a,b,\nabla n,\nabla a,\nabla b) \qquad (6)$$

where $\mathbf{J_n}$, $\mathbf{J_a}$, and $\mathbf{J_b}$ are the dimensionless fluxes of capillary tips, chemoattractant, and blood vessels, respectively, and f_n, f_a, and f_b are dimensionless kinetic quantities. Note that the ∇ operator is also dimensionless.

Turning to the general governing equation for the capillary tip density, n, the dimensionless tip flux $\mathbf{J_n}$ in 1-D rectangular coordinates is given by

$$\mathbf{J_n} = -\mu_n \left[\frac{\partial n}{\partial x} + \chi n \frac{\partial a}{\partial x} \right] \mathbf{e_x} \qquad (7)$$

where $\mathbf{e_x}$ is the x-direction unit vector. Eq. 7 can be rewritten more generally as

$$\mathbf{J_n} = -u_n \nabla n + \chi n \nabla a \qquad (8)$$

Substituting Eq. 8 into Eq. 4 and expanding each term results in the following:

$$\frac{\partial n}{\partial t} = -\nabla \bullet (-\mu_n \nabla n + \chi n \nabla a) + f_n \qquad (9)$$

$$\frac{\partial n}{\partial t} = \mu_n \nabla^2 n - \chi \nabla \bullet (n \nabla a) + f_n \qquad (10)$$

$$\frac{\partial n}{\partial t} = \mu_n \nabla^2 n - \chi \left[n(\nabla^2 a) + \nabla a(\nabla n) \right] + f_n \qquad (11)$$

Evaluating the r-component of the differential operators in cylindrical coordinates gives the desired dimensionless governing equation describing the radial distribution of the capillary tip density n within the wound:

$$\frac{\partial n}{\partial t} = \mu_n \frac{1}{r} \frac{\partial}{\partial r} \left(r \frac{\partial n}{\partial r} \right) - \chi n \frac{1}{r} \frac{\partial}{\partial r} \left(r \frac{\partial a}{\partial r} \right) - \chi \frac{\partial a}{\partial r} \frac{\partial n}{\partial r} + \lambda_1 ab - \lambda_2 n - \lambda_0 n^2 \qquad (12)$$

Turning to the chemoattractant, a, the dimensionless flux in 1-D Cartesian coordinates and in general differential form, respectively, is given by

$$\mathbf{J}_\mathbf{a} = -\frac{\partial a}{\partial x}\mathbf{e}_\mathbf{x} \quad (13)$$

$$\mathbf{J}_\mathbf{a} = -\nabla a \quad (14)$$

Substituting Eq. 14 into Eq. 4 yields

$$\frac{\partial a}{\partial t} = \nabla^2 a + f_a \quad (15)$$

which is further developed by evaluating the r-component of ∇^2 in cylindrical coordinates and expanding the kinetic term f_a to give the governing equation of chemoattractant in the r-direction:

$$\frac{\partial a}{\partial t} = \frac{1}{r}\frac{\partial}{\partial r}\left(r\frac{\partial a}{\partial r}\right) + \frac{\lambda_4}{2}\left[1 + \tanh\left(\frac{1-b}{\delta}\right)\right] - (\lambda_4 + \lambda_5 b)a \quad (16)$$

Applying the same approach for the blood vessel density b results in the following:

$$\mathbf{J}_\mathbf{b} = -\mu_b n\nabla b \quad (17)$$

$$\frac{\partial b}{\partial t} = \mu_n\left[n\nabla^2 b + \nabla b(\nabla n)\right] + f_b \quad (18)$$

$$\frac{\partial b}{\partial t} = \mu_n\left[n\frac{1}{r}\frac{\partial}{\partial r}\left(r\frac{\partial b}{\partial r}\right) + \frac{\partial b}{\partial r}\frac{\partial n}{\partial r}\right] - \mu_n\frac{\partial n}{\partial r} + \chi n\frac{\partial a}{\partial r} \quad (19)$$

Thus, the dimensionless forms of the governing equations in cylindrical coordinates are given by Equations 12, 16, and 19 for variables n, a, and b, respectively.

Definitions of Dimensionless Quantities

All dimensionless parameters and quantities that appear in Eqs. 12, 16, and 19 retain their original definitions and forms from Pettet et al. (found between Equations 9 and 10 in Pettet et al.) except that, instead of scaling x by L (the wound half-length in Pettet et al.), we scale the radial coordinate

r by *R*, the wound radius in our system. The characteristic length (L) in the original model described by Pettet et al. was L = 2.5 mm. The radius of the wound (R) described by our model in cylindrical coordinates is R = 5 mm. Accordingly, L is replaced with R according to R = $2L$ in the definitions of all dimensionless parameters and quantities, where applicable. The time coordinate *t* is made dimensionless in our model by scaling it by the quantity D/R^2, where D is the diffusivity of chemoattractant. The physical interpretations of all common parameters in our model are the same as those described by Pettet et al. Descriptions and values for these parameters are given in Table 4-3.

Supplemental Note 2: Conversion of Initial and Boundary Conditions

Converting the coordinate system from Cartesian coordinates to cylindrical coordinates in r requires that the initial and boundary conditions be rewritten accordingly with the wound center defined at $r = 0$ (instead of $x = L$) and the wound edge at $r = R$ (instead of $x = 0$), where R is the dimensional wound radius. For derivatives defined at the wound boundaries, x is simply substituted for r in the conversion to cylindrical coordinates. After converting to dimensionless variables, the wound center in Cartesian coordinates at $x = L$ becomes $x = 1$ after scaling x by L; similarly for r in cylindrical coordinates, the wound edge at $r = R$ becomes $r = 1$ after scaling r by R.

Dimensionless Cartesian boundary and initial conditions (from Pettet et al.)

The following are the initial and boundary conditions used in the wound healing model described by Pettet et al. It is assumed that the wound margin has penetrated an initial distance $\tilde{x}$ into the wound such that the open wound has the dimensionless width $1 - \tilde{x}$.

Initial conditions:

$$n(x,0) = \begin{cases} \frac{\hat{n}}{\tilde{x}^3}(x - \tilde{x})(2x^2 - \tilde{x}x - \tilde{x}^2), & 0 \le x \le \tilde{x} \\ 0, & \tilde{x} < x \le 1 \end{cases} \tag{20}$$

$$a(x,0) = 0, \qquad 0 \le x \le 1 \tag{21}$$

$$b(x,0) = \begin{cases} \left(\frac{\hat{b}-\tilde{b}}{\tilde{x}^3}\right)(x - \tilde{x})(2x^2 - \tilde{x}x - \tilde{x}^2) + b, & 0 \le x \le \tilde{x} \\ \tilde{b}, & \tilde{x} < x \le 1 \end{cases} \tag{22}$$

Boundary conditions:

$$n(0,t) = \hat{n}e^{-\alpha t} \qquad (23) \qquad\qquad \frac{\partial n}{\partial x}(1,t) = 0 \qquad (24)$$

$$\frac{\partial a}{\partial x}(0,t) = -\lambda_7 a(0,t)\hat{b} \qquad (25) \qquad\qquad \frac{\partial a}{\partial x}(1,t) = 0 \qquad (26)$$

$$b(0,t) = \hat{b} \qquad (27) \qquad\qquad \frac{\partial b}{\partial x}(1,t) = 0 \qquad (28)$$

Dimensionless cylindrical boundary and initial conditions

After converting to cylindrical coordinates, the above boundary and initial conditions take the forms listed below. It is again assumed that the wound margin has penetrated an initial distance R – $\tilde{r}$ such that the radius of the open wound is $\tilde{r}$.

<u>*Initial conditions:*</u>

$$n(r,0) = \begin{cases} \frac{\hat{n}}{\tilde{r}^3}(r - \tilde{r})(2r^2 - \tilde{r}r - \tilde{r}^2), & \tilde{r} < r \le 1 \\ 0, & 0 \le r \le \tilde{r} \end{cases} \qquad (29)$$

$$a(r,0) = 0, \qquad 0 \le r \le 1 \qquad (30)$$

$$b(r,0) = \begin{cases} \left(\frac{\hat{b}-\tilde{b}}{\tilde{r}^3}\right)(r - \tilde{r})(2r^2 - \tilde{r}r - \tilde{r}^2) + b, & \tilde{r} < r \le 1 \\ \tilde{b}, & 0 \le r \le \tilde{r} \end{cases} \qquad (31)$$

<u>*Boundary conditions:*</u>

$$\frac{\partial n}{\partial r}(0,t) = 0 \qquad (32) \qquad\qquad\qquad n(1,t) = \hat{n}e^{-\alpha t} \qquad (33)$$

$$\frac{\partial a}{\partial r}(0,t) = 0 \qquad (34) \qquad\qquad\qquad \frac{\partial a}{\partial r}(1,t) = -\lambda_7 a(1,t)\hat{b} \qquad (35)$$

$$\frac{\partial b}{\partial r}(0,t) = 0 \qquad (36) \qquad\qquad\qquad b(1,t) = \hat{b} \qquad (37)$$

Supplemental Note 3: Discretization Method Using Finite Differences

Forward difference method for first-order time derivatives.

First-order derivatives in time were discretized using an explicit forward finite difference formula, where $h = t_{i+1} - t_i$ is the time step size between two discretized time points, C represents the concentration of an arbitrary field variable, and λ is an arbitrary constant whose definition depends on the specific field variable being evaluated:

$$\frac{\partial C}{\partial t} = \lambda C \qquad (38)$$

$$\frac{C_{j,i+1} - C_{j,i}}{h} = \lambda C_{j,i} \qquad (39)$$

Central difference method for first-order spatial derivatives.

First-order derivatives in space were discretized using an explicit first-order central finite difference formula, where k is the spatial step size in r between two discretized spatial nodes ($k = r_{j+1} - r_j$), as follows for species C:

$$\frac{\partial C}{\partial r} = \lambda C \qquad (40)$$

$$\frac{C_{j+1,i} - C_{j-1,i}}{2k} = \lambda C_{j,i} \qquad (41)$$

Central difference method for second-order spatial derivatives. Second-order derivatives in space were discretized using an explicit second-order central finite difference formula:

$$\frac{\partial^2 C}{\partial r^2} = \lambda C \qquad (42)$$

$$\frac{C_{j+1,i} - 2C_{j,i} + C_{j-1,i}}{k^2} = \lambda C_{j,i} \qquad (43)$$

Discretization of model equations in cylindrical coordinates.

Implementation of the finite difference schemes is illustrated with the following example of discretizing the governing equation and boundary conditions for the density of capillary tips, n. Evaluating the r-component of the differential operators in cylindrical coordinates, expanding the differentials, and discretizing the result yields

$$\frac{\partial n}{\partial t} = \mu_n \left(\frac{1}{r}\frac{\partial n}{\partial r} + \frac{\partial^2 n}{\partial r^2} \right) - \chi n \left(\frac{1}{r}\frac{\partial a}{\partial r} + \frac{\partial^2 a}{\partial r^2} \right) - \chi \frac{\partial a}{\partial r}\frac{\partial n}{\partial r} + \lambda_1 ab - \lambda_2 n - \lambda_0 n^2 \qquad (44)$$

$$\frac{n_{j,i+1} - n_{j,i}}{h} = \mu_n \left(\frac{1}{r_j}\frac{n_{j+1,i} - n_{j-1,i}}{2k} + \frac{n_{j+1,i} - 2n_{j,i} + n_{j-1,i}}{k^2} \right) - \chi n \left(\frac{1}{r_j}\frac{a_{j+1,i} - a_{j-1,i}}{2k} + \frac{a_{j+1,i} - 2a_{j,i} + a_{j-1,i}}{k^2} \right) -$$
$$\chi \left(\frac{a_{j+1,i} - a_{j-1,i}}{2k} \right)\left(\frac{n_{j+1,i} - n_{j-1,i}}{2k} \right) + \lambda_1 a_{j,i} b_{j,i} - \lambda_2 n_{j,i} - \lambda_0 n_{j,i}^2 \qquad (45)$$

This discretized equation can be rearranged to solve for the dimensionless tip density n at time t_{i+1} and spatial node r_j ($n_{j,i+1}$), given that values for n are known at spatial nodes r_{j-1}, r_j, and r_{j+1} at time point t_i (represented by $n_{j-1,i}$, $n_{j,i}$, and $n_{j+1,i}$, respectively) accordingly:

$$n_{j,i+1} = \left\{ \mu_n \left(\frac{1}{r_j} \frac{n_{j+1,i} - n_{j-1,i}}{2k} + \frac{n_{j+1,i} - 2n_{j,i} + n_{j-1,i}}{k^2} \right) - \chi n \left(\frac{1}{r_j} \frac{a_{j+1,i} - a_{j-1,i}}{2k} + \frac{n_{j+1,i} - 2a_{j,i} + a_{j-1,i}}{k^2} \right) - \right.$$
$$\left. \chi \left(\frac{a_{j+1,i} - a_{j-1,i}}{2k} \right) \left(\frac{n_{j+1,i} - n_{j-1,i}}{2k} \right) + \lambda_1 a_{j,i} b_{j,i} - \lambda_2 n_{j,i} - \lambda_0 n_{j,i}^2 \right\} h + n_{j,i} \qquad (46)$$

Discretized boundary conditions. Discretization of Dirichlet boundary conditions requires relating the concentration of species of interest at time t_i to the value prescribed by the condition, as follows:

$$n(1,t) = \hat{n}e^{-\alpha t} \qquad (47)$$

$$n_{j,i} = \hat{n}e^{\alpha t_i} \qquad (48)$$

where j corresponds to the spatial node at the wound edge.

No-flux Neumann boundary conditions at the wound center require that the concentration of a given species at the boundary node be set equal to the interior node immediately adjacent to it. Thus, at the wound center:

$$\frac{\partial n}{\partial r}(0,t) = 0 \qquad (49)$$

$$\frac{n_{j+1,i} - n_{j,i}}{k} = 0 \qquad (50)$$

$$n_{j,i} = n_{j+1,i} \qquad (51)$$

where j in this case indicates the boundary node, located at the wound center.

Reactive Robin boundary conditions are similarly discretized and solved. Using the boundary condition for chemoattractant at the wound edge as an example:

$$\frac{\partial a}{\partial r}(1,t) = -\lambda_7 a(1,t)\hat{b} \qquad (52)$$

$$\frac{a_{j+1,i} - a_{j,i}}{k} = -\lambda_7 a_{j+1,i}\hat{b} \qquad (53)$$

$$a_{j+1,i} = \frac{a_{j,i}}{1 + k\lambda_7 a_{j+1,i}\hat{b}} \qquad (54)$$

where $j+1$ in this case indicates the boundary node, located at the wound edge.

Solutions to discretized model equations.

At a given time point, the partial differential equations for the field variables were discretized using the explicit finite difference method described above. The system of algebraic equations which results from discretizing over the wound space domain was then explicitly solved using the known concentrations of the field variables from the previous time point, followed by evaluating the discretized boundary conditions. The system of equations was then advanced to the next time point, and this process was repeated until the final time point was reached. The general method is summarized according to the following steps:

1) All partial differential equations were discretized using finite difference methods.

2) Concentrations of all field variables were defined for the initial time.

3) The model was advanced one time step, and the concentrations of all field variables were solved for in the bulk (i.e., everywhere except the wound center and wound edge boundaries).

4) At the same time step, the concentrations of all field variables at the wound center were solved for using the appropriate boundary conditions at $r = 0$.

5) At the same time step, the concentrations of all field variables at the wound edge were solved for using the appropriate boundary conditions at $r = 1$.

Steps 3-5 were repeated until the final time point was reached.

REFERENCES

1. Luo, J., Wu, M., Gopukumar, D. & Zhao, Y. Big Data Application in Biomedical Research and Health Care: A Literature Review. *Biomed Inform Insights* **8**, 1-10 (2016).
2. Clancy, C.E. et al. Multiscale Modeling in the Clinic: Drug Design and Development. *Ann Biomed Eng* **44**, 2591-2610 (2016).
3. Walpole, J., Papin, J.A. & Peirce, S.M. Multiscale computational models of complex biological systems. *Annu Rev Biomed Eng* **15**, 137-154 (2013).
4. Moreno, J.D. et al. A computational model to predict the effects of class I anti-arrhythmic drugs on ventricular rhythms. *Sci Transl Med* **3**, 98ra83 (2011).
5. Klank, R.L., Rosenfeld, S.S. & Odde, D.J. A Brownian dynamics tumor progression simulator with application to glioblastoma. *Converg Sci Phys Oncol* **4** (2018).
6. Vempati, P., Popel, A.S. & Mac Gabhann, F. Formation of VEGF isoform-specific spatial distributions governing angiogenesis: computational analysis. *BMC Syst Biol* **5**, 59 (2011).
7. Artel, A., Mehdizadeh, H., Chiu, Y.C., Brey, E.M. & Cinar, A. An agent-based model for the investigation of neovascularization within porous scaffolds. *Tissue Eng Part A* **17**, 2133-2141 (2011).
8. Aguado-Sierra, J. et al. Patient-specific modeling of dyssynchronous heart failure: a case study. *Prog Biophys Mol Biol* **107**, 147-155 (2011).
9. Bjornsson, B. et al. Digital twins to personalize medicine. *Genome Med* **12**, 4 (2019).
10. Gal, J. et al. Optimizing drug development in oncology by clinical trial simulation: Why and how? *Brief Bioinform* **19**, 1203-1217 (2018).
11. Brubaker, D.K. & Lauffenburger, D.A. Translating preclinical models to humans. *Science* **367**, 742-743 (2020).
12. Viceconti, M. et al. In silico trials: Verification, validation and uncertainty quantification of predictive models used in the regulatory evaluation of biomedical products. *Methods* (2020).
13. Ud-Din, S. & Bayat, A. Non-animal models of wound healing in cutaneous repair: In silico, in vitro, ex vivo, and in vivo models of wounds and scars in human skin. *Wound Repair Regen* **25**, 164-176 (2017).
14. Slayton, R.B. et al. Vital Signs: Estimated Effects of a Coordinated Approach for Action to Reduce Antibiotic-Resistant Infections in Health Care Facilities - United States. *MMWR Morb Mortal Wkly Rep* **64**, 826-831 (2015).
15. Lee, B.Y. et al. A computer simulation of vaccine prioritization, allocation, and rationing during the 2009 H1N1 influenza pandemic. *Vaccine* **28**, 4875-4879 (2010).
16. Haidari, L.A. et al. The economic and operational value of using drones to transport vaccines. *Vaccine* **34**, 4062-4067 (2016).
17. Zeigler, A.C. et al. Network model-based screen for FDA-approved drugs affecting cardiac fibrosis. *CPT Pharmacometrics Syst Pharmacol* **10**, 377-388 (2021).

REFERENCES

18. Grimm, V. et al. Pattern-oriented modeling of agent-based complex systems: lessons from ecology. *Science* **310**, 987-991 (2005).
19. Janssen, M. & Grimm, V. Individual-Based Modelling and Ecology. *Jasss-J Artif Soc S* **9** (2006).
20. Hoertel, N. et al. A stochastic agent-based model of the SARS-CoV-2 epidemic in France. *Nat Med* **26** (2020).
21. Perez, L. & Dragicevic, S. An agent-based approach for modeling dynamics of contagious disease spread. *Int J Health Geogr* **8** (2009).
22. Bonabeau, E. Agent-based modeling: Methods and techniques for simulating human systems. *P Natl Acad Sci USA* **99**, 7280-7287 (2002).
23. Reynolds, E.R., Himmelwright, R., Sanginiti, C. & Pfaffmann, J.O. An agent-based model of the Notch signaling pathway elucidates three levels of complexity in the determination of developmental patterning. *Bmc Systems Biology* **13** (2019).
24. Warsinske, H.C. et al. Computational Modeling Predicts Simultaneous Targeting of Fibroblasts and Epithelial Cells Is Necessary for Treatment of Pulmonary Fibrosis. *Front Pharmacol* **7**, 183 (2016).
25. Zeigler, A.C., Richardson, W.J., Holmes, J.W. & Saucerman, J.J. A computational model of cardiac fibroblast signaling predicts context-dependent drivers of myofibroblast differentiation. *J Mol Cell Cardiol* **94**, 72-81 (2016).
26. Rouillard, A.D. & Holmes, J.W. Mechanical regulation of fibroblast migration and collagen remodelling in healing myocardial infarcts. *J Physiol* **590**, 4585-4602 (2012).
27. Lee, J.J., Talman, L., Peirce, S.M. & Holmes, J.W. Spatial scaling in multiscale models: methods for coupling agent-based and finite-element models of wound healing. *Biomech Model Mechanobiol* (2019).
28. Walpole, J., Mac Gabhann, F., Peirce, S.M. & Chappell, J.C. Agent-based computational model of retinal angiogenesis simulates microvascular network morphology as a function of pericyte coverage. *Microcirculation* **24** (2017).
29. Thorne, B.C., Bailey, A.M. & Peirce, S.M. Combining experiments with multi-cell agent-based modeling to study biological tissue patterning. *Briefings in Bioinformatics* **8**, 245-257 (2007).
30. Travasso, R.D.M., Poire, E.C., Castro, M., Rodrguez-Manzaneque, J.C. & Hernandez-Machado, A. Tumor Angiogenesis and Vascular Patterning: A Mathematical Model. *Plos One* **6** (2011).
31. Olsen, M.M. & Siegelmann, H.T. Multiscale Agent-based Model of Tumor Angiogenesis. *Procedia Comput Sci* **18**, 1016-1025 (2013).
32. Soheilypour, M. & Mofrad, M.R.K. Agent-Based Modeling in Molecular Systems Biology. *Bioessays* **40** (2018).
33. Cilfone, N.A., Kirschner, D.E. & Linderman, J.J. Strategies for efficient numerical implementation of hybrid multi-scale agent-based models to describe biological systems. *Cell Mol Bioeng* **8**, 119-136 (2015).

REFERENCES

34.   Rouillard, A.D. & Holmes, J.W. Coupled agent-based and finite-element models for predicting scar structure following myocardial infarction. *Prog Biophys Mol Biol* **115**, 235-243 (2014).

35.   Pathmanathan, P. & Gray, R.A. Validation and Trustworthiness of Multiscale Models of Cardiac Electrophysiology. *Front Physiol* **9**, 106 (2018).

36.   El-Sayed, A.M., Scarborough, P., Seemann, L. & Galea, S. Social network analysis and agent-based modeling in social epidemiology. *Epidemiol Perspect Innov* **9**, 1 (2012).

37.   Blume, L. Agent-Based Models for Policy Analysis. *Assessing the Use of Agent-Based Models for Tobacco Regulation*, 195-215 (2015).

38.   Brainard, J., Hunter, P.R. & Hall, I.R. An agent-based model about the effects of fake news on a norovirus outbreak. *Rev Epidemiol Sante Publique* **68**, 99-107 (2020).

39.   Grauer, J., Lowen, H. & Liebchen, B. Strategic spatiotemporal vaccine distribution increases the survival rate in an infectious disease like Covid-19. *Sci Rep* **10**, 21594 (2020).

40.   Coughlin, S., Roberts, D., O'Neill, K. & Brooks, P. Looking to tomorrow's healthcare today: a participatory health perspective. *Intern Med J* **48**, 92-96 (2018).

41.   Bates, D.W., Saria, S., Ohno-Machado, L., Shah, A. & Escobar, G. Big Data In Health Care: Using Analytics To Identify And Manage High-Risk And High-Cost Patients. *Health Affair* **33**, 1123-1131 (2014).

42.   Clancy, C.M. Reducing Hospital Readmissions: Aligning Financial and Quality Incentives. *Am J Med Qual* **27**, 441-443 (2012).

43.   , Vol. 2021 (Centers for Medicare and Medicaid Services; 2020).

44.   Kocher, R.P. & Adashi, E.Y. Hospital Readmissions and the Affordable Care Act Paying for Coordinated Quality Care. *Jama-J Am Med Assoc* **306**, 1794-1795 (2011).

45.   Artetxe, A., Beristain, A. & Grana, M. Predictive models for hospital readmission risk: A systematic review of methods. *Comput Methods Programs Biomed* **164**, 49-64 (2018).

46.   Mahmoudi, E. et al. Use of electronic medical records in development and validation of risk prediction models of hospital readmission: systematic review. *Bmj-Brit Med J* **369** (2020).

47.   Chen, M., Tan, X. & Padman, R. Social determinants of health in electronic health records and their impact on analysis and risk prediction: A systematic review. *J Am Med Inform Assn* **27**, 1764-1773 (2020).

48.   Roth, G.A. et al. Global, Regional, and National Burden of Cardiovascular Diseases for 10 Causes, 1990 to 2015. *J Am Coll Cardiol* **70**, 1-25 (2017).

49.   From the Centers for Disease Control and Prevention. Ten great public health achievements--United States, 1900-1999. *JAMA* **281**, 1481 (1999).

50.   Centers for Disease, C. & Prevention Ten great public health achievements--United States, 1900-1999. *MMWR Morb Mortal Wkly Rep* **48**, 241-243 (1999).

51.   Murthy, V.H. Surgeon General's Perspectives. *Public Health Rep* **130**, 296-298 (2015).

REFERENCES

52.   From the Centers for Disease Control and Prevention. Achievements in public health, 1900-1999: fluoridation of drinking water to prevent dental caries. *JAMA* **283**, 1283-1286 (2000).

53.   Fielding, J.E. Public health in the twentieth century: advances and challenges. *Annu Rev Public Health* **20**, xiii-xxx (1999).

54.   Kannel, W.B., Gordon, T., Castelli, W.P. & Margolis, J.R. Electrocardiographic left ventricular hypertrophy and risk of coronary heart disease. The Framingham study. *Ann Intern Med* **72**, 813-822 (1970).

55.   Leichter, H.M. "Evil habits" and "personal choices": assigning responsibility for health in the 20th century. *Milbank Q* **81**, 603-626 (2003).

56.   Mills, M.C. & Rahal, C. A scientometric review of genome-wide association studies. *Commun Biol* **2**, 9 (2019).

57.   Mattick, J.S. et al. The impact of genomics on the future of medicine and health. *Med J Aust* **201**, 17-20 (2014).

58.   Cutler, D.M. Early Returns From the Era of Precision Medicine. *JAMA* **323**, 109-110 (2020).

59.   Taylor, C.A. & Figueroa, C.A. Patient-specific modeling of cardiovascular mechanics. *Annu Rev Biomed Eng* **11**, 109-134 (2009).

60.   Redaelli, A. & Votta, E. Cardiovascular patient-specific modeling: Where are we now and what does the future look like? *APL Bioeng* **4**, 040401 (2020).

61.   Meddings, J. et al. The Impact of Disability and Social Determinants of Health on Condition-Specific Readmissions beyond Medicare Risk Adjustments: A Cohort Study. *J Gen Intern Med* **32**, 71-80 (2017).

62.   Zajacova, A. & Lawrence, E.M. The Relationship Between Education and Health: Reducing Disparities Through a Contextual Approach. *Annu Rev Public Health* **39**, 273-289 (2018).

63.   Ahnquist, J., Wamala, S.P. & Lindstrom, M. Social determinants of health--a question of social or economic capital? Interaction effects of socioeconomic factors on health outcomes. *Soc Sci Med* **74**, 930-939 (2012).

64.   Braveman, P. & Gottlieb, L. The social determinants of health: it's time to consider the causes of the causes. *Public Health Rep* **129 Suppl 2**, 19-31 (2014).

65.   Hood, C.M., Gennuso, K.P., Swain, G.R. & Catlin, B.B. County Health Rankings: Relationships Between Determinant Factors and Health Outcomes. *Am J Prev Med* **50**, 129-135 (2016).

66.   (World Health Organization (WHO); 2012).

67.   Global Burden of Cardiovascular Diseases, C. et al. The Burden of Cardiovascular Diseases Among US States, 1990-2016. *JAMA Cardiol* **3**, 375-389 (2018).

68.   Roth, G.A. et al. Global Burden of Cardiovascular Diseases and Risk Factors, 1990-2019: Update From the GBD 2019 Study. *J Am Coll Cardiol* **76**, 2982-3021 (2020).

REFERENCES

69. Sidney, S. et al. Recent Trends in Cardiovascular Mortality in the United States and Public Health Goals. *JAMA Cardiol* **1**, 594-599 (2016).

70. Wang, H., Schumacher, A.E., Levitz, C.E., Mokdad, A.H. & Murray, C.J. Left behind: widening disparities for males and females in US county life expectancy, 1985-2010. *Popul Health Metr* **11**, 8 (2013).

71. Ezzati, M., Friedman, A.B., Kulkarni, S.C. & Murray, C.J. The reversal of fortunes: trends in county mortality and cross-county mortality disparities in the United States. *PLoS Med* **5**, e66 (2008).

72. Graham, G. Disparities in cardiovascular disease risk in the United States. *Curr Cardiol Rev* **11**, 238-245 (2015).

73. Benjamin, E.J. et al. Heart Disease and Stroke Statistics-2018 Update: A Report From the American Heart Association. *Circulation* **137**, e67-e492 (2018).

74. Holman, H.R. The Relation of the Chronic Disease Epidemic to the Health Care Crisis. *ACR Open Rheumatol* **2**, 167-173 (2020).

75. Leon, B.M. & Maddox, T.M. Diabetes and cardiovascular disease: Epidemiology, biological mechanisms, treatment recommendations and future research. *World J Diabetes* **6**, 1246-1258 (2015).

76. Paneni, F., Beckman, J.A., Creager, M.A. & Cosentino, F. Diabetes and vascular disease: pathophysiology, clinical consequences, and medical therapy: part I. *Eur Heart J* **34**, 2436-2443 (2013).

77. Falanga, V. Wound healing and its impairment in the diabetic foot. *Lancet* **366**, 1736-1743 (2005).

78. Han, G. & Ceilley, R. Chronic Wound Healing: A Review of Current Management and Treatments. *Adv Ther* **34**, 599-610 (2017).

79. Rodrigues, M., Kosaric, N., Bonham, C.A. & Gurtner, G.C. Wound Healing: A Cellular Perspective. *Physiol Rev* **99**, 665-706 (2019).

80. Frantz, S., Bauersachs, J. & Ertl, G. Post-infarct remodelling: contribution of wound healing and inflammation. *Cardiovasc Res* **81**, 474-481 (2009).

81. Czubryt, M.P. Common threads in cardiac fibrosis, infarct scar formation, and wound healing. *Fibrogenesis Tissue Repair* **5**, 19 (2012).

82. Sinno, H. & Prakash, S. Complements and the wound healing cascade: an updated review. *Plast Surg Int* **2013**, 146764 (2013).

83. Lambert, J.M., Lopez, E.F. & Lindsey, M.L. Macrophage roles following myocardial infarction. *Int J Cardiol* **130**, 147-158 (2008).

84. Jeffcoate, W.J., Price, P., Harding, K.G., International Working Group on Wound, H. & Treatments for People with Diabetic Foot, U. Wound healing and treatments for people with diabetic foot ulcers. *Diabetes Metab Res Rev* **20 Suppl 1**, S78-89 (2004).

85. Corliss, B.A., Azimi, M.S., Munson, J.M., Peirce, S.M. & Murfee, W.L. Macrophages: An Inflammatory Link Between Angiogenesis and Lymphangiogenesis. *Microcirculation* **23**, 95-121 (2016).

REFERENCES

86.   Bruce, A.C. et al. Monocytes are recruited from venules during arteriogenesis in the murine spinotrapezius ligation model. *Arterioscler Thromb Vasc Biol* **34**, 2012-2022 (2014).

87.   Krzyszczyk, P., Schloss, R., Palmer, A. & Berthiaume, F. The Role of Macrophages in Acute and Chronic Wound Healing and Interventions to Promote Pro-wound Healing Phenotypes. *Frontiers in Physiology* **9** (2018).

88.   Murray, P.J. Macrophage Polarization. *Annu Rev Physiol* **79**, 541-566 (2017).

89.   Ferrante, C.J. & Leibovich, S.J. Regulation of Macrophage Polarization and Wound Healing. *Adv Wound Care (New Rochelle)* **1**, 10-16 (2012).

90.   Wang, Y. et al. Mathematical modeling and stability analysis of macrophage activation in left ventricular remodeling post-myocardial infarction. *BMC Genomics* **13 Suppl 6**, S21 (2012).

91.   Martin, K.S. et al. In Silico and In Vivo Experiments Reveal M-CSF Injections Accelerate Regeneration Following Muscle Laceration. *Ann Biomed Eng* **45**, 747-760 (2017).

92.   Roe, M.T. et al. Treatments, trends, and outcomes of acute myocardial infarction and percutaneous coronary intervention. *J Am Coll Cardiol* **56**, 254-263 (2010).

93.   Bucholz, E.M. et al. Life Expectancy and Years of Potential Life Lost After Acute Myocardial Infarction by Sex and Race: A Cohort-Based Study of Medicare Beneficiaries. *J Am Coll Cardiol* **66**, 645-655 (2015).

94.   Kochar, A. et al. Long-Term Mortality of Older Patients With Acute Myocardial Infarction Treated in US Clinical Practice. *J Am Heart Assoc* **7** (2018).

95.   Fomovsky, G.M., Clark, S.A., Parker, K.M., Ailawadi, G. & Holmes, J.W. Anisotropic reinforcement of acute anteroapical infarcts improves pump function. *Circ Heart Fail* **5**, 515-522 (2012).

96.   Christman, K.L., Fok, H.H., Sievers, R.E., Fang, Q. & Lee, R.J. Fibrin glue alone and skeletal myoblasts in a fibrin scaffold preserve cardiac function after myocardial infarction. *Tissue Eng* **10**, 403-409 (2004).

97.   Ryan, L.P. et al. Dermal filler injection: a novel approach for limiting infarct expansion. *Ann Thorac Surg* **87**, 148-155 (2009).

98.   Park, S., Nguyen, N.B., Pezhouman, A. & Ardehali, R. Cardiac fibrosis: potential therapeutic targets. *Transl Res* **209**, 121-137 (2019).

99.   Lewis, G.A. et al. Pirfenidone in Heart Failure with Preserved Ejection Fraction-Rationale and Design of the PIROUETTE Trial. *Cardiovasc Drugs Ther* **33**, 461-470 (2019).

100.   Brem, H. & Tomic-Canic, M. Cellular and molecular basis of wound healing in diabetes. *J Clin Invest* **117**, 1219-1222 (2007).

101.   Raghav, A. et al. Financial burden of diabetic foot ulcers to world: a progressive topic to discuss always. *Ther Adv Endocrinol Metab* **9**, 29-31 (2018).

102.   Rosenberg, C.S. Wound healing in the patient with diabetes mellitus. *Nurs Clin North Am* **25**, 247-261 (1990).

103.   Aldana, P.C. & Khachemoune, A. Diabetic Foot Ulcers: Appraising Standard of Care and Reviewing New Trends in Management. *Am J Clin Dermatol* **21**, 255-264 (2020).

REFERENCES

104. O'Loughlin, A., McIntosh, C., Dinneen, S.F. & O'Brien, T. Review paper: basic concepts to novel therapies: a review of the diabetic foot. *Int J Low Extrem Wounds* **9**, 90-102 (2010).

105. Frykberg, R.G. & Banks, J. Management of Diabetic Foot Ulcers: A Review. *Fed Pract* **33**, 16-23 (2016).

106. Frykberg, R.G. et al. Evaluation of tissue engineering products for the management of neuropathic diabetic foot ulcers: an interim analysis. *J Wound Care* **25 Suppl 7**, S18-25 (2016).

107. Lopes, L. et al. Stem cell therapy for diabetic foot ulcers: a review of preclinical and clinical research. *Stem Cell Res Ther* **9**, 188 (2018).

108. Wietecha, M.S. & DiPietro, L.A. Therapeutic Approaches to the Regulation of Wound Angiogenesis. *Adv Wound Care (New Rochelle)* **2**, 81-86 (2013).

109. Barrientos, S., Brem, H., Stojadinovic, O. & Tomic-Canic, M. Clinical application of growth factors and cytokines in wound healing. *Wound Repair Regen* **22**, 569-578 (2014).

110. Zubair, M. & Ahmad, J. Role of growth factors and cytokines in diabetic foot ulcer healing: A detailed review. *Rev Endocr Metab Disord* **20**, 207-217 (2019).

111. Jin, Y.F., Han, H.C., Berger, J., Dai, Q. & Lindsey, M.L. Combining experimental and mathematical modeling to reveal mechanisms of macrophage-dependent left ventricular remodeling. *BMC Syst Biol* **5**, 60 (2011).

112. Hao, W., Rovin, B.H. & Friedman, A. Mathematical model of renal interstitial fibrosis. *Proc Natl Acad Sci U S A* **111**, 14193-14198 (2014).

113. Hao, W., Marsh, C. & Friedman, A. A Mathematical Model of Idiopathic Pulmonary Fibrosis. *PLoS One* **10**, e0135097 (2015).

114. Pettet, G.J., Byrne, H.M., McElwain, D.L. & Norbury, J. A model of wound-healing angiogenesis in soft tissue. *Math Biosci* **136**, 35-63 (1996).

115. Virgilio, K.M., Martin, K.S., Peirce, S.M. & Blemker, S.S. Agent-based model illustrates the role of the microenvironment in regeneration in healthy and mdx skeletal muscle. *J Appl Physiol (1985)* **125**, 1424-1439 (2018).

116. Dutta-Moscato, J. et al. A Multiscale Agent-Based in silico Model of Liver Fibrosis Progression. *Front Bioeng Biotechnol* **2**, 18 (2014).

117. Nim, H.T. et al. CARFMAP: A Curated Pathway Map of Cardiac Fibroblasts. *PLoS One* **10**, e0143274 (2015).

118. Zeigler, A.C., Richardson, W.J., Holmes, J.W. & Saucerman, J.J. Computational modeling of cardiac fibroblasts and fibrosis. *J Mol Cell Cardiol* **93**, 73-83 (2016).

119. Ma, Y., Iyer, R.P., Jung, M., Czubryt, M.P. & Lindsey, M.L. Cardiac Fibroblast Activation Post-Myocardial Infarction: Current Knowledge Gaps. *Trends Pharmacol Sci* **38**, 448-458 (2017).

120. Spinale, F.G. et al. Crossing Into the Next Frontier of Cardiac Extracellular Matrix Research. *Circ Res* **119**, 1040-1045 (2016).

121. Mouton, A.J. et al. Fibroblast polarization over the myocardial infarction time continuum shifts roles from inflammation to angiogenesis. *Basic Res Cardiol* **114**, 6 (2019).

122. Chen, W. & Frangogiannis, N.G. Fibroblasts in post-infarction inflammation and cardiac repair. *Biochim Biophys Acta* **1833**, 945-953 (2013).

123. Fix, C., Bingham, K. & Carver, W. Effects of interleukin-18 on cardiac fibroblast function and gene expression. *Cytokine* **53**, 19-28 (2011).

124. Turner, N.A. Effects of interleukin-1 on cardiac fibroblast function: relevance to post-myocardial infarction remodelling. *Vascul Pharmacol* **60**, 1-7 (2014).

125. Fredj, S. et al. Role of interleukin-6 in cardiomyocyte/cardiac fibroblast interactions during myocyte hypertrophy and fibroblast proliferation. *J Cell Physiol* **204**, 428-436 (2005).

126. Clarke, S.A., Richardson, W.J. & Holmes, J.W. Modifying the mechanics of healing infarcts: Is better the enemy of good? *J Mol Cell Cardiol* **93**, 115-124 (2016).

127. Hammerman, H., Kloner, R.A., Hale, S., Schoen, F.J. & Braunwald, E. Dose-dependent effects of short-term methylprednisolone on myocardial infarct extent, scar formation, and ventricular function. *Circulation* **68**, 446-452 (1983).

128. Hammerman, H. et al. Indomethacin-induced scar thinning after experimental myocardial infarction. *Circulation* **67**, 1290-1295 (1983).

129. Brown, E.J., Jr. et al. Scar thinning due to ibuprofen administration after experimental myocardial infarction. *Am J Cardiol* **51**, 877-883 (1983).

130. An, G., Mi, Q., Dutta-Moscato, J. & Vodovotz, Y. Agent-based models in translational systems biology. *Wiley Interdiscip Rev Syst Biol Med* **1**, 159-171 (2009).

131. Horiguchi, M., Ota, M. & Rifkin, D.B. Matrix control of transforming growth factor-beta function. *J Biochem* **152**, 321-329 (2012).

132. Azghani, A.O. et al. Mechanism of fibroblast inflammatory responses to Pseudomonas aeruginosa elastase. *Microbiology* **160**, 547-555 (2014).

133. Enriquez-de-Salamanca, A. et al. Cytokine responses by conjunctival epithelial cells: an in vitro model of ocular inflammation. *Cytokine* **44**, 160-167 (2008).

134. Baran, P. et al. The balance of interleukin (IL)-6, IL-6.soluble IL-6 receptor (sIL-6R), and IL-6.sIL-6R.sgp130 complexes allows simultaneous classic and trans-signaling. *J Biol Chem* **293**, 6762-6775 (2018).

135. Dower, S.K. et al. Detection and characterization of high affinity plasma membrane receptors for human interleukin 1. *J Exp Med* **162**, 501-515 (1985).

136. Issafras, H., Corbin, J.A., Goldfine, I.D. & Roell, M.K. Detailed mechanistic analysis of gevokizumab, an allosteric anti-IL-1beta antibody with differential receptor-modulating properties. *J Pharmacol Exp Ther* **348**, 202-215 (2014).

137. Grell, M., Wajant, H., Zimmermann, G. & Scheurich, P. The type 1 receptor (CD120a) is the high-affinity receptor for soluble tumor necrosis factor. *Proc Natl Acad Sci U S A* **95**, 570-575 (1998).

REFERENCES

138.   Fallahi-Sichani, M., Schaller, M.A., Kirschner, D.E., Kunkel, S.L. & Linderman, J.J. Identification of key processes that control tumor necrosis factor availability in a tuberculosis granuloma. *PLoS Comput Biol* **6**, e1000778 (2010).

139.   Wakefield, L.M., Smith, D.M., Masui, T., Harris, C.C. & Sporn, M.B. Distribution and modulation of the cellular receptor for transforming growth factor-beta. *J Cell Biol* **105**, 965-975 (1987).

140.   Maeda, S., Dean, D.D., Gomez, R., Schwartz, Z. & Boyan, B.D. The first stage of transforming growth factor beta1 activation is release of the large latent complex from the extracellular matrix of growth plate chondrocytes by matrix vesicle stromelysin-1 (MMP-3). *Calcif Tissue Int* **70**, 54-65 (2002).

141.   Hawinkels, L.J. et al. Tissue level, activation and cellular localisation of TGF-beta1 and association with survival in gastric cancer patients. *Br J Cancer* **97**, 398-404 (2007).

142.   Campaner, A.B. et al. Upregulation of TGF-beta1 expression may be necessary but is not sufficient for excessive scarring. *J Invest Dermatol* **126**, 1168-1176 (2006).

143.   Bolivar, S. et al. Lipopolysaccharide Activates Toll-Like Receptor 4 and Prevents Cardiac Fibroblast-to-Myofibroblast Differentiation. *Cardiovasc Toxicol* **17**, 458-470 (2017).

144.   Cartledge, J.E. et al. Functional crosstalk between cardiac fibroblasts and adult cardiomyocytes by soluble mediators. *Cardiovasc Res* **105**, 260-270 (2015).

145.   Campbell, S.E. & Katwa, L.C. Angiotensin II stimulated expression of transforming growth factor-beta1 in cardiac fibroblasts and myofibroblasts. *J Mol Cell Cardiol* **29**, 1947-1958 (1997).

146.   Rollins, B.J. et al. Environment-dependent growth inhibition of human epidermal keratinocytes by recombinant human transforming growth factor-beta. *J Cell Physiol* **139**, 455-462 (1989).

147.   Hazuda, D.J., Lee, J.C. & Young, P.R. The kinetics of interleukin 1 secretion from activated monocytes. Differences between interleukin 1 alpha and interleukin 1 beta. *J Biol Chem* **263**, 8473-8479 (1988).

148.   Friedman, A. & Siewe, N. Chronic hepatitis B virus and liver fibrosis: A mathematical model. *PLoS One* **13**, e0195037 (2018).

149.   Turner, N.A. et al. Mechanism of TNFalpha-induced IL-1alpha, IL-1beta and IL-6 expression in human cardiac fibroblasts: effects of statins and thiazolidinediones. *Cardiovasc Res* **76**, 81-90 (2007).

150.   Ancey, C. et al. Secretion of IL-6, IL-11 and LIF by human cardiomyocytes in primary culture. *Cytokine* **18**, 199-205 (2002).

151.   Turner, N.A. et al. Interleukin-1alpha stimulates proinflammatory cytokine expression in human cardiac myofibroblasts. *Am J Physiol Heart Circ Physiol* **297**, H1117-1127 (2009).

152.   Gerhartz, C. et al. Biosynthesis and half-life of the interleukin-6 receptor and its signal transducer gp130. *Eur J Biochem* **223**, 265-274 (1994).

153. Zahn, G. & Greischel, A. Pharmacokinetics of tumor necrosis factor alpha after intravenous administration in rats. Dose dependence and influence of tumor necrosis factor beta. *Arzneimittelforschung* **39**, 1180-1182 (1989).

154. Fomovsky, G.M. & Holmes, J.W. Evolution of scar structure, mechanics, and ventricular function after myocardial infarction in the rat. *Am J Physiol Heart Circ Physiol* **298**, H221-228 (2010).

155. MacKenna, D.A., Omens, J.H., McCulloch, A.D. & Covell, J.W. Contribution of collagen matrix to passive left ventricular mechanics in isolated rat hearts. *Am J Physiol* **266**, H1007-1018 (1994).

156. Carpenter AE, J.T., Lamprecht MR, Clarke C, Kang IH, Friman O, Guertin DA, Chang JH, Lindquist RA, Moffat J, Golland P, Sabatini DM CellProfiler: Image analysis software for identifying and quantifying cell phenotypes. *Genome Biology* **7** (2006).

157. Mia, M.M., Boersema, M. & Bank, R.A. Interleukin-1beta attenuates myofibroblast formation and extracellular matrix production in dermal and lung fibroblasts exposed to transforming growth factor-beta1. *PLoS One* **9**, e91559 (2014).

158. Perez-Rodriguez, S., Tomas-Gonzalez, E. & Garcia-Aznar, J.M. 3D Cell Migration Studies for Chemotaxis on Microfluidic-Based Chips: A Comparison between Cardiac and Dermal Fibroblasts. *Bioengineering (Basel)* **5** (2018).

159. Ware, M.F., Wells, A. & Lauffenburger, D.A. Epidermal growth factor alters fibroblast migration speed and directional persistence reciprocally and in a matrix-dependent manner. *J Cell Sci* **111 (Pt 16)**, 2423-2432 (1998).

160. Chen, M.M., Lam, A., Abraham, J.A., Schreiner, G.F. & Joly, A.H. CTGF expression is induced by TGF- beta in cardiac fibroblasts and cardiac myocytes: a potential role in heart fibrosis. *J Mol Cell Cardiol* **32**, 1805-1819 (2000).

161. Reed, M.J., Vernon, R.B., Abrass, I.B. & Sage, E.H. TGF-beta 1 induces the expression of type I collagen and SPARC, and enhances contraction of collagen gels, by fibroblasts from young and aged donors. *J Cell Physiol* **158**, 169-179 (1994).

162. Thannickal, V.J. et al. Myofibroblast differentiation by transforming growth factor-beta1 is dependent on cell adhesion and integrin signaling via focal adhesion kinase. *J Biol Chem* **278**, 12384-12389 (2003).

163. Friedman, A. & Hao, W. Mathematical modeling of liver fibrosis. *Math Biosci Eng* **14**, 143-164 (2017).

164. Figueredo, G.P., Siebers, P.O., Owen, M.R., Reps, J. & Aickelin, U. Comparing stochastic differential equations and agent-based modelling and simulation for early-stage cancer. *PLoS One* **9**, e95150 (2014).

165. Warsinske, H.C., DiFazio, R.M., Linderman, J.J., Flynn, J.L. & Kirschner, D.E. Identifying mechanisms driving formation of granuloma-associated fibrosis during Mycobacterium tuberculosis infection. *J Theor Biol* **429**, 1-17 (2017).

REFERENCES

166.   Bailey, A.M., Lawrence, M.B., Shang, H., Katz, A.J. & Peirce, S.M. Agent-based model of therapeutic adipose-derived stromal cell trafficking during ischemia predicts ability to roll on P-selectin. *PLoS Comput Biol* **5**, e1000294 (2009).

167.   Bailey, A.M., Thorne, B.C. & Peirce, S.M. Multi-cell agent-based simulation of the microvasculature to study the dynamics of circulating inflammatory cell trafficking. *Ann Biomed Eng* **35**, 916-936 (2007).

168.   Stern, J.R., Christley, S., Zaborina, O., Alverdy, J.C. & An, G. Integration of TGF-beta- and EGFR-based signaling pathways using an agent-based model of epithelial restitution. *Wound Repair Regen* **20**, 862-871 (2012).

169.   Loftis, M.J., Sexton, D. & Carver, W. Effects of collagen density on cardiac fibroblast behavior and gene expression. *J Cell Physiol* **196**, 504-511 (2003).

170.   van Spreeuwel, A.C.C. et al. Mimicking Cardiac Fibrosis in a Dish: Fibroblast Density Rather than Collagen Density Weakens Cardiomyocyte Function. *J Cardiovasc Transl Res* **10**, 116-127 (2017).

171.   Fomovsky, G.M., Rouillard, A.D. & Holmes, J.W. Regional mechanics determine collagen fiber structure in healing myocardial infarcts. *J Mol Cell Cardiol* **52**, 1083-1090 (2012).

172.   Martin, K.S., Virgilio, K.M., Peirce, S.M. & Blemker, S.S. Computational Modeling of Muscle Regeneration and Adaptation to Advance Muscle Tissue Regeneration Strategies. *Cells Tissues Organs* **202**, 250-266 (2016).

173.   Keeley, E.C., Boura, J.A. & Grines, C.L. Primary angioplasty versus intravenous thrombolytic therapy for acute myocardial infarction: a quantitative review of 23 randomised trials. *Lancet* **361**, 13-20 (2003).

174.   Nielsen, P.H. et al. Primary angioplasty versus fibrinolysis in acute myocardial infarction: long-term follow-up in the Danish acute myocardial infarction 2 trial. *Circulation* **121**, 1484-1491 (2010).

175.   Velagaleti, R.S. et al. Long-term trends in the incidence of heart failure after myocardial infarction. *Circulation* **118**, 2057-2062 (2008).

176.   Chen, J., Hsieh, A.F., Dharmarajan, K., Masoudi, F.A. & Krumholz, H.M. National trends in heart failure hospitalization after acute myocardial infarction for Medicare beneficiaries: 1998-2010. *Circulation* **128**, 2577-2584 (2013).

177.   O'Gara, P.T. et al. 2013 ACCF/AHA guideline for the management of ST-elevation myocardial infarction: executive summary: a report of the American College of Cardiology Foundation/American Heart Association Task Force on Practice Guidelines: developed in collaboration with the American College of Emergency Physicians and Society for Cardiovascular Angiography and Interventions. *Catheter Cardiovasc Interv* **82**, E1-27 (2013).

178.   Peet, C., Ivetic, A., Bromage, D.I. & Shah, A.M. Cardiac monocytes and macrophages after myocardial infarction. *Cardiovasc Res* **116**, 1101-1112 (2020).

REFERENCES

179. Lindsey, M.L., Saucerman, J.J. & DeLeon-Pennell, K.Y. Knowledge gaps to understanding cardiac macrophage polarization following myocardial infarction. *Biochim Biophys Acta* **1862**, 2288-2292 (2016).

180. Ma, Y., Mouton, A.J. & Lindsey, M.L. Cardiac macrophage biology in the steady-state heart, the aging heart, and following myocardial infarction. *Transl Res* **191**, 15-28 (2018).

181. Yan, X. et al. Temporal dynamics of cardiac immune cell accumulation following acute myocardial infarction. *J Mol Cell Cardiol* **62**, 24-35 (2013).

182. Mills, C.D., Kincaid, K., Alt, J.M., Heilman, M.J. & Hill, A.M. M-1/M-2 macrophages and the Th1/Th2 paradigm. *J Immunol* **164**, 6166-6173 (2000).

183. Stein, M., Keshav, S., Harris, N. & Gordon, S. Interleukin 4 potently enhances murine macrophage mannose receptor activity: a marker of alternative immunologic macrophage activation. *J Exp Med* **176**, 287-292 (1992).

184. Nathan, C.F., Murray, H.W., Wiebe, M.E. & Rubin, B.Y. Identification of interferon-gamma as the lymphokine that activates human macrophage oxidative metabolism and antimicrobial activity. *J Exp Med* **158**, 670-689 (1983).

185. Mouton, A.J. et al. Mapping macrophage polarization over the myocardial infarction time continuum. *Basic Res Cardiol* **113**, 26 (2018).

186. Walter, W. et al. Deciphering the Dynamic Transcriptional and Post-transcriptional Networks of Macrophages in the Healthy Heart and after Myocardial Injury. *Cell Rep* **23**, 622-636 (2018).

187. Korenczuk, C.E., Barocas, V.H. & Richardson, W.J. Effects of Collagen Heterogeneity on Myocardial Infarct Mechanics in a Multiscale Fiber Network Model. *J Biomech Eng* (2019).

188. Caggiano, L.R., Lee, J.J. & Holmes, J.W. Surgical reinforcement alters collagen alignment and turnover in healing myocardial infarcts. *Am J Physiol Heart Circ Physiol* **315**, H1041-H1050 (2018).

189. Richardson, W.J. & Holmes, J.W. Emergence of Collagen Orientation Heterogeneity in Healing Infarcts and an Agent-Based Model. *Biophys J* **110**, 2266-2277 (2016).

190. Nair, A.R. et al. Reperfused hemorrhagic myocardial infarction in rats. *PLoS One* **15**, e0243207 (2020).

191. Italiani, P. & Boraschi, D. From Monocytes to M1/M2 Macrophages: Phenotypical vs. Functional Differentiation. *Front Immunol* **5**, 514 (2014).

192. Yu, T. et al. Enhanced Activity of the Macrophage M1/M2 Phenotypes and Phenotypic Switch to M1 in Periodontal Infection. *J Periodontol* **87**, 1092-1102 (2016).

193. Armulik, A., Genove, G. & Betsholtz, C. Pericytes: developmental, physiological, and pathological perspectives, problems, and promises. *Dev Cell* **21**, 193-215 (2011).

194. Ray, H.C. et al. Myh11+ microvascular mural cells and derived mesenchymal stem cells promote retinal fibrosis. *Sci Rep* **10**, 15808 (2020).

195. Quijada, P., Trembley, M.A. & Small, E.M. The Role of the Epicardium During Heart Development and Repair. *Circ Res* **126**, 377-394 (2020).

196. Iyer, D. et al. Robust derivation of epicardium and its differentiated smooth muscle cell progeny from human pluripotent stem cells. *Development* **142**, 1528-1541 (2015).

197. Rao, K.S. & Spees, J.L. Harnessing Epicardial Progenitor Cells and Their Derivatives for Rescue and Repair of Cardiac Tissue After Myocardial Infarction. *Curr Mol Biol Rep* **3**, 149-158 (2017).

198. Smits, A.M., Dronkers, E. & Goumans, M.J. The epicardium as a source of multipotent adult cardiac progenitor cells: Their origin, role and fate. *Pharmacol Res* **127**, 129-140 (2018).

199. Klopsch, C. et al. Cardiac Mesenchymal Stem Cells Proliferate Early in the Ischemic Heart. *Eur Surg Res* **58**, 341-353 (2017).

200. Miquerol, L. et al. Endothelial plasticity drives arterial remodeling within the endocardium after myocardial infarction. *Circ Res* **116**, 1765-1771 (2015).

201. Zhang, H., Lui, K.O. & Zhou, B. Endocardial Cell Plasticity in Cardiac Development, Diseases and Regeneration. *Circ Res* **122**, 774-789 (2018).

202. Talman, V. & Ruskoaho, H. Cardiac fibrosis in myocardial infarction-from repair and remodeling to regeneration. *Cell Tissue Res* **365**, 563-581 (2016).

203. Jugdutt, B.I. Ventricular remodeling after infarction and the extracellular collagen matrix: when is enough enough? *Circulation* **108**, 1395-1403 (2003).

204. Feneley, M.P., Chang, V.P. & O'Rourke, M.F. Myocardial rupture after acute myocardial infarction. Ten year review. *Br Heart J* **49**, 550-556 (1983).

205. Shamshad, F. et al. Fatal myocardial rupture after acute myocardial infarction complicated by heart failure, left ventricular dysfunction, or both: the VALsartan In Acute myocardial iNfarcTion Trial (VALIANT). *Am Heart J* **160**, 145-151 (2010).

206. Nahrendorf, M. et al. The healing myocardium sequentially mobilizes two monocyte subsets with divergent and complementary functions. *J Exp Med* **204**, 3037-3047 (2007).

207. Hilgendorf, I. et al. Ly-6Chigh monocytes depend on Nr4a1 to balance both inflammatory and reparative phases in the infarcted myocardium. *Circ Res* **114**, 1611-1622 (2014).

208. Zhuang, L., Lu, L., Zhang, R., Chen, K. & Yan, X. Comprehensive Integration of Single-Cell Transcriptional Profiling Reveals the Heterogeneities of Non-cardiomyocytes in Healthy and Ischemic Hearts. *Front Cardiovasc Med* **7**, 615161 (2020).

209. Chakarov, S. et al. Two distinct interstitial macrophage populations coexist across tissues in specific subtissular niches. *Science* **363** (2019).

210. Panizzi, P. et al. Impaired infarct healing in atherosclerotic mice with Ly-6C(hi) monocytosis. *J Am Coll Cardiol* **55**, 1629-1638 (2010).

211. Maekawa, Y. et al. Prognostic significance of peripheral monocytosis after reperfused acute myocardial infarction:a possible role for left ventricular remodeling. *J Am Coll Cardiol* **39**, 241-246 (2002).

212. Dick, S.A. et al. Self-renewing resident cardiac macrophages limit adverse remodeling following myocardial infarction. *Nat Immunol* **20**, 29-39 (2019).

213. Shiraishi, M. et al. Alternatively activated macrophages determine repair of the infarcted adult murine heart. *J Clin Invest* **126**, 2151-2166 (2016).

214. Sager, H.B. et al. Targeting Interleukin-1beta Reduces Leukocyte Production After Acute Myocardial Infarction. *Circulation* **132**, 1880-1890 (2015).

215. Ridker, P.M. et al. Antiinflammatory Therapy with Canakinumab for Atherosclerotic Disease. *N Engl J Med* **377**, 1119-1131 (2017).

216. Yang, J.H. & Saucerman, J.J. Computational models reduce complexity and accelerate insight into cardiac signaling networks. *Circ Res* **108**, 85-97 (2011).

217. Liu, X. et al. Network Analysis Reveals a Distinct Axis of Macrophage Activation in Response to Conflicting Inflammatory Cues. *J Immunol* **206**, 883-891 (2021).

218. Zeigler, A.C. et al. Computational model predicts paracrine and intracellular drivers of fibroblast phenotype after myocardial infarction. *Matrix Biol* **91-92**, 136-151 (2020).

219. Zaman, R., Hamidzada, H. & Epelman, S. Exploring cardiac macrophage heterogeneity in the healthy and diseased myocardium. *Curr Opin Immunol* **68**, 54-63 (2021).

220. Tarbit, E., Singh, I., Peart, J.N. & Rose'Meyer, R.B. Biomarkers for the identification of cardiac fibroblast and myofibroblast cells. *Heart Fail Rev* **24**, 1-15 (2019).

221. Ivey, M.J. & Tallquist, M.D. Defining the Cardiac Fibroblast. *Circ J* **80**, 2269-2276 (2016).

222. Fu, X., Liu, Q., Li, C., Li, Y. & Wang, L. Cardiac Fibrosis and Cardiac Fibroblast Lineage-Tracing: Recent Advances. *Front Physiol* **11**, 416 (2020).

223. Sun, N. et al. Modified VEGF-A mRNA induces sustained multifaceted microvascular response and accelerates diabetic wound healing. *Sci Rep* **8**, 17509 (2018).

224. Ko, J. et al. Comparison of EGF with VEGF non-viral gene therapy for cutaneous wound healing of streptozotocin diabetic mice. *Diabetes Metab J* **35**, 226-235 (2011).

225. Brem, H. et al. Mechanism of sustained release of vascular endothelial growth factor in accelerating experimental diabetic healing. *J Invest Dermatol* **129**, 2275-2287 (2009).

226. Hanft, J.R. et al. Phase I trial on the safety of topical rhVEGF on chronic neuropathic diabetic foot ulcers. *J Wound Care* **17**, 30-32, 34-37 (2008).

227. Peirce, S.M. Computational and mathematical modeling of angiogenesis. *Microcirculation* **15**, 739-751 (2008).

228. Fuhr, M.J. et al. A modeling approach to study the effect of cell polarization on keratinocyte migration. *PLoS One* **10**, e0117676 (2015).

229. Andasari, V. et al. Computational model of wound healing: EGF secreted by fibroblasts promotes delayed re-epithelialization of epithelial keratinocytes. *Integr Biol (Camb)* **10**, 605-634 (2018).

230. Safferling, K. et al. Wound healing revised: a novel reepithelialization mechanism revealed by in vitro and in silico models. *J Cell Biol* **203**, 691-709 (2013).

231. Sun, T., Adra, S., Smallwood, R., Holcombe, M. & MacNeil, S. Exploring hypotheses of the actions of TGF-beta1 in epidermal wound healing using a 3D computational multiscale model of the human epidermis. *PLoS One* **4**, e8515 (2009).

232. Menke, N.B. et al. An in silico approach to the analysis of acute wound healing. *Wound Repair Regen* **18**, 105-113 (2010).

233. Staddon, M.F. et al. Cooperation of dual modes of cell motility promotes epithelial stress relaxation to accelerate wound healing. *PLoS Comput Biol* **14**, e1006502 (2018).

234. Nagaraja, S., Chen, L., DiPietro, L.A., Reifman, J. & Mitrophanov, A.Y. Predictive Approach Identifies Molecular Targets and Interventions to Restore Angiogenesis in Wounds With Delayed Healing. *Front Physiol* **10**, 636 (2019).

235. Almquist, J. et al. Model-Based Analysis Reveals a Sustained and Dose-Dependent Acceleration of Wound Healing by VEGF-A mRNA (AZD8601). *CPT Pharmacometrics Syst Pharmacol* **9**, 384-394 (2020).

236. Stokes, C.L., Rupnick, M.A., Williams, S.K. & Lauffenburger, D.A. Chemotaxis of human microvessel endothelial cells in response to acidic fibroblast growth factor. *Lab Invest* **63**, 657-668 (1990).

237. Braga, J., McNally, J.G. & Carmo-Fonseca, M. A reaction-diffusion model to study RNA motion by quantitative fluorescence recovery after photobleaching. *Biophys J* **92**, 2694-2703 (2007).

238. Wu, B., Eliscovich, C., Yoon, Y.J. & Singer, R.H. Translation dynamics of single mRNAs in live cells and neurons. *Science* **352**, 1430-1435 (2016).

239. Katz, Z.B. et al. Mapping translation 'hot-spots' in live cells by tracking single molecules of mRNA and ribosomes. *Elife* **5** (2016).

240. Wong, V.W., Sorkin, M., Glotzbach, J.P., Longaker, M.T. & Gurtner, G.C. Surgical approaches to create murine models of human wound healing. *J Biomed Biotechnol* **2011**, 969618 (2011).

241. Pehrsson, S., Holtta, M., Linhardt, G., Danielson, R.F. & Carlsson, L. Rapid Production of Human VEGF-A following Intradermal Injection of Modified VEGF-A mRNA Demonstrated by Cutaneous Microdialysis in the Rabbit and Pig In Vivo. *Biomed Res Int* **2019**, 3915851 (2019).

242. Waugh, H.V. & Sherratt, J.A. Modeling the effects of treating diabetic wounds with engineered skin substitutes. *Wound Repair Regen* **15**, 556-565 (2007).

243. Flegg, J.A., McElwain, D.L., Byrne, H.M. & Turner, I.W. A three species model to simulate application of Hyperbaric Oxygen Therapy to chronic wounds. *PLoS Comput Biol* **5**, e1000451 (2009).

244. Gatenby, R.A., Silva, A.S., Gillies, R.J. & Frieden, B.R. Adaptive therapy. *Cancer Res* **69**, 4894-4903 (2009).

245. Enriquez-Navas, P.M. et al. Exploiting evolutionary principles to prolong tumor control in preclinical models of breast cancer. *Sci Transl Med* **8**, 327ra324 (2016).

246. Gallaher, J.A., Enriquez-Navas, P.M., Luddy, K.A., Gatenby, R.A. & Anderson, A.R.A. Spatial Heterogeneity and Evolutionary Dynamics Modulate Time to Recurrence in Continuous and Adaptive Cancer Therapies. *Cancer Res* **78**, 2127-2139 (2018).

247. Offeddu, G.S., Mohee, L. & Cameron, R.E. Scale and structure dependent solute diffusivity within microporous tissue engineering scaffolds. *J Mater Sci Mater Med* **31**, 46 (2020).

248. Stylianopoulos, T. et al. Diffusion of particles in the extracellular matrix: the effect of repulsive electrostatic interactions. *Biophys J* **99**, 1342-1349 (2010).

249. Cross, S.E. & Roberts, M.S. Defining a model to predict the distribution of topically applied growth factors and other solutes in excisional full-thickness wounds. *J Invest Dermatol* **112**, 36-41 (1999).

250. Wang, W., Lu, K.J., Yu, C.H., Huang, Q.L. & Du, Y.Z. Nano-drug delivery systems in wound treatment and skin regeneration. *J Nanobiotechnology* **17**, 82 (2019).

251. Saghazadeh, S. et al. Drug delivery systems and materials for wound healing applications. *Adv Drug Deliv Rev* **127**, 138-166 (2018).

252. Ozdemir, D. & Feinberg, M.W. MicroRNAs in diabetic wound healing: Pathophysiology and therapeutic opportunities. *Trends Cardiovasc Med* **29**, 131-137 (2019).

253. Lee, P. & Wolgemuth, C.W. Crawling cells can close wounds without purse strings or signaling. *PLoS Comput Biol* **7**, e1002007 (2011).

254. Ziraldo, C. et al. A Computational, Tissue-Realistic Model of Pressure Ulcer Formation in Individuals with Spinal Cord Injury. *PLoS Comput Biol* **11**, e1004309 (2015).

255. Ziraldo, C., Mi, Q., An, G. & Vodovotz, Y. Computational Modeling of Inflammation and Wound Healing. *Adv Wound Care (New Rochelle)* **2**, 527-537 (2013).

256. Bowden, L.G. et al. An ordinary differential equation model for full thickness wounds and the effects of diabetes. *J Theor Biol* **361**, 87-100 (2014).

257. Okonkwo, U.A. & DiPietro, L.A. Diabetes and Wound Angiogenesis. *Int J Mol Sci* **18** (2017).

258. Zimny, S., Schatz, H. & Pfohl, M. Determinants and estimation of healing times in diabetic foot ulcers. *J Diabetes Complications* **16**, 327-332 (2002).

259. Martin, A.B., Hartman, M., Lassman, D., Catlin, A. & National Health Expenditure Accounts, T. National Health Care Spending In 2019: Steady Growth For The Fourth Consecutive Year. *Health Aff (Millwood)* **40**, 14-24 (2021).

260. Papanicolas, I., Woskie, L.R., Orlander, D., Orav, E.J. & Jha, A.K. The Relationship Between Health Spending And Social Spending In High-Income Countries: How Does The US Compare? *Health Aff (Millwood)* **38**, 1567-1575 (2019).

261. Schneider, E.C., Sarnak, D.O., Squires, D., Shah, A., Doty, M.M. Mirror, mirror 2017: International comparison reflects flaws and opportunities for better U.S. health care. *The Commonwealth Fund* (2017).

262. Turrentine, F.E., Buckley, P.J., Sohn, M.W. & Williams, M.D. Travel Time Influences Readmission Risk: Geospatial Mapping of Surgical Readmissions. *Am Surg* **83**, 573-582 (2017).

263. Getz, K.D. et al. Neighborhood education status drives racial disparities in clinical outcomes in PPCM. *Am Heart J* (2021).

264. Ma, C.T., Gee, L. & Kushel, M.B. Associations between housing instability and food insecurity with health care access in low-income children. *Ambul Pediatr* **8**, 50-57 (2008).

265. Telfair, J. & Shelton, T.L. Educational attainment as a social determinant of health. *N C Med J* **73**, 358-365 (2012).

266. Dube, S.R., Felitti, V.J., Dong, M., Giles, W.H. & Anda, R.F. The impact of adverse childhood experiences on health problems: evidence from four birth cohorts dating back to 1900. *Prev Med* **37**, 268-277 (2003).

267. Bonomi, A.E., Anderson, M.L., Rivara, F.P. & Thompson, R.S. Health care utilization and costs associated with physical and nonphysical-only intimate partner violence. *Health Serv Res* **44**, 1052-1067 (2009).

268. Warhover, A. (Health Affairs, 2014).

269. Magnan, S. Social determinants of health 101 for health care: five plus five. *NAM Perspectives* (2017).

270. Alderwick, H. & Gottlieb, L.M. Meanings and Misunderstandings: A Social Determinants of Health Lexicon for Health Care Systems. *Milbank Q* **97**, 407-419 (2019).

271. Molfenter, T.D., Bhattacharya, A. & Gustafson, D.H. The roles of past behavior and health beliefs in predicting medication adherence to a statin regimen. *Patient Prefer Adher* **6**, 643-650 (2012).

272. Takahashi, P.Y. et al. Health behaviors and quality of life predictors for risk of hospitalization in an electronic health record-linked biobank. *Int J Gen Med* **8**, 247-254 (2015).

273. Billioux, A., K. Verlander, S. Anthony, and D. Alley. Standardized Screening for Health-Related Social Needs in Clinical Settings. The accountable health communities screening tool. *National Academy of Medicine* (2017).

274. Thomas-Henkel, C., Schulman, M. (Center for Health Care Strategies, Inc., 2017).

275. in Capturing Social and Behavioral Domains and Measures in Electronic Health Records: Phase 2 (Washington (DC); 2015).

276. Navathe, A.S. et al. Hospital Readmission and Social Risk Factors Identified from Physician Notes. *Health Serv Res* **53**, 1110-1136 (2018).

277. Vest, J.R. & Ben-Assuli, O. Prediction of emergency department revisits using area-level social determinants of health measures and health information exchange information. *Int J Med Inform* **129**, 205-210 (2019).

278. Pines, J.M., Mullins, P.M., Cooper, J.K., Feng, L.B. & Roth, K.E. National trends in emergency department use, care patterns, and quality of care of older adults in the United States. *J Am Geriatr Soc* **61**, 12-17 (2013).

279. Naouri, D. et al. Factors associated with inappropriate use of emergency departments: findings from a cross-sectional national study in France. *BMJ Qual Saf* **29**, 449-464 (2020).

280. Ward, C., Patel, V., Elsaid, M.I., Jaisinghani, P. & Sharma, R. A case-control study of length of stay outliers. *Am J Manag Care* **27**, e66-e71 (2021).

281. McCormick, P.J., Lin, H.M., Deiner, S.G. & Levin, M.A. Validation of the All Patient Refined Diagnosis Related Group (APR-DRG) Risk of Mortality and Severity of Illness Modifiers as a Measure of Perioperative Risk. *J Med Syst* **42**, 81 (2018).

282. Feller, D.J., Zucker, J., Yin, M.T., Gordon, P. & Elhadad, N. Using Clinical Notes and Natural Language Processing for Automated HIV Risk Assessment. *J Acquir Immune Defic Syndr* **77**, 160-166 (2018).

283. Zhang, Y. et al. Assessing the impact of social determinants of health on predictive models for potentially avoidable 30-day readmission or death. *PLoS One* **15**, e0235064 (2020).

284. Solberg, L.I. Theory vs Practice: Should Primary Care Practice Take on Social Determinants of Health Now? No. *Ann Fam Med* **14**, 102-103 (2016).

285. Gottlieb, L., Hessler, D., Long, D., Amaya, A. & Adler, N. A randomized trial on screening for social determinants of health: the iScreen study. *Pediatrics* **134**, e1611-1618 (2014).

286. Larimer, M.E. et al. Health care and public service use and costs before and after provision of housing for chronically homeless persons with severe alcohol problems. *JAMA* **301**, 1349-1357 (2009).

287. Sandberg, S.F. et al. Hennepin Health: a safety-net accountable care organization for the expanded Medicaid population. *Health Aff (Millwood)* **33**, 1975-1984 (2014).

288. Gottlieb, L.M., Tirozzi, K.J., Manchanda, R., Burns, A.R. & Sandel, M.T. Moving electronic medical records upstream: incorporating social determinants of health. *Am J Prev Med* **48**, 215-218 (2015).

289. Lee, V.S. et al. Implementation of a Value-Driven Outcomes Program to Identify High Variability in Clinical Costs and Outcomes and Association With Reduced Cost and Improved Quality. *JAMA* **316**, 1061-1072 (2016).

290. Atlus, A. in The DO (2017).

291. Palano, G. et al. A high-content, in vitro cardiac fibrosis assay for high-throughput, phenotypic identification of compounds with anti-fibrotic activity. *J Mol Cell Cardiol* **142**, 105-117 (2020).

292. Zhao, H. et al. Microengineered in vitro model of cardiac fibrosis through modulating myofibroblast mechanotransduction. *Biofabrication* **6**, 045009 (2014).

293. Derakhshandeh, H., Kashaf, S.S., Aghabaglou, F., Ghanavati, I.O. & Tamayol, A. Smart Bandages: The Future of Wound Care. *Trends Biotechnol* **36**, 1259-1274 (2018).

294. Robson, M.C. et al. Sequential cytokine therapy for pressure ulcers: clinical and mechanistic response. *Ann Surg* **231**, 600-611 (2000).

295. Yamakawa, S. & Hayashida, K. Advances in surgical applications of growth factors for wound healing. *Burns Trauma* **7**, 10 (2019).

296. Nurkesh, A., Jaguparov, A., Jimi, S. & Saparov, A. Recent Advances in the Controlled Release of Growth Factors and Cytokines for Improving Cutaneous Wound Healing. *Front Cell Dev Biol* **8**, 638 (2020).

297.	Stevens, S.M., von Gise, A., VanDusen, N., Zhou, B. & Pu, W.T. Epicardium is required for cardiac seeding by yolk sac macrophages, precursors of resident macrophages of the adult heart. *Dev Biol* **413**, 153-159 (2016).

298.	Zhou, B. & Pu, W.T. Epicardial epithelial-to-mesenchymal transition in injured heart. *J Cell Mol Med* **15**, 2781-2783 (2011).

299.	Blom, J.N. & Feng, Q. Cardiac repair by epicardial EMT: Current targets and a potential role for the primary cilium. *Pharmacol Ther* **186**, 114-129 (2018).

300.	Kovacic, J.C. et al. Endothelial to Mesenchymal Transition in Cardiovascular Disease: JACC State-of-the-Art Review. *J Am Coll Cardiol* **73**, 190-209 (2019).

301.	Alonso-Herranz, L. et al. Macrophages promote endothelial-to-mesenchymal transition via MT1-MMP/TGFbeta1 after myocardial infarction. *Elife* **9** (2020).

302.	Marx, V. Method of the Year: spatially resolved transcriptomics. *Nat Methods* **18**, 9-14 (2021).

303.	Blanco, R. & Gerhardt, H. VEGF and Notch in tip and stalk cell selection. *Cold Spring Harb Perspect Med* **3**, a006569 (2013).

304.	Johnson, N.R. & Wang, Y. Drug delivery systems for wound healing. *Curr Pharm Biotechnol* **16**, 621-629 (2015).

305.	Kasiewicz, L.N. & Whitehead, K.A. Recent advances in biomaterials for the treatment of diabetic foot ulcers. *Biomater Sci* **5**, 1962-1975 (2017).

306.	Mahdipour, E. & Sahebkar, A. The Role of Recombinant Proteins and Growth Factors in the Management of Diabetic Foot Ulcers: A Systematic Review of Randomized Controlled Trials. *J Diabetes Res* **2020**, 6320514 (2020).

307.	Zhou, H., Della, P.R., Roberts, P., Goh, L. & Dhaliwal, S.S. Utility of models to predict 28-day or 30-day unplanned hospital readmissions: an updated systematic review. *BMJ Open* **6**, e011060 (2016).

308.	Obuobi, S., Chua, R.F.M., Besser, S.A. & Tabit, C.E. Social determinants of health and hospital readmissions: can the HOSPITAL risk score be improved by the inclusion of social factors? *BMC Health Serv Res* **21**, 5 (2021).

309.	Nagasako, E.M., Reidhead, M., Waterman, B. & Dunagan, W.C. Adding socioeconomic data to hospital readmissions calculations may produce more useful results. *Health Aff (Millwood)* **33**, 786-791 (2014).

310.	Bernheim, S.M. et al. Accounting For Patients' Socioeconomic Status Does Not Change Hospital Readmission Rates. *Health Aff (Millwood)* **35**, 1461-1470 (2016).

311.	Donze, J., Aujesky, D., Williams, D. & Schnipper, J.L. Potentially avoidable 30-day hospital readmissions in medical patients: derivation and validation of a prediction model. *JAMA Intern Med* **173**, 632-638 (2013).

312.	Ketterer, M.W., Draus, C., McCord, J., Mossallam, U. & Hudson, M. Behavioral factors and hospital admissions/readmissions in patients with CHF. *Psychosomatics* **55**, 45-50 (2014).

REFERENCES

313. Barnes, E.L. et al. Modifiable Risk Factors for Hospital Readmission Among Patients with Inflammatory Bowel Disease in a Nationwide Database. *Inflamm Bowel Dis* **23**, 875-881 (2017).

314. Young, S.D. Social Media as a New Vital Sign: Commentary. *J Med Internet Res* **20**, e161 (2018).

315. Merchant, R.M. et al. Evaluating the predictability of medical conditions from social media posts. *PLoS One* **14**, e0215476 (2019).

316. Ryall, K.A. et al. Network reconstruction and systems analysis of cardiac myocyte hypertrophy signaling. *J Biol Chem* **287**, 42259-42268 (2012).

317. Wynn, M.L., Consul, N., Merajver, S.D. & Schnell, S. Logic-based models in systems biology: a predictive and parameter-free network analysis method. *Integr Biol (Camb)* **4**, 1323-1337 (2012).

318. Peng, G.C.Y. et al. Multiscale modeling meets machine learning: What can we learn? *Arch Comput Methods Eng* **28**, 1017-1037 (2021).

319. Kirschner, D.E., Hunt, C.A., Marino, S., Fallahi-Sichani, M. & Linderman, J.J. Tuneable resolution as a systems biology approach for multi-scale, multi-compartment computational models. *Wiley Interdiscip Rev Syst Biol Med* **6**, 289-309 (2014).

320. Taschuk, M. & Wilson, G. Ten simple rules for making research software more robust. *PLoS Comput Biol* **13**, e1005412 (2017).

321. Swat, M.H. et al. Multi-scale modeling of tissues using CompuCell3D. *Methods Cell Biol* **110**, 325-366 (2012).

322. Ghaffarizadeh, A., Heiland, R., Friedman, S.H., Mumenthaler, S.M. & Macklin, P. PhysiCell: An open source physics-based cell simulator for 3-D multicellular systems. *PLoS Comput Biol* **14**, e1005991 (2018).

323. Dowden, H. & Munro, J. Trends in clinical success rates and therapeutic focus. *Nat Rev Drug Discov* **18**, 495-496 (2019).